UNIVERSIDADE DE SÃO PAULO

INSTITUTO DE ENERGIA E AMBIENTE
PROGRAMA DE PÓS-GRADUAÇÃO EM CIÊNCIA AMBIENTAL

ALYNNE ALMEIDA AFFONSO

Caracterização e monitoramento da dinâmica de alagamento e dos ambientes sazonalmente alagáveis da Volta Grande do Xingu através de sensoriamento remoto

São Paulo
2023

ALYNNE ALMEIDA AFFONSO

Caracterização e monitoramento da dinâmica de alagamento e dos ambientes sazonalmente alagáveis da Volta Grande do Xingu através de sensoriamento remoto

Versão Corrigida

Tese apresentada ao Programa de Pós-Graduação em Ciência Ambiental do Instituto de Energia e Ambiente da Universidade de São Paulo para a Obtenção do título de Doutor em Ciência Ambiental.

Área de Concentração: Ciência Ambiental

Orientador: Prof. Dr. Carlos Henrique Grohmann de Carvalho

São Paulo
2023

AUTORIZO A REPRODUÇÃO E DIVULGAÇÃO TOTAL OU PARCIAL DESTE TRABALHO, POR QUALQUER MEIO CONVENCIONAL OU ELETRÔNICO, PARA FINS DE ESTUDO E PESQUISA, DESDE QUE CITADA A FONTE.

FICHA CATALOGRÁFICA

Affonso, Alynne Almeida.

Caracterização e monitoramento da dinâmica de alagamento e dos ambientes sazonalmente alagáveis da Volta Grande do Xingu através de sensoriamento remoto. Alyne Almeida Affonso; orientador: Carlos Henrique Grohmann de Carvalho. – São Paulo, 2023.

234 f.: il., 30 cm.

Tese (Doutorado em Ciência Ambiental) – Programa de Pós-Graduação em Ciência Ambiental – Instituto de Energia e Ambiente da Universidade de São Paulo.

1. Sensoriamento remoto – Volta Grande do Xingu. 2. Mudança de uso e cobertura do solo. 3. Altimetria. Habitats alagáveis 4. Modelagem espacial 5. Espaçotemporal – análise I. Título.

Elaborado por Maria Penha da Silva Oliveira CRB-8/6961

Nome: AFFONSO, Alynne Almeida

Título: Caracterização e monitoramento da dinâmica de alagamento e dos ambientes sazonalmente alagáveis da Volta Grande do Xingu através de sensoriamento remoto

Título: Tese apresentada ao Programa de Pós-Graduação em Ciência Ambiental do Instituto de Energia e Ambiente da Universidade de São Paulo para a obtenção do título de Doutor em Ciência Ambiental.

Aprovado em: ____ / ____ / ____

Banca Examinadora

Prof. Dr. _____ Instituição: _____

Julgamento: _____Assinatura: _____

Prof. Dr. _____ Instituição: _____

Julgamento: _____Assinatura: _____

Prof. Dr. _____ Instituição: _____

Julgamento: _____Assinatura: _____

Prof. Dr. _____ Instituição: _____

Julgamento: _____Assinatura: _____

Prof. Dr. _____ Instituição: _____

Julgamento: _____Assinatura: _____

Prof. Dr. _____ Instituição: _____

Julgamento: _____Assinatura: _____

DEDICATÓRIA

Dedico este trabalho aos meus pais, Bety e Marcos, ao meu marido Diego e aos povos tradicionais e indígenas da Amazônia e da Volta Grande do Xingu.

AGRADECIMENTOS

Concluir um doutorado que atravessou uma pandemia é um feito e tanto, então, tenho muito a agradecer.

Esse trabalho só pode ser concluído devido ao tripé mãe, pai e marido. Então, as três primeiras pessoas a quem eu agradeço são minha mãe Bety, meu pai Marcão e meu marido Diego (Fyona), sem os quais eu não teria conseguido finalizar essa jornada. Meus pais que, desde o meu primeiro suspiro, apoiam incondicionalmente cada passo que eu dou e que se esforçam muito até hoje para me proporcionar o privilégio de ser cientista. Meu companheiro e melhor amigo, que foi a base para que toda a difícil trajetória do doutoramento acontecesse, me oferecendo apoio, amor, incentivo e não deixando que nada me distraísse do meu objetivo final. Eu amo vocês com cada átomo do meu corpo.

Muito obrigada à minha família, que apesar de pequena, é muito unida e presente. Vovó, titio, titia, Letícia, Julia, meus sogros Lenice e Jorge, parentes mais distantes: eu sou só gratidão. Obrigada por compartilharem comigo a caminhada que me levou a ser a primeira doutora da família.

Agradeço também minhas companheiras de jornada acadêmica Carol (Tatu) e Raquel com quem eu dividi tantas angústias e de quem eu recebi tanto encorajamento e conselhos. Às minhas amigas Sharon, Carla e Tays que nunca me deixam desanimar e sempre são tão gentis em me ouvir quando eu tagarelo sobre ciência sem parar. Ao meu amigo Kyle, que além das conversas de alto nível sobre Sensoriamento Remoto e as Ciências da Informação Geográfica, revisou cada texto em inglês que eu produzi desde 2016. Às sempre essenciais Gatas sem Fim, que nunca deixaram de ser a mola do poço e a luz do fim do túnel. E aos amigos da Geo Supply pelo companheirismo e amizade de todas as horas.

Ao meu orientador Carlos Grohmann (Guano), meu mais sincero e profundo muito obrigada, por me oferecer a oportunidade de trabalhar num tema tão desafiador e gratificante e por viabilizar toda a estrutura do SPAMLab. Aos Spammers por sempre compartilharem conhecimento, apoio e bons momentos, na academia e fora dela. Muito obrigada aos professores Luis Américo Conti e José Quintanilha por participarem de perto da elaboração dos artigos da tese e ao professor André Sawakuchi que além de co-autor, viabilizou a ida ao campo e minha participação em eventos do Observatório da Volta Grande do Xingu.

Agradeço do fundo do coração ao IEE e ao PROCAM: ao corpo discente, docente e principalmente, ao pessoal da secretaria.

Por fim, agradeço à Coordenação de Aperfeiçoamento de Pessoal de Nível Superior - Brasil (CAPES) pelo financiamento a este trabalho (Código de Financiamento 001).

EPÍGRAFE

“Todos serão arrastados pela mesma catástrofe, a não ser que se compreenda que o respeito pelo outro é a condição de sobrevivência de cada um.”
(Lévi-Strauss, 1993, p. 7)

“Estamos apreensivos, para além de nossa própria vida, com a da terra inteira, que corre risco de entrar em caos. Os brancos não temem, como nós, ser esmagados pela queda do céu. Mas um dia talvez tenham tanto medo disso quanto nós!”
(Kopenawa; Albert, 2015 p. 455, 468)

“Quem vê o rio de fora, de longe, só pelos números, não entende que existe uma sincronia perfeita entre a água, a floresta e seus povos. Mas quem vê desde dentro sabe, e está de olho no Xingu, porque vive no mesmo pulso do rio”.
(ISA; AYMÏX; UFPA, 2018, 3m18s)

RESUMO

AFFONSO, Alynne Almeida. Caracterização e monitoramento da dinâmica de alagamento e dos ambientes sazonalmente alagáveis da Volta Grande do Xingu através de sensoriamento remoto. 2023. 234 f. Tese (Doutorado em Ciência Ambiental) – Instituto de Energia e Ambiente, Universidade de São Paulo, São Paulo, 2023

Palavras-chave: Habitats alagáveis; Mudança de uso e cobertura do solo; Análise espaçotemporal; Modelagem espacial; SfM-MVS; Altimetria

A região da Volta Grande do Xingu (VGX) se destaca por sua singular biodiversidade e riqueza ambiental. Com sua geomorfologia única, composta por diversos canais entrelaçados, cachoeiras e corredeiras, foi escolhida como local para abrigar o Complexo Hidrelétrico de Belo Monte. No entanto, esse megaempreendimento representa uma ameaça à viabilidade da Volta Grande do Xingu e aos ecossistemas que sustentam a vida. Além disso, as populações tradicionais que habitam a área também correm riscos.

Esta pesquisa utiliza técnicas de análise por sensoriamento remoto para monitorar as mudanças na dinâmica de alagamentos e caracterizar os ambientes sazonalmente alagáveis pela influência do barramento do Rio Xingu na Volta Grande. A tese é composta por uma coletânea de três artigos, cada um abordando uma perspectiva diferente da Volta Grande do Xingu e seus desafios ambientais.

O primeiro capítulo enfatiza a importância das ferramentas de sensoriamento remoto na monitorização dessas mudanças e ressalta a necessidade de combinar diferentes técnicas de classificação de imagens. O segundo capítulo introduz uma abordagem inovadora, utilizando modelagem 3D para caracterizar as áreas sazonalmente alagáveis na VGX. O terceiro capítulo se concentra nos impactos hidrológicos do Complexo Hidrelétrico de Belo Monte na VGX, com foco na extensão das áreas alagáveis e na elevação da superfície da água do Rio Xingu.

Essa pesquisa oferece contribuições significativas para as Ciências Ambientais, pois a combinação de sensoriamento remoto, modelagem 3D e medições hidrológicas possibilitou uma análise abrangente da área de estudo, permitindo uma compreensão mais profunda das mudanças que estão ocorrendo, ampliando as possibilidades de monitoramento e preservação.

ABSTRACT

AFFONSO, Alynne Almeida. Characterization and monitoring of the flooding dynamics and seasonally flooded environments of the Volta Grande do Xingu through remote sensing. 2023. 234 f. Tese (Doutorado em CIência Ambiental) – Instituto de Energia e Ambiente, Universidade de São Paulo

Keywords: Flooded habitats; Land use and land cover change; Spatiotemporal analysis; Spatial modeling; SfM-MVS; Altimetry

The Volta Grande do Xingu area stands out for its unique biodiversity and environmental richness. With its distinctive geomorphology, featuring several anabranching river channels, waterfalls, and rapids, it was chosen as the site to build the Belo Monte Hydroelectric Complex. However, this mega-project poses a threat to the viability of the Volta Grande do Xingu and the ecosystems that supports life. Additionally, the traditional populations living in the area are also at risk.

This research employs remote sensing analysis techniques to monitor changes in flooding dynamics and characterize seasonally flooded environments influenced by the damming of the Xingu River in the Volta Grande. The thesis consists of a collection of three scientific articles, each addressing a different perspective of the Volta Grande do Xingu and its environmental challenges.

The first chapter underscores the importance of remote sensing tools in monitoring these changes and emphasizes the need to combine different image classification techniques. The second chapter introduces an innovative approach, utilizing 3D modeling to characterize the seasonally flooded environments in Volta Grande. The third chapter focuses on the hydrological impacts of the Belo Monte Hydropower Complex, with a focus on the extent of flooded areas and the elevation of the Xingu River's water surface.

This research provides significant contributions to Environmental Sciences, as the combination of remote sensing, 3D modeling, and hydrological measurements has enabled a comprehensive analysis of the study area, allowing for a deeper understanding of the ongoing changes and expanding the possibilities for monitoring and preservation.

LISTA DE ILUSTRAÇÕES

LISTA DE MAPAS

LISTA DE TABELAS

SUMÁRIO

1. INTRODUÇÃO

1.1. Organização da tese

A presente tese foi organizada em forma de coletânea de artigos, e é composta por sete capítulos, cada um com um papel específico na construção do conhecimento e no alcance dos objetivos propostos.

No capítulo introdutório, estabelece-se o contexto geral da pesquisa, delineando-se os objetivos do estudo e apresentando uma visão geral das questões abordadas, contextualizando sobre a importância do tema e as perguntas a serem respondidas.

O segundo capítulo é dedicado à fundamentação teórica, que foi elaborada através de uma extensa e abrangente revisão bibliográfica. Esse capítulo fornece sólido embasamento conceitual, abordando as informações e peculiaridades da área de estudo, bem como as técnicas de sensoriamento remoto utilizadas ao longo do trabalho.

O terceiro capítulo detalha a metodologia empregada nesta pesquisa. Explica-se minuciosamente os procedimentos e abordagens adotados para a coleta, processamento e análise dos dados. Este capítulo fornece uma base clara para a compreensão dos métodos utilizados em nossa investigação, principalmente os que não foram esmiuçados nos artigos.

No capítulo 4, apresenta-se o primeiro dos três artigos que compõem esta tese. Este artigo descreve uma comparação entre diferentes métodos de classificação supervisionada em um estudo de uso e cobertura do solo na área de estudo, pré e pós a instalação do Complexo Hidrelétrico de Belo Monte. Os resultados desse artigo são fundamentais para o entendimento das mudanças na paisagem ao longo do tempo.

O quinto capítulo é dedicado ao segundo artigo, que aborda a modelagem 3D dos ambientes alagáveis ameaçados da VGX. Este trabalho fornece *insights* valiosos sobre a topografia e a morfologia dessas áreas críticas.

No sexto capítulo, apresentamos o terceiro artigo, que se concentra em uma observação abrangente da VGX, principalmente por meio de dados de satélite. Nesse estudo, investiga-se-se a variação da superfície da água e da extensão da área alagada na VGX, o que lança luz sobre as dinâmicas hídricas na região e sua relação com a instalação do complexo hidrelétrico.

O capítulo final resume numa breve discussão integrativa os principais resultados obtidos ao longo da pesquisa e suas implicações. Destaca-se as contribuições originais desta tese para o campo de estudo e as possíveis direções para pesquisas futuras.

1.2. Contexto Geral

O bioma Amazônia abrange no Brasil uma área de 4.871.000km², sendo formado por 23 unidades biogeográficas e representa aproximadamente 48% do território brasileiro (Ferreira, 2003). Sua bacia hidrográfica é a maior do mundo, com drenagem de aproximadamente 6 milhões de km², sendo que destes, 3,9 milhões estão no Brasil (Ayres, 1995) (Figura 1a). Isso faz com que o complexo amazônico compreenda o maior sistema de água doce do mundo, contendo cerca de 20% do suprimento mundial do recurso (Oltman, 1968). A floresta amazônica pode ser dividida em apenas três grandes formações vegetais: florestas de igapó, de várzea (que juntas, estima-se serem 2% de toda a Amazônia brasileira, ou seja mais 120.000 km² de terras alagáveis) e de terra firme (RadamBrasil, 1978; Kubitzki, 1989).

Figura 1: (a) Bacia hidrográfica amazônica com seus principais rios. (b) Detalhe da bacia hidrográfica do Xingu. (c) Área de estudo em destaque com a localização do CHBM, das terras indígenas Paquiçamba e Arara da Volta Grande e da estação ANA 18850000.

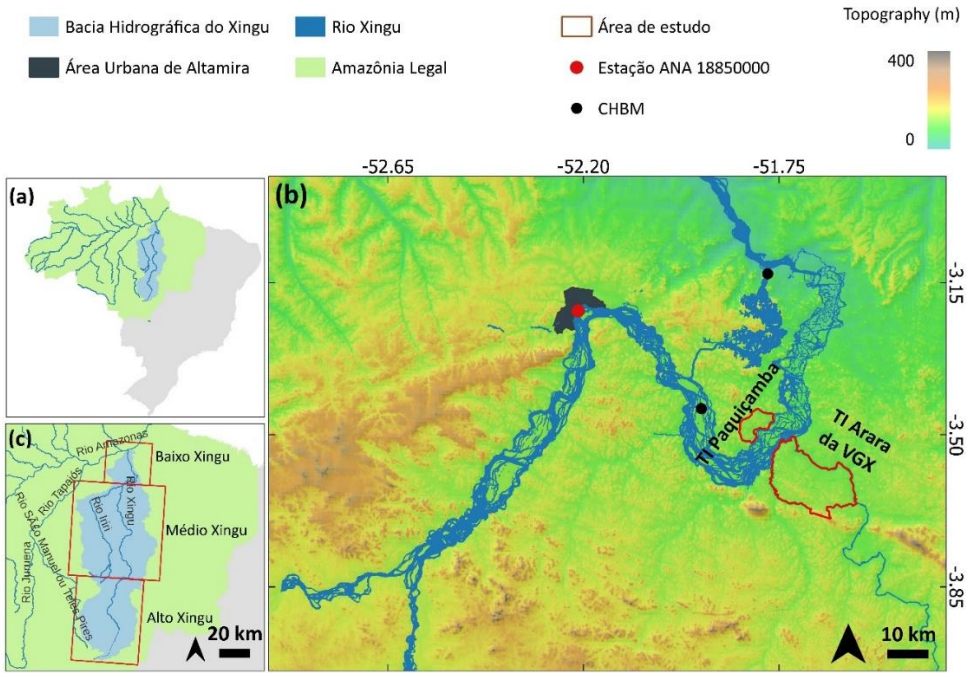

Fonte: Autoria própria

O leste da Amazônia é dominado por rios de água clara, os quais drenam os planaltos das Guianas e do Brasil Central e são caracterizados pela baixa concentração de sedimentos em suspensão e sólidos dissolvidos. Nesta região, os rios Xingu e Tapajós, em conjunto com o Rio Tocantins, formam os principais sistemas fluviais de água clara da América do Sul. Estes rios destacam-se por sustentar grande variedade de ambientes aquáticos e alagáveis (Ayres, 1995).

Alterações nos padrões da drenagem, induzidas por variações de precipitação e instalação de barragens determinam as características e distribuição dos ambientes aquáticos e alagáveis, uma vez que influenciam em seu equilíbrio. As dinâmicas fluvial e sedimentar controlam as características da coluna d'água e do substrato dos canais fluviais, pois regulam a concentração de sedimentos em suspensão e proporcionam variação temporal e espacial de erosão, transporte e deposição de sedimentos, além de determinar as áreas de alagamento, essenciais para a manutenção da vegetação e habitats aluviais. Em determinados setores da drenagem a dinâmica sedimentar e fluvial mantém o equilíbrio que sustenta a diversidade de ambientes aquáticos e de transição e a biodiversidade dos rios amazônicos de água clara (Archer, 2005).

A ciclicidade natural dos pulsos de cheia e seca no ambiente amazônico é de extrema importância, vital para a manutenção da biodiversidade, já que determina a extensão das áreas alagáveis, que abrigam muitas espécies endêmicas, adaptadas ao ciclo de inundação (Junk *et al.*, 1989).

Impactos relacionados à perda de nichos ecológicos em áreas à montante e à jusante das barragens em grandes rios tropicais não podem ser negligenciados. De acordo com Winemiller *et al.* (2016) estes impactos têm sido avaliados de modo tardio, afetando sua capacidade de recuperação.

No caso do rio Xingu, alterações causadas pelas barragens do Complexo Hidrelétrico de Belo Monte (CHBM) podem provocar transformações nos habitats, ecossistemas e biomas, resultando em perda de espécies endêmicas e de importância socioeconômica, visto que impactos antropogênicos podem trazer desequilíbrio de padrões e processos geológicos e geomorfológicos e das funções ecológicas dos ambientes afetados, que comprometem inclusive os modos de vida de comunidades tradicionais que dependem diretamente da vazão do rio Xingu e de seus pulsos de cheia (Costa *et al.*, 2012; Assahira, 2014).

A Volta Grande do Xingu (VGX) é trecho de impacto direto da usina do CHBM, e vem sofrendo com o processo de barramento do rio Xingu (que ocorreu em novembro de 2015). Nesse trecho, houveram mudanças que alteraram radicalmente o rio: a montante da barragem foi criado um imenso lago que alagou floresta, ilhas e deslocou povos tradicionais. A jusante do barramento, a calha do rio secou, dificultando a navegação e afetando a saúde da fauna aquática e da vegetação, dificultando a pesca e alterando de forma profunda o modo de vida das populações tradicionais, tão dependentes do rio (Figura 1b) (Pezzuti *et al.*, 2018).

Em 2019, era prevista a implementação de um esquema de hidrogramas artificiais, nomeado “Hidrograma de Consenso (HC)”, por parte da operadora da UHE Belo Monte. O HC deveria ser o instrumento principal de mitigação dos efeitos adversos da redução de vazão na VGX devido ao barramento do rio, e se propunha a conciliar a geração de energia, a quantidade de água indispensável para as funções ecológicas da região e a manutenção de suas condições de navegabilidade (Eletrobrás, 2009b). A recomendação do Estudo de Impacto Ambiental (EIA) elaborado como parte dos requisitos para a implementação e operação do CHBM propõe uma alternância de hidrogramas, a ser testada por um período de seis anos, iniciado em 2019 (após o CHBM começar a operar em capacidade máxima), que seria intercalado entre hidrograma A, disponibilizando para a época de cheia 4.000 m³/s e hidrograma B, disponibilizando 8.000 m³/s, simulando os pulsos de cheias e secas naturais do rio (Tabela 1). No entanto, esses valores significam uma redução de até 80% da vazão total do Xingu no pulso da cheia (Zuanon *et al.*, 2019).

Tabela 1: Vazões médias dos Hidrogramas A e B a serem implementados no Trecho de Vazão Reduzida.

Hidrograma	Jan	Fev	Mar	Abr	Mai	Jun	Jul	Ago	Set	Out	Nov	Dez
A (m^3/s)	1.100	1.600	2.500	4.000	1.800	1.200	1.000	900	750	700	800	900
B (m^3/s)	1.100	1.600	4.000	8.000	4.000	2.000	1.200	900	750	700	800	900

Fonte: Brasil, Ministério do Meio Ambiente, Agência Nacional de Águas. Resolução n° 740, de 06 de outubro de 2009. Anexo III1

Antes mesmo do início dos trabalhos de construção do CHBM e da operação das turbinas, haviam evidências de que o HC sugerido traria uma série de impactos, em parte já prognosticados, que poderiam inviabilizar a vida na região (Fearnside, 2006; Barreto *et al.*, 2011; Costa *et al.*, 2012; Ritter *et al.*, 2017; Pezzuti *et al.*, 2018; Zuanon *et al.*, 2019), impactos esses que vem sendo confirmados ao longo do tempo, com a consolidação da operação completa do complexo hidrelétrico (Kalacska *et al.*, 2020a; Calvi, 2020a; Monteiro Neto *et al.*, 2021; Affonso *et al.*, 2023a).

1.3. Hipótese

Partindo-se da premissa que a Volta Grande do Xingu vem sofrendo alterações em sua dinâmica espaço-temporal devido ao barramento do fluxo natural do Rio Xingu e da implementação de hidrogramas artificiais, a hipótese deste estudo é a de que técnicas de sensoriamento remoto e modelagem espacial serão capazes de mensurar tais alterações, principalmente nos ambientes sazonalmente alagáveis da Volta Grande do Xingu, sendo possível caracterizá-los em cenários pré e pós intervenção.

1.4. Objetivos

Uma vez que o manejo de ecossistemas sob elevada pressão deve abranger uma descrição explícita de sua estrutura, funções e variabilidade, visando caracterizar diferenças entre as condições atuais, as anteriores ao impacto e as desejadas pós intervenção, e buscando definir o significado ecológico e os indicadores responsáveis pela manutenção de condições capazes de sustentar a vida nos

[1] BRASIL, Ministério do Meio Ambiente, Agência Nacional de Águas. Gerência de Regulação de Uso. Nota Técnica n° 129/2009/GEREG/SOF-ANA. Brasília, 2009.

ecossistemas sazonalmente alagáveis, protegendo sua biodiversidade e suas funções ecossistêmicas, este trabalho se propõe a caracterizar e monitorar a dinâmica do alagamento e dos ambientes sazonalmente alagáveis da VGX por meio de diferentes técnicas de processamento digital de imagens aéreas e de satélite.

Como a dinâmica posterior à construção e início das operações do complexo hidrelétrico têm potencial para afetar os ecossistemas sazonalmente alagáveis de forma significativa, e muitas vezes, até irreversível, principalmente através do barramento do rio, é importante estabelecer as condições precedentes à intervenção, possibilitando identificar os processos e dinâmica naturais, e assim, elaborar e estabelecer boas estratégias de mitigação que permitam a manutenção das funções ecossistêmicas, mesmo após a interferência antrópica. Para tal, apresentam-se os seguintes objetivos:

- Analisar as mudanças na cobertura do solo na região da VGX no período 2000-2017 por meio de diferentes técnicas de classificação supervisionada de imagens;
- Caracterizar as áreas sazonalmente alagáveis na região da VGX por meio de modelagem 3D de imagens aéreas obtidas por Aeronave Remotamente Pilotada;
- Analisar os impactos hidrológicos do CHBM na VGX, com foco na extensão das áreas alagáveis e elevação da superfície da água do rio Xingu, por meio de dados de altimetria por satélite e imagens de radar de abertura sintética.

A intenção da análise espaço-temporal da calha e do fluxo do rio Xingu no trecho da Volta Grande é estabelecer as linhas de base naturais anteriores ao barramento e assim, avaliar os impactos atuais e planejar melhor o manejo para garantir um futuro sustentável, tanto do ecossistema, como da geração de energia pelo CHBM.

1.5. Justificativa e originalidade do trabalho

A implantação de barragens, alterações no uso do solo e mudanças climáticas são apontados como os grandes responsáveis na alteração dos padrões de fluxo e volume de água e do aporte sedimentar para corpos de água em todo o planeta (Fearnside, 2015). O barramento de grandes rios, como os realizados para a implantação de usinas hidrelétricas pode comprometer o fluxo natural de corpos de água, uma vez que a dinâmica de vazão é alterada drasticamente para a construção de reservatórios.

No caso do CHBM, os impactos causados pela retenção do rio Xingu se referem à redução da vazão natural do rio na VGX. Os setores afetados por este barramento possuem elevada relevância ecossistêmica, e os nichos ecológicos e a biodiversidade local correm riscos quando o fluxo natural do Xingu, que obedece a pulsos de cheia e seca bem definidos, é alterado bruscamente, acarretando em redução da complexidade e diversidade de habitats de espécies aquáticas e vegetais. O impacto da interrupção do ciclo de alagamento causado pela barragem gera supressão da vegetação adaptada aos ambientes alagados (Assahira, 2014) e consequente perda de habitat para as espécies ajustadas a esse tipo de ambiente, gerando perigo real de extinção de espécies locais e endêmicas (Souza, 2015), o que coloca em risco o modo de vida e a segurança de populações tradicionais e que dependem do rio.

Se por um lado, Nelson e Oliveira (2001) afirmam que trabalhos que descrevam a florística e a estrutura da vegetação periodicamente inundadas da Amazônia são escassos quando comparados ao esforço de pesquisa no Norte global, com apenas poucos inventários florestais disponíveis no Brasil, o nível das informações científicas sobre os mais diversos aspectos dos ecossistemas amazônicos, incluindo ambientes alagáveis, como solos, geomorfologia, hidrologia, limnologia, geologia, biogeografia, paleoecologia e ecologia, aumentou consideravelmente nos últimos anos, embora se reconheça que muito conhecimento científico adicional ainda precisa ser gerado (Salomão *et al.*, 2007).

Como bem lembra Sabaj-Perez (2015), o que se perde na VGX com os impactos decorrentes do barramento do rio não são pontos em um mapa ou uma mera descrição de organismos e sua distribuição em inventários. Perde-se cachoeiras, canais, e o dinâmico pulso de inundação que fomenta a excepcional complexidade

física e sazonal do Xingu. Perde-se a resiliência de um sistema que era, até recentemente, um incubador da diversidade e evolução de organismos e do ambiente aquático. A perda é principalmente pronunciada na região do Xingu, que é o segundo maior sistema de águas claras na América do Sul (o maior, Tocantins, foi barrado ainda em 1984).

Dessa forma, levando em consideração o potencial dos impactos causados pela implementação e operação do CHBM, e num contexto de carência de trabalhos de descrição e compreensão dos ambientes sazonalmente alagáveis e sua dinâmica de alagamento, esta pesquisa pretende gerar resultados de grande relevância à manutenção do ambiente amazônico e oferecer subsídios à operação sustentável de complexos hidrelétricos, sendo de grande interesse para a comunidade científica, sociedade e tomadores de decisão.

1.5.1. A Questão Indígena e Ribeirinha

O rio Xingu e seus afluentes possuem áreas de pesca tradicionais, piracemas e berçários de peixes, aves e quelônios, muitos deles endêmicos, em toda a sua extensão, e qualquer alteração no fluxo das águas da Volta Grande afeta diversos processos ecológicos e sociais interdependente (ISA; AYMÏX, 2018).

A construção do CHBM afetou a pesca das comunidades tradicionais. Os pescadores são unânimes em afirmar que a instalação do complexo hidrelétrico foi a grande responsável pela perda de áreas pesqueiras e o aumento dos custos da atividade pesqueira, tornando-a inviável como fonte de renda principal para muitas das famílias que dela dependiam. Como impactos diretos da obra, são citados a forte iluminação, as explosões, o aumento da turbidez da água e o aterramento das piracemas. O alagamento das áreas destinadas aos reservatórios suprimiu ilhas e igarapés, afetando as piracemas, os berçários da fauna aquática e alterando as áreas de alimentação dos peixes e quelônios, prejudicando a ecologia das espécies e a atividade pesqueira da região (ISA, 2016a).

Especificamente na VGX, o barramento desviou o fluxo do rio para o abastecimento do reservatório intermediário, afetando de forma impactante a configuração da paisagem: a montante da barragem as ilhas foram inundadas, as cachoeiras foram suprimidas e a vegetação foi submersa. A jusante da barragem, a vazão de água está reduzida. A Volta Grande do Xingu passa a ser conhecida como o Trecho de Vazão Reduzida (TVR), perdendo assim sua identidade. A seca

permanente dificultou a navegação e locais de pesca desapareceram, segundo relata o Cacique Gilliard Juruna, da Aldeia Miratu (ISA, 2016b, 1m14s):

“Mudou muita coisa aqui. Várias cachoeiras que tinham foram tudo pro fundo d’água, né? As ilhas tão debaixo da água. E a vegetação toda aqui tá debaixo d’água, né? E isso não volta mais atrás, a beleza que a gente tinha antigamente, foi tudo embora. Acabou com tudo”.

Essas mudanças atingiram em cheio as principais fontes de renda das populações da Volta Grande: a pesca ornamental e a pesca para subsistência e comercialização (Pezzuti *et al.*, 2018; Zuanon *et al.*, 2019) (Figura 2).

Figura 2: Peixes do Xingu adaptados às cachoeiras e quedas d´água, endêmicas do Xingu, fonte de renda e subsistência aos pescadores da região.

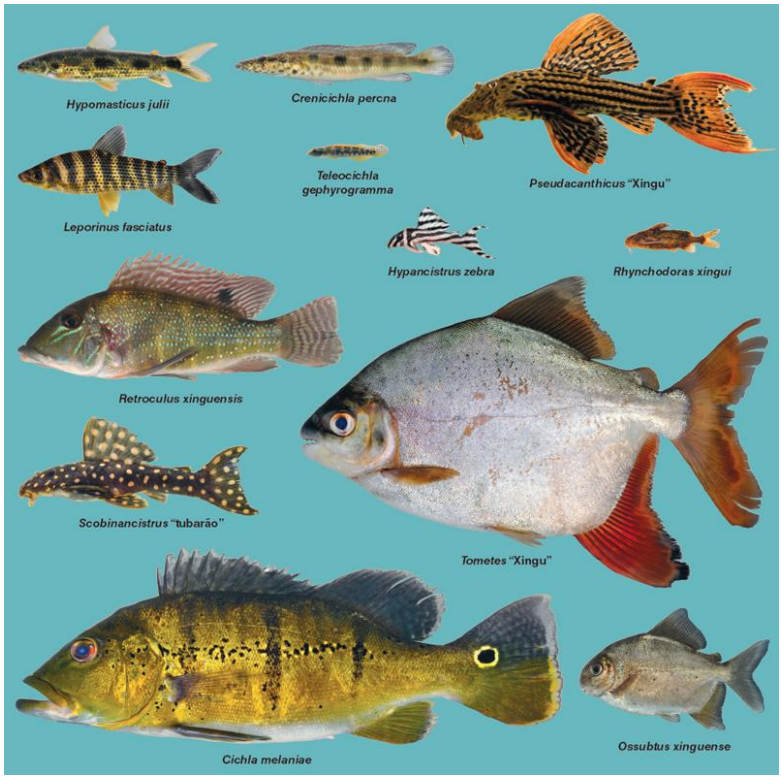

Fonte: Mark Sabaj Pérez (https://www.americanscientist.org/article/where-the-xingu-bends-and-will-soon-break)

Os cascudos ornamentais do Xingu (família *Loricariidae*, endêmica da América do Sul) tem representantes exclusivos endêmicos na Volta Grande (Figura 3), conhecidos como peixe zebra (*Hypancstrus zebra*) (Figura 4). Embora os lucros de sua comercialização fiquem, em grande parte, nas mãos dos atravessadores, muitos pescadores de Altamira garantem importante parte de sua renda coletando peixes zebra, destinados ao aquarismo. O barramento do rio coloca em risco não só o

habitat natural e a ocorrência desta importante espécie endêmica, mas também, uma importante atividade econômica da região (Sabaj-Perez, 2015).

Figura 3: Cascudos ornamentais (família *Loricariidae*) e raias de água doce endêmicos da Volta Grande do Xingu, adaptados às corredeiras, cachoeiras e piscinas formadas nos pedrais.

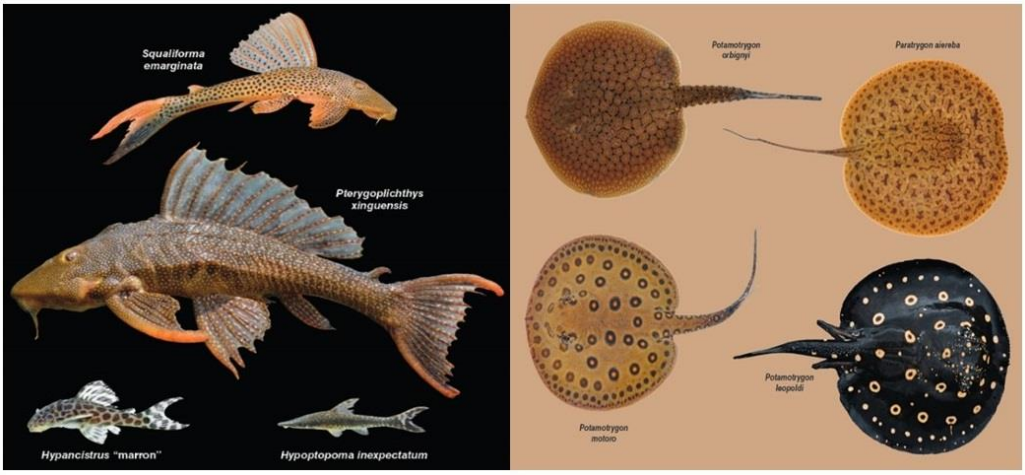

Fonte: Mark Sabaj Pérez (https://www.americanscientist.org/article/where-the-xingu-bends-and-will-soon-break)

Figura 4: *Hypancistrus zebra*, o peixe-zebra, símbolo da Volta Grande do Xingu.

Fonte: SILVA *et al.*, 2014[2], disponível em https://www.researchgate.net/figure/Hypancistrus-zebra-specimen_fig1_261221536

As áreas de pesca que abastecem a Terra Indígena Paquiçamba e a Terra Indígena Arara da VGX podem ser afetadas de forma irremediável, colocando em risco a segurança alimentar dos povos tradicionais, uma vez que não só a qualidade do pescado é afetada (há abundantes relatos de que os peixes e as tracajás – quelônios típicos da região – tem adoecido), mas também a qualidade da água tem sido prejudicada (Pezzuti *et al.*, 2018; Zuanon *et al.*, 2019; Palmquist, 2023). Além

[2] Silva, M; Ribeiro, E.D.; Matoso, D.A.; Sousa, L.M.; Hrbek, T.; Py-Daniel, L.R.; Feldberg, E. 2014. Chromosomal polymorphism in two species of *Hypancistrus* (Siluriformes: Loricariidae): na integrative approach for understanding their biodiversity. Genetica, 142, 127-139. 10.1007/s10709-014-9760-y

disso, os conhecimentos tradicionais ligados ao rio e à floresta dos povos que habitam as margens do Xingu na Volta Grande estão ameaçados. As comunidades de pescadores e seu conhecimento sobre a ecologia do Xingu não se sustentam numa terra onde o rio não mais existe, conforme a fala de Jailson Juruna, liderança da Aldeia Miratu (ISA; AYMÏX, 2017, 1m44s):

"O rio Xingu é tudo. Tem um ditado que a gente fala, é o nosso pai e a nossa mãe. Ele nos fornece a nossa vida, a nossa alimentação, nos dá tudo. Tudo que a gente quer o Rio Xingu nos fornece. Então ele é tudo para nós".

As comunidades afetadas alegam que as medidas mitigatórias (como a transposição das embarcações e a escada de peixes) e de compensação não remediam satisfatoriamente os impactos sobre a navegação, a pesca, a migração dos peixes os pulsos de cheia e seca (ISA, 2016a).

2. FUNDAMENTAÇÃO TEÓRICA

2.1. Área de estudo

De acordo com a classificação de Sioli (1950), o rio Xingu, que é um dos maiores e mais volumosos afluentes do Rio Amazonas, pertence ao grupo de rios de águas claras – ou seja, pobres em sedimentos inorgânicos dissolvidos (Irion; Adis, 1979). A bacia do Xingu é dividida em Alto, Médio e Baixo Xingu, e possui uma extensão de cerca de 1.900 km, desde sua nascente localizada no Planalto Central (a oeste da Serra do Roncador e ao norte da Serra Azul, leste do Mato Grosso) no Alto Xingu, até sua foz na margem direita do rio Amazonas no Baixo Xingu, desaguando ao sul da ilha de Gurupá no Pará, correndo na direção sul-norte, paralelo aos rios Tapajós e Tocantins. Sua área de drenagem é de aproximadamente 530.000 km² (Figura 1c).

A vazão média é de 9.700 m³/s, mas pode variar significativamente ao longo do ano, com médias tão baixas quanto 1.000 m³/s na estação seca a extremos médios em torno de 20.000 m³/s nas estações chuvosas (Latrubesse; Franzinelli, 2005). A região é regida pelo Sistema de Monção da América do Sul (SMAS), sendo que o Baixo Xingu recebe grande influência dos ventos trazidos pela Zona de Convergência Intertropical (ZCIT) (Garreaud *et al.*, 2009). Esses fenômenos, através do regime de pluviosidade, influenciam o pulso de inundação. A estação chuvosa é entre Novembro e Julho, sendo os picos de vazão máxima entre Março, Abril e Maio. A estação seca ocorre entre Agosto e Novembro, com picos de vazão

mínima entre Setembro e Outubro. A bacia hidrográfica do Xingu possui cobertura vegetal diversa, uma vez que o avanço da floresta amazônica para outras regiões influencia sua fisionomia, que se modifica devido ao clima (Soares, 1953). A vegetação ao longo do rio Xingu inclui floresta tropical aberta a densa, trechos de savana e vegetação de influência fluvial e lacustre (IBGE, 2004).

Sabaj-Perez (2015) descreve de forma bastante detalhada o trecho de 130 km da VGX. A "volta grande" responsável pelo seu nome é o resultado de uma queda de 90 metros, que muda o curso do rio em cerca de 90° em cada uma das três grandes voltas. A primeira volta é em frente à cidade de Altamira, onde uma estrutura de basalto redireciona o fluxo do sentido norte para sudeste. Ao adentrar na Volta Grande, o rio se abre em diversos canais entremeados por ilhas e baixios. No Sul da Volta Grande, uma nova interrupção do curso do rio, causada pelos pedrais de Três Palmeiras, direcionam o rio à nordeste. A porção inferior do Xingu é um emaranhado de canais desenhados por diversas fraturas no embasamento rochoso, formando um labirinto de riachos, corredeiras e cachoeiras formadas e delimitadas por afloramentos graníticos (Figura 1b).

O autor continua: "As cascatas mais espetaculares são a cachoeira de Jericoá, no ponto médio da Volta Grande, onde grande parte da água do Xingu ziguezagueia através de um estreito canal em forma de Z no leito rochoso (Figura 5). No limite a jusante de Volta Grande, três tranças principais se aglutinam em um canal que tem cerca de meio quilômetro de largura em seu ponto mais estreito e 80 metros de profundidade. Aqui, o Xingu completa sua saída do Escudo Brasileiro e gradualmente se alarga em uma ria semelhante a um estuário enquanto flui através de rochas sedimentares do Paleozóico ao Cretáceo até sua confluência com o Amazonas".

Figura 5: A esquerda, Canal em forma de Z, por onde fluem as águas que formam a cachoeira do Jericoá (a direita).

Fonte: Mark Sabaj Pérez (https://www.americanscientist.org/article/where-the-xingu-bends-and-will-soon-break)

Segundo Sawakuchi *et al.* (2015), o leito do Xingu é constituído por areia fina e grossa, baixa carga em suspensão e águas neutras a alcalinas. Ele flui como um rio dominado por rochas até adentrar na bacia sedimentar amazônica. Nesta transição, há uma queda repentina de uma altitude de 50-60 metros até 5-20 metros e, a partir daí, passa a sofrer influência das marés.

2.2. Ambientes alagáveis

Os ambientes alagáveis do planeta vêm consistentemente sendo convertidos para áreas não-alagáveis (IPCC, 2022). Em alguns países, as taxas de destruição são alarmantes, e estimativas mostram que cerca de 50% dos ambientes alagáveis do mundo todo já foram perdidos (Russi *et al,*. 2013). Atividades relacionadas exclusivamente ao desenvolvimento humano como drenagem para agricultura, desmatamento (seja para atividade madeireira ou produção de carvão), conversão para pasto ou cultivo, aterramento para construção de portos ou expansão de áreas urbanas e construção de reservatórios para produção de energia estão entre as principais atividades que colocam em risco as áreas alagáveis globais (Diegues, 1994; Prigent *et al.*, 2012). Mapear e conhecer estes ambientes é uma das principais ações de conservação, para que medidas apropriadas de manejo possam ser tomadas corretamente.

De forma geral, há uma carência histórica na investigação científica das áreas alagáveis ao redor do planeta. Não há uma abundância de inventários de ambientes alagáveis e seus componentes na maioria dos países por três principais razões: (1) O custo de se conduzir um levantamento detalhado, principalmente em grande escala; (2) os desafios técnicos de mapeamento e análise quantitativa, seja por

complexidades nas técnicas de sensoriamento remoto ou desafios em campo e (3) o financiamento para esse tipo de pesquisa que as vezes, compete com outras prioridades de governos e universidades (Tiner, 2015). Os inventários de ambientes alagáveis muitas vezes não são consistentes em suas metodologias, gerando diferentes definições e classificações, dificultando iniciativas de análises comparativas entre diferentes ambientes.

Enquanto há abundância de dados para as regiões temperadas do Hemisfério Norte, a pesquisa em ambientes alagáveis tropicais, subtropicais ou temperados meridionais é ainda incipiente, até mesmo inexistente para alguns biomas e regiões. A necessidade ou possibilidade de estudar as áreas alagadas era limitada ao hemisfério norte (Junk, 1980), onde se concentram a maior parte dos estudos em limnologia, devido ao histórico de modificações e destruição destes ambientes, que perderam espaço para a industrialização pós Revolução Industrial. Nas regiões tropicais, o estudo das áreas inundadas era tão incipiente que a limnologia - "a ciência abrangente das águas doces" (Junk, 1980, p. 775) - podia ser descrita como uma ciência de regiões temperadas, uma vez que os manuais existentes até aquele momento haviam sido elaborados para o hemisfério norte em geral, e os modelos desenvolvidos para estas regiões eram extrapolados para todas as áreas do globo.

Tal afirmação pode ser verificada pelos esquemas de classificação de ambientes alagáveis, que não são homogêneos na literatura e variam geograficamente ou de acordo com os interesses ou da disciplina da classificação. Os ambientes alagáveis podem ser identificados pelo seu tipo de solo, sua geomorfologia, pelas características biogeoquímicas da água, pela vegetação ou pela paisagem em que estão inseridos. A classificação de áreas alagáveis pode ser biológica, física, química ou hidrogeomorfológica, não havendo uma definição universalmente aceita. Apesar dessas diferenças, ambientes alagáveis podem ser categorizados em vários tipos, baseados em propriedades comuns a todos eles.

No entanto, a maioria dos trabalhos corrobora que as variações na hidrologia são o fator principal que cria os diferentes tipos de ambientes alagáveis (Tiner, 2015). Os padrões de inundação podem ser regulares, quando as áreas são alagadas ou inundadas periodicamente e de forma consistente e previsível (como em áreas influenciadas por marés ou ciclos sazonais) ou áreas irregularmente alagáveis, que não seguem um padrão de inundação, como áreas que se alagam ou inundam por

excesso de chuvas ou áreas influenciadas por repiquetes em rios (subida e descida vertiginosa das águas num curto espaço de tempo).

Existem alguns sistemas de classificação internacionais que utilizam um sistema de classificação horizontal (ou seja, uma lista simples com um número finito de tipos baseados em características gerais). Essas classificações, apesar de abrangentes, não são universalmente aceitas por não incluírem especificidades de sistemas alagáveis do mundo todo e vêm sendo utilizados de forma inconsistente. Como exemplo, temos o sistema de classificação internacional RAMSAR (RAMSAR, 1971), o sistema de classificação de Cowardin *et al.* (1979) e o Sistema de Classificação Hidrogeomórfica (HGM) de Brinson (1993) (Classificação HGM). Como exemplo de sistemas de classificação regionais, específicas para regiões ou países, temos adaptações do sistema de Cowardin *et al.*para as áreas mediterrâneas (Farinha *et al.*, 2015), as classificações canadenses (Warner; Rubec, 1997), australianas (Green, 1997) e do leste da África (FAO, 1998).

Segundo Junk (1980), esse desequilíbrio geográfico nos esforços de investigação entre ambientes alagáveis setentrionais e meridionais resultou em um número menor de pesquisas sobre os corpos d'água mais comumente encontrados nas regiões tropicais até o começo da segunda metade do século XX, quando os estudos de áreas alagadas eram, de fato, mais restritivos quanto à grande variedade de corpos d'água existentes no mundo todo. Observando as diferenças na classificação de águas paradas e águas correntes e os distintos padrões de alagamento dos rios do hemisfério norte em relação aos rios do hemisfério sul, o autor apontou a importância de se considerar uma área de transição entre ambientes terrestres e aquáticos como uma unidade ecológica a fim de investigá-la de maneira abrangente, sugerindo que áreas inundáveis deveriam ser consideradas como ecossistemas específicos.

Na segunda metade do século XX, devido à relação entre meio ambiente terrestre e aquático, os trabalhos a respeito de áreas alagáveis começaram a se destacar também nas regiões tropicais, onde problemas decorrentes de projetos desenvolvimentistas (como hidrelétricas, áreas agricultáveis em grande escala e represas) exigiam detalhes destas regiões.

Sioli (1951 e 1961) e Gessner[3] (1955, *apud* Junk, 1980, p. 778) foram pioneiros em discutir as relações entre rios e ambiente terrestre nos trópicos e as consequências morfológicas para flora e fauna resultantes da transição entre os dois ambientes, destacando a necessidade de investigações minuciosas em áreas de vegetação.

A partir dessas necessidades, se elabora um esquema de classificação específico para as planícies amazônicas, desenvolvido por Junk *et al.* (2011), que classifica os ambientes alagáveis em dois grupos: (1) com níveis de água relativamente estáveis e (2) com níveis de água oscilantes. Dentro do grupo (2), está a subdivisão (2.1) "Áreas alagáveis sujeitas a pulsos de inundação monomodais previsíveis e duradouros", categoria esta que contém as subcategorias de planícies alagadas por rios de águas pretas e rios de águas claras, ambas relacionadas ao igapó, e também a categoria de planícies alagadas por rios de águas brancas, que representa a vegetação de várzea. Há também a categoria (2.3) "Áreas alagadas sujeitas a pulsos de inundação curtos, imprevisíveis e polimodais, que contém as subclassificações "áreas alagáveis associadas a pequenos rios e riachos" e "áreas alagadas em depressões alimentadas pela água da chuva". Todos esses ambientes são contemplados na VGX.

2.2.1. Ambientes alagáveis amazônicos

Embora Kubitzki (1989) afirme que não há dúvidas de que tenham existido condições para a existência de vegetação fluvial por longos períodos desde o Cretáceo Superior, o autor afirma não haver evidências precisas que permitam estipular quando começaram os pulsos por inundação na região amazônica. Segundo Irion e Adis (1979), os primeiros ambientes de inundação amazônicos, como os conhecemos, se desenvolveram há cerca de 1 milhão de anos atrás, nas adjacências das margens do rio Negro. Estes ambientes estão expostos à flutuações anuais do nível da água desde então, com destaque às repetidas mudanças de precipitação e nível do mar durante o Plioceno. Estas flutuações tiveram impacto na configuração hidrológica da região e na duração dos períodos de enchente, sujeitas à grandes flutuações devido aos períodos glaciais e interglaciais (Kubitzki, 1989). Durante este período de formação, os pulsos de inundação foram

[3] Gessner, F. (1955). *Hydrobotanik*. Band 1: *Energiehaushalt*. VEt3 Deutscher Verlag der Wlssenschaften. Berlin, 517 p.

gradualmente construindo os habitats atuais, típicos de ambientes aluviais (interessante observar que a vegetação aluvial poderia ter sido reprimida pela vegetação de terra firme durante períodos de descida do nível do mar) (Irion; Adis, 1979).

De fato, em seu trabalho Kubitzki (1989) cita evidências, baseadas na disposição de ambientes pobres em nutrientes (águas pretas e claras), datando do Terciário, em contraste com os ambientes ricos em nutrientes (águas brancas), originados da erosão dos Andes, evento muito mais atual, e chama a atenção para o fato dos ecossistemas de várzea serem mais recentes que os de igapó. Esta hipótese está em contraste com a de Grabert[4] (1984 *apud* Kubitzki, 1989, p. 301), de uma formação holocênica dos igapós do Rio Negro. Todavia, Irion e Adis (1979) afirmam que há 6.000 anos atrás, o nível do mar esteve 5m acima do atual, o que elevou o nível de água do sistema de rios.

De qualquer forma, Kubitzki (1989) é categórico ao afirmar que a evolução da florística que diferencia os ambientes de igapó e várzea e as relações entre a fauna de peixes e a vegetação indicam que os ambientes alagáveis formados pelos igapós sejam ambientes mais antigos.

Wallace (1939) sugeriu uma abrangente e bem aceita classificação dos rios amazônicos, que foi posteriormente popularizada por Sioli (1951) baseada nas propriedades ópticas das águas: rios de águas brancas, que apresentam tons claros e a água bastante turva devido às altas concentrações de sedimentos em suspensão; rios de águas pretas, com baixa concentração de sedimentos em suspensão, porém com elevada concentração de componentes húmicos; e rios de águas claras, com baixa concentração de sedimentos em suspensão e águas com boa visibilidade, que podem ser ricas em matéria orgânica dissolvida (Archer, 2005). No entanto, as populações locais não costumam diferenciar os ambientes alagáveis de acordo com a qualidade da água. Segundo Kubitzki (1989), para as populações locais, todos os ecossistemas alagáveis são consideradas como “várzea”, e, quando as áreas alagadas tem mais água, são chamadas de “igapó”.

[4] Grabert, H., 1983: Das Amazonas-Entwisserungssystem in Raum und Zeit. - Geolog. Rundschau 72:671 - 683

Os rios de águas claras exibem uma ampla variação na química da água. Os maiores rios de águas claras incluem o Tapajós, o Xingu e o Tocantins, que são afluentes ao sul do sistema amazônico (Sioli, 1951).

Vários fatores influenciam os ciclos de inundação em rios de águas claras. No Rio Tapajós, a inundação é controlada por variações sazonais na precipitação. No Rio Xingu e no Rio Tocantins, as inundações periódicas estão relacionadas a efeitos de maré (no Baixo Xingu) e variações sazonais na precipitação (Archer, 2005).

Como as áreas inundáveis são ambientes em transformação constante, não apresentam estrutura uniforme. Junk (1980) cita frequentes mudanças do nível de água, que provocam variação das correntezas no sistema aquático, e a alteração dos níveis de oxigênio durante os períodos de seca e cheia, induzida por variações na temperatura, turbidez, profundidade da coluna d'água e disponibilidade de matéria orgânica. O autor frisa que muitos animais têm a capacidade de evitar as condições extremas dos ambientes alagáveis por meio de migrações horizontais e verticais, que também estão relacionadas às inundações.

As mudanças periódicas entre os ambientes terrestre e aquático são decisivas nos ciclos de vida dos organismos de áreas alagáveis, já que são adaptados para ocuparem esses habitats em ambas as fases. Para Junk (1980), entre as adaptações dos organismos de ecossistemas alagáveis, são notáveis a capacidade de suportar as baixas concentrações de oxigênio e a grande plasticidade morfológica e fisiológica dos organismos, que torna possível a sobrevivência em lugares úmidos e sombreados e em terra firme e seca.

No entanto, a vegetação alagável na Amazônia não apresenta raízes aéreas, como as vistas no mangue, e sim, um tecido esponjoso, que confere flutuabilidade às suas estruturas, como as sementes (Kubitzki, 1989). Durante a fase seca, a vegetação é capaz de colonizar permanentemente estas áreas, e terminar o ciclo de reprodução, produzindo assim um número suficiente de sementes, garantindo a sobrevivência delas e/ou de vegetais durante a cheia (Junk *et al.*, 1989).

Outros fatores que alteram a distribuição e diversidade da vegetação em áreas alagáveis, além da duração dos pulsos de cheia, são os processos sedimentares (que influenciam aspectos geomorfológicos da floresta) e as diferenças bioquímicas do solo e da água que inundam esses locais, responsáveis diretas pela qualidade e quantidade de nutrientes disponíveis (Worbes *et al.*, 1992). A química da água é

importante para a diferenciação florística dos ecossistemas alagáveis (Kubitzki, 1989).

De acordo com Worbes *et al.* (1992), a sedimentação, a erosão e as características físicas do solo são fatores ambientais determinantes para o desenvolvimento dos ambientes aluviais. O zoneamento da vegetação também se relaciona com o gradiente de deposição de sedimentos e com a textura do solo. A composição florística, riqueza de espécies e a estrutura da vegetação aluvial está fortemente ligada, portanto, à localização dos tipos de vegetação ao longo do gradiente de inundação (Junk *et al.*, 1989; Ayres, 1995).

Outro aspecto importante da distribuição das espécies nos ambientes alagáveis é sua relação com o gradiente topográfico, já que as variações topográficas podem resultar em diferenças na amplitude e tempo de inundação sazonal, fatores determinantes nos padrões de riqueza, diversidade e composição vegetal (Junk, 1980; Ayres, 1995) ao alcance das águas durante os períodos de inundação e ao comportamento geomorfológico, resultado de sua localização próxima aos sistemas fluviais.

A classificação de Prance (1980) considera ecossistemas periodicamente inundados e inundações por ciclos sazonais regulares dos rios. As florestas inundadas por água branca foram denominadas pelo autor como várzea estacional, e as florestas inundada por água preta e água clara, igapó estacional.

O igapó estacional está restrito à habitats inundáveis anualmente por rios de água preta ou clara e seu solo arenoso sustenta uma vegetação bem mais escassa que a da mata de várzea de rios de água branca. Na várzea, as árvores são mais altas, a biomassa e a diversidade de espécies é maior, e sua flora é mais uniforme que a de igapó, que exibe grande diferenciação regional (Kubitzki, 1989). Segundo Prance (1980, p.500), “em alguns lugares, o igapó suporta condições semelhantes às do deserto quando seco” sendo, portanto, menos abundante em espécies e adaptações xeromórficas do que a mata de várzea. Embora seja aceito que os igapós sejam menos abundantes que a várzea, devido principalmente aos solos dos rios de águas negras e claras, estudos recentes demonstram não haver diferenças marcantes no número de espécies que ocorrem nesses ambientes, enquanto outros afirmam inclusive haver maior número de espécies em igapós, devido à sua diferenciação regional (Kubitzki, 1989; Oliveira *et al.*, 2021). De qualquer forma, esses autores

afirmam ser de conhecimento que ambos – igapó e várzea – apresentam muitas espécies endêmicas.

Vegetações de igapó mais densas e fisiologicamente semelhantes às de várzea ocorrem em regiões do alto Amazonas, na Colômbia e Peru, e na região do delta amazônico, onde o solo é mais rico, ao contrário da areia usual (Adis, 1977).

A vegetação permanentemente inundada é chamada por Prance (1980) de igapó permanente, ou de igapó do estuário por Pires[5] (1961, *apud* Prance, 1980, p. 502). Nascem sobre o solo que está continuamente encharcado, sendo mais rara na Amazônia do que os tipos periodicamente inundados. Existem muito poucos igapós permanentes na Amazônia. Os ciclos de alagamento fazem com que o número de espécies aptas a viver em ambientes periodicamente inundados seja menor do que nas áreas de floresta de terra firme típica, onde é encontrada a maior diversidade da Amazônia.

Em seu estudo sobre a influência da geomorfologia nos estágios de sucessão na vegetação de várzea, Wittmann, Junk e Piedade (2004) observaram que a vegetação de baixa várzea é composta de diferentes etapas sucessionais sujeitas a inundações anuais entre diferentes gradientes de inundação, formando etapas sucessionais tardias. No entanto, o número de espécies da baixa várzea é restrito devido ao impacto causado pelas inundações altas e prolongadas. Já na alta várzea, a inundação é reduzida de tal forma que muitas espécies da terra firme ao redor podem também se estabelecer ali.

Embora haja uma diferenciação evidente entre os ecossistemas de várzea e igapó, Kubitzki (1989) aponta a existência de espécies em comum entre os dois ambientes (como *Caraipa densifolia, Pachira aquática, P. insignis* e *Swartzia polyphylla*, comuns a todos os tipos de rio) e também com ambientes de terra firme (*Vatairea guianensis* e *Licaria arrneniaca*).

2.2.2. Vegetação densa aluvial da VGX

A vegetação de igapó é mais comum nas margens do rio Xingu, principalmente na zona do baixo curso. Está localizada na planície de inundação, onde o desnível varia entre 4 e 8 m nos picos anuais de enchente e vazante. A mata muitas vezes

[5] PIRES, J. M. (1961). Esboço fitogeográfico da Amazonia. *Rev. Soc. Agron. Vet*, 3-8.

desce quase ao menor nível de água e, algumas regiões têm apenas dois meses de período seco. Os solos são geralmente de origem hidromórfica, do grupo glei húmico; exibem drenagem deficiente e incorporam considerável teor de matéria orgânica e nutrientes (Salomão *et al.*, 2007).

Kubitzki (1989) observa que quase não existe uma flora independente de igapós de águas claras e que sua flora pode parecer mais pobre que as dos igapós de águas negras (como o igapó da bacia do Rio Negro). Quanto à ictiofauna, não há diferenciação significativa entre igapós de águas claras ou pretas.

Fisionomicamente a vegetação de igapó tem árvores baixas e tortuosas e as folhas tendem a ser esclerófilas e os insetos são abundantes (Adis, 1977). O dossel da floresta de igapó é menos compacto e fechado do que na tipologia densa, com cerca de 20m de altura (Salomão *et al.*, 2007).

A VGX é ainda composta por outros ambientes alagáveis, como pedrais, restingas, ilhas e praias, que além dos igapós, têm uma vegetação associada, menos densa, composta de espécies arbustivas e herbáceas, conhecida como “sarobal”. O sarobal tem uma importância muito grande no ciclo de vida dos ecossistemas da Volta Grande, pois suas espécies que produzem os frutos que irão manter a temporada de reprodução da fauna aquática. Além disso, o sarobal é parte importante dos hábitos culturais das populações tradicionais que vivem na VGX.

2.2.3. Regime hidrológico

Mudanças entre a fase aquática e a fase terrestre afetam a vida nas áreas alagáveis de maneira significativa (Junk *et al.*, 1989). Uma área inundada pode ficar submersa por até 10 meses, e as árvores podem ficar cobertas por até 15 metros de coluna d’água (Kubitzki, 1989). São afetadas não só a fauna e flora aquática, mas todo o ecossistema indiretamente influenciados pelas variações do nível dos corpos d’água, como por exemplo, aqueles que se beneficiam da vegetação terrestre.

As variações hidrológicas dos ecossistemas alagáveis amazônicas são essenciais para a manutenção do ciclo de nutrientes (através, por exemplo, dos processos de decomposição). De acordo com Junk (1980), as fases aquáticas e terrestre são uma unidade funcional na manutenção das redes alimentares, que funcionam como fonte primordial de alimento para os peixes, exibindo oferta de itens alimentares bastante variável durante o ano. O ciclo de vida dos organismos é dependente do equilíbrio entre as fases seca e cheia.

Nos ambientes alagáveis, a água é a responsável pela distribuição das sementes, que são produzidas na enchente. Um dos mecanismos de distribuição das sementes são os organismos aquáticos, como algumas espécies de peixes, que, por serem frugívoros, as quebram ou engolem inteiras, transportando-as por grandes distâncias (Junk, 1980). A produção de frutos em habitats alagáveis é essencial para a manutenção das populações de peixes e tracajás, que por sua vez, contribui para a disseminação das sementes. A preferência de alimentação das populações aquáticas e sua migração rumo aos ecossistemas alagados à época da frutificação contribui para manutenção tanto das populações da fauna aquática como da vegetação, uma vez que ambos os sistemas, interdependentes, são altamente sensíveis à distúrbios (Kubitzki, 1989).

2.3. Usinas Hidrelétricas

2.3.1. Hidrelétricas Amazônicas e a Gestão das Águas

"Mais de uma centena de barragens hidrelétricas já foram construídas na bacia amazônica e inúmeras propostas para construções futuras estão sendo consideradas" (Latrubesse *et al.*, 2017, pg 363). O sistema de rios amazônicos compreende o mais complexo sistema de rios no mundo todo, sendo responsável pelo aporte de 16 a 18% de toda água doce do planeta no Oceano Atlântico (Archer, 2005), se tornando um ambiente bastante atraente para a construção destes empreendimentos.

Latrubesse *et al.* (2017) identificaram 78 usinas existentes ou em construção na bacia amazônica, e mais de uma centena de novos projetos futuros, desde pequenas centrais hidrelétricas até mega empreendimentos. Desde o racionamento de energia em 2001, há um crescente interesse em geração de energia limpa e renovável no Brasil (Carvalho, 2006). Na América do Sul, além do Brasil, Peru e Bolívia são os mais afetados, mas Equador, Colômbia, Venezuela, Guiana e Suriname também têm planos de novas hidrelétricas e empreendimentos já instalados (Fearnside, 2015).

A legislação nacional (Lei das Águas) preconiza que a gestão dos recursos hídricos deve priorizar os usos múltiplos da água, garantindo igualdade de acesso aos setores usuários, sociedade civil e comunidades. Os conflitos entre os usuários são mediados pela Agência Nacional de Águas (ANA) para as águas de domínio da

União, que controla a outorga em nível federal ou pelo órgão gestor estadual no caso das águas de domínio dos estados. Ou seja, a outorga do direito de uso dos recursos hídricos tem como objetivo assegurar o controle quantitativo e qualitativo dos usos e o efetivo exercício dos direitos de acesso a ela. Na região hidrográfica da bacia amazônica, a relação entre usos múltiplos dos recursos hídricos é diferente do verificado em outras regiões do país, já que tem abundância hídrica em termos de demanda de água (Sola, 2012) e, mesmo assim, conflitos pelo direito das populações ao uso e acesso.

Conforme apontado por Fearnside (2015), os impactos decorrentes da construção de barragens são vastos e abrangentes. Os efeitos sobre as comunidades tradicionais que dependem dos rios onde esses empreendimentos são implantados são particularmente alarmantes. Essas comunidades têm uma conexão profunda com os rios e seus ecossistemas, utilizando-os não apenas para a subsistência e fonte de renda, mas também como parte integrante de suas tradições culturais. Infelizmente, estas populações sofrem prejuízos significativos, seja permanecendo em seus territórios originais, enfrentando a deterioração da qualidade ambiental dos rios, ou sendo deslocadas para áreas urbanas ou rurais, onde correm o risco de serem forçados a abandonar seu patrimônio cultural e modos de vida tradicionais (Oswaldo; Switkes, 2005;Watts, 2014; Magalhães; Cunha, 2017).

A construção das barragens e a formação dos reservatórios alteram as características biogeoquímicas da água, o que pode resultar em riscos para a saúde, como a proliferação de insetos e a mortandade de organismos aquáticos (Santana *et al.*, 2014; ISA, 2015; Santos *et al.*, 2018). Além disso, a perda de vegetação nas áreas afetadas por barragens não é apenas resultado da inundação direta das regiões onde os reservatórios são instalados. Ela também decorre do desmatamento associado à chegada de mão de obra atraída pelas oportunidades de emprego geradas pelas obras, bem como do deslocamento das comunidades locais para outras regiões. Esses processos frequentemente estimulam a expansão de áreas urbanas, a criação de cidades e a subsequente construção de estradas e promoção do agronegócio (Skole *et al.*, 1994; Assahira, 2014; Soler; Verburg, 2010; Calvi *et al.*, 2020b).

Outro impacto relevante associado à construção de barragens é a emissão de gases do efeito estufa. Isso ocorre devido à decomposição das vegetação que ao ser permanentemente submersa pela água dos reservatórios, morrem e são

decompostas, contribuindo para as mudanças climáticas e seus efeitos adversos (Fearnside, 1997; Kemenes; Forsberg; Melack, 2011; Araújo *et al.*, 2019; Bertassoli *et al.*, 2021; Bertassoli *et al.*, 2021; Bertassoli *et al.*, 2021).

A maioria dos estados do Norte do país, (Pará, Acre, Rondônia, Roraima e Amapá) não dispõe de comitês de bacia hidrográfica para garantir a participação democrática e descentralizada da gestão hídrica estabelecida na Política Nacional de Recursos Hídricos (PNRH) (CBH, 2019), o que acaba agravando ainda mais os problemas de manejo e gestão das águas e dos impactos referentes à instalação de empreendimentos que necessitem do fluxo dos rios para operar. Na região Amazônica, além do CHBM, existem outras hidrelétricas de grande porte, todas elas com impactos ambientais documentados em literatura, na imprensa e reconhecidos pelos órgãos ambientais brasileiros e internacionais.

A hidrelétrica de Tucuruí foi instalada no Rio Tocantins (Pará) e inaugurada em 1984. Apesar de ser considerada um empreendimento modelo devido à sua ampla capacidade de geração de energia, a maioria dos benefícios da energia são destinados à indústria de beneficiamento do alumínio (Fearnside, 2015). Os impactos sociais da hidrelétrica de Tucuruí são muitos. O reservatório inundou 2.430 km², deslocando centenas de comunidades tradicionais e milhares de pessoas, que foram reassentadas em áreas em carência de serviços básicos, fragilizando a qualidade de vida e impactando suas tradições culturais e modos de vida (Mougeot, 1987; Magalhães, 1990). A compensação inadequada da população reassentada gerou conflitos sociais e tensões entre as comunidades afetadas. O enchimento do reservatório trouxe problemas de saúde pública como o aumento da incidência de malária e a praga de mosquitos, como os do gênero *Mansonia*, causadores de várias doenças, além de contaminação por mercúrio (Leino; Lodenius, 1995; Porvari, 1995; Tadei; Mascarenhas; Podestá, 1983).

A Usina Hidrelétrica (UHE) de Balbina, instalada no estado do Amazonas, no rio Uatumã, é frequentemente citada como um paradigma negativo na implementação de projetos hidrelétricos e criticada devido aos impactos ambientais e à insistência na continuação de um projeto caro, que logo no início, se mostrou inviável (Fearnside, 1989). A grande controvérsia ambiental de Balbina se dá em virtude da inundação de uma extensa área (2.360 km²) pelo seu reservatório, enquanto a capacidade de geração da usina é de apenas 112 MW (Fearnside, 1989). A UHE foi construída para fornecer energia elétrica para Manaus, que cresceu tanto

durante o longo período de construção da barragem que já não era mais suficiente para suprir as necessidades energéticas da cidade em sua inauguração, em 1989 (Fearnside, 2015). Os efeitos resultantes foram extremamente significativos em face de um potencial hidrelétrico tão reduzido. Os impactos ambientais associados à implantação do reservatório são amplamente conhecidos. A vegetação não foi previamente suprimida antes da inundação do reservatório, o que levou à decomposição contínua da floresta submersa (Assahira *et al.*, 2017). Esse processo resultou na acidificação e na condição anóxica da água, oferecendo riscos para o funcionamento das turbinas, uma vez que, devido à topografia do terreno (o que torna a represa rasa), as águas paradas não passam por renovação (Schöngart *et al.*, 2021). A decomposição contínua da matéria orgânica das árvores submersas no reservatório também produz emissões significativas de metano, um poderoso gás de efeito estufa (Kemenes; Forsberg; Melack, 2011).

As UHE de Jirau e Santo Antônio estão localizadas no Rio Madeira em Rondônia e foram inauguradas em 2012, entrando em plena operação em 2016. A área do reservatório de Jirau é de 361,6 km², e tem potência instalada de 3.750 MW, já o reservatório de Santo Antônio tem 546 km² de área inundada e potência instalada de 3568 MW. Os principais impactos do chamado Complexo do Rio Madeira têm relação, principalmente, à área inundada que extrapola as fronteiras do Brasil, atingindo território boliviano (Fearnside, 2015). A alteração dos ciclos fluviais bloqueou a migração de peixes para Bolívia e Peru, e os impactos são sentidos pelas populações tradicionais que dependem da pesca (Santos *et al.*, 2018). Outra consequência relatada são os *hydropeakings*, já que irregularidades no regime hidrológico vêm causando variações de curto prazo no nível da água, com eventos repentinos de subidas e descidas, o que coloca a população ribeirinha em risco (Almeida *et al.*, 2020).

Além desses três exemplos bastante discutidos e citados na literatura como barragens de grande impacto na Amazônia, existem mais algumas dezenas de grandes UHEs e pequenas centrais hidrelétricas em toda a Amazônia Legal brasileira.

2.3.2. Complexo Hidrelétrico de Belo Monte

Segundo relata Sabaj-Perez (2015), o ecologista Philip Fearnside teria descrito que um barrageiro (alguém que trabalha e defende a construção de barragens) a ele

afirmou: “Deus só faz um lugar como Belo Monte de vez em quando. Este lugar foi feito para a construção de uma barragem”, ressoando um anseio da sociedade e governos brasileiros que ambicionam projetos de barragens colossais, com a promessa de oferecer energia limpa e renovável. De fato, nos anos 1980, os barrageiros ostentavam duas super usinas importantes: Itaipu (considerada uma das sete maiores façanhas da engenharia do século 20) e Tucuruí (no Rio Tocantins), a quinta maior barragem do mundo, até Belo Monte entrar em operação.

Tal afirmação proferida pelo barrageiro, descrita por Fearnside, se dá pelo fato do rio Xingu ser formado por rias, resultantes do bloqueio dos rios Xingu e Tapajós por sedimentos do Rio Amazonas. Estas rias desencadeiam na formação de desníveis (Archer, 2005) como os encontrados na região do Médio e Baixo Xingu, onde alcançam até os 85 metros de altura (Sevá Filho, 2005).

Esta peculiaridade topográfica (setores de alternância brusca de altitudes) gera interesse em termos de aproveitamento hidrelétrico. O trecho da VGX, por oferecer um dos maiores potenciais hidrelétricos do baixo Amazonas, foi o escolhido para a implementação da usina de Belo Monte, cuja área abrange territórios de 11 municípios das mesorregiões do Baixo e Médio Xingu (Sevá Filho, 2005; Salomão *et al.*, 2007).

A região escolhida para a obra da usina é extremamente rica e diversa em fauna e flora, com cerca de 174 espécies de peixes, 440 espécies de aves, 259 espécies de mamíferos, além de espécies endêmicas e outras ameaçadas de extinção (Costa *et al.*, 2012).

Em sua capacidade de pico, Belo Monte se propõe a gerar 11.233 megawatts, afetando diretamente cerca de 180 km do rio Xingu, inundando quase metade deste trecho, e secando o restante (Sabaj-Perez, 2015). Políticos e governantes promoveram publicamente Belo Monte como essencial à segurança energética e progresso econômico, aumentando o apelo pela sua construção.

A usina de Belo Monte (Figura 6a) é conhecida como “usina a fio d’água”, com duas barragens principais. Na barragem de Pimental (Figura 6b), a primeira delas, localizada a montante da Volta Grande, foram inundados 134 km² em um trecho de 80 km do rio Xingu, reduzindo a complexidade dos canais anastomosados formado pelas corredeiras a um reservatório entre Altamira e a foz do rio Iriri. Acima de Pimental, um canal artificial desvia a água represada para um reservatório fora do curso do rio, que inundou 382 km² de terreno (Figura 6c) anteriormente drenados

por 4 pequenos afluentes do Xingu. A água deste segundo reservatório abastece 20 turbinas da barragem de Belo Monte. Um sistema de diques auxilia que o barramento volte a alimentar o curso principal do Rio Xingu no trecho da Volta Grande (Figura 6).

Figura 6: (a) Volta Grande do Xingu e os reservatórios principal e intermediário do CHBM. Destaque para a área de estudo considerada no escopo desta pesquisa; (b) Porção final do reservatório principal sendo encerrado pela Barragem Pimental, com o canal de derivação se projetando do reservatório; (c) Usina de Belo Monte na porção final do reservatório intermediário e (d) Imagem de satélite da VGX (set/2023).

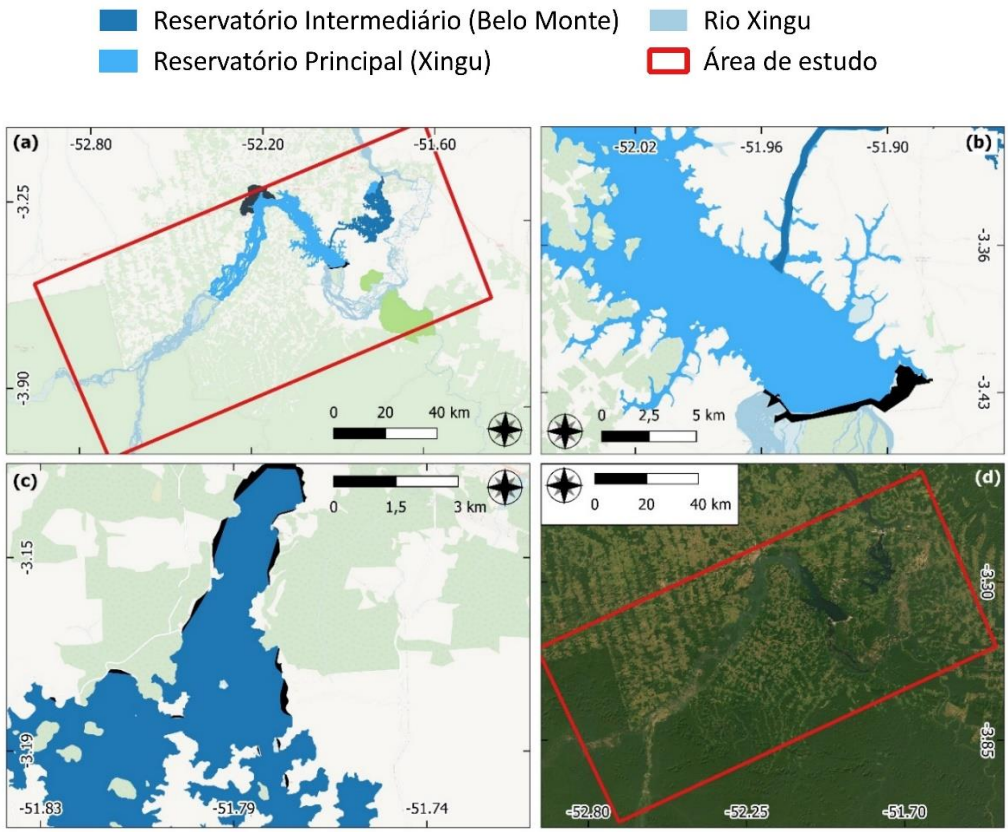

Fonte: OpenStreetMap; Esri Imagery/Autoria própria

A Barragem de Pimental tem potencial de transformar grande parte do trecho a montante da Volta Grande de um ambiente dinâmico de fluxo livre para um sistema deposicional, conforme observado por Sawakuchi *et al.* (2015), que projetaram que o fundo do rio pode estar se transformando de rocha em areia, lodo e lama. A jusante da Volta Grande, o fornecimento reduzido de água devido à barragem do rio adicionou "becos sem saída ao labirinto de canais", prejudicando o ciclo de vida dos peixes, tracajás e outros organismos das corredeiras (Sabaj-Perez, 2015).

2.3.3. O hidrograma de “consenso”

Regimes hidrológicos desempenham um papel essencial na determinação da composição biótica, estrutura e funções de ecossistemas aquáticos e vegetação alagável e habitats aluviais, uma vez que a variação intra-anual das condições hidrológicas é essencial para completar com sucesso o ciclo de vida das espécies que habitam estes ambientes (Richter *et al.*, 1996).

A quantidade de água e a sincronia dos pulsos são componentes críticas do fluxo de corpos d’água para manutenção de sua saúde e qualidade (Poff, *et al.*, 1997). Richter *et al.* (1996), reconhecem na literatura que modificações dos regimes hidrológicos podem, indiretamente, alterar a composição, estrutura ou função de ecossistemas alagáveis, uma vez que variações nas condições destes ambientes são de grande importância na dinâmica das populações das espécies que ali habitam, já que influenciam nos ciclos reprodutivos e na competição natural por recursos. Isso ocorre porque alterações na composição, estrutura e função de ecossistemas dependentes da água modificam as variáveis físicas e biogeoquímicas dos ambientes. Sparks (1992) é categórico ao afirmar que ao invés de otimizar o regime hidrológico para algumas espécies após alguma alteração induzida pelo homem, o ideal seria aproximar o máximo possível a nova configuração hidrológica do regime natural, a fim de manter a totalidade de espécies que compõem o ecossistema. De acordo com Poff, *et al.* (1997) muitos rios não mais sustentam ecossistemas saudáveis, provedores de importantes bens e serviços, devido à extensiva degradação ecológica e perda de biodiversidade geradas pela exploração intensiva dos cursos d’água.

Também é de conhecimento na literatura que os esforços de manejo e restauração dos sistemas aquáticos apresentam falhas na manutenção do regime hidrológico. Poff, *et al.* (1997) reconhecem que a importância da variabilidade natural dos fluxos na manutenção de ecossistemas saudáveis era ignorada até pouco tempo atrás. As decisões de manejo e mitigação se restringiam às necessidades observadas ou conhecidas de apenas algumas poucas espécies de fauna, vegetação, processos e funções ecossistêmicas, enquanto as gamas de fluxos para sustentar a vida de forma plena eram, e ainda são, negligenciadas (Richter *et al.*, 1996), inclusive, negligenciando o conhecimento dos povos tradicionais e originários (Pezzuti *et al.*, 2018). Richter *et al.* (1996) ainda citam omissões às mudanças

geomorfológicas e geoquímicas que dão suporte às funções ecossistêmicas, como transporte de sedimento e manutenção da cadeia trófica, nos planos de mitigação de ambientes dependentes da água, além da desvalorização da variação temporal nos regimes hidrológicos.

"Historicamente, a "proteção" de ecossistemas alagáveis tem sido limitada, enfatizando a qualidade da água e apenas um único aspecto relacionado ao volume de água: o fluxo mínimo" (Poff, *et al.*, 1997, p. 769). São necessários testes e modelagem para que as características naturais sejam mantidas a fim de manter a integridade de um ecossistema aluvial sob pressão de alterações antrópicas.

Durante o ciclo hidrológico do Xingu, o pico da cheia (março a maio) pode alcançar e até ultrapassar os 32.000 m³/s (na estação de Altamira). Em contrapartida, de setembro a outubro, pico da seca, a vazão fica em torno de 450-500 m³/s. Além disso, o ciclo de inundação pode ser bastante variável entre um ano e outro, com importante alternância de valores médios, máximos e mínimos entre anos secos e anos úmidos. De qualquer forma, em todos os anos, o volume de água que chega na Volta Grande durante o mês mais seco é de apenas 4 a 7 por cento do pico de vazão, representando uma queda de até 5 metros no nível do rio (Sabaj-Perez, 2015; Pezzuti *et al.*, 2018).

O fluxo drasticamente reduzido, induzido pelo barramento do curso do rio, fragmenta ainda mais os habitats do Xingu, isolando canais de várzea, poças e lagos do tronco principal. Isolados da capacidade de amortecimento proporcionada pelo curso principal, as características das águas mudam drasticamente, tornando-as anóxicas e aquecidas, ou pobres em oxigênio devido à proliferação do fitoplâncton. O Xingu se torna, como descreve Sabaj-Perez (2015) um "rio de rios", com canais se ramificando em riachos menores, sem ligação com o curso principal, na estação seca.

O TVR, nada mais é, portanto, que a porção da VGX desabastecida pelo curso principal de água, desviado para alimentar o reservatório de Belo Monte. O operador do sistema, que é a empresa concessionária que gere o CHBM, é quem define o aporte de água que abastece o curso principal do Xingu, procurando sempre maximizar a eficiência da produção de energia. Tal gestão se dá através da aplicação do chamado *Hidrograma de Consenso*: à parte inferior da Volta Grande é destinado um fluxo de água que se propõe a reproduzir artificialmente o pulso sazonal natural de cheia e seca, porém, num nível muito inferior às médias observadas

naturalmente, e sem a variação natural dos períodos de enchente e vazante (que ocorrem entre os pulsos de cheia e seca) (Sabaj-Perez, 2015; Pezzuti *et al.*, 2018).

O HC se propõe a mitigar os efeitos adversos da vazão reduzida, estipulando um mínimo de água que seria suficiente para que a VGX permaneça saudável, sustentável ambientalmente e capaz de manter o ecossistema e as populações que dependem do rio, e ainda garantir a produção de energia (Sabaj-Perez, 2015; Pezzuti *et al.*, 2018).

O hidrograma apresentado e aprovado pela ANA em 2009 deveria garantir as seguintes condições: navegabilidade, alagamento anual dos pedrais e alagamento das planícies a cada dois anos. Estas condições seriam alcançadas garantindo uma vazão mínima de 700 m³/s durante o período de seca, 4.000 m³/s durante o período de cheia e, a cada dois anos, uma vazão de 8.000 m³/s (que garantiria o alagamento das planícies) (Eletrobrás, 2009a; Pezzuti *et al.*, 2018). As demais vazões, para os outros meses, foram definidas com base nestes valores mínimos, a fim de garantir uma transição gradual entre o pico da cheia e o pico da seca.

A implementação do HC, portanto, consiste na alternância de dois hidrogramas: hidrograma A, que visa alagar anualmente os pedrais com uma vazão máxima de 4.000 m³/s, e hidrograma B, que pretende alagar as planícies a cada dois anos, com vazão máxima de 8.000 m³/s.

As previsões, que vêm se cumprindo desde 2016, dão conta de que a redução dos pulsos naturais além de isolar permanentemente os habitats aquáticos do curso principal, prejudica a característica biológica mais produtiva deste ecossistema, que ocorre durante o pico máximo do pulso de cheia. Não raro, nas discussões que envolvem as populações tradicionais e ribeirinhas que dependem do rio, os hidrogramas propostos são chamados “hidrogramas de conflito”.

As etapas de aplicação do novo esquema hidrológico previam um período de teste de aplicação dos hidrogramas, com duração de 6 anos, a serem iniciados após a conclusão da instalação da plena capacidade de geração de energia da usina (o que ocorreu em dezembro de 2019). Neste período de teste, o TVR deveria ser extensamente monitorado a fim de detectar seus impactos negativos, e, caso sejam constatados, a licença prévia garante a possibilidade de alteração dos hidrogramas (Pezzuti *et al.*, 2018).

2.3.4. O monitoramento independente dos impactos do CHBM pelas populações tradicionais

Desde 2009, quando novos Estudos de Impacto Ambiental (EIA) para a obra da Usina de Belo Monte foram apresentados, o empreendimento vem sendo alvo de debates. Isso porque os grandes atingidos alegam não ter havido consulta prévia das comunidades ribeirinhas e indígenas afetadas direta e indiretamente pelo empreendimento, ao longo do procedimento administrativo para a concessão de licenças prévias (Pezzuti *et al.*, 2018).

Com a expedição da licença de instalação (fase posterior à licença prévia) de Belo Monte, o Brasil foi chamado a prestar esclarecimentos junto a Comissão de Direitos Humanos da Organização dos Estados Americanos por expedir licenças sem que fossem cumpridos todos os procedimentos devidos (Sola, 2012). O Ministério Público Federal (MPF) também entrou na Justiça contra a Agência Nacional de Águas (ANA) devido à liberação de autorizações de aproveitamento de recursos hídricos na Amazônia sem a constituição e anuência da instância de planejamento participativo e descentralizado prevista na legislação, responsável por balizar essas autorizações (Villas-Boas; Rojas, 2014).

Os impactos do barramento do Xingu e da redução drástica da vazão do rio foram estabelecidos sem pactuação social no processo de licenciamento, à revelia das evidências científicas que alertavam para os danos que seriam causados com a instalação do complexo hidrelétrico. O que se vê na prática é uma desigualdade de poder entre os argumentos que priorizavam as vantagens econômicas do megaempreendimento e os esforços em minimizar seus impactos socioambientais, com a consequente inviabilização dos territórios e da existência digna de populações locais, além da destruição de delicados ecossistemas. No caso do CHBM, foram muitas as formas de despolitização dos efeitos negativos e dos impactos em detrimento da produção energética (Pezzuti *et al.*, 2018).

A ausência de representatividade fez com que os Juruna da aldeia Miratu da Volta Grande do Xingu buscassem uma estratégia de participação forçada na gestão das águas do Xingu: eles estão comprometidos desde 2013 com a realização de um monitoramento independente da empresa concessionária e dos órgãos do poder público, para registrar eles próprios, juntamente a um observatório de cientistas e

universidades, os impactos do CHBM em seu povo e em seu território (Pezzuti *et al.*, 2018; Zuanon *et al.*, 2019).

Pesquisadores de diversas áreas se aliaram aos indígenas da Volta Grande na geração de dados e reflexões acerca da chegada do complexo hidrelétrico e seus impactos atuais e futuros, principalmente do ponto de vista da pesca, atividade mais ameaçada pelo barramento no modo de vida dos povos originários (ISA; AYMÏX, 2018)

O monitoramento independente descreve a região e as relações ecossistêmicas que ali se encontram e aponta os impactos, alguns irreversíveis, que a instalação do complexo vem trazendo. Com a publicação dos resultados do monitoramento (MPF, 2019; Zuanon *et al.*, 2019; MPF, 2023), espera-se qualificar e ampliar os espaços de decisão sobre o futuro de tudo e todos na região da Volta Grande do Xingu. “É uma ação de resistência contra as tentativas de esvaziamento simbólico do território” (Pezzuti *et al.*, 2018).

Poff, *et al.* (1997) reconhecem algumas iniciativas da sociedade como interesse em manter a integridade de sistemas aquáticos. Os autores citam a criação de conselhos gestores de bacias hidrográficas, a criação de órgãos do governo responsáveis por fiscalizar as atividades nos cursos d’água, a criação de legislação específica para proteção de ambientes sensíveis e, por fim, iniciativas da sociedade civil. Embora os autores afirmem que todas estas resoluções, para terem efeito, devam estar firmemente amparadas em conhecimento científico, reconhecem que, não raro, abordagens de manejo e mitigação falham em reconhecer o papel fundamental da ciência na manutenção da dinâmica natural dos cursos d’água. Os autores citam também as responsabilidades fragmentadas de agências de fiscalização e órgãos governamentais, que tornam difícil, senão impossível, o manejo completo e íntegro de ecossistemas alagáveis. Ações coordenadas são essenciais para proteção e restauração dos fluxos naturais dos rios.

A dependência e conhecimento dos povos tradicionais que habitam a VGX em relação às aguas e processos que nelas ocorrem deve ser levada em consideração na identificação e monitoramento de impactos, assim como na definição e avaliação de medidas de compensação.

2.4. Sensores Remotos

2.4.1. Sensores remotos como ferramenta de análise ambiental

O sensoriamento remoto tem contribuído de forma importante para o estudo de diversos ambientes, pois auxilia na compreensão de estruturas ecossistêmicas e suas interações. É usado para identificar e quantificar a distribuição da floresta desde a escala global até a local (Myers, 1988; Archard *et al.*, 2002). Sensores remotos facilitam a compreensão da variação espacial e temporal dos ambientes, principalmente em áreas extensas, de difícil acesso e que exibem complexa variabilidade sazonal, onde o trabalho de campo e mapeamento tradicionais acabam por ser prejudicados ou inviabilizados. O sensoriamento remote é essencial para a aquisição de informações sobre o território, tornando a técnica uma ferramenta indispensável no monitoramento e gerenciamento dos recursos naturais (Palha *et al.*, 2003; Freitas; Cruz, 2003).

Imagens de satélite são um conjunto de dados em formato matricial, cujos vetores x, y (localização) e z (valores radiométricos) podem ser transformados algebricamente para obtenção de realce espectral e/ou espacial (com a geração ou não de novos conjuntos de dados) e análises estatísticas (Ferreira; Ferreira; Ferreira, 2008). O uso de imagens e técnicas de sensoriamento remoto para mapear a variação no tempo e no espaço de diferentes habitats dos ecossistemas alagáveis da região amazônica, que são extremamente dinâmicos, são muito convenientes. E isto porque as imagens adquiridas pelos sensores são registradas com elevada frequência por constelações de satélites, facilitando a evidenciação das variações e mudanças na dinâmica e na paisagem desses ambientes (Novo *et al.*, 2005). O uso de sensores remotos oferece um método rápido e preciso para obter mapas de uso e cobertura do solo (Vasconcelos; Novo, 2004), já que atualmente, existe no mercado um vasto conjunto de técnicas de segmentação e classificação automática de imagens digitais (Palha *et al.*, 2003).

As informações provenientes do sensoriamento remoto podem ser usadas como indicadores das condições da vegetação através de medidas de biomassa, produtividade, fenologia e diversidade (Foody, 2003). Outra possibilidade dos produtos de sensoriamento remoto, aliados à coleta de dados em campo é a elaboração de mapas geomorfológicos (Verstappen, 2011).

Atributos estruturais são indicadores do estágio de desenvolvimento da vegetação e de sua relação com o ambiente (Feldpausch *et al.*, 2003; Quesada *et al.*, 2012). Tipos de florestas são caracterizados justamente pelas diferenças estruturais da vegetação e por associações com clima, geomorfologia e tipos de solo. As diferenças quantitativas da estrutura da floresta podem contribuir para o entendimento de relações ecológicas entre vegetação e gradientes ambientais e em estudos de viabilidade de manejo (Uhl; Kauffman, 1990; Hubbel *et al.*, 1999; Vierling *et al.*, 2008).

Embora o sensoriamento remoto seja uma técnica abrangente, de fácil acesso e relativamente barata, uma vez que os produtos de vários satélites são oferecidos gratuitamente, o método apresenta limitações, principalmente relacionadas aos sensores óticos. Uma questão fundamental que limita seu uso nos ambientes tropicais é o prolongado período com cobertura de nuvens, que prejudica a periodicidade de aquisição de imagens com cobertura de nuvens inferior a 60%, sendo isso possível apenas durante o verão (Souza Filho *et al.*, 2005; Novo, 2008; Zanotta; Ferreira; Zortea, 2019).

Igualmente problemática é a questão da definição dos requisitos mínimos de resolução espacial, radiométrica, e temporal necessários para atender às necessidades de informação sobre a superfície de interesse. Observa-se também problemas de mistura espectral, que ocorrem devido à resolução espacial dos sensores que, em geral, permitem que um elemento de cena que corresponde a um pixel da imagem contenha mais de um tipo de cobertura do alvo (Freitas; Novo; Shimabukuro, 2003; Novo, 2008; Zanotta; Ferreira; Zortea, 2019).

Por exemplo, embora sejam frequentes trabalhos que discriminem áreas florestais de outros tipos de cobertura e uso da terra, no caso dos trópicos, onde a floresta é um mosaico de estágios sucessivos com limites não-claros (Whitmore, 1990), torna-se difícil especificar diferentes tipos de vegetação, devido às características do sensor e ao gradiente contínuo formado pela vegetação adjacente (Freitas; Cruz, 2003). Existe também a questão relacionada ao limite máximo ao qual a resolução espacial pode ser degradada sem que haja perda significativa de informação.

Para superar estes desafios, um variado leque de abordagens tem sido proposto para uso em conjunto com sistemas óticos, como radares de abertura sintética (SAR, da sigla em inglês *Synthetic Aperture Radar*) e tecnologias a laser (LiDAR, do

inglês *Light Detection And Ranging*). Dados orbitais dos sensores SAR podem fornecer informações de qualidade pois são pouco influenciados pelas condições atmosféricas, uma vez que geram produtos que operam na faixa espectral das micro-ondas. Além disso, possuem potencial de transpor os alvos e registrar o que está abaixo de algumas superfícies (como por exemplo, a vegetação) (Flores-Anderson *et al.*, 2019), característica que pode ser explorada para identificar formas do relevo em áreas alagáveis florestadas.

Já a tecnologia LiDAR pode ser utilizada para facilitar a mensuração de alguns atributos e aperfeiçoar diferentes técnicas de sensoriamento. Este é um sistema de sensoriamento remoto ativo utilizado para medir distâncias das estruturas em função do tempo percorrido entre a emissão e o retorno do raio laser (Lefsky *et al.*, 2002).

Sensores LiDAR coletam dados altimétricos que podem ser utilizados tanto para a superfície da água como para a topografia terrestre. Alguns autores como Brown (2002) e Drake *et al.* (2003) acreditam que a tecnologia LiDAR é um aperfeiçoamento de muitas técnicas de sensoriamento remoto existentes que atualmente são incapazes de obter estimativas ambientais precisas confiáveis (Freitas; Shimabukuro, 2007).

Dados orbitais de sensores remotos podem fornecer informações geomorfológicas de qualidade das áreas emersas e de águas rasas, tendo como base a textura, geometria e conteúdo de umidade dos alvos (Souza Filho; Paradella; Silveira, 2005). Imagens orbitais SAR, combinadas a sensores remotos ópticos devidamente ortorretificadas e corrigidas para um sistema de projeção comum, permitem a manipulação e comparação de dados pixel a pixel. Desta forma, os dados orbitais podem ser precisos no mapeamento geomorfológico em ambientes tropicais úmidos (Souza Filho *et al.*, 2005).

2.4.2. Radares de abertura sintética (SAR) como ferramenta para análise de ambientes alagáveis

Radares são sensores ativos que transmitem na frequência das micro-ondas. Sensores ativos são aqueles que proporcionam sua própria fonte (portanto, artificial) de energia (diferente dos sensores óticos, que são sensores passivos, e dependem de uma fonte de iluminação externa, como o sol) (Meyer, 2019).

Inicialmente o uso dos radares para imageamento remoto era limitado por dificuldades relacionadas à resolução azimutal, que se degrada linearmente com o aumento da distância entre o sensor e os alvos no solo. A resolução da direção azimutal é função do comprimento da "sombra" da antena que emite e recebe de volta as micro-ondas (Figura 7a), tornando impraticável o uso de radares convencionais em grandes altitudes, ou até mesmo em plataformas espaciais (como a Estação Espacial Internacional), já que a antena não teria o tamanho suficiente para manter uma resolução azimutal dentro do limite aceitável para a formação das imagens. Uma solução para este problema, portanto, seria aumentar o comprimento da antena. No entanto, na prática, isto seria inexequível, uma vez que para manter um radar em altitude orbital as dimensões da antena teriam que ser colossais (com comprimento na ordem de centenas de metros) para que a resolução azimutal não se degrade. Para solucionar este problema, surge então a metodologia conhecida como "radar de abertura sintética", desenvolvida em 1952, que consiste em criar uma antena virtual (e por isso, sintética) longa o suficiente para manter a resolução azimutal dentro do aceitável. O comprimento da antena sintética se dá a partir do imageamento em diversas visadas (ou *looks*) de antenas menores (Figura 7b) (Richards, 2015; Flores-Anderson *et al.*, 2019).

Figura 7: (a) Geometria de um radar convencional onde a resolução azimutal é função do comprimento da antena do sensor e (b) geometria de um radar de abertura sintética, onde o tamanho da antena é simulado através de diferentes aquisições de imagens de um mesmo alvo.

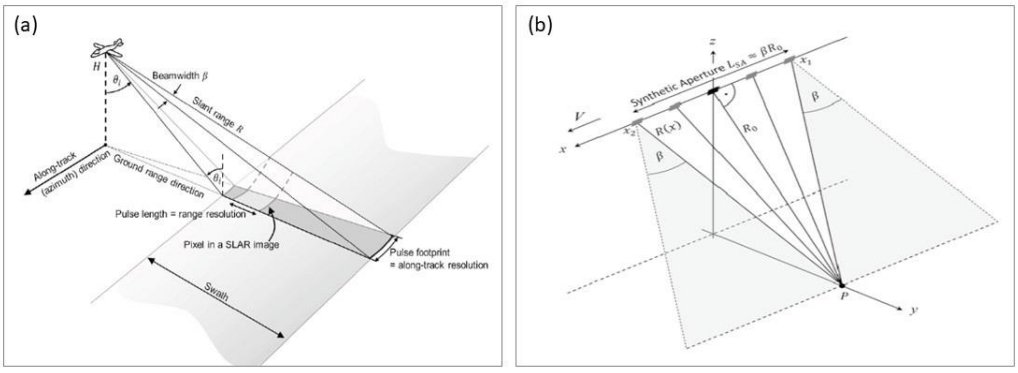

Fonte: Meyer, 2019

Outra questão relevante ao trabalhar com imagens SAR é o efeito *speckle* nas imagens, um ruído que se assemelha a uma textura granulada, comumente comparada a grãos de "sal e pimenta". O *speckle* é inerente aos sistema de

imageamento por radar, porque é resultado da interferência do espalhamento do sinal de retorno dos alvos imageados (Figura 8) (Meyer, 2019).

Figura 8: Efeito speckle de um pixel, que é a soma de vários eventos de espalhamento individuais dos pixels.

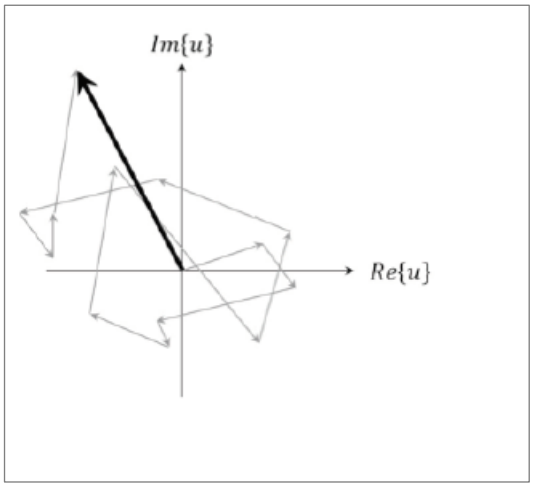

Fonte: Meyer, 2019

A distribuição do efeito *speckle* é função do parâmetro gamma0 (σ0), também conhecido como seção transversal de espalhamento normalizada (NRCS, do inglês *Normalized Radar Cross Section*) do alvo, que nada mais é que a medida calibrada da energia transmitida pelo radar que é espalhada de volta na direção do sensor. Em outras palavras, é a razão entre a intensidade do sinal recebida e incidente (1) (Meyer, 2019).

$$\sigma = \frac{I\ recebida}{I\ incidente} 4\pi R^2 [m^2] \qquad (1)$$

Como o ruído é constante por toda imagem e facilmente distingue-se de outros possíveis ruídos, pode ser atenuado através de filtros. O filtro ideal é aquele que tem a capacidade de reduzir o aspecto granulado sem perder informação e conteúdo do pixel, enquanto preserva as bordas e as características originais da imagem (Santoso *et al.*, 2016). Há diversas opções de filtros nos programas de processamento de imagens e a escolha vai depender do usuário, do tipo de análise proposta e dos resultados desejados.

A seção transversal de retrospalhamento é influenciada principalmente pela rugosidade (que mede o quanto de energia é mandada de volta para o sensor) e pelas propriedades dielétricas do alvo (que mede a capacidade de penetração do sinal na superfície). Esses parâmetros são função do comprimento de onda e da frequência do sinal enviado pelo radar (Meyer, 2019).

Superfícies suaves (como por exemplo águas abertas, como rios e mares, ou rodovias) se comportam como superfícies especulares: o retorno do sinal é praticamente nulo, e portanto, o pixels dessas superfícies serão bem escuros (Figura 9a). Superfícies de rugosidade intermediária irão apresentar retorno moderado de energia refletida, e os pixels serão de tonalidade cinza escuro (solo exposto e plantações) (Figura 9b). Já superfícies bastante rugosas, como a vegetação densa, têm retorno intenso do sinal e espalhamento difuso, apresentando pixels de tonalidade clara (Figura 9c) (Flores-Anderson *et al.*, 2019).

Figura 9: Tipos de retroespalhamento baseados na rugosidade dos alvos. Da esquerda pra direita: (a) superfície suave, (b) superfície moderada, (c) superfície rugosa e (d) double-bounce.

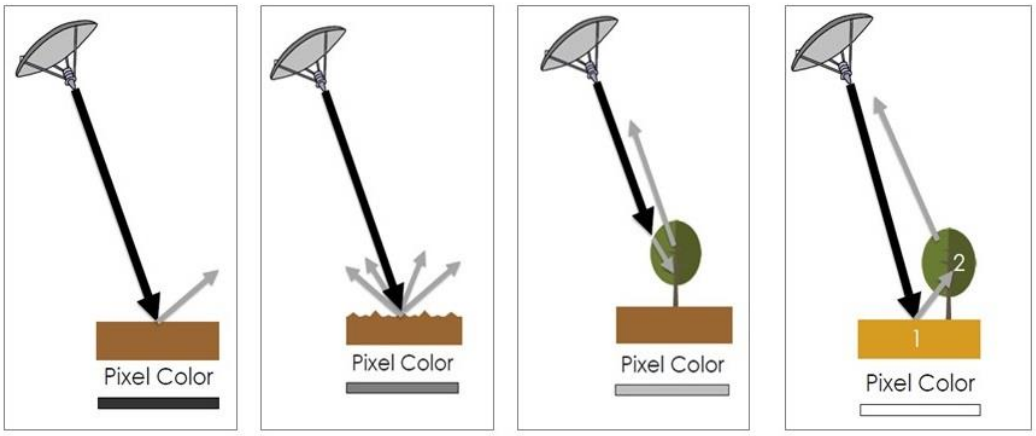

Fonte: Erika Podest (Forest mapping and monitoring with SAR Data: Time Series Analysis – NASA ARSET Course)

Há ainda o espalhamento conhecido como *double-bounce*, ideal para detectar florestas alagadas. Nesta interação, o sinal do radar atinge primeiro a superfície horizontal (no caso, a água), e depois uma superfície vertical (como um poste, prédio ou tronco de árvore). Como a maior parte da energia enviada pelo radar é refletida de volta, o sinal, neste caso, tende a ser alto, e o pixel será bastante claro (Figura 9d) (Meyer, 2019).

Existem sensores SAR operando em diferentes comprimentos de onda e frequências, da banda Ka (27-40 GHz de frequência e 1,1-0,8 cm de comprimento de onda) à banda P (0,3-1 GHz de frequência e 100-30 cm de comprimento de onda). Frequência e comprimento de onda são inversamente proporcionais, e quanto maior o comprimento de onda, maior o poder de penetração do sinal no alvo. Por esta razão, para o monitoramento de vegetação, as bandas de comprimento de onda longa (como L e P) são as mais adequadas (Figura 10). A banda L opera na

frequência entre 1-2 GHz e entre 30 e 15 cm de comprimento de onda (Meyer, 2019).

Figura 10: Exemplo de penetração do sinal enviado pelo radar na vegetação nas bandas X, C e L.

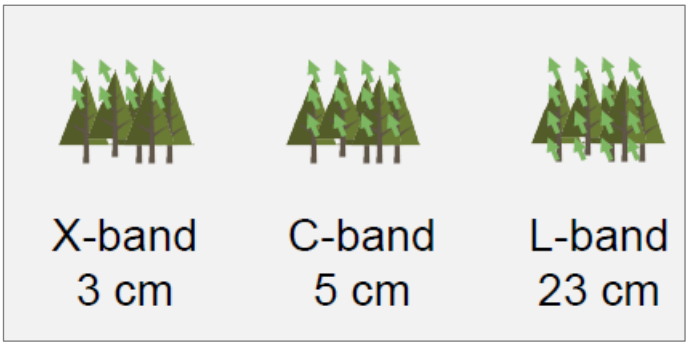

Fonte: Adaptada de ESA Radar Course 2 (disponível em https://earth.esa.int/web/guest/missions/esa-operational-eo-missions/ers/instruments/sar/applications/radar-courses/content-2/-/asset_publisher/qIBc6NYRXfnG/content/radar-course-2-parameters-affecting-radar-backscatter)

Nas imagens SAR, a polarização descreve a orientação do plano de oscilação do sinal de onda propagado, que pode ser horizontal (H) ou vertical (V). Os sensores podem transmitir o sinal co-polarizado (HH/VV – transmite e recebe na mesma orientação) ou em polarização cruzada (HV/VH – transmite numa polarização e recebe em outra). Cada polarização interage de uma forma diferente com os alvos (Meyer, 2019).

Figura 11: Oscilação das polarizações VV e HH.

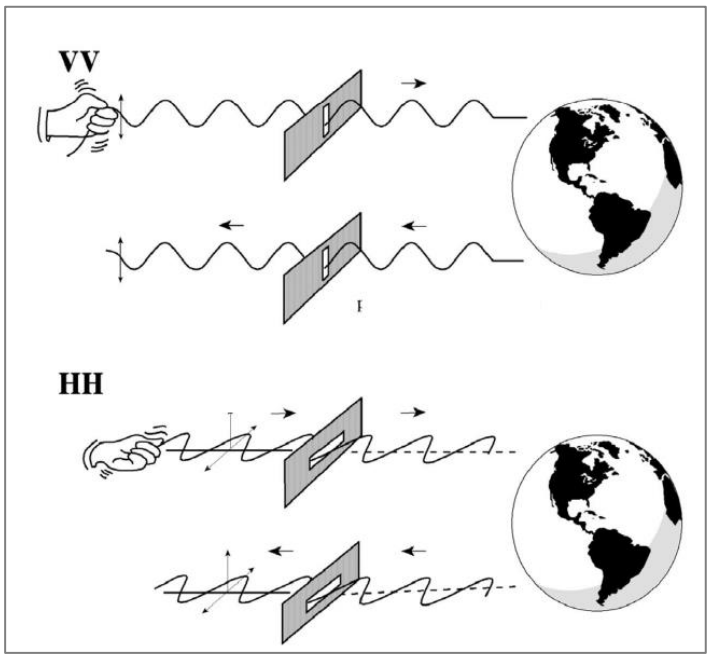

Fonte: Jensen, 2000

Em geral, a polarização HH interage melhor com o espalhamento tipo *double-bounce*, sendo ideal para destacar áreas alagadas (que terão o sinal bem claro, com valores de pixel elevados). A polarização VV é a mais adequada para realçar a rugosidade das superfícies, como solo exposto ou com vegetação baixa. A superfície da água também responde bem a esta polarização. Já as polarizações cruzadas (HV/VH) destacam aspectos volumétricos dos alvos, sendo ideais para evidenciar a vegetação densa, porque interage com o dossel das árvores (Meyer, 2019).

2.4.3. Altimetria por satélites

Altimetria é a prática de medir a altitude ou elevação de um ponto específico na superfície terrestre, representando a diferença vertical entre esse ponto e um nível de referência comum, geralmente o nível do mar. Esse tipo de medição é frequentemente realizado por meio de instrumentos como o altímetro.

A altimetria por sensores remotos tem como principal objetivo medir a distância entre o sensor e a superfície da Terra, e é realizada por radares ou sistemas LiDAR. Mede-se o tempo que o pulso do radar leva para ir e voltar da antena do sensor até a superfícies (o chamado eco do radar). Sabendo-se a localização da órbita do satélite e através de correções atmosféricas e de marés, a distância medida pode ser

convertida em uma elevação da superfície - geralmente fornecida em relação a um *datum* de elipsoide de referência.

Inicialmente, a altimetria por satélites foi desenvolvida para observar a superfície dos oceanos, mas nas últimas duas décadas têm se mostrado como uma ferramenta confiável para obter séries temporais da superfície das águas de lagos, reservatórios e rios (Busker *et al.*, 2019). Num contexto de baixa densidade de estações fluviométricas *in situ* na região amazônica, que acabam dificultando bastante o monitoramento dos rios (Alsdorf; Rodríguez; Lettenmaier, 2007), a altimetria por satélite se torna essencial para estimar e monitorar a bacia amazônica.

As missões de satélites portando altímetros datam desde os anos 70, mas é a partir da década de 90 que há um crescimento significativo no número de missões, consequentemente, ampliando os conjuntos de dado e expandindo as possibilidades de análise (Figura 12).

Figura 12: Série temporal das missões de altimetria por satélite.

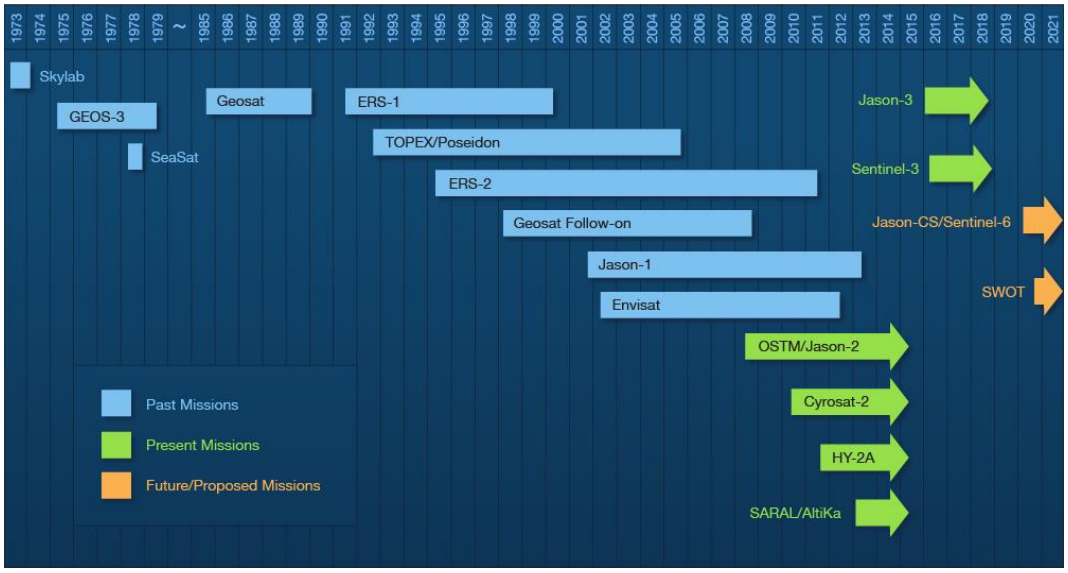

Fonte: NASA/Jet Propulsion Laboratory/Physical Oceanography Distributed Active Archive Center (https://podaac.jpl.nasa.gov/Altimetric_Data_Information/Missions)

Diversos satélites já foram utilizados nos estudos de rios e bacias hidrográficas, como o Topex/Poseidon (Frappart *et al.*, 2005), ENVISAT (Frappart *et al.*, 2006), Jason 1 (Jensen; Rietbroek; Kusche, 2013) e 2 (Paris *et al.*, 2016), ERS (Santos *et al.*, 2010) e Cryosat (Shi; Dong; Zhang, 2021). No entanto, a área de cobertura (*footprint*) dos sensores a bordo desses satélites era de centenas de metros até alguns quilômetros, o que inviabilizava a observação de corpos de água menores.

Com o lançamento pela NASA dos satélites ICESat e ICESat-2 (do inglês *Ice, Cloud and Land Elevation Satellite*), a medição de corpos de água da magnitude de poucos quilômetros passa a ser possível (Xu *et al.*, 2021), embora não sejam capazes de efetuar um monitoramento contínuo, já que o tempo de revisita de ambos os satélites é de 91 dias.

O satélite ICESat foi lançado em janeiro de 2003 e operou até outubro de 2009 carregando o altímetro GLAS (do inglês *Geoscience Laser Altimeter System*) que tinha área de cobertura entre 50 a 90 metros. A missão ICESat foi projetada para fornecer dados para avaliação de calotas de gelo e propriedades de nuvens, embora tenha se mostrado útil para também levantar dados de topografia, corpos d'água e vegetação em todo o mundo. Os dois feixes de lasers do altímetro operavam no comprimento de onda na faixa do visível (verde, 532 nm) e infravermelho próximo (1.064 nm), efetuando 40 disparos por segundo, com cada *footprint* espaçado em 172 metros uma da outra (Figura 13). A precisão horizontal é de 3,7 metros e a resolução vertical é de 15 cm. O off-nadir é de aproximadamente 0.3º, podendo chegar até 5° (NSIDC, [n.d.]). O altímetro oferece 11 produtos, e a versão utilizada neste trabalho foi a GLAH06 1-B, versão 34 (Zwally*et al.*, 2014). Este produto contem elevações da superfície, incluindo geolocalização da *footprint* e refletância, além de correções geodésicas, instrumentais e atmosféricas.

Figura 13: Ilustração esquemática do instrumento GLAS fazendo medições a bordo do ICESat enquanto orbita a Terra.

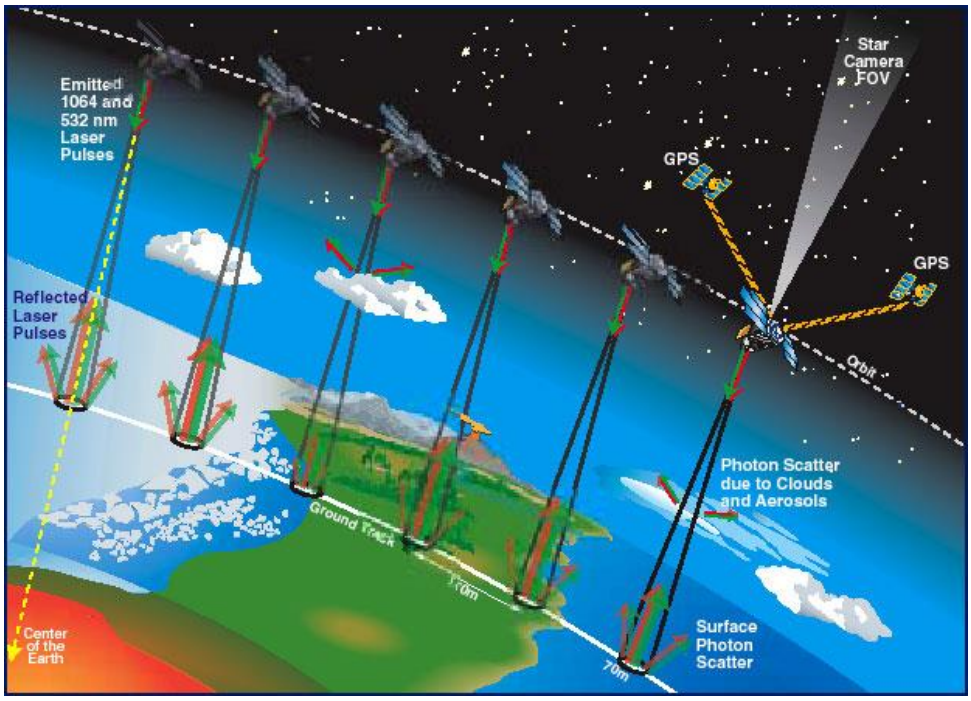

Fonte: National Aeronautics and Space Administration Goddard Space Flight Center (https://attic.gsfc.nasa.gov/glas/about.html)

Dados ICESat/GLAS não têm sido usados de forma extensiva na Amazônia, e não há vastos estudos para se avaliar a qualidade dos dados na medição de altura da superfície da água na escala regional. No entanto, bons exemplos de uso dos dados ICESat/GLAS na análise de corpos d'água estão em Urban, Schutz e Neuenschwander (2008), Zhang *et al.* (2011) e no estudo conduzido por Baghdadi *et al.* (2011), que conclui que a precisão das medidas do GLAS diminui para alvos pequenos que contenham apenas algumas observações por *track* (o trajeto do satélite), tornando difícil o seu uso para rios de largura pequena, correndo o risco de tornar o cálculo para os dados de elevação de água do ICESat inconsistentes, dependendo dos objetivos de seu uso. No entanto, para corpos d'água menos dinâmicos como lagos e reservatórios, os dados foram bem correlacionados com as medidas *in situ*, tanto em Zhang *et al.* (2011) como em Baghdadi *et al.* (2011).

O instrumento ATLAS (do inglês *Advanced Topographic Laser Altimeter System*) está a bordo ICESat-2, que é a continuação da missão iniciada pelo ICESat. Foi lançada em setembro de 2018 e se encontra ativo atualmente. O altímetro possui três pares de feixes e diâmetro de cobertura do solo de aproximadamente 17 metros, emitindo pulsos na frequência de 532 nm, efetuando 10.000 pulsos por segundo. A trajetória de cada par de lasers é de 3,3 km, e cada feixe em um par é separado por

2,5 km. A trilha de pares se distancia em aproximadamente de 90 metros (NSIDC, 2022). O laser é capaz de realizar uma medição de elevação a cada 70 centímetros. Esse arranjo de feixes faz com que a capacidade de cobertura seja muito mais ampla que a de seu antecessor (Figura 14).

Figura 14: Esquema de 3 pares de feixes do sensor ATLAS a bordo do satélite ICESat-2.

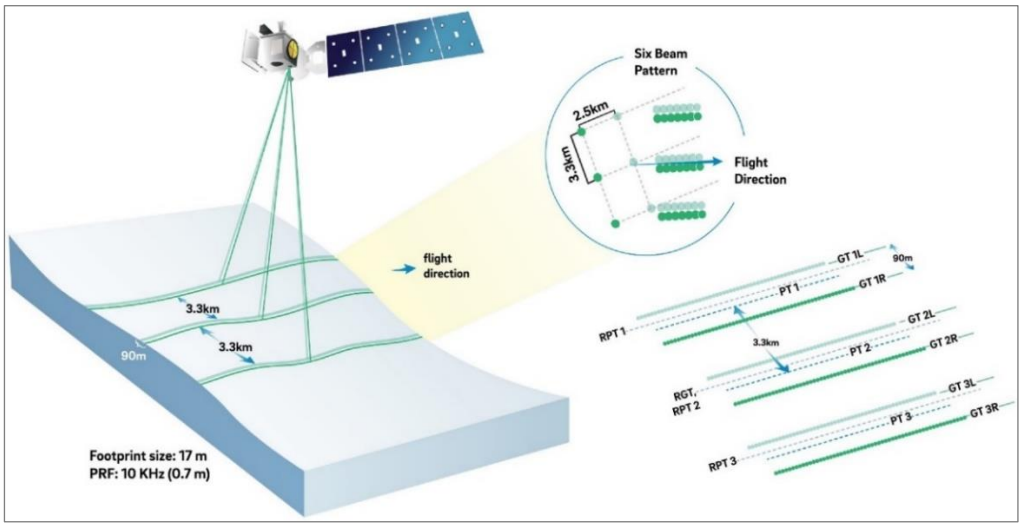

Fonte: National Snow and Ice Data Center (https://nsidc.org/news-analyses/news-stories/mission-and-support-icesat-2-data)

O ICESat-2/ATLAS oferece 10 produtos diferentes, sendo que o ATL13 fornece a altimetria das águas superficiais interiores, o que inclui lagos, reservatórios, baías, estuários e rios, além de uma faixa de 7 km na costa. Os principais parâmetros medidos incluem a altura da superfície da água, a altura significativa das ondas, a velocidade do vento e a profundidade superficial até o fundo. As alturas da superfície da água são fornecidas tanto em relação à elipsoide WGS 84 (quadro de referência ITRF2014) quanto em relação ao nível médio do mar do Modelo Gravitacional da Terra 2008 (EGM2008) (Jasinski *et al.*, 2020).

Existem estudos baseados no uso dos dados ICESat/ATL-13, mas a maioria deles com foco na cobertura de lagos e reservatórios globais (Chen *et al.*, 2022; Narin; Abdikan, 2023). Nestes trabalhos, em geral, os dados apresentam boas correlações com as condições *in situ*. No entanto, os usos para as bacias amazônicas, como em Fassoni-Andrade; De Paiva; Fleischmann (2020a) e Fassoni-Andrade *et al.* (2020b) ainda são incipientes, e praticamente inexistentes para a escala local.

2.4.4. Aeronaves Remotamente Pilotadas (ARP)

Imagens de satélite apresentam limitações de uso e operação, tais como cobertura de nuvens, distorções geométricas e radiométricas, bem como restrições de escala em análises locais e regionais. Imagens gratuitas, como as disponibilizadas pelos satélites Landsat, podem ser inadequadas para representar em detalhe a escala de processos e características ecológicas e geomorfológicas, e a obtenção de imagens de alta resolução podem ter um alto custo (Wulder *et al.*, 2004; Anderson; Gaston, 2013).

Nesse contexto, as Aeronaves Remotamente Pilotadas (ARP) surgiram como uma ferramenta valiosa para superar essas limitações. Eles captam imagens de alta resolução (escala centimétrica) e detalham as características físicas de elementos bióticos e abióticos em escala local e regional (Horne; Thompson, 2008; Herrero-Tejedor *et al.*, 2020), utilizando câmeras digitais que permanecem estáveis durante o vôo. Essas aeronaves têm capacidade de voar automaticamente em baixas altitudes, seguindo rotas predefinidas com a ajuda de sistemas de navegação por satélite integrados. Devido ao seu tamanho e peso reduzidos, as ARPs oferecem plataformas de coleta de dados acessíveis, portáteis e de fácil implantação, especialmente em regiões remotas ou de difícil acesso (Anderson; Gaston, 2013; Chiabrando; Donadio; Rinaudo, 2015).

Nos últimos anos, vêm aumentando o interesse e as possibilidades de uso de ARPs. São ferramentas vantajosas para fins de monitoramento por permitirem frequente atualização de informações, além de, muitas vezes, serem simples de manusear e oferecerem produtos de fácil processamento (Shahbazi; Théau; Ménard, 2014). Alguns dos principais usos das ARPs são a agricultura de precisão e monitoramento de pastagens (Maddikunta, 2021), a gestão de desastres naturais (Giordan *et al.*, 2018), a gestão e monitoramento de ecossistemas e paisagens (Boon; Greenfield; Tesfamichael, 2016) e a manutenção e gestão do patrimônio cultural e arquitetônico (Reid; Ramos; Sukkarieh, 2011; Bakirman *et al.*, 2020), monitoramento das condições da vegetação, como cultivos e florestas (Ferreira *et al.*, 2020), elaboração de estratégias de mitigação ambiental (Albuquerque *et al.*, 2022), modelagem de parâmetros biofísicos e geomorfológicos (Viana *et al.*, 2018; Grohmann *et al.*, 2020), estudo das características do solo (Menzies Pluer *et al.*, 2020), mapeamento e medição de deslizamentos de terra (Garcia *et al.*, 2022).

Existem vários tipos de plataformas de vôo, que vão desde grandes aeronaves asa-fixa com elevada autonomia de vôo (500 km e até dois dias no ar), capazes de voar até 20km de altitude, como por exemplo, a aeronave NASA *Ikhana*, até os dispositivos pequenos, como os asa-rotativa (que lembram pequenos helicópteros) como os *drones Parrot* e *Phantom* (Figura 15) (Anderson; Gaston, 2013).

Figura 15: A esquerda, ARP asa-fixa Nasa Ikhana. A direita, *drone* asa-rotativa Phantom 4-DJI.

Fonte: NASA (https://www.nasa.gov/image-detail/ikhana-flight-over-rogers-dry-lake/) / DJI (https://www.dji.com/br/phantom-4)

Há uma série de considerações operacionais para o trabalho com ARPs. As restrições relacionadas ao tamanho, autonomia e custo de vôo das plataformas se estendem aos sensores, já que a capacidade de carga será diretamente proporcional ao seu tamanho, e portanto, à magnitude dos sensores. Aeronaves menores terão capacidade de carregar sensores menores e mais simples, e isso irá afetar a qualidade dos dados adquiridos por eles. Além disso, ARPs muito pequenas e leves podem apresentar dificuldades no voo, já que serão mais suscetíveis às condições climáticas, como o vento. Desafios relacionados ao pouso e decolagem também devem ser considerados. Enquanto asas-rotativa conseguem decolar e pousar verticalmente, equipamentos asa-fixa necessitam de pista para pouso e decolagem. Além disso, as restrições de voo relacionam-se também às leis e regulamentações (Anderson; Gaston, 2013). No Brasil, a Agência Nacional de Aviação Civil (ANAC) é o órgão que estabelece o código legal para a operação de ARPs (ANAC, 2017).

2.4.5. Structure-from-Motion Multi View Stereo

A fotogrametria digital automatizada tem se tornado uma ferramenta poderosa e bastante utilizada na modelagem espacial ambiental. O avanço na tecnologia tem

democratizado o acesso à modelagem fotogramétrica, ampliando seus usos na geomorfologia. Uma das técnicas fotogramétricas mais utilizadas é a *Structure-from-Motion Multi View Stereo* (SfM-MVS), popular por ser uma metodologia de baixo custo para modelagem em alta resolução (Westboy *et al.*, 2012). Esta técnica foi desenvolvida nos anos 1990, buscando preencher lacunas na tecnologia de visão computacional (Boufama *et al.*, 1993). No entanto sua aplicação nas geociências ainda é recente, tendo ganhado destaque em volume de trabalhos de a partir de 2015 (Carrivick; Smith; Quincey, 2016).

Essa técnica é uma abordagem fotogramétrica totalmente automatizada, uma combinação de dois algoritmos capaz de produzir nuvens de pontos tridimensionais densas e de alta qualidade dos alvos por meio da sobreposição múltipla de imagens 2D obtidas pela câmera fotográfica a partir de diversos pontos de vista. A técnica segue um fluxo de trabalho estruturado que pode ser dividido em dois módulos: *Structure-from-Motion* (SfM), que consiste em identificar características correspondentes entre o conjunto de imagens, estimar parâmetros da câmera e triangular as posições 3D dos atributos correspondentes; e *Multi View Stereo* (MVS), que densifica a reconstrução 3D estimando a geometria 3D da cena para cada pixel no conjunto de imagens. Ambos os resultados combinados geram um modelo 3D detalhado e denso da cena, capturando suas informações de forma, estrutura e textura (Westboy *et al.*, 2012; Chiabrando; Donadio; Rinaudo, 2015; Smith; Carrivick; Quincey, 2015).

A técnica é muito similar à fotogrametria estereoscópica, e a diferença principal entre elas é que a geometria da cena, as posições e orientações da câmera são obtidas de forma automática, não havendo necessidade de se especificar alvos com posições conhecidas. Na técnica SfM, se utiliza um ajuste iterativo baseado em um conjunto de imagens múltiplas e sobrepostas, coletadas de diferentes locais e em diferentes ângulos (Westboy *et al.*, 2012). Por isso, a coleta de imagens com uma alta taxa de sobreposição durante o vôo é importante. Há estudos que estimam que para um objeto na cena ser adequadamente reconstruído, é necessário estar visível em pelo menos três imagens (e em cinco ou seis imagens para alvos densos, como vegetação ou corpos d'água) (Iglhaut *et al.*, 2019).

Conforme descrevem Smith, Carrivick e Quincey (2015) o posicionamento do sensor é feito através da identificação de similaridades entre as várias imagens, que são identificadas pelo algoritmo de uma imagem para outra, dando estimativas

iniciais das posições da câmera e das coordenadas dos objetos. As estimativas de posicionamento são aprimoradas através de um ajuste iterativo, a medida que mais informações das características identificadas nas imagens são coletadas. A transformação das coordenadas dos objetos num sistema de coordenadas é feita através de pontos de controle em solo, com a ajuda de um GPS. No entanto, também opera sem a necessária associação à coordenadas geográficas ou pontos de controle.

A identificação de características correspondentes em diferentes imagens é realizada pelo algoritmo por meio de um sistema de reconhecimento de padrões conhecido como Transformação de Características Invariantes à Escala (SIFT, do inglês *Scale Invariant Feature Transform*), que detecta pontos-chave (*keypoints*). O algoritmo identifica estruturas e associa a elas descritores numéricos únicos para cada ponto da imagem. Esses descritores são, então, empregados para identificar os mesmos pontos em todas as imagens (Westboy *et al.*, 2012; Iglhaut *et al.*, 2019). Importante notar que o algoritmo é capaz de reconhecer esses padrões, independentemente das condições de iluminação, escala e rotação, identificando objetos em imagens obtidas de diferentes perspectivas e em diferentes condições (Lowe, 2004). O número de *keypoints* depende da textura e resolução das imagens, sendo que imagens mais complexas retornarão mais *keypoints*, gerando um modelo mais nítido com maior qualidade de dados na nuvem de pontos. Após obter um número suficiente de *keypoints* e de correspondências entre eles, o algoritmo calcula as posições das imagens no espaço através de parâmetros da câmera, e gera uma nuvem de pontos esparsa.

O algoritmo MVS opera, então, para densificar esta nuvem de pontos esparsa. Segundo Smith, Carrivick e Quincey (2015), há diversos tipos de algoritmos MVS diferentes disponíveis, como os métodos baseados em voxel (preenchimento de grades 3D), métodos baseados na evolução de superfícies (evolução iterativa de malhas poligonais), métodos de fusão de mapas de profundidade (combinação de informações de profundidade de várias imagens num único modelo) e métodos baseados em patches (divisão da cena em pequenas áreas). O método PMVS (*Patch-based MVS*) é frequentemente utilizado em geografia física e é considerado eficaz. Esse método cria uma representação tridimensional de uma cena dividindo-a em pequenos "*patches*" (ou remendos), os combinando entre várias imagens. Os *patches* são expandidos ao redor das correspondências para construir um modelo 3D detalhado da cena (Furukawa; Ponce, 2010). O método é o mais utilizado por

sua eficácia na correspondência de características, embora dependa de informações de textura para funcionar bem.

3. METODOLOGIA

3.1. Levantamento de dados hidrológicos

A estação fluviométrica principal utilizada para levantar dados hidrológicos foi a estação ANA 18850000, localizada em frente à ilha do Arujá, no município de Altamira (Figura 1b). Os dados foram baixados do portal Hidroweb (https://www.snirh.gov.br/hidroweb/serieshistoricas). Existem outras estações distribuídas pela Volta Grande, porém, que não puderam ser utilizadas para observação da série temporal de forma contínua e consistente, seja porque operaram por um curto período de tempo, ou por estarem ativas em anos que não puderam ser comparadas com outras bases de dados.

3.2. Levantamento de imagens de sensores remotos

As imagens foram adquiridas principalmente das seguintes bases:

- *ASF Data Search* (https://search.asf.alaska.edu/#/): mantido pela *Alaska Satellite Facility* em parceria com a *Nasa Earth Data*, oferece extenso acervo de imagens SAR de forma gratuita. Neste banco de dados, foram baixadas as imagens ALOS 1 (*Advanced Land Observing Satellite*) PALSAR (*Phased Array Type L-Band SAR*).
- G-PORTAL (https://gportal.jaxa.jp/gpr/search?tab=1): mantido pela JAXA (*Japan Aerospace Exploration Agency*), oferece de maneira gratuita todo o acervo dos sensores remotos da agência espacial japonesa. Foram adquiridas nesse domínio as imagens JERS-1 (*Japanese Earth Resources Satellite*).
- EO CAT (https://eocat.esa.int/sec/#data-services-area): Catálogo de imagens mantido pela Agência Espacial Europeia (ESA da sigla em inglês *European Space Agency*), tem em seu acervo imagens óticas e de radar, de sensores de diversas agências espaciais do mundo, oferecidas gratuitamente.
- GLOBAL SURFACE WATER (https://global-surface-water.appspot.com/#): neste projeto mantido pela Comissão Europeia (*European Comission*, um braço da União Europeia que propõe legislação,

políticas e programas de ação) com apoio da ONU (Organizações das Nações Unidas) é possível acessar o mapeamento espaço-temporal das águas de superfície de todo o planeta desde 1989. São fornecidas estatísticas de extensão e mudanças do ambiente aquático através da ferramenta online *Freshwater Ecosystems Explorer* (https://www.sdg661.app/), uma plataforma de dados online que permite que o usuário acesse dados acurados, atualizados, de alta resolução e georreferenciados dos ecossistemas de água doce.

3.2.1. JERS-1

O JERS-1 (ou Fuyo-1) foi lançado pela JAXA em fevereiro de 1992 e ficou operacional por 6 anos e meio, quando a missão foi interrompida em Outubro de 1998. O satélite carregou, além de um sensor ótico multiespectral, um sensor SAR que operou na Banda L (1275 MHz/23.5 cm) em polarização HH, com off-nadir fixo num ângulo de 35° à direita do satélite. Este satélite repetia seu ciclo a cada 44 dias, com um faixa de imageamento de 75 km. A resolução espacial das imagens é de 18 metros (ESA EO, [s.d.]).

Produtos JERS *level* 2.1 são definidos no documento de especificações fornecidos pela JAXA da seguinte forma: “Depois de efetuada a compressão de azimute de alcance e *multi-look*, as correções radiométricas e geométricas são realizadas de acordo com a projeção do mapa”. Ou seja, as imagens já são disponibilizadas para o usuário final corrigidas radiométrica e geometricamente. A projeção do mapa é em UTM, reamostrada pela técnica conhecida como “Vizinho mais Próximo” (*Nearest Neighbor*), em coordenada geodésica ITRF97. O tamanho do pixel para os produtos 2.1 é de 12.5 metros, e as imagens são processadas em 4 *looks* (visadas) (JAXA, 2015).

Ao serem baixadas do G-Portal, um único produto vem dividido em 5 tipos de arquivos, que juntos, compõem a imagem final. Cada arquivo compõe uma parte da imagem (diretório de volume, arquivo líder, arquivo de imagem, arquivo trailer e volume de diretório nulo) (JAXA, 2015) e por isso, para que possa ser utilizada plenamente pelo usuário final, precisa ser convertido em uma imagem GeoTIFF. Para isto a ferramenta *Format Conversion Tool for Jers-1* é disponibilizada pela JAXA, e pode ser acessada em https://gportal.jaxa.jp/gpr/information/tool#JERS-1.

3.2.2. ALOS PALSAR

O satélite ALOS (ou Daichi), do inglês *Advanced Land Observing Satellite*, operou de 2006 a 2011. Carregou dois sensores óticos (um pancromático – PRISM e um radiômetro que operou nas bandas RGB e do infravermelho próximo – AVNIR-2) e um radar de abertura sintética – PALSAR (*Phased Array Type L-band SAR*). Este sensor operou na banda L (1270 MHz de frequência), com período de revisita de 46 dias. O ALOS PALSAR evoluiu da tecnologia de seu antecessor (JERS-1), exibindo uma melhor performance no que diz respeito à resolução e precisão geométrica dos produtos e à velocidade e capacidade de tratamento dos dados (EMBRAPA, [s.d.]; JAXA, [s.d.]). As bandas espectrais disponíveis para o PALSAR são (ASF, [s.d.a]):

- Fine:

(1) *Beam Mode FBS*, ou *Fine Beam Single Polarization*: Polarização única (HH ou VV), ângulo off-nadir de 34,3°, resolução espacial de 10 metros e feixe de imageamento de 70 km.

(2) *Beam Mode FBD*, ou *Fine Beam Double Polarization*: Polarização dupla (HH/HV ou VV/VH), ângulo off-nadir de 34,3°, resolução espacial de 20 metros e feixe de imageamento de 70 km.

- Polarimetric:

Beam Mode PLR: Polarização quádrupla (*quad pol*) (HH, VV, VH E HV), ângulo off-nadir de 21,5°, resolução espacial de 30 metros e feixe de imageamento de 30 km.

- ScanSAR:

Beam Mode *WB1* ou *WB2:* Polarização única (HH ou VV), ângulo off-nadir de 27,1°, resolução espacial de 100 metros e feixe de imageamento de 250-350 km.

Estão disponíveis para download produtos L1.0, que não passaram por nenhum processamento, L1.5 que são imagens de amplitude (próprias para uso após correções) georreferenciadas e RTC (*Radiometric Terrain Corrected*) que são imagens em formato GeoTIFF já corrigidas geométrica e radiometricamente e geocodificadas, prontas para uso ao usuário final.

Os produtos RTC são disponibilizados em baixa resolução (30 metros) e alta resolução (12,5 metros), e deu-se preferência pelos produtos em alta resolução. Os

pixels nas imagens estão em *gamma zero (gamma naught* – γ0) e por isso, precisam ser convertidos radiometricamente em dB.

3.2.3. Imagens óticas - Global Surface Water

O projeto Global Surface Water é uma iniciativa governamental (União Européia e Nações Unidas) que disponibiliza o mapeamento em alta resolução (30 metros), gratuito e em formato de dado aberto, das águas expostas e visíveis na superfície de todo o planeta.

A metodologia utilizada foi desenvolvida por Pekel *et al.* (2016). Os mapas e estatística foram elaborados a partir de cenas individuais disponibilizados pelos satélites Landsat 5 (que operou entre 1984 e 2011), 7 (operacional desde 1999) e 8 (operacional desde 2013), distribuídas pelo Serviço Geológico dos Estados Unidos, e foram processadas no Level 1T (Nível de Correção de Terreno Padrão – *Standard Terrain Correction Level*). As órbitas individuais de cada satélite, quando operam simultaneamente, permitem um período de revisita global a cada 8 dias (GSW, 2020).

As características de reflectância espectral das diferentes coberturas do solo tem diferentes assinaturas nos diferentes comprimentos de onda, e essa peculiaridade (assinaturas espectrais contrastantes) são utilizadas nos canais do infravermelho visível, infravermelho próximo e ondas curtas para separar os pixels que detectam a água de outros ambientes (GSW, 2020). A acurácia descrita por Pekel *et al.* (2016) dão conta de que menos de 1% dos pixels detectados dão um resultado falso, e que menos de 5% das detecções foram perdidas.

Os dados disponibilizados permitem mapear os seguintes parâmetros:

- Ocorrência: são as variações espaciais e temporais da superfície da água. Este dado é calculado com base na frequência de ocorrência da água num dado período.

- Intensidade de mudança: mostra a mudança na intensidade da ocorrência da água de superfície, ou seja, onde a superfície da água aumentou, diminuiu ou permaneceu igual.

- Sazonalidade: Descreve a distribuição intra-anual das águas, classificando-as em permanente (visível o ano todo) e sazonal (visível em períodos determinados do ano).

- Recorrência: É a medida do grau de variabilidadeda água de ano para ano, expressa em porcentagem.

- Transição: mostra a conversão dos ambientes de acordo com as classes “sem água”, “sazonal” e “permanente”.

3.2.4. ICESat e ICESat-2

Os dados dos altímetros dos satélites ICESat e ICESat-2 foram adquiridos por meio da plataforma interativa OpenAltimetry (openaltimetry.org). Essa plataforma, fruto de uma colaboração entre várias instituições e universidades dos Estados Unidos, é uma ferramenta online que possibilita ao usuário localizar, visualizar e baixar dados de elevação da superfície coletados pelos satélites ICESat e ICESat-2 em qualquer lugar do mundo. O OpenAltimetry também disponibiliza acesso aos dados por meio de APIs (do inglês *Application Programming Interface* ou interface de programa de aplicações), permitindo a manipulação dos dados em plataformas como o Jupyter Notebook.

A maior vantagem do OpenAltimetry é a sua interface amigável e intuitiva, o que torna seu uso fácil mesmo para iniciantes, ao mesmo tempo em que permite um acesso rápido a conjuntos de dados completos. Essa plataforma é particularmente útil porque a estrutura de dados das missões ICESat pode ser complexa e volumosa, o que poderia dificultar o acesso para potenciais usuários.

Os dados foram inicialmente baixados no formato de arquivos .csv e, posteriormente, também em formato HDF5. Isso permitiu o acesso a grupos de dados individuais.

3.2.5. ARP e SfM-MVS

A ARP utilizada para o escopo desse trabalho utilizou uma plataforma DJI Phantom 4 Pro V2. A câmera digital utilizada possui um sensor CMOS de 1" com 20 MP, medindo 13,2 x 8,8 mm e capaz de produzir imagens de alta resolução com dimensões de 5472 x 3648 pixels. O aplicativo MapPilotPro (https://www.mapsmadeeasy.com/) foi utilizado para planejar e executar as missões de voo, que foram realizadas em diferentes altitudes, possibilitando a geração de imagens com resoluções de pixel variáveis, com base na precisão desejada e no nível de detalhe. As sobreposições entre as imagens foram consistentemente superiores a 60% ao longo e através das faixas de voo. O ângulo da câmera foi ajustado para -85° (5° do nadir). Durante o trabalho de campo, as condições

climáticas variaram de ensolaradas a parcialmente ensolaradas, com eventual cobertura de nuvens.

Todos os produtos gerados foram georreferenciados no Sistema de Coordenadas WGS84 usando o sistema inercial e o receptor de navegação GPS acoplado ao equipamento (não foram utilizados pontos de controle no solo devido a questões logísticas relacionadas a restrições de acesso e às características acidentadas da área de estudo).

3.3. Processamento dos produtos

3.3.1. JERS-1

Os produtos JERS-1 2.1 (já corrigidos radiometrica e geometricamente, e georreferenciados em UTM) após serem baixados em formato CEOS (do inglês *Committee on Earth Observation Satellites*, um formato cru, sem extensão específica), foram convertidos na ferramenta fornecida pela JAXA (*Format Conversion Tool*) em imagens GeoTIFF, adequadas para serem trabalhadas em plataformas SIG. Porém, estas imagens precisam ser filtradas para que o ruído *speckle* seja atenuado. Além disso, o valor de pixel dessas imagens após a conversão está em DN (número digital com valor adimensional de 0 a 255. Para uma melhor interpretação visual e análise das cenas, o ideal é que as imagens SAR estejam em dB (Decibel), ou seja, o valor de cada pixel é associado à sua energia de retroespalhamento.

3.3.2. ALOS PALSAR 1

Os produtos ALOS PALSAR no formato RTC, em alta resolução, já estão georreferenciados em UTM e corrigidos geométrica e radiometricamente, porém, apresentam ruído *speckle* e precisam ser radiometricamente convertidos em dB (sigma naught – σ0) já que os produtos são baixados em gamma0, uma imagem que é mais escura, tornando a análise visual difícil.

3.3.3. SAR Quad-Pol

As imagens ALOS PALSAR *quad-pol* (ou seja, adquiridas nas polarizações HH, VV, HV, VH) foram utilizadas para identificar as áreas de vegetação alagada durante os períodos de cheia na VGX. Isto porque a vegetação alagada se destaca

na polarização HH devido ao efeito *double-bouce*, o que faz com que a sensibilidade trazida por esta característica do sensor seja bastante conveniente para este objetivo.

No software ENVI 5.6, para cada data dos produtos adquiridos durante os pulsos de cheia, foi criado um *stack* com a imagem HH na banda do vermelho, HV na banda verde e VV na banda azul. As polarizações HH e VV evidenciam mais as contribuições do solo, uma vez que podem penetrar através da vegetação, e a polarização HV destaca mais a vegetação densa, porque está relacionada ao volume dos alvos.

Depois de finalizada esta etapa, as imagens foram classificadas através do algoritmo *Random Forest* no software SNAP (*Sentinel Application Platform*), elaborado pela ESA. Apesar de ter sido elaborado para processar imagens Sentinel-1, o programa contém um conjunto de ferramentas poderosas para a observação da Terra e é capaz de processar diferentes tipos de imagens SAR.

A técnica de classificação *Random Forest* faz uma amostragem aleatória e iterativa dos dados e variáveis para gerar um grande grupo (floresta) de árvores de classificação e regressão. O produto final da classificação representa o modo estatístico de muitas árvores de decisão (no caso da classificação aqui empregada, foram usadas 10), ao invés de uma única árvore de classificação produzida por uma única execução de modelo (como é o caso de outras classificações supervisionadas baseadas em valores de pixel). A imagem classificada representa a média de todas as árvores de regressão. O algoritmo calcula, ainda, estimativas de erros internos, a capacidade de estimar a importância das variáveis e a capacidade de lidar com variáveis “fracas” (Breiman, 2001).

As classes selecionadas para a classificação foram “vegetação” e “água”. No momento, não há interesse em identificar diferentes tipos de vegetação ou usos do solo, e o principal objetivo da classificação foi tornar mais clara a identificação das florestas alagadas destacadas pela polarização HH.

3.3.4. SAR Dual-Pol

As imagens de polarização dupla foram agrupadas de acordo com o pulso do rio (seca ou cheia) e de acordo com a polarização (HH ou HV) e foram criados mosaicos de imagens que representassem o período do ano para a Volta Grande, separadas pela polarização (ou seja, Seca HH, Seca HV, Cheia HH e Cheia HV para cada ano selecionado).

Após a formação dos mosaicos, razão HH/HV foi calculada (na verdade, como as imagens estão em escala logarítmica – dB – foi realizada uma subtração entre as imagens HH e HV), e um *stack* com as polarizações HH na banda vermelha, HV na banda verde e HH/HV na banda azul foi criado.

Além disso, outro *stack* foi criado para observar as diferenças nos padões de alagamento entre os períodos de cheia e seca, com o período de seca na banda vermelha e de cheia nas bandas verde e azul.

3.3.5. Global Surface Water

Toda a base de dados da iniciativa *Global Surface Water* está disponível no catálogo *Google Earth Engine*, que é uma plataforma de análise geoespacial baseada em nuvem, que permite aos usuários visualizar, analisar e manipular conjuntos de imagens de satélite disponibilizadas pelos seus proprietários. Esta capacidade de manipulação de largas bases de dados online é bastante conveniente quando se deseja manusear os dados e as estatísticas hidrológicas em variadas escalas de tempo, visando produtos visuais mais convenientes à observação do fenômeno que se deseja investigar.

Os dados Global Surface Water foram trabalhados de forma que mapas anuais de águas superficiais classificadas em “sem dados”, “água permanente”, “água sazonal”, “não é água” fossem criados. Estes mapas então foram baixados para serem trabalhados no software QGIS 3.10.6.

No QGIS, os mapas foram analisados com o plugin SCP (*Semi-Automatic Classification Plugin*) para que as mudanças anuais das classes de água superficial fossem detectadas e posteriormente, mensuradas. Para esta etapa, utilizou-se a ferramente “*Change Detection*” oferecida pelo SCP. Esta ferramenta calcula a quantidade de pixels transformados de uma classe para outra entre duas imagens. Para quantificar a área transformada, utilizou-se a função *r.report* da extensão GRASS oferecida pelo QGIS, que calcula a quantidade de pixels em cada classe. Dessa forma, é possível quantificar a área de águas permanentes e sazonais que foram transformadas em outro tipo de cobertura ao longo dos anos.

3.3.6. SfM-MVS

A técnica SfM-MVS foi utilizada para obter ortofotos e modelos 3D a partir das imagens coletadas pela ARP. As ortofotos foram geradas no Pix4Dmapper versão

4.6.4 (https://www.pix4d.com) e os modelos 3D foram processados no Agisoft Metashape Pro (versão 1.8.3) (https://www.agisoft.com). As configurações utilizadas foram as configurações padrão oferecidas pelos programas.

3.3.7. ICESat e ICESat-2

Os dados de altimetria foram inicialmente filtrados através uma máscara de água criada com base nos dados GSW para cada ano utilizado na análise, garantindo que apenas os dados relacionados à superfície da água fossem incluídos nas análises, o que filtrou dados espúrios e que não tivessem relação com o ambiente aquático.

Após esta etapa, os dados altimétricos passaram por um processo adicional de filtragem, desta vez com base nas classes anuais de inundação (Sem Água, Água Sazonal e Água Permanente), para cada um dos anos de análise.

4. A COMPARISON BETWEEN SUPERVISED CLASSIFICATION METHODS: STUDY CASE ON LAND COVER CHANGE DETECTION CAUSED BY A HYDROELECTRIC COMPLEX INSTALLATION IN THE BRAZILIAN AMAZON

Este capítulo é baseado no artigo publicado no periódico *Sustainability* (ISSN 2071-1050): Affonso, A. A. *et al.* A comparison between supervised classification methods: Study case on land cover change detection caused by a hydroelectric complex installation in the Brazilian Amazon. Sustainability, v. 15, n. 2, p. 1309, 2023. Disponível em: https://doi.org/10.3390/su15021309

Abstract

The Volta Grande do Xingu (VGX) in the Amazon Forest of Brazil was chosen to analyze the land use and land cover changes (LULCC) from 2000 to 2017, with the aim of assessing the most suitable classification method for the area. Three parametric (Mahalanobis distance, maximum likelihood and minimum distance) and three non-parametric (neural net, random forest and support vector machine) classification algorithms were tested in two Landsat scenes. The accuracy assessment was evaluated through a confusion matrix. Change detection of the landscape was analyzed through the post-classification comparison method. While maximum likelihood was more capable of highlighting errors in individual classes, support vector machine was slightly superior when compared with the other non-parametric options, these being the most suitable classifiers within the scope of this study. The main changes detected in the landscape were from forest to agro-pasture, from forest/agro-pasture to river, and from river to non-river, resulting in rock exposure. The methodology outlined in this research highlights the usefulness of remote sensing tools in follow-up observations of LULCC in the study area (with the possibility of application to the entire Amazon rainforest). Thus, it is possible to carry out adaptive management that aims to minimize unforeseen or underestimated impacts in previous stages of environmental licensing.

Keywords: land use and land cover changes; LULCC; Volta Grande do Xingu; Belo Monte; remote sensing; Xingu River

4.1. Introduction

The Amazon Forest is a megadiverse biome, distributed across nine countries, mostly in Brazil. Since the 1970s, unprecedented tropical deforestation rates have been transforming the Brazilian Amazon into a mosaic of agriculture, pasture and different stages of successional vegetation patches (Skole *et al.*, 1994; De Mello *et al.*, 2018; Kalacska *et al.*, 2020b). In the past 20 years, many anthropogenic activities have pressured this biome, such as the construction of hydroelectric dams since the 1990s (Moretto, *et al.*, 2012; Rosa; Gabriel; Carreiras, 2017). Until 2022, seven of the largest existing hydroelectric dams (Tucuruí, Balbina, Samuel, Santo Antônio, Jirau, Teles Pires and Belo Monte) have been in full operation in the legal Brazilian Amazon (Fearnside, 2015; Athayde *et al.*, 2019).

Regional environmental changes caused by hydropower development can lead to non-trivial implications in climate, hydrological and biodiversity regimes in all Amazon regions. The magnitude of the plans and impacts caused by such development projects makes it extremely important to learn all possible lessons from hits and misses in the planning and construction of hydroelectric dams in the Amazon Forest (Fearnside, 2015).

Former experiences in the area indicate the need to improve the systems of development planning, impact analysis and environmental licensing. Furthermore, the role of climate and land cover change in energy planning in emergent economies remains a critical issue that could play a major role in the sustainability of hydropower projects (Marengo *et al.*, 2018; Farinosi *et al.*, 2019).

Dams' impacts in large tropical rivers have been generally assessed belatedly or are underestimated in terms of their socio-environmental changes, affecting socio-ecological sustainability (Winemiller *et al.*, 2016; Jiang *et al.*, 2018). This is the case of the Belo Monte Hydroelectric Complex (BMHC) in the Volta Grande do Xingu (VGX), where the presence of dams has resulted in changes within habitats and biomes (Calvi *et al.*, 2020b). Although it is very common to find in the literature studies that debate the pros and cons of this mega operation (Fearnside, 2015), a search on indexed journal databases reveals that the VGX is a much lesser explored and studied area compared with the rivers and floodplain environments where the other largest Amazon hydroelectric dams are installed.

Land use and land cover changes (LULCC) have been important tools for the assessment of the impacts of large dams on the environment (Swanson; Bohlman, 2021). This is especially essential for the Amazon Forest due to its high cultural and biodiversity values. LULCC evaluation, classification and accuracy are some of the most important applications in remote sensing, and its applicability and enhancement are major concerns in Earth observation sciences (Singh, 1989; Li *et al.*, 2011). Classification methods in remote sensing are the basis for several LULCC environmental applications (Lu; Weng, 2007).

There is no consensus on which classification algorithms are the best for LULCC analysis (Lu; Weng, 2007). The individualities of each study, such as their aims and objectives, the dataset used or the area under study, make the choice for a classification method very particular for each case (Lu *et al.*, 2004). A better comprehension of the use of different classifiers, aiming to gather most relevant and reliable land cover information, is a continuous demand, and this is the reason why the selection of a suitable classifier is so unique and requires the consideration of factors that include algorithm performance, accuracy results, computational resources and limitations inherent to the methodology (Lefsky; Cohen, 2003; Lu; Weng, 2007).

Some of the most important and susceptible aspects that can bring uncertainty to a final product happen during the image acquisition process and during the different stages of the classification procedures. These can, in turn, affect the spatial and radiometric resolutions, generating position and interpretation errors (Zhu, 2017). The poor quality of training samples, which affect the area estimation of land-cover classes and the interaction between the instrument resolution and the scale of processes being analyzed on the ground, is also an issue of concern (Lu *et al.*, 2004). For tropical forests in particular, atmospheric conditions (clouds are often a problem for remote sensing in tropical areas, due to the difficulty of collecting cloud-free orbital imagery), complex vegetation composition and the lack of reliable reference data that can be used for validation must be considered when assessing classification quality (Asner, 2001). To overcome challenges related to the intrinsic complexity of the landscape and elaborate image processing techniques, research has been developed in the LULC classification methods and comparative studies of different classifiers are frequent in literature (Lu; Weng, 2007).

As important as the debates around the advantages and disadvantages of a mega operation such as the BMHC are the measurements of the imbalances caused to such a fragile ecosystem, an issue much less explored in the literature. A better understanding of the relationships between a dam's construction, its operation and the resulting land-cover changes on the part of decision makers and public policy makers is essential for effective land management that promotes both economic development and a conceivable level of sustainability and environmental wholeness. Therefore, it is fundamental to make available the most suitable and straightforward methodologies and data sources, embracing even users outside the remote sensing community.

Considering all of the arguments above, this study seeks to compare the applications and accuracy assessment of supervised parametric (Mahalanobis distance, maximum likelihood, and minimum distance) and non-parametric (neural net, random forest, and support vector machine) classification algorithms, which are very popular in image processing software, in the VGX field.

To do so, we analyzed the land use and land cover change using Landsat images from 2000 and 2017. This study discusses which classification algorithms might be more suitable to evaluate LULCC in VGX and identifies potential alterations in land use and land cover that might be related to the construction of the BMHC.

4.2. Materials and Methods

4.2.1. Study Area

The Amazon is mainly covered by evergreen forest, wetlands and water surface. The main land uses of the biome are cattle ranching, agriculture, mining, logging, non-timber forestry production and uses related to occupation processes, such as road building (Rosa; Gabriel; Carreiras, 2017; Souza *et al.*, 2020). The watershed of the Xingu River is located in the Brazilian states of Pará and Mato Grosso (Mapa 1). The lowest part of the middle Xingu is known as The Volta Grande do Xingu, located totally in Pará.

Cattle have been present in the Xingu floodplains for at least the last 100 years (Michael *et al.*, 2010). More recently, cattle ranches have been replaced by large-scale agriculture, increasing deforestation rates (Barona *et al.*, 2010). Indeed, mega-scale soy plantations are a dangerous threat to the environment in the Amazon

Forest—the Xingu basin alone provides 8% of global soy production (Fearnside, 2001). In the VGX, most of the land cover and land use include primary forest, secondary forest, agriculture (such as cocoa and *açaí* plantations and other kinds of crops), pasture, exposed soil, and alluvial forests under the influence of flood pulses (Salomão *et al.*, 2007; Jiang *et al.*, 2018). The local economy is based on familiar agriculture, and has riverside agriculture and traditional extractive activities, such as rubber and Brazilian nuts (Zuanon *et al.*, 2019).

The construction of BMHC began in 2001 and was completed in 2016. BMHC is the third-largest hydroelectric plant in the world, with 11.2 GW of capacity (Feng, *et al.*, 2017). The major alteration caused to the Xingu River was the inundation of an extensive area of vegetation (as can be seen from Mapa 2a and 2b). It has drained approximately 130 km of the river channel between Pimental and the outlet of the BMHC dam (downstream—the focus of this study). From there, the water is returned to the Xingu's main channel (Eletrobrás, 2009a; Kalacska *et al.*, 2020a).

The BMHC has two dams (Pimental and Belo Monte). The main dam of Belo Monte, which resulted in the Xingu reservoir, is 40 km downstream of the municipality of Altamira, which is the largest Brazilian municipality and concentrates the core urban area nearby (Mapa 1) (Pará, 2011).

Mapa 1: (a) The Xingu watershed and the municipality of Altamira (Pará state, Brazil) within the Brazilian legal Amazon. (b) Location of the VGX, northward of the municipality of Altamira (red square) and the Xingu watershed. (c) The VGX area comprising the Belo Monte and Pimental dams (white dots) in the study area (red square). (d) The study area and its topography in detail.

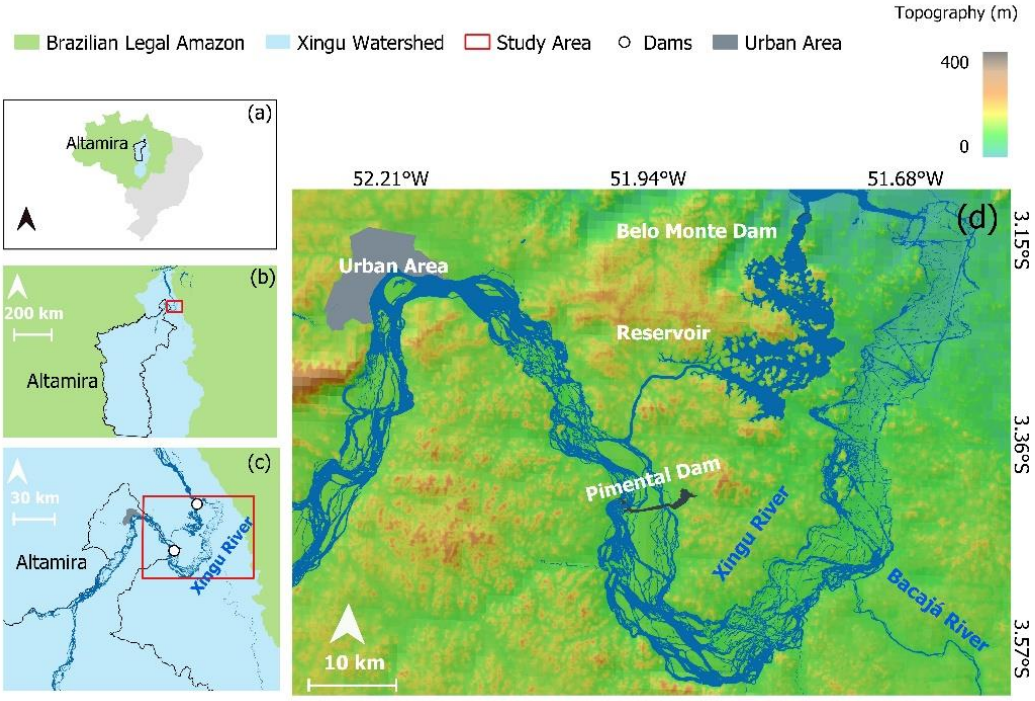

Fonte: Autoria própria

The geomorphology of the Xingu watershed is complex, with large boulders of rock in the Xingu River channel with associated vegetation, mainly downstream of its encounter with the Bacajá River and close to its encounter with the Iriri River (Eletrobrás, 2009a; Sawakuchi *et al.*, 2015). This configuration promotes abundance and diversity in fauna and flora, with about 174 species of fish, 440 species of birds, 259 species of mammals, as well as endemic and endangered species (Costa *et al.*, 2012). Surrounding the VGX, there are different conservation units and indigenous lands (Villas-Boas, 2012).

Tropical rivers, such as the Xingu River, are ruled by a well-pronounced flood pulse (Junk, 1980). Its peak is from March to May, while the dry season is from September to November. The BMHC altered the natural flood pulse in an extreme way when the river flow was diverted for the construction of the reservoir (Zuanon *et al.*, 2019). The average flow, able to reach 20,000 m³/s during its peak, was reduced to 4,000 m³/s yearly, rotating with an 8,000 m³/s flow every two years, a reduction of 80% of the river flow in the VGX area (Pezzuti *et al.*, 2018). This new hydrological regime imposed by the dam operators has been implemented since the

end of 2019, with some occasional interruptions due to judicial interferences caused by the proven unsustainable conditions to keep healthy riverine ecosystems (Fearnside, 2021; O Globo, 2021). Indeed, some studies already indicated that the artificial regulation of the Xingu water flow level is failing to simulate the natural flood pulse and specialized vegetation and aquatic organisms are not able to survive the new conditions (Pezzuti *et al.*, 2018; Zuanon *et al.*, 2019; Kalacska *et al.*, 2020a; Monteiro Neto *et al.*, 2021).

4.2.2. Dataset

Two Landsat (Landsat sensor products are commonly used for local and regional scales—the case of this work—and have been one of the most frequent sources of data for LULC classification and analysis due to the benefits associated with being free of charge and having registered the Earth's surface for decades. Despite the cloud-free issue, Landsat 7 and 8 are able to distinguish many different kinds of surface targets, mainly when supported by good quality field survey data (Feng, *et al.*, 2017) multispectral products were analyzed: a Landsat 7 image from May 26th, 2000 (Mapa 2a) and a Landsat 8 image from July 20th, 2017 (Mapa 2b). The year 2000 represents a scenario before the dam's construction, and 2017 represents a scenario the year right after the dam's full operation. This long time interval was chosen mainly due to the sparse availability of cloud-free images for the VGX, since frequent observations in the Brazilian Amazon are highly improbable using optical images (Asner, 2001). Both images were acquired from the USGS Landsat Image Gallery platform (USGS, [n.d.]) and have spatial resolution of 30 meters. The bands used for the image classification and analysis were the visible, near and short-wave infrared for both. The two images were radiometric calibrated, stacked and mosaicked.

Mapa 2: (a) Landsat 7 image from May 26th, 2000; (b) Landsat 8 image from July 20th, 2017.

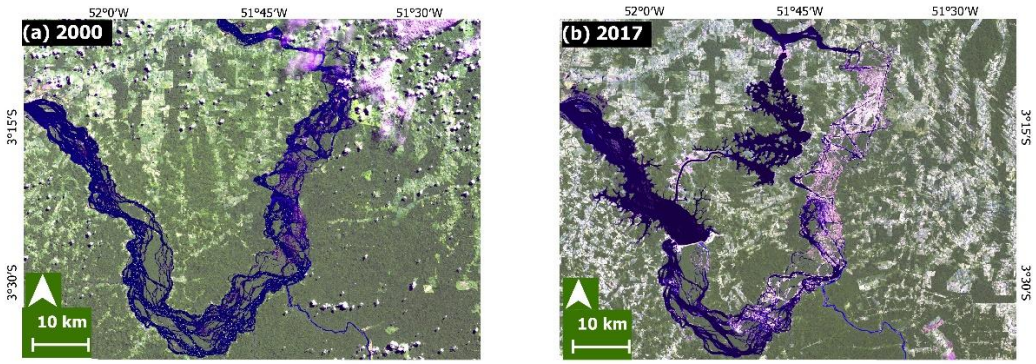

Fonte: USGS, [n.d.]

4.2.3. Class Selection and Spectral Signatures

Based on the Amazon landscape, in a first attempt of class selection, primary and secondary forest, crops, exposed soils, agricultural lands, pasture, river, rocks and clouds were chosen based on a thematic vegetation map from the area (Affonso *et al.*, 2022). It was not possible to completely remove clouds and their shadows from the 2000-year Landsat image using a mask, so it was determined that clouds/shadows would be considered a single class, one that was easier to disregard on the post-classification analysis and other quantitative approaches.

To avoid misinterpretations during the classification process, a prior selection of classes was performed that considering spectral signatures, based on the analysts' previous knowledge. Using the function "Statistics" in ENVI 5.5.3, a spectral profile for both Landsat images (2000 and 2017) for each class was created. The spectral information is the mean spectral signature, or reflectance, of the targets, in digital numbers (DN), for all the bands in the image, collected through polygons represented as region of interest (ROIs) for each of the classes.

A significant overlapping of spectral signatures (primary and secondary forests and agricultural lands) was observed, indicating that the algorithms would misinterpret some of the classes. This might occur due to the heterogeneity and complexity in vegetation structure in tropical forests. Remote sensors primarily capture canopy information and structures between different vegetation stages (e.g., secondary succession and mature forest). This way, different vegetation species may look similar. Besides that, a single pixel might contain more than one

vegetation type, forest stage or land-cover class in a 30m resolution Landsat imagery, resulting in confusion between classes (Li *et al.*, 2011).

Therefore, intermediate stages of vegetation and different kinds of crops and bare soil environments were merged in unique classes: primary and secondary forest and developed mature crops were grouped into “vegetation” and agricultural lands; and fresh crops and pasture were grouped into “agro-pasture”. Ultimately, this study considered five classes: clouds (which were disregarded on the quantitative analysis); forest (which included different types of vegetation, such as alluvial forest, inland forest, primary and secondary vegetation); agro-pasture (including different types of crops, pasture areas, exposed soil and logging areas); river (comprising different depths of the water column); and rocks (large exposed boulders of gneiss rock covered by low vegetation and ferruginous crusts, eventually crossed by the watercourse) (Figura 16). Examples of these classes in the ground are shown in Mapa 3e, f and g.

The fusion of classes worked well for vegetation, but it was observed that, for agro-pasture and rocks in the year 2000 (Figura 16a), the reflectance still has overlaps, corroborating the spectral confusion already reported in the literature between bare soils and non-vegetated wetlands (Lu *et al.*, 2013) in the study area. For the year 2017 (Figura 16b), although river and rocks are well distinguished from other classes in band 5, there is a superposition of rocks and agro-pasture and forest and rivers at the visible band, exhibiting a pattern of two spectral signature clusters in the visible band. Although there are some distinctions between the classes, mainly in the NIR bands, at no wavelength was the separation of spectral signatures complete, including overlapping of error bars.

Figura 16: Spectral profiles and their respective error bars for each class selected for the classification of the images of the VGX area extracted from Landsat 7, May 2000 (a) and Landsat 8, July 2017 (b).

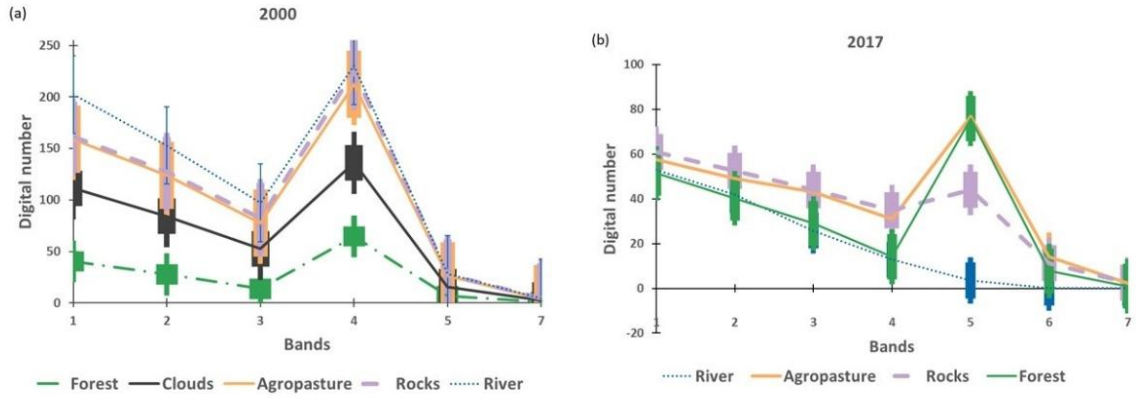

Fonte: Autoria própria

4.2.4. Reference Data

Good classification results strongly depend on the selection of reliable training datasets for each class (Lu *et al.*, 2004) and field visits are important to improve the quality of the reference data (Congalton; Green, 2019). To support and guide the selection of more accurate sample plots to be used in the training stage and improve the accuracy assessment of the final products, very-high resolution orthomosaics, at the order of centimeters and capable of revealing great details of the landscape, were employed. These orthomosaics represent interest zones in the scope of the study, are small compared to the VGX and are therefore not representative of the whole area. These were created through orthophotos collected using a Phantom 4 Remotely Piloted Aircraft (RPA) (examples of orthophotos are in Mapa 3, b, c and d). The images generated by the flights were processed on Agisoft Metashape Pro version 1.8.3. For more information on this methodology, the reader can refer to Westboy *et al.* (2012) and Viana *et al.* (2018). The flights occurred between 07–14 November 2021 in a field trip to the study area, mainly over the floodplain, where different environments (such as wetlands, forests, river, bare soil, and rocks) could be detected. Agro-pasture areas could not be reached by the RPA from where the flights took place and were not imaged. The training sample polygons were then drawn with consideration of the analyst's knowledge of the area, of the imagery dataset acquired from the RPA flights during the field trip, of the high-resolution

imagery set used as reference of the ground and of the spectral signatures of each class.

Mapa 3: Ground reference dataset based on the Planet Labs platform (4.77 m resolution) and used in the accuracy assessment step. The yellow squares are the location from orthophotos (b), (c) and (d). (b) Orthophoto and (e) field example from a rocky environment among narrow river channels and rapids. (c) Orthophoto and (f) field example from exposed soil, rocks and associated rock vegetation. (d) Orthophoto and (g) field example from dense wetland and upland forest vegetation being crossed by the Xingu River (which has its main course diverted into channels) and blocks of rocks. (e-g) are not georreeferenced and are examples of interest zones within environments (b-d).

Fonte: Autoria própria

The last step of the process is the accuracy assessment of the map generated through the classification process using a confusion (or error) matrix. High-resolution aerial or satellite imagery is often used to assess the accuracy of maps made from moderate-resolution satellite imagery, such as Landsat. Simple classification schemes (from two to eight classes) can be reliably assessed from the interpretation of high-resolution imagery (Congalton; Green, 2019).

Due to the small coverage of the orthomosaics generated by the RPA, this dataset could not be used in the accuracy assessment stage as a ground reference. This is why, for this study, a 4.77 meter resolution image, able to cover the entire study area, was created. The imagery was generated by calculating the median of all reflectance values by each pixel, from all imagery products made available for November 2021 by the Planet Labs platform (Mapa 3a), in the Planet Labs Catalog for Google Earth Engine (Planet and NICFI Basemap for Tropical Forest Monitoring Collection). This image was used as a ground reference in the assessment of the classification performances, comparing the classes of the sample training areas on the map with the samples representing the same classes in the reference data set, which were confirmed through field validation, to generate the error matrix (Congalton; Green, 2019).

4.2.5. Complementary Data

A long time series analysis might not capture some important land cover changes. Land cover change at different detection periods (long and short) can provide different conclusions regarding the processes that induce transformations (Li *et al.*, 2018). In a long detection interval, the general trends may be observable, but the intermediate change processes will not necessarily be detected, especially for a land cover in continuous transformation, such as the VGX area.

That is why the dataset from the European Commission's Joint Research Centre Global Surface Water (JRC GSW) initiative was also used for the LULCC analysis. The JRC GSW dataset is an initiative from the European Commission's Joint Research Centre in the framework of the Copernicus Programme which maps the location and temporal distribution of water surfaces at the global scale. These freely available data allow the mapping occurrence, intensity, seasonality, recurrence and transition of water bodies all around the world over the last four decades, providing statistics on the extent and change of water surfaces. The dataset is produced from

Landsat imagery, where each pixel is individually classified into water/non-water using an expert system, and the results are combined into monthly history maps for change detection (Pekel *et al.*, 2016). Data are available from both the GSW website (GSW, [n.d.]) and from the Google Earth Engine (GEE) catalog (GEE, [n.d.]).

For this work, the JRC GSW dataset was handled on GEE using the "JRC Yearly Water Classification History", a dataset containing maps of the location and temporal distribution of surface water from 1984 until 2021. The interval used was from 2000 to 2017. The collection offers a year-by-year classification of the seasonality of water based on the occurrence values detected throughout the year. The dataset's original classes are "no data", "not water", "seasonal water" and "permanent water". The yearly images were downloaded from GEE and the ground surface water maps were treated in QGIS 3.16.14 (Hannover) using the post-classification comparison method through SCP plugin tool "Land Cover Change" (Congedo, 2021). Thus, it was possible to quantify how much of the permanent/seasonal/no water turned into emerged or submerged habitats or remained unchanged.

Tabela 2 presents a summary of all the dataset sources and where they can be reached.

Tabela 2: Summary of dataset sources used in the present study.

Dataset	Source	Link
Landsat 7—May 26th, 2000	U.S. Geological Survey	USGS, [n.d.]
Landsat 8—July 20th, 2017	U.S. Geological Survey	USGS, [n.d.]
Complementary data	JRC GSW	GSW, [n.d.]
Reference data	Planet Labs	GEE, [n.d.]

4.2.6. Image Classification

Image classification methods are divided into many different categories: supervised and unsupervised, parametric and non-parametric, hard and soft (fuzzy), per-pixel, subpixel and per-field and object-based, each of which has many algorithms to suit them (the reader is referred to Dhingra and Kumar (2019) and Ouchra and Belangour (2021) for in-depth reviews on the subject). For this work,

we focused on the supervised (where the algorithm is trained to learn characteristics of the image), parametric, and non-parametric pixel-based (where each pixel stores the spectral information as digital numbers) classifications. While parametric classification assumes that a normally distributed dataset exists and the statistical parameters from the training samples are representative, for non-parametric models, the assumption of a normal distribution of the dataset is not demanded and the statistical parameters do not necessarily split the images into classes (Lu; Weng, 2007).

Six different classification algorithms were tested in the VGX area. Three of these are parametric: Mahalanobis distance (MH), maximum likelihood (ML) and minimum distance (MD). The other three are non-parametric: neural net (NN), random forest (RF) and support vector machine (SVM). MH, ML, MD, SVM (NV5, [S.d.a]; NV5, [S.d.b]) and NN (NV5 [s.d.c]) algorithms were performed on ENVI 5.5.3. RF classification algorithm was performed on the European Spatial Agency's (ESA) SentiNel Application Platform (SNAP) 8.0 toolbox (NV5, [S.d.a]). All of these were performed using the standard configurations of the software. These classification algorithms were chosen because they are very popular in image processing software and are extensively used in the already available literature, allowing for a good basis of comparison (Lu; Weng, 2007; Li *et al.*, 2011; Zhu, 2017).

The MD classifier characterizes each class by its mean reflectance in each band from the training site with unknown pixels assigned to the class with the nearest mean value. In other words, the candidate pixels are assigned to the class that is spectrally closer to the sample mean. In the ML classification, the probability assumes a normal spectral distribution for each class and an equal probability that the pixel belongs to a particular class, taking the variability of classes into account. The MH classification is a direction-induced distance classifier where a probability statistics calculation is used for each class, but assuming that all covariance is equal (Dhingra; Kumar, 2019; Ouchra; Belangour; 2021).

NN is a pixel segmentation technique trained to recognize patterns. It has a non-parametric advantage of taking arbitrary decisions, since it does not make assumptions on a feature's distribution. No prior knowledge about any statistical parameters of a class is required, ensuring an easy adaptation to different types of data (Lu; Weng, 2007; Li *et al.*, 2011). The RF algorithm is a technique that

randomly and iteratively samples the data to generate a large group of classification trees (the so-called forest) at the training stage. This represents the statistical mode of many decision trees, where the outputs are the classes selected by most trees. This usually gets a more robust classification than a single model run (Breiman, 2001).

Lastly, the SVM algorithm, which is a method derived from statistical learning theory, separates the classes based on a decision surface that maximizes the margin between those classes. The closest points to these surfaces are the support vectors, which are the critical elements of the training set. This algorithm has become a popular classification method due to its excellent empirical performance (Hsu; Chang; Lin, 2003).

The sampling strategy was designed to select a large number of sample polygons for each land cover or land use class in different areas of the image, aiming to capture the greatest possible spectral variability of the classes. Samples were located where there was certainty that the land cover/use did not change between 2000, 2017 and 2021. This strategy was chosen since there were no available reference images obtained in the field from years 2000 and 2017. Training samples were overlaid on the 2000, 2017 and 2021 images separately to adjust the land cover classes based on visual interpretation. The same strategy was adopted to select test samples in the reference image for the accuracy assessment step, making sure that they were different from the training polygons. Tabela 3 describes the number of pixels within the training and test sample polygons used for each class for the years 2000, 2017 and 2021 respectively.

Tabela 3: Number of pixels within the ROIs for training and testing polygons used for each class, for all classifications, for 2000, 2017 and 2021.

	2000	2017	2021
Classes	Training		Test
Forest	66,605	42,449	560,556
Agropasture	17,568	17,736	221,591
River	5,054	28,749	129,179
Rocks	1,575	6,890	43,396
Clouds	20,602	X	X

It is notable that forest, agro-pasture and river classes have more training pixels than rocks. This approach was used because, in addition to being less frequent in the landscape, the rocky environment in the Landsat images could easily be visually confused with other environments (such as water or vegetation associated with the rocks), even when using NIR bands or the reference image to select them. Rock training classes were chosen considering only emerging areas in both 2000 and 2017 images, in the reference image from 2021 and on orthophotos acquired in the field. Therefore, considering the other classes, many less samples labeled as rocks were available to be selected as training samples.

4.2.7. Accuracy Assessment

Quantitative accuracy assessment of maps relies on the comparison of the area represented on the map against reference information for the same site. A common method for classification accuracy assessment is through the use of confusion (or error) matrices. The reader is referred to Congalton and Green (2019) (pp. 74–76) and NV5 ([S.d.b]) for mathematical representation and examples of confusion matrices. In this work, they were calculated using ENVI 5.5.3 post classification tool “Confusion Matrix Using Ground Truth ROIs”. This pairs ground truth reference ROIs with the classes of the classified image, to show what percentage of the ROI pixels were or were not contained in the resulting classes. It also provides a specific evaluation of the agreement between the classified result and the reference data, giving details even on misclassification (Li *et al.*, 2011). The report

generated when a confusion matrix is calculated contains the following diagonal elements:

Overall Accuracy (OA): calculated by summing the number of reliable classified pixels divided by the total number of training pixels.

Errors of Commission (Comm): are the fraction of sample pixels that were predicted to be in a class but do not belong to that class (false positives).

Errors of Omission (Om): are the fraction of pixels that belong to a class but were predicted to be in a different class (false negatives).

Producer Accuracy (PA): a measure of the probability that a pixel in a given class was classified properly.

User Accuracy (UA): a measure of the probability that a pixel predicted to be in a certain class really belongs to that class.

Kappa Coefficient (Kappa): takes non-diagonal elements into account and measures how equivalent classification and reference values are. A kappa value of 1 represents a perfect match, while a value of 0 represents no equivalence. Despite the criticism by some authors, the kappa coefficient is considered a powerful tool when analyzing a single error matrix and for comparing the differences between various error matrices (Pontius; Millones, 2011; Congalton; Green, 2019).

Although the literature recommends accuracies of 85% as acceptable, for contemporary mapping this suggestion may be inappropriate and unrealistic (Foody, 2008; Anderson *et al.*, 2018). In fact, there are no agreements in the scientific community about limits on how accurate a classification must be to be considered reliable (Nguyen *et al.*, 2020). The approach usually used in the literature follows the selection of the most accurate classifier, either among the simultaneously evaluated classifiers or the comparison with classifiers from other studies. With this in mind, for this study, a range of values were defined to categorize the performance of the classification algorithms (Tabela 4):

Tabela 4: Accuracy assessment performance categories considered for this study. OA: Overall Accuracy; Comm: Commission; Om: Omission.

	OA/Kappa	Comm/Om Errors	Producer/User Accuracy
Satisfactory	Larger than 0.8	Smaller than 10%	Larger than 80%
Regular	Between 0.7 and 0.8	Between 10% and 25%	Between 60% and 80%
Unsatisfactory	Smaller than 0.7	Larger than 25%	Smaller than 60%

4.2.8. Detecting Land Cover Change

A great number of change detection techniques have been developed, but many are able to detect only binary transformations on the landscape (change/non-change categories). A "from–to" change track strategy, otherwise, provides a superior comprehensive understanding of LULCC patterns and rates (Zhu, 2017).

The post-classification comparison is a very popular change detection analysis, and was the method chosen for this work. It was performed using QGIS 3.16.14 (Hannover) through the Semi-Automatic Classification Plugin (SCP) post processing tools "Cross Classification" and "Land Cover Change" (Viana *et al.*, 2018). Studies have shown that this method offers good accuracy in representing changes in land use (Prenzel; Treitz, 2006; Virk; King, 2006).

The classification results from years 2000 and 2017 were cross-tabulated on a pixel-to-pixel comparison, where each pixel represents a class transforming into a different class between the dates (i.e., the direction of transformation). Then, maps regarding these changes (or tracks) were generated for forest/non-forest and for river/non-river transformation categories.

The directions of changes were also tabulated and represented as graphics, in which transformations were estimated through ten change tracks: agro-pasture to forest (AgrPa-For), rock to forest (Roc-For), river to forest (Riv-For), forest to agro-pasture (For-AgrPa), forest to rock (For-Roc), forest to river (For-Riv), river to agro-pasture (Riv-AgrPa), river to rock (Riv-Roc), agro-pasture to river (AgrPa-Riv), and rock to river (Roc-Riv).

Since the classification process and LULCC analysis are complex and involve many different steps, Figura 17 summarizes all the methodology described above in a comprehensive workflow.

Figura 17: Classification process and LULCC analysis workflow.

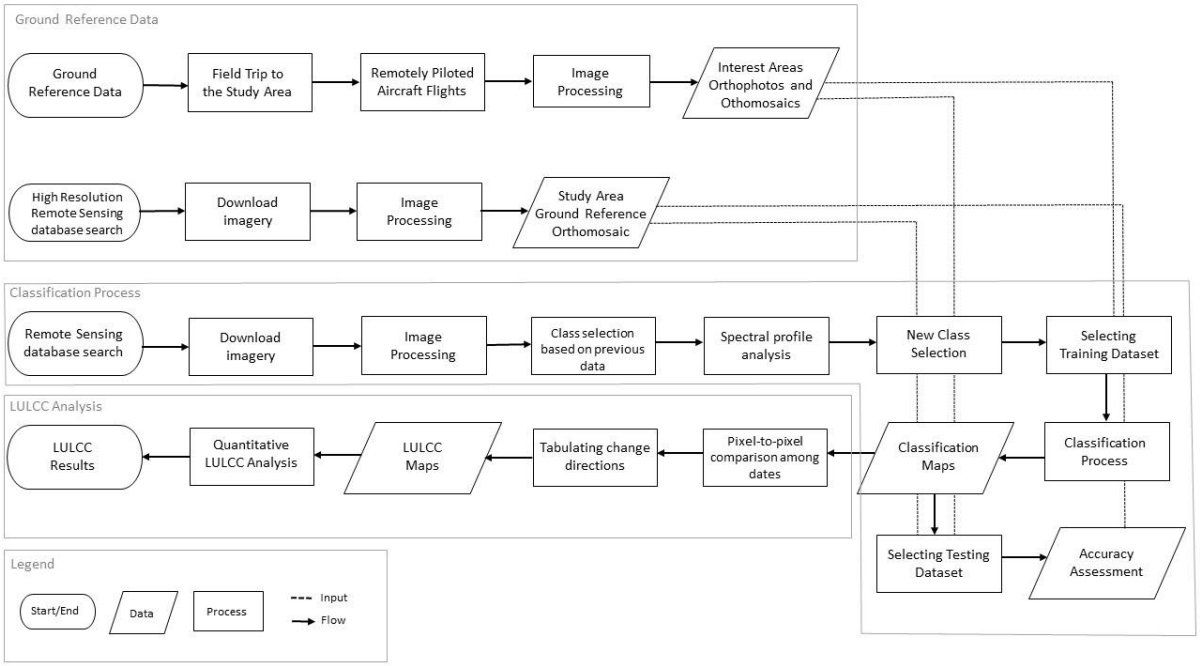

Fonte: Autoria Própria

4.3. Results

4.3.1. Classification Accuracy Assessment

Map accuracy assessment assumes that the information contained within the error matrix is a true characterization of the classified map being assessed. Analysis of the causes of its differences might be one of the most important steps in the construction of a thematic map (Congalton; Green, 2019). Tabela 5 shows a summary of all accuracy metrics calculated for river, forest, agro-pasture, and rock classes. Columns represent true classes, while rows represent the classifier's predictions.

According to Tabela 4, regarding Overall Accuracy and Kappa Coefficient, all the classifiers were considered satisfactory, which means that all the classifications are in good agreement with the reference data. All values were above 0.9, except Kappa for MD in 2017 (0.88) (Tabela 5). However, these two measures alone are not enough to point to misclassifications of individual map classes. Although some authors consider the Kappa Coefficient a more meaningful statistic when compared to Overall Accuracy, the similarity between them in this study makes Kappa less efficient as an assessment parameter (Congalton; Green, 2019).

All the algorithms had good performances for the forest class, for both years, with Comm and Om errors and PA and UA considered satisfactory in all cases, which was expected due to its homogeneity, major area coverage in the image and distinct spectral signature from the other land classes. Major omission errors happened in the rock class for both MH (32.70%) and MD (41.21%) in 2000, and for MD in 2017 (41.14%) (Tabela 5). This means that an elevated percentage of the area predicted to be classified as rocks was excluded (omitted) from the rock category. Commission errors were unsatisfactory only for RF in 2000 (32.11%) and 2017 (25.23%—a border value) (Tabela 5), which means that for both, the algorithm included pixels predicted to be classified as rocks in other categories. There were also regular performances for Comm and Om errors for agro-pasture (MH in 2000 and 2017 and MD in 2017), river (MH, MD and RF in 2000) and rocks (MD in 2000 and for all the algorithms in 2017) (Tabela 5).

Tabela 5: Confusion matrices containing overall accuracy, kappa coefficient, commission and omission errors and producer and user accuracies calculated for all classification methods, for 2000 and 2017. OA: Overall Accuracy; Comm: Errors of Commission; Om: Errors of Omission; PA: Producer Accuracy; UA: User Accuracy; Kappa: Kappa Coefficient; MH: Mahalanobis Distance ML: Maximum Likelihood; MD: Minimum Distance; NN: Neural Net; RF: Random Forest; SVM: Support Vector Machine.

2000												
	MH				ML				MD			
OA	0.95				0.99				0.96			
Kappa	0.92				0.99				0.94			
	Comm (%)	Om (%)	PA (%)	UA (%)	Comm (%)	Om (%)	PA (%)	UA (%)	Comm (%)	Om (%)	PA (%)	UA (%)
Forest	6.41	0.00	100.00	93.59	0.46	0.28	99.72	99.54	1.29	0.08	99.92	98.71
Agropasture	1.00	15.53	84.47	99.00	0.00	1.24	98.76	100.00	1.92	2.55	97.45	98.07
River	10.72	0.08	99.92	89.28	2.10	2.15	97.85	97.90	12.13	0.16	99.84	87.87
Rocks	0.47	32.70	67.30	99.53	8.05	5.02	94.98	91.15	15.82	41.21	58.79	84.18
	NN				SVM				RF			
	Comm (%)	Om (%)	PA (%)	UA (%)	Comm (%)	Om (%)	PA (%)	UA (%)	Comm (%)	Om (%)	PA (%)	UA (%)
OA	0.95				0.99				0.96			
Kappa	0.92				0.99				0.94			
Forest	0.78	0.04	99.96	99.22	0.58	0.11	99.89	99.42	1.46	0.52	99.48	98.54
Agropasture	0.21	1.82	98.18	99.79	0.29	1.66	98.34	99.71	0.41	3.26	96.74	99.59
River	0.83	8.01	91.99	99.17	2.63	0.72	99.28	97.37	3.36	14.02	85.98	96.64
Rocks	17.01	2.67	97.33	82.99	3.26	7.16	92.84	96.74	32.11	7.24	92.76	67.89
2017												
	MH				ML				MD			
OA	0.95				0.98				0.93			
Kappa	0.91				0.96				0.88			
	Comm (%)	Om (%)	PA (%)	UA (%)	Comm (%)	Om (%)	PA (%)	UA (%)	Comm (%)	Om (%)	PA (%)	UA (%)
Forest	6.53	0.02	99.98	93.47	0.93	0.51	99.49	99.07	6.43	0.00	100.00	93.57
Agropasture	2.70	17.64	82.36	97.30	0.66	5.18	94.82	99.34	9.83	18.20	81.80	90.17
River	2.78	2.44	97.56	97.22	0.00	4.35	95.65	100.00	2.31	1.11	98.89	97.69
Rocks	11.36	15.75	84.25	88.64	16.71	2.22	97.78	83.29	15.80	41.14	58.86	84.20
	NN				SVM				RF			
	Comm (%)	Om (%)	PA (%)	UA (%)	Comm (%)	Om (%)	PA (%)	UA (%)	Comm (%)	Om (%)	PA (%)	UA (%)
OA	0.97				0.98				0.97			
Kappa	0.96				0.96				0.94			
Forest	1.27	0.12	99.88	98.73	1.25	0.09	99.91	98.75	1.96	0.08	99.92	98.04
Agropasture	3.89	5.50	94.50	96.11	2.25	5.48	94.52	97.75	2.07	9.13	90.87	97.93
River	0.30	1.96	98.04	99.70	0.41	3.11	96.89	99.59	0.06	5.68	94.32	99.94
Rocks	14.31	14.48	85.52	85.69	15.43	8.13	91.87	84.57	25.23	7.24	92.76	74.77

For both years, and for parametric and non-parametric classification algorithms, user and producer accuracies were predominantly above 80% for forest, river and agro-pasture. Nevertheless, the rock class had lower rates mainly when compared with other classes, for almost all algorithms and both years. The only exception is for ML and SVM in 2000. The matrices reveal especially high Comm and Om errors for MH, MD and RF algorithms in both years. PA is much lower than 80% for Maha and MD in the year 2000. RF and MD also have higher errors in the year 2017. For the other classifiers, Comm and Om errors, PA and UA, although still adequate, had their performances below other classes, such as forest and agro-pasture.

The performance of the parametric algorithms in the rock class is more accurate than the non-parametric algorithms, mainly for MD and MH classifiers, in both years. The visualization of the classification maps of all the methods are presented in Mapa 4 and Mapa 5 for 2000 and 2017 respectively.

Mapa 4: Pixel-based classification from Mahalanobis distance (a), maximum likelihood (b), minimum distance (c), neural net (d), SVM (e) and random forest (f) for the year 2000.

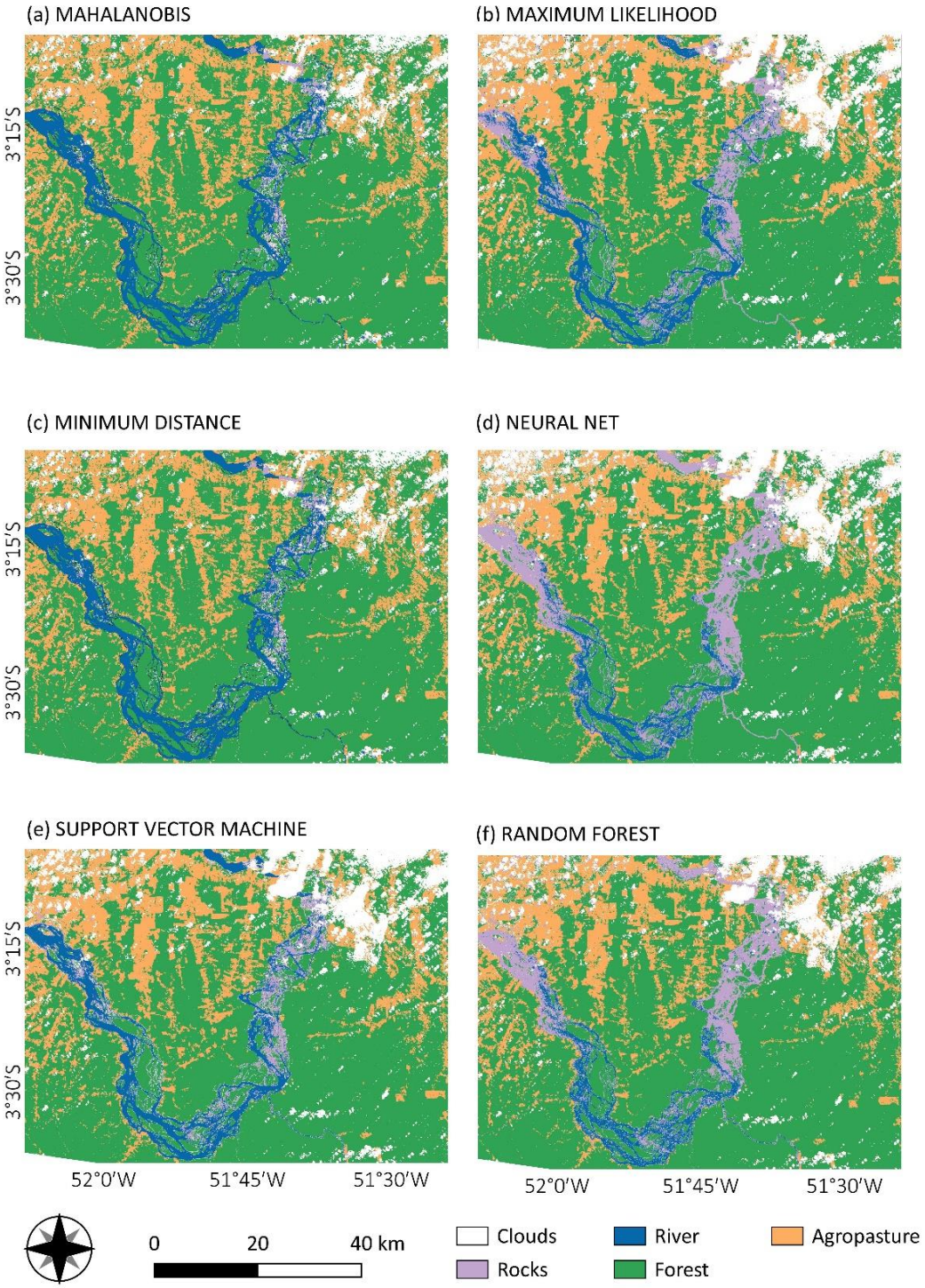

Fonte: Autoria própria

Mapa 5: Pixel-based classification from Mahalanobis distance (a), maximum likelihood (b), minimum distance (c), neural net (d), SVM (e) and random forest (f) for the year 2017.

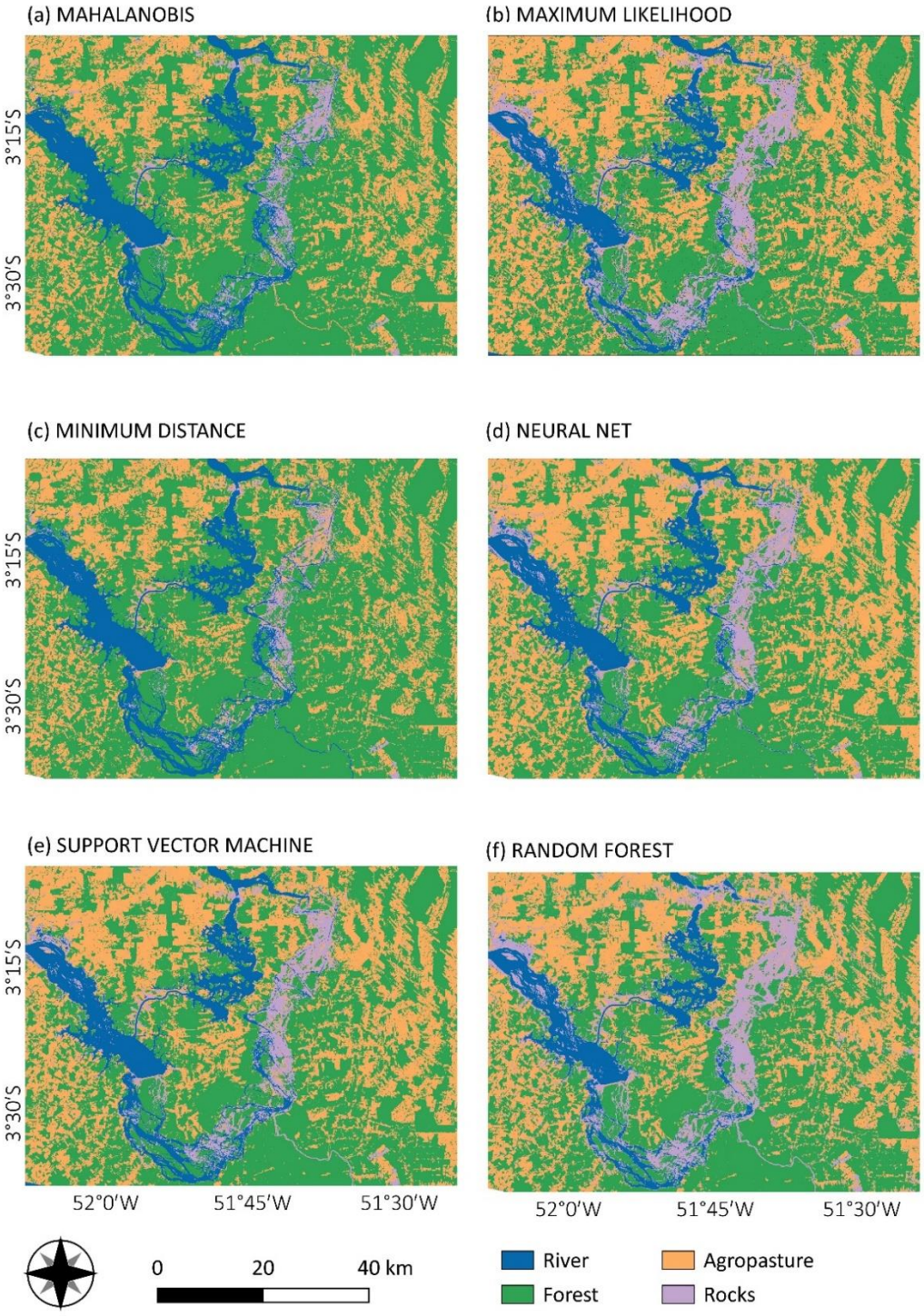

Fonte: Autoria própria

Class area estimation for each classification algorithm for both years are shown in Figura 18, revealing the variation of the classified area between classification outputs. Forest and agro-pasture were the most homogeneous classes (less variation between all classifications), with emphasis on the year 2000, where there was only

an 8% difference in area between the algorithms which classified the smaller (ML) and greater (MH) forest area. In opposition, rock and river classes had more than a 50% difference in the classified areas, for both years, between the algorithms. Rock class, as expected, was the most heterogeneous class, with a more than 70% difference between the areas classified using MD—which detected the smaller rock area—and NN (79% for the year 2000) and RF (72% for 2017), which classified the larger rock areas.

Figura 18: Variation of classified areas, for each different class and for each classification algorithm, for 2000 and 2017.

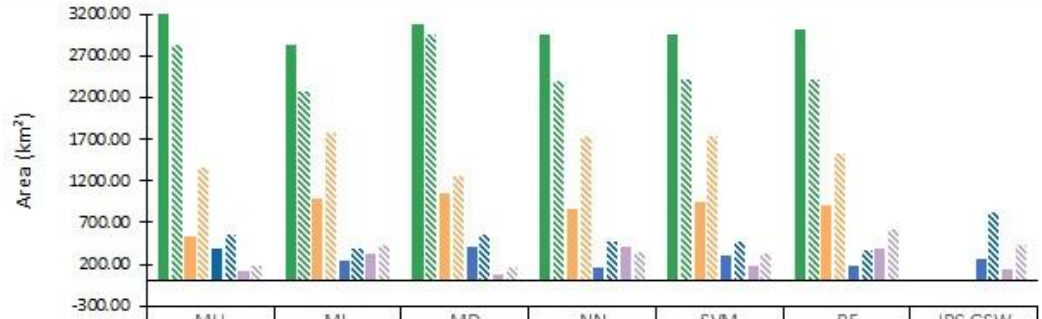

	MH	ML	MD	NN	SVM	RF	JRC GSW
Forest_2000	3585.53	2825.38	3080.26	2957.06	2957.92	3017.73	
Forest_2017	2827.17	2278.69	2949.41	2393.28	2406.31	2417.70	
Agropasture_2000	528.85	982.15	1040.18	861.45	954.81	907.46	
Agropasture_2017	1369.58	1776.35	1266.04	1723.52	1730.94	1531.30	
River_2000	385.38	252.77	400.67	166.78	305.44	175.24	269.81
River_2017	561.75	383.59	555.16	475.92	481.02	373.86	825.52
Rocks_2000	109.73	319.60	83.54	408.49	172.94	392.23	141.60
Rocks_2017	182.75	431.49	170.64	348.53	322.97	616.82	431.74

Fonte: Autoria própria

4.3.2. Land Cover Change

Due to the land flooding necessary for the reservoir construction and the expansion and installation of secondary economic activities triggered by the power plant construction, the most significant transformation was from forest to non-forest classes. For instance, the conversion from forest to agro-pasture in all classification methods (Mapa 6). A few agro-pasture areas have been converted to forest, mainly in the north of the study area, similar to what is observed in Figura 19. Mapa 6 and Figura 19 show the land cover transformation for forest and non-forest classes in the VGX area.

Mapa 6: Land cover change for forest and non-forest transitions from 2000 to 2017, derived from Mahalanobis distance (a), maximum likelihood (b), minimum distance (c), neural net (d), SVM (e) and random forest (f) classifications.

Fonte: Autoria própria

Figura 19: Land use and land cover change from 2000 to 2017 for forest to non-forest areas using minimum distance (MD), Mahalanobis distance (MH), maximum likelihood (ML), neural net (NN), random forest (RF) and support vector machine (SVM) classifiers. Trajectories: forest to agro-pasture (For-AgrPa), forest to rocks (For-Roc), forest to river (For-Riv), agro-pasture to forest (AgrPa-For), rock to forest (Roc-For) and river to forest (Riv-For).

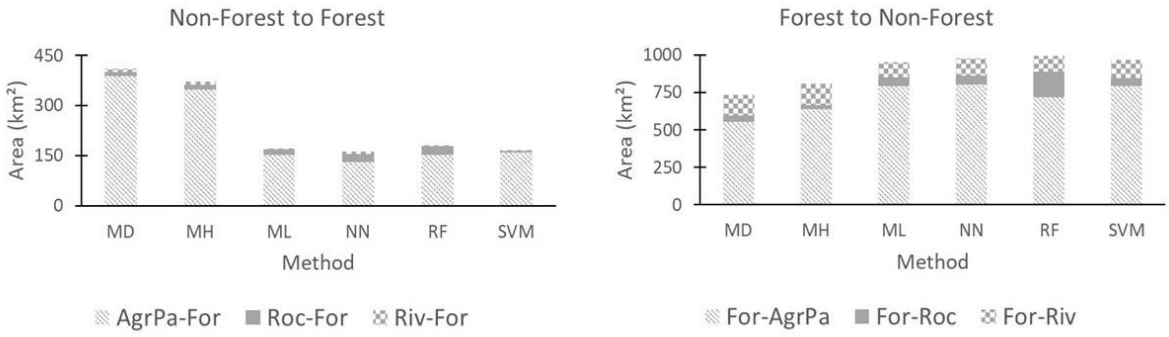

Fonte: Autoria própria

Mapa 7 and Figura 20 show the land cover transformation for river and non-river classes. Downstream of the Xingu River, the main alteration is the conversion from river to non-river areas, while upstream and in a channel area northward, there is an increase in the river area (non-river to river classes). Both changes are associated with the construction of the reservoir. In the first case, the reduction of the water flow caused by the river damming exposed environments that were previously submerged, mainly rocks, but also soil that ultimately turned into agro-pasture areas and even recovered forest (Figura 20) Upstream, due to the flooding of land areas, mainly forest areas, but also crops, were transformed into water (the Belo Monte reservoir) (Mapa 7).

Mapa 7: Land cover change for river and non-river transitions from 2000 to 2017, derived from Mahalanobis distance (a), maximum likelihood (b), minimum distance (c), neural net (d), SVM (e) and random forest (f) classifications.

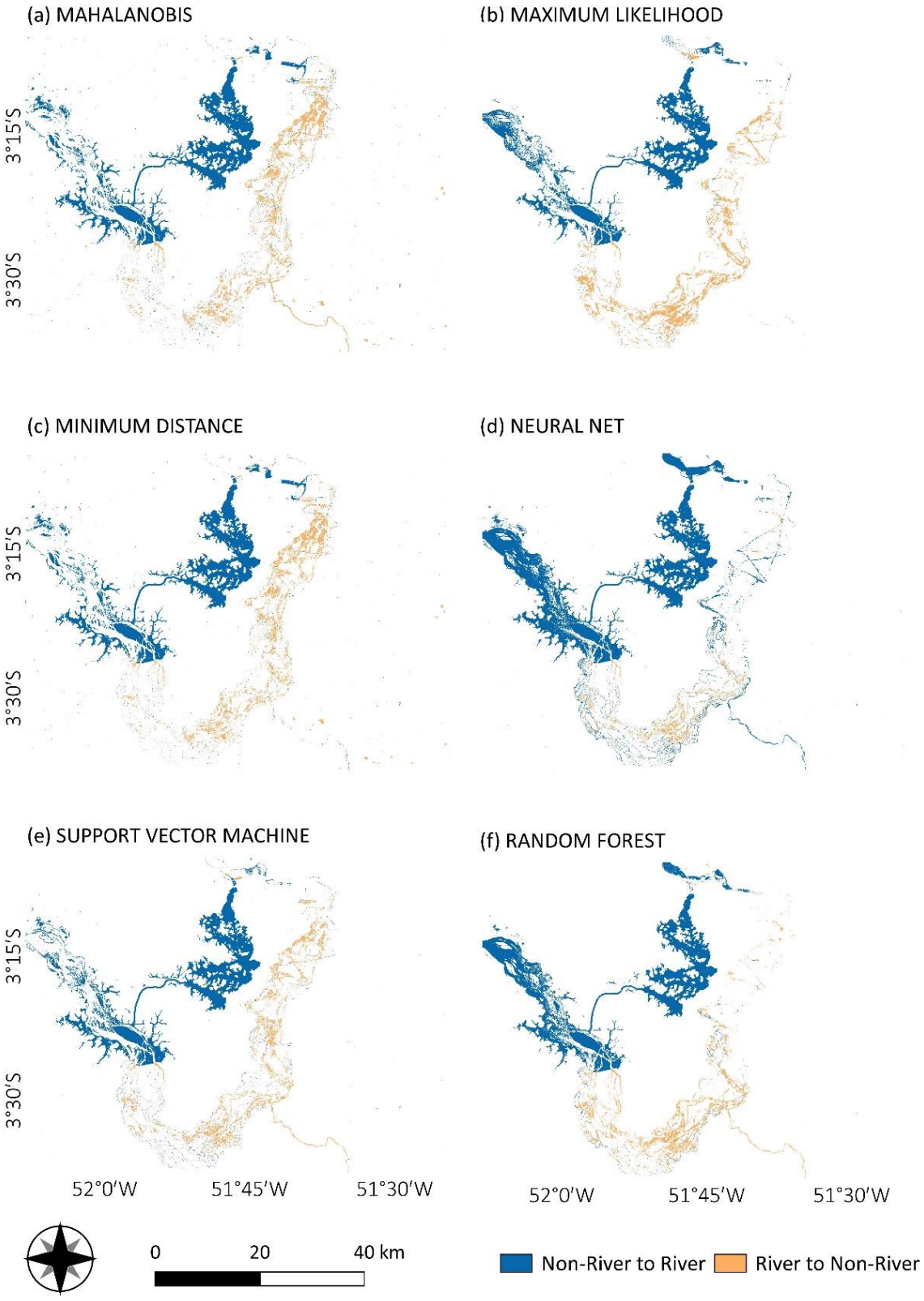

Fonte: Autoria própria

Figura 20: Land use and land cover change from 2000 to 2017 for river to non-river areas using minimum distance (MD) Mahalanobis distance (MH), maximum likelihood (ML), neural net (NN), random forest (RF) and support vector machine (SVM) classifiers. Trajectories: river to agro-pasture (Riv-AgrPa), river to rocks (Riv-Roc), river to forest (Riv-For), agro-pasture to river (AgrPa-Riv), rock to river (Roc-Riv) and forest to river (For-Riv).

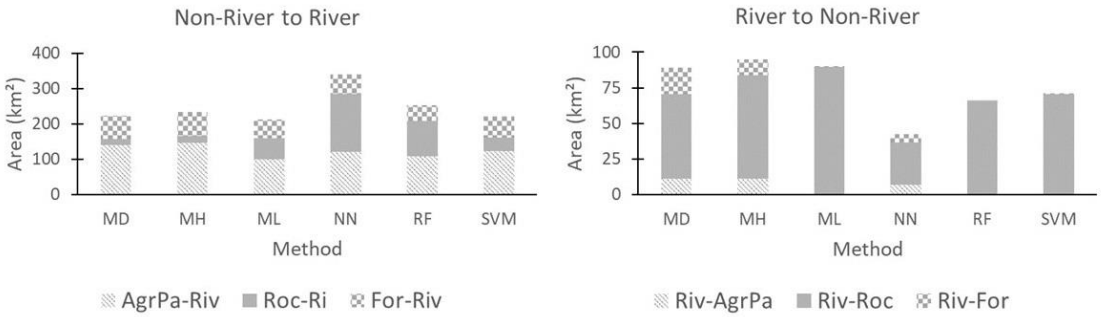

Fonte: Autoria própria

Tabela 6 gives a summary of the areas of LULCC for each classifier in both years shown in Mapa 6.

Tabela 6: LULCC areas from forest to non-forest and river to non-river areas, for each year, using minimum distance (MD) Mahalanobis distance (MH), maximum likelihood (ML), neural net (NN), random forest (RF) and support vector machine (SVM) classifiers.

	Area (km²)			
	2000		2017	
	Forest to Non-Forest	Non-Forest to Forest	River to Non-River	Non-River to River
MH	809.07	372.64	95.06	233.32
ML	950.05	169.79	89.56	212.09
MD	734.11	410.59	89.32	223.72
NN	980.41	161.92	42.37	340.38
SVM	969.51	164.06	70.45	220.12
RF	996.48	177.41	65.81	253.56

4.3.3. JRC Ground Surface Water Dataset

Figura 21 shows yearly changes in the water availability during the analyzed period. Quantifying this information is important since the different performances of the algorithms, mainly regarding river and rock classes, could have biased the analysis in relation to the impacts caused in these environments when the river was dammed. This could have led to a misinterpretation in which the classifier would be responsible for the difference between the areas, and not the impact caused by the dam shows the alteration in key years (the year when the dam construction was concluded, one year before and one year after the river damming).

Figura 21: Products from JRC ground surface water data. The graphics represent (a) permanent water turned into not water (red) and seasonal water (orange), (b) seasonal water turned into not water (red) and permanent water (blue), and (c) not water turned into seasonal water (orange) and permanent water (blue).

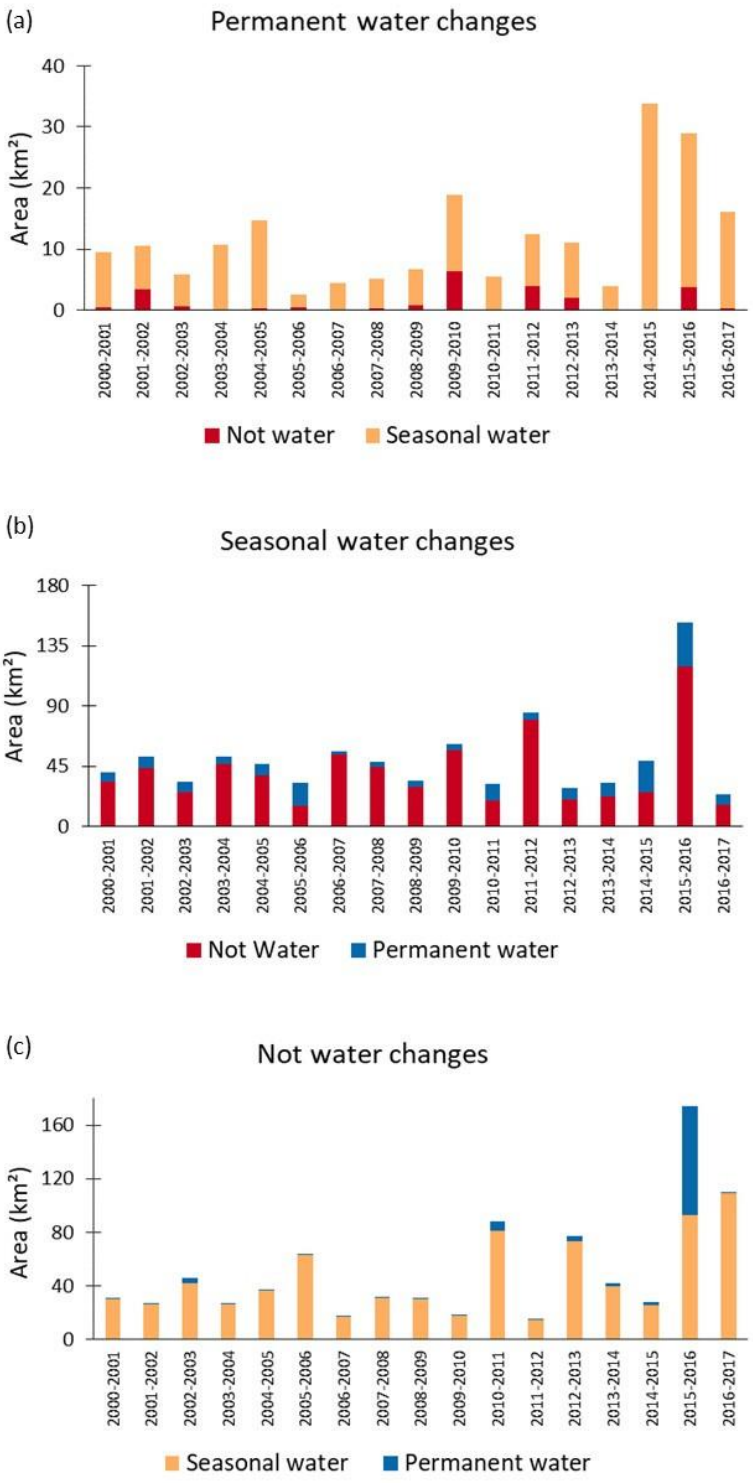

Fonte: Autoria própria

Mapa 8: Ground surface water transformations in three key periods: (a) before the river damming (2013–2014), (b) the year of the dam's conclusion (2014–2015), and (c) one year after the conclusion (2015 to 2016).

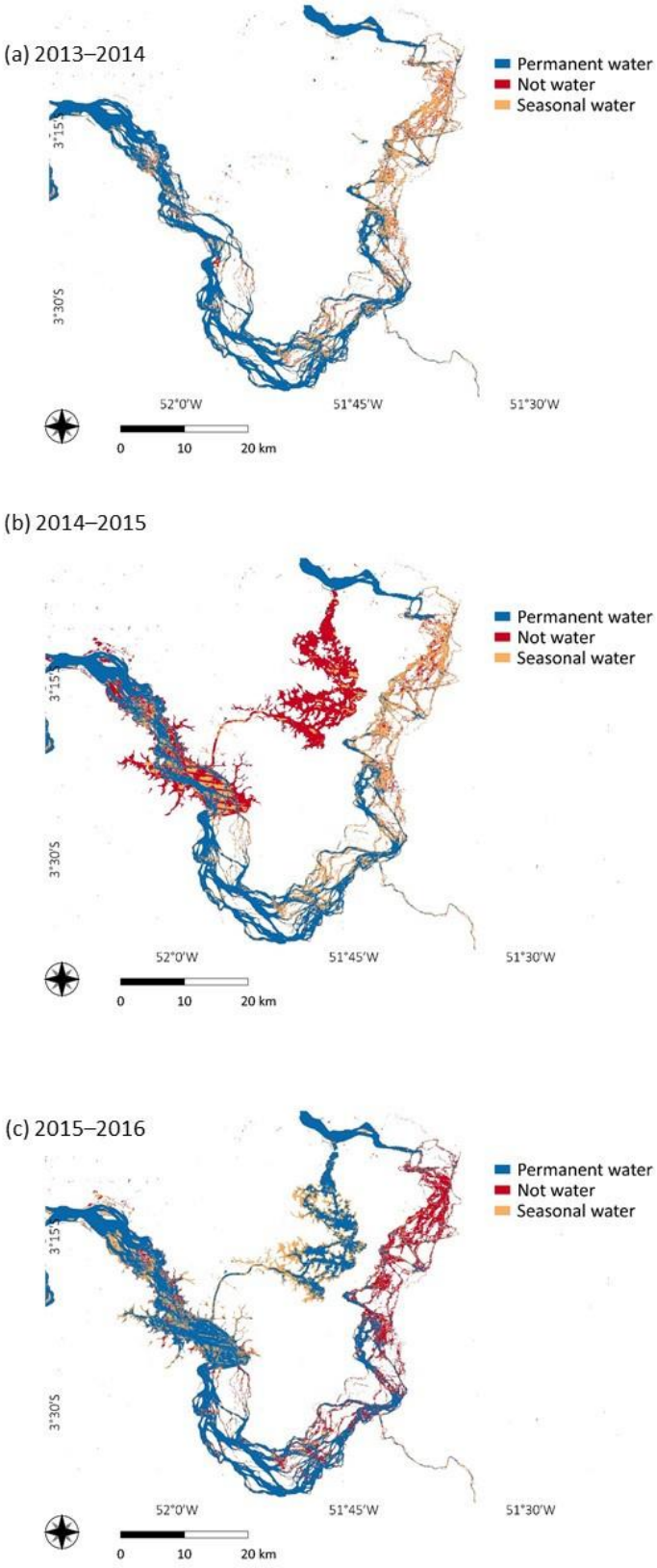

Fonte: Autoria própria

For the years prior to the damming of the river, the pattern of alterations is induced by natural phenomena, such as the ones caused by the El Niño South Oscillation (ENSO), that can influence the natural hydrological cycles through the rainfall regime (Marengo *et al.*, 2018). From Figura 21, it is very clear to see that the natural pattern of flooding was substantially altered from 2015 onwards.

4.4. Discussion

Due to the importance of a comprehensive comparison of different algorithms for LULC classification, aiming to improve knowledge on issues such as accuracy assessment and the selection of suitable algorithms for a historical remote sensing analysis for the VGX, the discussion section intends to sum with other previous initiatives that sought to measure and evaluate manmade transformations in study areas using remote sensing (Li *et al.*, 2011; Li *et al.*, 2012; Lu *et al.*, 2013; Feng, *et al.*, 2017; Jiang *et al.*, 2018; Li *et al.*, 2018; Kalacska *et al.*, 2019; Kalacska *et al.*, 2020a; Kalacska *et al.*, 2020b; Monteiro Neto *et al.*, 2021).

4.4.1. Accuracy Assessment of Classification Methods

Regarding general statistics (Tabela 5), Overall Accuracy and Kappa Coefficients were very similar among all classifications, both higher than 80%, which was expected for results which are highly correlated. The parameters also corroborate with other results already described in the literature for the area (Feng, *et al.*, 2017; Jiang *et al.*, 2018; Li *et al.*, 2018; Kalacska *et al.*, 2020a). A previous study (Feng, *et al.*, 2017) achieved overall accuracies (90–92%) and kappa coefficients (0.85–0.90) using ancillary data and more than one orbital sensor product. Another study (Li *et al.*, 2018) obtained an overall accuracy of 84.3% and a kappa coefficient of 0.79 in their classification for the VGX area using six Landsat images between 1991 and 2017. Jiang *et al.* (2018) applied the ML classification on multi-temporal Landsat imagery of the VGX, achieving overall classification accuracies of 89.7% (2011) and 92.3% (2017).

Commission (Comm) and Omission (Om) errors and Producer's (PA) and User's Accuracies (UA) were determinative to better understand what the map represents and what is actually on the ground, so that potential confusion between classes can be understood. It is expected that commission and omission errors have the lowest possible values (since they represent percentage errors of inclusion and exclusion

of classified pixels in the correct class or different classes), and PA and UA to be as close as possible to 100% (since they are used to determine the probability of a predicted pixel to be in the correct or different class) (Story, 1986).

Three major possibilities might be associated with the misclassifications revealed by the Om and Comm errors: 1) the overlapping of spectral signatures, since the algorithm understands a class as a different one; 2) the resolution of the image, since a unique pixel might contain more than one class; and 3) the heterogeneity of the class.

The Om errors associated with agro-pasture can be related primarily with its spectral signature, mainly for the year 2017 where agro-pasture and forest reflectances are overlapped in all bands of the image (Figura 16). Additionally, agro-pasture areas are more heterogeneous than forest, and, depending on the time of the year, pasture can have similar radiation measures as dense vegetation, which might cause confusion during the classification process. Furthermore, this category is spatially well defined and detached in the landscape, being easily visually identified. For 2017, MH and MD had similar performances, with regular omission errors, while the other classifications were satisfactory. Where there are omission errors for agro-pasture, there are also more than 5% of commission errors for forest, an indication that forest pixels might be wrongly classified as agro-pasture.

River spectral signature (NIR band) and error bars (RGB bands) are overlapped with rock spectral signature for 2000 (Figura 16), where there are also Comm errors for MH and MD (Tabela 5), indicating that river pixels were probably classified as rocks, since for the same algorithms, Om errors for the rock class are unsatisfactory. Different river depths and spatial mixing with the rocky environment are detected in the variation of classified areas between the algorithms, higher than 50% (Figura 18). Pixel resolution issues and the heterogeneity of the different rock surfaces were detected in 2017 in all classifiers. Only ML and SVM for the year 2000 do not have significant Comm and Om errors for this class. For 2017, these same algorithms have regular Comm errors, probably because rock pixels are being classified as river due to the image resolution (both land uses are being imaged in a single pixel) and heterogeneity. Indeed, the confusion between the classifiers is evident in , since there is a demonstrated variation of 70% for classified rock areas between the algorithms for both years: some classifiers underestimated the classification for the

exposed rock area, and others, overestimated (as can be seen in Mapa 4 and Mapa 5).

Poor performances of MH (2000) and MD (2000 and 2017) for rocks are corroborated through PA statistics, which represents the probability of a pixel being correctly classified—for low PA numbers, high omission errors are expected– which is indeed verified for the case (Tabela 5). On the same hand, low UA implicates higher Comm errors—which is the situation for RF in both years for the rock class.

All the six classification algorithms, from the simplest to the most complex, had similar overall performances in detecting critical trends of LULCC in the study area. Notably, MH, MD and RF were the algorithms with major issues to properly classify the rock land cover, which ended up affecting the river area quantification, since there was confusion between the two classes.

Regarding the parametric classifiers, for both years, ML was more capable of highlighting errors in individual classes. As to the non-parametric classifiers, SVM was slightly superior when compared to NN, for both years, which demonstrate that these two algorithms are the most suitable options within the scope of this study

The difference between the performances of parametric classifiers can be explained because, while MH and MD work by classifying a pixel based on the reflectance values of the closer pixels, ML assigns each pixel to a class using as criterion the probability that a pixel belongs to its class based on reflectance values, demonstrating it to be more accurate in a heterogeneous environment. Indeed, ML is the most common parametric classifier and is available in any commercial image processing software (Li *et al.*, 2012).

Regarding non-parametric algorithms, RF uses an average of several aleatory decision trees based on training samples and NN recognizes training patterns and classifies data using a neural net. While both are based on random clustering techniques, which might have biased the classification and overestimated the rock class (as seen in Mapa 4, Mapa 5 and Mapa 8), SVM creates a hyperplane that separates data in to different categories through vectors. RF and NN might not be good choices when there are not many training classes (as is the case of the rock class as seen in Tabela 3), while SVM is a good option for targets with any level of spectral separability. Moreover, NN and RF can perform slowly even when training a reduced number of samples, while SVM demands less computing power. Li *et al.*

(2011) found that non-parametric algorithms had some advantage in relation to traditional classification methods and the result of Lu *et al.* (2013) agreed, identifying the way in which the complex biophysical environment of tropical forests induced misinterpretations, both of which corroborate our findings.

Concerning the specific characteristics of the study area that influence the classification, an important aspect must be emphasized regarding the date of the images used and the water pulse that rules the Amazonian rivers. The Xingu River is controlled by seasonal floodings, and, while individual images might offer a general trend of LULCC, important changes related to aquatic environments and wetlands, such as river and rocks, might not be properly detected. The image from the year 2000 is from May, and the one from 2017 is from July, and, although the majority of alterations are indeed caused by the river damming from 2015 onwards, the fact that the river is in different moments of the natural flood pulse in both images might influence the final classification results. This important and seasonal short term environmental characteristic does not affect forests, pasture and crops, which were indeed the best classified classes.

This important issue was also identified for the study area by other authors. Li *et al.* (2018) reported that fluctuations in water reservoirs and rivers in different seasons might cause misclassification of water and other land cover types, such as lowlands and floodplains. The alterations over the Xingu River basin are core to the research lead by Kalacska *et al.*In three different studies, they realized that, from 1989 to 2018, the surface water was not the focus in most classification studies for the Xingu River basin, which makes the surface water classifications rapidly out of date in an area where large LULCC are ongoing due to large engineering projects (Pontius; Millones, 2011; Kalacska *et al.*, 2020a; Kalacska *et al.*, 2020b). These authors point to a problem also detected in our study, which is the difficulty in properly classifying the Xingu River and the floodable habitats in the VGX area.

Another important aspect that might influence the classification in a complex landscape such as tropical forests is the reference data. In a first attempt to classify the two Landsat images using only parametric algorithms, the training stage was based on the user's expertise of the area and on previously collected ground information data based on a 2008 raster image elaborated for the BMHC Environmental Impact Study, resulting in a poor performance of the classification algorithms (Affonso *et al.*, 2022). Existing data are rarely acceptable for accuracy

assessment, since the data might not represent the classes being mapped. This is because the existing field inventory was collected for a goal other than accuracy assessment or because the classification schemes employed to create the existing map differ from the one being used to create the new map, which was precisely the case in this previous attempt (Congalton; Green, 2019).

4.4.2. Land Use and Land Cover Changes

Based on the BMHC Environmental Impact Statement, the construction of Belo Monte reservoir was expected to deviate 42% of the Xingu River and remove 24% of the forests of the region (Eletrobrás, 2009b). This study confirmed both transformations in land cover: river to non-river downstream of the Xingu River (Mapa 7; Figura 20; Figura 21 and Mapa 8) and from forest to non-forest near the reservoir (Mapa 6 and Figura 19). An increase in the river area was observed upstream of the Xingu River and in a channel northward of the VGX, as seen in the non-river to river class (Mapa 7 and Mapa 8), due to the creation of the reservoir. This caused a conversion from a lotic (flowing water) to a lentic (still water) environment, affecting both water quality and biodiversity (Moran *et al.*, 2018).

One of the main impacts was the conversion from river to non-river areas (Mapa 7) in the south of the VGX, observed in the results from all the classification methods (Figura 20 and Tabela 6) corroborated by the JRC GSW ancillary data (Figura 21 and Mapa 14). For the study area, the river course deviation altered the rocks' exposure, as observed from Mapa 7, Mapa 8 and Tabela 6.

We can see from Mapa 8 that an extensive area (east, where the rocks are predominant) changed from permanent water to seasonal water (in orange) and non-water (in red), confirming the rock exposure trend found by the classification algorithms.

From Figura 21 it is possible to confirm that this transformation dramatically deflected from the pattern observed from previous years in the period 2014–2015, a period marked by the initial deviation of the watercourse, and in the period 2015–2016, when the deviation was concluded. A very worrisome pattern is also observed in Figura 21b, where a significant extension of seasonal waters (the ones controlled by the flood pulse of the river) also turned into non-water in 2015–2016, the first year after the conclusion of the dam construction, something which would permanently change the natural flood pulse. Finally, in Figura 21c we can see how

the influence of the new reservoir is clearly reproduced, when an extensive area of no water changed into seasonal/permanent water in 2015–2016. This transformation is also highlighted in Mapa 8, which consists of three year-by-year maps where we can see the reservoir being created.

The rock's exposure can pose a threat to the biodiversity that is adapted to and associated with the rocks, such as the rock vegetation, which is dependent on flood pulses, i.e., periodic river flow pulsing that supports ecosystem productivity (Junk *et al.*, 2013). There is a consensus that the mortality of fishes observed in 2015–2016 is directly related to the interruption of the migratory flow and the way that areas for feeding and spawning were no longer flooded due to the reduced flow of water that year (Zuanon *et al.*, 2019; Fearnside, 2021). The absence of flooded areas also affected the nutritional quality of the surviving fish. The years 2015 and 2016 light a red alert about the new hydrological flow that the Xingu River is about to be subject to after the damming.

The deforestation (forest to non-forest class) (Mapa 6 and Figura 19) process is a consequence of associated activities related to great enterprises, such as roads, accommodation/workers houses, construction sites, plant structures, and equipment assembly. The increase in infrastructure works attracted by the Belo Monte power plant is also responsible for improving transport access to remote areas, which may have contributed to the conversion of forest to agro-pasture (Figura 19) (Fearnside, 2019). Indeed, it is well known that deforestation patterns are associated with road access, especially in areas of agrarian projects (Soler; Verburg, 2010). The region also had economic incentives for activities related to cattle ranching, resulting in a growth of 116% from 2000 to 2017 (Calvi *et al.*, 2020b; IBGE, 2004).

The literature’s recommendation states that the creation of mitigation measures, such as the intensification of environmental monitoring and the creation of protected areas, with the aim to avoid or reduce deforestation, are the most effective strategies to attenuate the harmful impacts of such great enterprises (Barreto *et al.*, 2011; Monteiro Neto *et al.*, 2021).

As there are large and small hydroelectric power plants planned to be constructed in the Amazon, it is important to understand the land use and land cover changes associated with these activities, as well as to describe reliable methods to analyze these transitions. The present study validates the use of parametric and non-parametric classification methodologies, from the simplest and widely used to the

most complex and restricted available in popular software packages. All of these fulfill their purposes, mainly when associated with good ground reference information, well-selected training samples and prior knowledge of the area. When available in popular software, they are not complex to implement and are accessible to a wide range of users, even those who are not experts in image processing and geoprocessing techniques.

4.5. Conclusions

This research corroborates and increases the knowledge of remote sensing techniques for the VGX already gathered by other studies, reaffirming the idea that the construction of the BMHC is the current most important source of negative impacts in the VGX area. Thus, a follow-up is a relevant part of the environmental licensing of the mega project. The present study is focused on the VGX and BMHC, but it is possible to extend our findings and methodologies to the surroundings of other enterprises, given the similarity and homogeneity of the Amazon region in the context of land use and occupation.

This study points out that a combination among different classification techniques is fundamental. When possible, and if available, using non-parametric algorithms is an achievable and reliable way to detect different changes in a complex landscape such as tropical forests. In this context, fieldwork, good high-resolution dataset, and ancillary data are requirements to increase the quality of the analyses.

All the parametric and non-parametric pixel-based algorithms showed many similarities among the indexes of accuracy analyzed by the present study. All of them had general good performances in identifying classes and detecting changes, being able to provide an overall trend of the transformations from 2000 to 2017. The analysis of producer and user accuracies and omission and commission errors were more consistent in the detection of errors in misclassified classes (such as rocks), mainly when associated with ancillary data (such as the JRC GSW dataset). However, SVM and ML were the best classifiers among all options, mainly for the most heterogeneous classes (river, and mainly, rocks).

The analysis in the VGX had two major challenges specific to this study area: (1) the complex landscape and the medium resolution from Landsat imagery resulted in spectral overlapping of targets and classes and misclassification, as well

as spectral mixture, and (2) the presence of clouds most of the year, preventing multitemporal images from being selected for the analysis.

In all cases, the main conversions concerning land use and land cover were from forest to agro-pasture, from forest/agro-pasture to river upstream of the Xingu River, and from river to non-river in the south of the VGX, resulting in rock exposure. These impacts were associated mainly with the construction of the reservoir, the river deviation to install the main dam of the BMHC and the expansion of agro-pasture, as demonstrated by the JRC GSW ancillary data.

Our study was able to detect a significant exposure in the rocks that once remained submerged for most of the year (and now, are permanently exposed), a transformation that has not yet been properly addressed in the literature. In addition, according to previous research, this study observed that deforestation continues to cause the most significant transformation in the VGX area.

For the future, it is mandatory that the monitoring of landscape changes continues to be undertaken in the VGX, as they will only increase from now on. It is important to keep previous data to compare with the new knowledge being produced. Time series analysis comparing the pre-dam situation with the current situation and comparing different stages of implementation of the hydroelectric complex must be continuously assessed according to the improvement of digital image processing technologies and new investigation technologies. There should be a focus on extracting as much detail as possible from the transformations underway, over the longest possible time period. Other orbital sensors, optical and radar, RPAs and even more high-resolution datasets need to be increasingly incorporated into this monitoring effort.

The authors also encourage future studies to better investigate the rocky environment of the VGX, which notably is the most complex in the area, and at the same time, most susceptible to changes.

Author Contributions: Conceptualization, A.A.A., S.S.M. and T.P.P.; methodology, A.A.A. and T.P.P.; validation, A.A.A. and T.P.P.; formal analysis, A.A.A., S.S.M. and T.P.P.; investigation, A.A.A., S.S.M. and T.P.P.; writing – original draft preparation, A.A.A.; writing – review & editing, A.A.A., S.S.M., T.P.P., J.A.Q., C.H.G. and L.A.C.; supervision, J.A.Q., C.H.G. and L.A.C.; funding acquisition, A.A.A.

Funding: This study was supported by the Coordination for the Improvement of Higher Education Personnel (CAPES)—Financing Code 001 (A.A.A., S.S.M. and T.P.P.). APC was funded by PROEx (Academic Excellence Program) fund #0725/2020 / 23038.001810/2020-11. S.S.M. is a research fellow of São Paulo Research Foundation (FAPESP, grant #2020/07372-4,). J.A.Q. is a research fellow of Brazil's National Council of Scientific and Technological Development (CNPq, grant #305188/2020-8). L.A.C. is a research fellow of São Paulo Research Foundation (FAPESP, grant #19/22028-0). C.H.G. is a research fellow of Brazil's National Council of Scientific and Technological Development (CNPq, grants #311209/2021-1).

Data Availability Statement: All data generated or analyzed during this study are included in this published article. Landsat 7 and 8 images are courtesy of the U.S. Geological Survey and can be downloaded at [40].

Acknowledgments: The authors thank the University of São Paulo Institute of Energy and Environment and the Graduate Program in Environmental Science. The authors acknowledge Mr. Kyle Flavin, for the revision of the text. Acknowledgements are extended to the editor-in-chief, the associate editor, and the anonymous reviewers for their criticism and suggestions, which helped to improve this paper. This study was financed in part by Coordination for the Improvement of Higher Education Personnel (CAPES), São Paulo Research Foundation (FAPESP), and National Council for Scientific and Technological Development (CNPq).

Conflicts of Interest: The authors have no conflicts of interest to declare that are relevant to the content of this article.

5. 3D MODELING AS A CONSERVATION TOOL TO CHARACTERIZE ENDANGERED SEASONALLY FLOODED ECOSYSTEMS IN THE VOLTA GRANDE DO XINGU, AMAZON FOREST, PARÁ, BRAZIL

Alynne Almeida Affonso, Marília Prado Freire, André Oliveira Sawakuchi, Carlos Henrique Grohmann

Este capítulo é baseado em artigo submetido ao periódico *Journal for Nature Conservation* (ISSN 1618-1093).

Abstract

The Volta Grande do Xingu (VGX) region in the southeastern Amazon forest of Brazil, characterized by its exceptional geomorphology and biodiversity, faces significant ecological challenges due to the construction of the Belo Monte Hydroelectric Complex (BMHC). This study aims to characterize the seasonally flooded areas within the VGX that are at risk due to the BMHC's operation by employing 3D modeling techniques. Remotely Piloted Aircraft (RPA) were used to collect imagery, which was then processed using Structure-from-Motion Multi-View Stereo (SfM-MVS) techniques, resulting in the creation of high-resolution 3D models, orthophotos, and digital surface models. These datasets offer unprecedented insights into the unique habitats of the VGX. The models representing the main flooded habitats of the VGX are openly accessible on the Sketchfab online platform, ensuring broad availability to researchers and policymakers. This research underscores the importance of preserving natural heritage in the face of growing environmental challenges, emphasizing the need for comprehensive protection mechanisms for irreplaceable assets like the VGX.

Keywords: Spatial Modeling; Seasonally Flooded Habitats; Sarobal; Pedral; Environmental Awareness; Landscape

5.1. Introduction

The landscapes of a country are an important part of its heritage (Herrero-Tejedor *et al.*, 2020) and can be seen as a connection between what is inherited from the past and what we will leave for the future (Remondino *et al.*, 2009). According to UNESCO (2009), "Natural heritage refers to natural features, geological and physiographical formations, and delineated areas that constitute the habitat of threatened species of animals and plants and natural sites of value from the point of view of science, conservation or natural beauty". With this definition in mind, the Volta Grande do Xingu (VGX, or, the Great Bend of the Xingu) area, located in the southeastern Amazon forest (Pará State, Brazil), can be considered a natural heritage. The VGX is a stretch of 130 km in the middle Xingu River, which is the fourth largest tributary of the Amazon River (Salomão *et al.*, 2007). Due to its unique characteristics such as curves, waterfalls, and rapids, it is a site of great scenic beauty and high ecological relevance (Sabaj-Perez, 2015) and was the chosen place for the construction of the Belo Monte Hydroelectric Complex (BMHC) due to its distinctive geomorphological characteristics.

On the Recommendation Concerning the Protection of the World Cultural and Natural Heritage, UNESCO (1972) attests that "natural heritage areas are increasingly threatened with destruction, not only by traditional causes of degradation but also by the evolution of social and economic life". Heritage sites all over the planet, whether they are natural, cultural, or mixed, are vulnerable to the effects of human interference (Remondino; Rizzi, 2010), which is the case of the VGX, where the construction of the BMHC led to drastic modifications of its geomorphology, hydrology and ecosystems (Pezzuti *et al.*, 2018; Zuanon *et al.*, 2019).

To degrade or even definitely lose a natural asset, which is irreplaceable, is harmful not only to the nation where the heritage is located but to the whole planet. UNESCO’s recommendation is clear in emphasizing that natural assets are important for all peoples of the world, and it is essential to establish effective protection mechanisms for natural heritage. However, protecting these heritage areas is a complicated task, and often protection efforts are insufficient due to the complexity of the safeguarding process, which requires economic, scientific, and

technical resources of the country in the territory where the asset to be protected is located.

The VGX meets the UNESCO requirements for natural heritage, as it has physical and biological formations of exceptional value from an aesthetic and scientific point of view and geological and physiographic formations that are habitats of threatened animal and plant species, being recognized by its high geodiversity (de Paula Silva; Rodrigues; Pereira, 2014). However, it has not been officially endorsed as a Natural Heritage by UNESCO, nor as a "Brazilian Cultural Landscape". The Brazilian Cultural Landscape is an instrument created by the Brazilian Institute of Historical and Artistic Heritage (IPHAN) that aims to promote broad and territorial preservation of unique portions of Brazilian territory that are representative of the interactive process of humans with the natural environment (IPHAN, 2009), a requirement that the VGX area also meets, due to the strong link of the indigenous and river dwelling traditional peoples living there with the Xingu River and the Amazon Forest (Magalhães; Cunha, 2017). However, UNESCO itself is clear in stating that the fact that a natural heritage asset has not been officially endorsed by a preservation agency cannot in any way mean that such an asset does not have exceptional value. Also IPHAN (2009 p. 13) attests "it is the duty of Brazilians to protect the wealth and diversity of the unique cultural and natural beauties of Brazil", and these efforts should indeed be directed towards the VGX.

The main goals of this research are endorsed by the conservation needs of such a sensitive area and focussed on the intense transformation of the landscape, mainly seasonally flooded areas, resulting from the BMHC's impact at the VGX that are still being improperly addressed in literature. Our specific aims are based on a literature gap highlighted by Affonso *et al.* (2023a), who identified significant exposure in the VGX seasonally flooded habitats, including rocky riverbed environments, its surroundings and its associated seasonally flooded vegetation. These environments used to be gradually submerged during the raining season before the damming of the river, being exposed only in the dry season, and are now permanently exposed or flooded respectively, both downstream and upstream of the dam. With this specific context in mind, this research also looks forward to contributing with more consistent information on these seasonally flooded environments of the VGX, since descriptive and spatial modeling for these areas, as well as for the amazonian environments in general, are still scarce in literature.

For this purpose, a series of aerial imagery of sensitive microenvironments formed by rocky and sedimentary substrates in the Xingu River channel and their associated vegetation were taken through a Remotely Piloted Aircraft (RPA), popularly known as “drone” in order to create orthophotos and 3D models. This study aims to develop an unprecedented 3D very high resolution visual database of important riverine microenvironments of the VGX area. These ideally will be freely available, to be cataloged, documented and used by the scientific community, the government and the policy and decision makers as a means of digital preservation, conservation, environmental education, and safeguarding of the VGX natural heritage that has been little explored in scientific literature. This study also hopes to encourage the recognition of the VGX as a natural heritage site by the responsible agencies.

5.1.1. Environmental Awareness of Landscapes and Visualization

Close contact with the environment can positively affect the public perception of ecosystems, leading to increased environmental awareness and favorable emotions towards conservation, inducing a will to care from public authorities, academics, the government and the society (Kamarainen *et al.*, 2013; Lu; Liu, 2014). However, the physical proximity with nature in the real world might be challenging for some natural heritage areas and landscapes – which is the case of the VGX area. The high costs involved with the logistics of displacement, the difficulty of planning a field trip and access restrictions result in a lack of opportunity for *in situ* observation for the public in general, which can hinder the development of environmental awareness Lu and Liu (2014), especially in an isolated environment such as the study area. Indeed, research by Kolb (1984) and Zeppel (2008) has shown that experiential learning about nature can still evoke positive emotions even in individuals who are not physically located near the environment.

In this context, visual resources can play a crucial role in safeguarding natural heritage areas and landscapes. Visual components are deeply entrenched in our culture and daily lives (Urry, 2002; Bauman, 2007) and our society is completely immersed in an era of vision and induced visuality based on a widespread use of smartphones, digital photography and online photo-hosting platforms (de San Eugenio Vela; Nogué; Govers, 2017). Visual landscapes evoke a feeling called by

some authors as “sense of place” (Tuan, 2011; Campelo, 2014; de San Eugenio Vela; Nogué; Govers, 2017), “sense of belonging” (Pietroni, 2017) or “sense of landscape” (Backhaus, 2009), connecting cultural aspects with human geography, attributing meaning to the environment and activating affective responses (Bishop, 2015).

Graphical representations, including charts, maps, photographs and 2D images, have been used to raise awareness about places, bringing the environment closer to the public (Campelo; Aitken; Gnoth, 2010). However, innovative approaches are needed to create a greater visual impact for conservation goals. The use of 3D models, widely employed in cultural, historical and architectural heritage research and documentation, can be adapted and still be further explored to offer the potential to digitally represent landscapes and create immersive experiences, particularly for inaccessible areas (Champion; Rahaman, 2019).

3D models provide geometric accuracy and visual realism, closely resembling reality (Remondino *et al.*, 2009; Remondino, 2011). They allow users to freely explore and interact with the virtual environment, moving through the scene, filling the gap between reality and perception anywhere in the world where a computer is available (Horne; Thompson, 2008; An & Powe, 2015; de San Eugenio Vela; Nogué; Govers, 2017; Basantes *et al.*, 2017). By reducing the complexity of landscape representation while maintaining a connection to the real world, 3D models enhance user understanding of ecosystems and create the so called sense of place, meeting the expectations of the *in situ* landscape experience through its visual impact (Horne; Thompson, 2008; An & Powe, 2015; Bishop, 2015; de San Eugenio Vela; Nogué; Govers, 2017). Indeed, research indicates that people trust realistic displays more than less-realistic alternatives such as maps or 2D representations, and are more able to relate to physical visualizations than drawings, providing an opportunity for 3D models to replace traditional spatial data representations (Lai; Kwong; Mak, 2010; Wabiński; Mościcka, 2019).

The availability and use of detailed accurate 3D data offers various applications, allowing for new analyses, interpretations and conservation policies (Remondino, 2011), being a valuable tool for linking and translating scientific and technical knowledge to policies and the decision making process (An & Powe, 2015). Furthermore, as already seen in the cultural heritage field and archeology, one of its great advantages is the potential of permanently recording the form of sites so

they can be passed down to future generations (Remondino *et al.*, 2009; Remondino, 2011). Additionally, 3D visualization can be generated from low-cost digital survey techniques, making them strategic in resource-limited sectors (Chiabrando; Donadio; Rinaudo, 2015).

Recently, geotechnologies have been combined with 3D models to create geographically accurate digital reconstructions for visualization and analysis purposes. These technologies, including remote sensing products and Geographical Information Systems (GIS) offer more opportunities for data representation, interaction, and dissemination (Yin, 2010). By incorporating spatial attribute data into landscape models, and therefore, shape, size and volume of features, robust analysis and queries can be performed, providing advantages over traditional 2D maps in terms of land use investigation and visualization (Yin, 2010).

However, satellite imagery has limitations for 3D modeling of landscapes, such as cloud cover, geometric and radiometric distortions, and scale restrictions. Free imagery as offered through Landsat and Sentinel missions might be too general for the scale of ecological processes and geomorphological features, and very high resolution imagery might have a high cost per scene (Wulder *et al.*, 2004; Anderson; Gaston, 2013). RPAs have emerged as a valuable tool to overcome these limitations, capturing high-resolution images and detailed physical characteristics of biotic and abiotic elements in small areas (Horne; Thompson, 2008; Herrero-Tejedor *et al.*, 2020) using stabilized digital cameras. They are capable of performing vertical take-off and landings and able to fly in low-altitude autonomously following predefined routes using integrated GNSS. Due to its reduced size and weight, RPAs offer low-cost, portable, and easily deployable platforms for data collection in remote or inaccessible regions (Anderson; Gaston, 2013; Chiabrando; Donadio; Rinaudo, 2015).

5.1.2. Landscape 3D Modeling and Data Sharing

As reality-based 3D landscape models are an important way to promote natural heritage sites and their conservation (Wabiński; Mościcka, 2019), they must include elements of landform, vegetation, water and atmosphere to achieve “honest and accurate visualizations with high standards of defensibility”, including the correct cartographic message (Ervin; Hasbrouck, 2011; Shaw *et al.*, 2009, p. 6; Lai; Kwong; Mak, 2010; Wabiński; Mościcka, 2019). For that, detailed information on

the physical environment, for example, soil study, hydrology, flora and fauna information and spatial organization of these entities is vital for creating effective landscape models (Herrero-Tejedor *et al.*, 2020).

The generation of 3D models involves using specific software and methodologies that utilize image data from passive sensors, such as satellites and digital cameras. They capture RGB information and convert it into spatial 2D image data. Good results depend on the characteristics of the sensor, the scanned material, the scene being imaged, the working environment, the backscattered light and the chromatic content of the targets. Mathematical formulations are applied to transform unstructured 2D data into structured 3D data, which includes geospatial, geometric and appearance modeling. Geometric modeling is responsible for data registration and processing (such as editing, cleaning, and meshing), while appearance modeling deals with texturing, blending, rendering, and simplification. Precise color mapping is achieved through texture and the RGB information collected from the sensor (Remondino; Rizzi, 2010; Remondino, 2011).

While 3D models facilitate the observation of systems that are either too small or too large to be seen on a normal scale (Lai; Kwong; Mak, 2010), generating digital 3D models of large sites can be a challenge. While the scale must be sufficiently precise to illustrate the arrangement of vegetation elements, topography and water flows, an accurate comprehension of the basic features of the spatial, functional, and visual layout of the landscape may be hindered by an excess of information (Herrero-Tejedor *et al.*, 2020). The main difficulties are associated with acquiring, processing and visualizing heavy datasets of complex large sites. The dimensions and level of detail along with interactive visualization are critical issues (Remondino *et al.*, 2009). Choosing an appropriate methodology, data processing procedures and an efficient workflow is crucial to ensure the accuracy and interaction capabilities of the 3D model while addressing technical specifications (Remondino; Rizzi, 2010; Remondino, 2011). Although integrating different 3D modeling methodologies like Terrestrial Laser Scanner (TLS) or Light Detection and Ranging (lidar) is desirable for modeling large territories, it may not always be feasible due to budget constraints and operational difficulties related to instrument portability, usability, and data processing complexities (Remondino; Rizzi, 2010; Remondino, 2011).

Systematic documentation and visualization of the model's features are key factors for assessment and management (Herrero-Tejedor *et al.*, 2020) and one of its main goals. Even with the advance of technology, there are still crucial issues regarding how to document, present and store the vast amount of data that forms these complex 3D models. There is a growing interest in making information accessible on the web, considering its potential for storage and accessibility (Bishop, 2015; Pietroni, 2017). For example, research on 3D Digital Heritage Models as Sustainable Scholarly Resources found that functional external links were lacking, highlighting the ongoing importance of addressing these issues, particularly in academic research (Champion; Rahaman, 2019).

5.2. Methodology

5.2.1. Study Area

The 1,900 km extension of the Xingu River can be divided in three compartments, crossing two states. It originates in Mato Grosso, in the Brazilian Midwest, and while traversing this state, it is known as the Upper Xingu, with headwater tributaries flowing over the sedimentary rocks of the Phanerozoic Parecis Basin, which converge to a mainstem running over a Precambrian basement composed of an assemblage of igneous and metamorphic rocks. The Middle Xingu comprises the portion of the river mostly flowing over Precambrian basement rocks, including the sector where it enters the state of Pará and through the municipality of Altamira. The VGX area is located at the end of the Middle Xingu and the beginning of the Lower Xingu, marked by the boundary between the Precambrian basement and the sedimentary rocks of the Phanerozoic Amazonas basin. The complex array of anabranching-like bedrock channels with rapids of the Middle Xingu shift to a single lake-like tidally-influenced channel of the Lower Xingu (Bertassoli *et al.*, 2017) until it meets the right margin of the Amazon River, already under sea tide influence (Mapa 9a). The VGX area has a complex geomorphology formed by an anabranching pattern with many zig-zag channels controlled by fracture zones and patches of boulders and mid-channel bars covered by vegetation adapted to seasonal flooding. These very heterogeneous freshwater and seasonally flooded environments associated with the riparian forest promote great biodiversity of flora and fauna, including endemic and threatened species, and are also an

important means of livelihood for indigenous and river dwelling traditional peoples of the region (Pezzuti *et al.*, 2018).

The VGX is marked by exceptional geomorphologic attributes, such as the 3 "bends", which are abruptly 90 degrees sequential deflections of the river flow from NE to SE, NE and NW, and a complex of large rapids and waterfalls formed by the steeper riverbed in the area (Mapa 9). These moderate slopes combined with a high water discharge have made it a desirable location for building a hydroelectric power plant, and as such, the Belo Monte Hydroelectric Complex (BMHC) was installed there (Costa *et al.*, 2012). The construction of the complex, which consists of two dams, Pimental e Belo Monte (Mapa 9b), began in 2010, and it has been in operation since April 2016, achieving its full performance capacity (i.e., with all turbines working) only in 2019.

The most heavily deforested areas in the whole Xingu River watershed are in the Lower Xingu, including the VGX area, around the Trans-Amazonian highway in the state of Pará. This deforestation is primarily caused by cattle ranching and agriculture (Barona *et al.*, 2010; Fearnside, 2001). The environmental impact only got worse after the construction of the BMHC reservoirs, which led to a drastic modification of the natural flood pulse of the Xingu River, as at least 42% (reaching 80% during specific months) of the flow was diverted (Pezzuti *et al.*, 2018). Two main severe impacts resulted from this: the permanent flood of approximately 500 km² of upland forest in the reservoir area (comprising Main and Intermediate reservoirs) while seasonally flooded environments are now continually or partially exposed downstream of the dam (Jiang *et al.*, 2018; Pezzuti *et al.*, 2018; Zuanon *et al.*, 2019; Affonso *et al.*, 2023a). The hydrological changes imposed by the BMHC affected the whole VGX environment from a biotic, abiotic and cultural aspect (de Paula Silva; Rodrigues; Pereira, 2014).

Mapa 9: Study area and RPA flight missions. (a) Location of the Volta Grande do Xingu (VGX), showing the Brazilian Legal Amazon and the compartments of the Xingu watershed. (b) The Belo Monte Hydroelectric Complex (BMHC) with its two dams, Pimental and Belo Monte, and the Reduced Flow Zone (RFZ) between them. The 37 flight missions locations realized for this study are represented here; the 9 selected flights chosen for this study are represented by the stars, and the remainder are represented by the red dots. Flight a: Nov 09, 2021, #4; Flight b: Nov 09, 2021, #6; Flight c: Nov 09, 2021, #7; Flight d: Nov 10, 2021, #3; Flight e: Nov 10, 2021, #5; Flight f: Nov 10, 2021, #7; Flight g: Nov 12, 2021, #7; Flight h: Nov 13, 2021, #1; Flight i: Nov 13, 2021, #5. (c) Only the selected flights in detail.

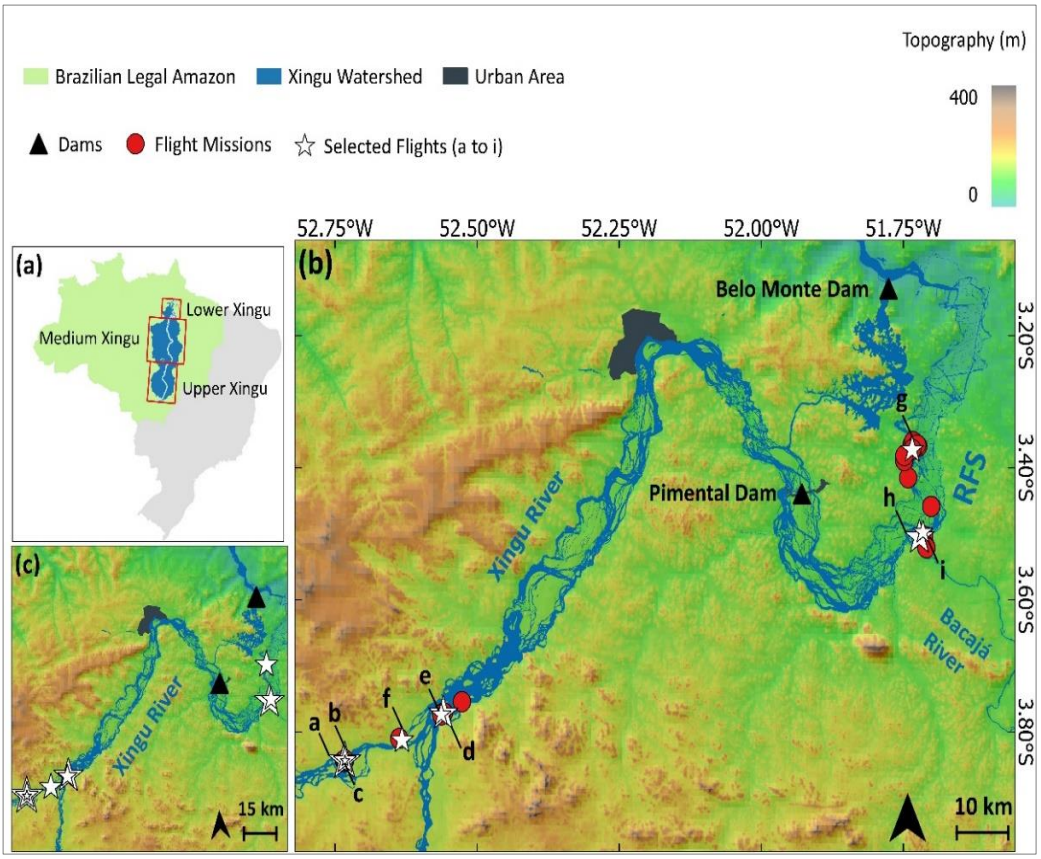

Fonte: Autoria própria

5.2.2. Image Acquisition

A field trip to the study area occurred from November 07-14/2021, where a DJI Phantom 4 Pro V2 RPA flew 37 missions over the seasonally flooded area (Mapa 9b) of the VGX capturing several environments such as water, sedimentary and rocky substrates and diverse vegetation adapted to seasonal flooding, from incipient to mature seasonally flooded forest.

On the 9th, 10th, and 11th of November, the flights took place in the final stretch of the Iriri River, one of the most important tributaries of the Xingu River. This area is located within bounded indigenous lands and is therefore well-preserved. On the other hand, on the 12th, 13th, and 14th, the flights were conducted over the area known as the "reduced flow zone" of the VGX, which is heavily influenced by the water flow regulation from the dam (Mapa 9).

The digital camera on the aircraft has a 1" CMOS 20 MP sensor measuring 13.2 x 8.8 mm able to produce high-resolution images with dimensions of 5472 x 3648 pixels. The MapPilotPro app (https://www.mapsmadeeasy.com/) was used to plan and execute the flight missions, which were flown at different heights, enabling the generation of images with varying pixel resolutions based on the desired precision and level of detail (Tabela 7). The overlaps between images were consistently larger than 60% along and across flight tracks. The camera angle was set to -85° (5° from nadir). Throughout the field work, the weather conditions ranged from sunny to partially sunny, with occasional cloud cover.

100% of the images were geolocated on the WGS84 Coordinate System using the inertial system and GPS navigation receiver coupled to the RPA platform (no Ground Control Points were used due to logistic issues related to access restraints and the rough characteristics of the study area).

For the sake of clarity and improved organization of the outcomes of this work, the products resulting from the flights were grouped based on their scales, considering flight mission altitudes, resolution (px/cm) and point cloud densities (points/m^3). Flight missions conducted at altitudes ranging from 300 to 100 meters, with resolutions between 10.0 to 2.0 px/cm and point cloud density below 200 points/m^3 were classified as "Medium Resolution" in the scope of this research (the reader must keep in mind that in comparison to freely available conventional remote sensing products, these products are still considered as high resolution). The second

category, “High Resolution”, encompasses flights conducted between 60 to 25 meters in altitude, with resolutions between 2.0 and 0.7 px/cm and point cloud densities ranging from 200 to 5,000 points/m³. Lastly, flights conducted below 20 meters in altitude, with resolutions below 0.7 px/cm, and dense point clouds (above 13,000 points/m³) were assigned as the “Very High-Resolution” category.

Five High Resolution and four Very High-Resolution (Mapa 9c) outcomes from all the 37 missions were chosen to be presented and discussed on this work, for being representative of all the products generated and from the whole study area in general. In the Supplementary Material (Apêndice A), Tabela A_1 shows the flight mission parameters for all the 37 missions and the selected flights, identified from (a) to (i).

5.2.3. Image Processing Techniques

The technique known as Structure-from-Motion Multi View Stereo (SfM-MVS) was used to obtain orthophotos and 3D models from the imagery collected using the RPA. This technique is a fully-automated photogrammetric approach that can produce high-quality, dense, three-dimensional point clouds of landforms through the multiple overlapping of 2D images obtained from a photographic camera from multiple viewpoints. The technique follows a structured workflow that can be divided in two modules: Structure-from-Motion (SfM), which consists of identifying matching features between the set of images, estimating camera parameters and triangulating the 3D positions of the corresponding attributes; and Multi View Stereo (MVS), which densifies the 3D reconstruction by estimating the 3D geometry of the scene for every pixel in the image set. Both results combined generate a detailed and dense 3D model of the scene, capturing its shape, structure and texture information (Westboy *et al.*, 2012; Chiabrando; Donadio; Rinaudo, 2015; Smith; Carrivick; Quincey, 2015).

For this research, the SfM-MVS workflow was processed in Agisoft Metashape Pro (version 1.8.3) (https://www.agisoft.com) (Figura 22a) using its default parameters. The first step was to import into the software the imagery set acquired through the RPA (Figura 22b). After that all the images were aligned and calibrated through the estimation of camera poses (Tabela A_2 from Supplementary Material (Apêndice A) gives the quality parameters for the calibration process), generating sparse point clouds by matching common features across the imagery (Figura 22c),

when the SfM stage of the workflow is completed. In the next stage, the MVS algorithm densifies the aligned point cloud estimating the 3D geometry for each pixel in the images in order to generate detailed 3D dense clouds (Figura 22d), that can be now used to create Digital Surface Models (DSM) (Guth *et al.*, 2021), orthorectified images (orthophotos) and 3D polygonal meshes. The point cloud parameters as the densified points and its average density for each product can be found in the Tabel A_3in the Supplementary Material (Apêndice A). The final step is the texturization of the mesh using the photographs acquired in the flights, a process known as texture mapping. For this study, the 3D models were built based on the internal GPS cameras, and the results are expressed in a local coordinate framework (derived from the relative orientation). The orthophotos were georeferenced using the SIRGAS 2000 Coordinate Reference System – UTM Zone 22 Southern hemisphere. The geolocation variance errors are in Tabela A_4 from the Supplementary Material (Apêndice A).

Figura 22: Workflow of the methodology process applied in this research, from the field trip to the image processing on Agisoft Metashape, generating the Final 3D Model, Orthophotos and DSM (b) Imagery acquisition at the field with the RPA (c) Camera poses, calibration and sparse point cloud (d) Matching features between 2 images and (e) Dense point cloud.

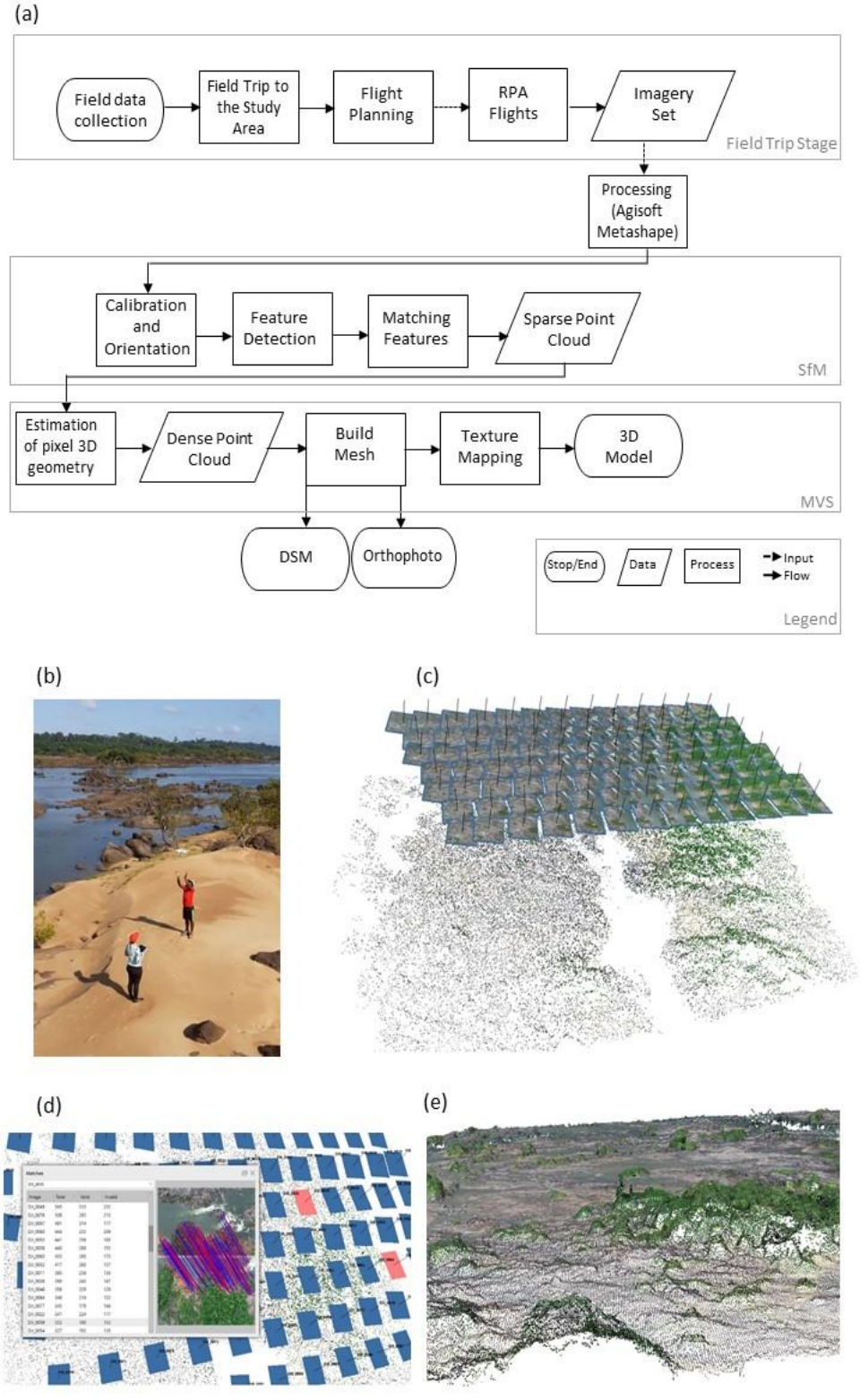

Fonte: Autoria própria

Since it is not the intention of this work to elaborate on the SfM-MVS technique, the readers can refer to Westboy *et al.* (2012), Smith, Carrivick and Quincey (2015), Carrivick, Smith and Quincey (2016) and Iglhaut *et* al. (2019) for more detailed information on the methodology, as well as good literature reviews on the subject, and to Chiabrando; Donadio; Rinaudo, 2015) for the detailed description of how the SfM-MVS algorithms run on Agisoft Metashape.

5.2.4. Sharing

As observed by Champion; Rahaman (2019), access to and maintenance of digital 3D models are important issues when considering the sharing and usability of data by the general public. The use of tools to improve accessibility and user-friendliness of platforms is a key factor for the visibility and usage of digital models. That is why some authors (Remondino; Rizzi, 2010; Champion; Rahaman, 2019; Herrero-Tejedor *et al.*, 2020) consider that sharing is also a significant part of spatial modeling, as important as data processing. Furthermore, one of the next big steps in the technological improvement of 3D modeling is its integration with web-based applications, aiming to reach wider audiences (Guarnieri; Pirotti; Vettore, 2010).

With this in mind, and aiming to reach a larger audience and enable them to interact with the final products, providing an alternative to traditional observation methodologies (such as photographic reports), this research used the Sketchfab platform (www.sketchfab.com) to share the final 3D models. This platform is a free and easy-to-use tool that allows visualization from top-down, ground-level, and 360° views on any device, enabling users to change the viewing angles of the models and observe them in high resolution. However, due to file size upload restrictions, the versions of our models on Sketchfab are simplified versions of the original models. The original models can be downloaded at https://doi.org/10.5281/zenodo.8251029.

5.3. Results

Two of the complete products resulted from the mission flights and image processing are presented on Mapa 10. They are the orthophoto (Mapa 10a and d), DSM (Mapa 10b and e) and static model (Mapa 10c and f) from flight 6 from November 09, 2021 (Mission ID b), depicting the rocky environment and its

associated vegetation, with ironstones and sand; and flight 7 from November 10, 2021 (Mission ID f), representing a sandy beach with the floodable forest behind it. In the Supplementary Material (Apêndice A) are the Figuras A_1 to A_7. In these, the reader will find the static views, orthophotos, and DSMs of the other selected products highlighted in this study. These products provide representative examples of different floodable environments found within the VGX. The collection of interactive models that allow users to virtually explore the scenes is hosted at https://skfb.ly/oILVp.

Mapa 10: (a) Very High Resolution Orthophoto; (b) Digital Surface Models; (c) Static view of the 3D model generated from the imagery captured during flight #6 (ID b) realized on Nov 09, 2021. (d) High resolution Orthophoto; (e) Digital Surface Model; (f) Static view f the 3D model generated from the imagery captured during flight #10 (ID f) realized on Nov 10, 2021.

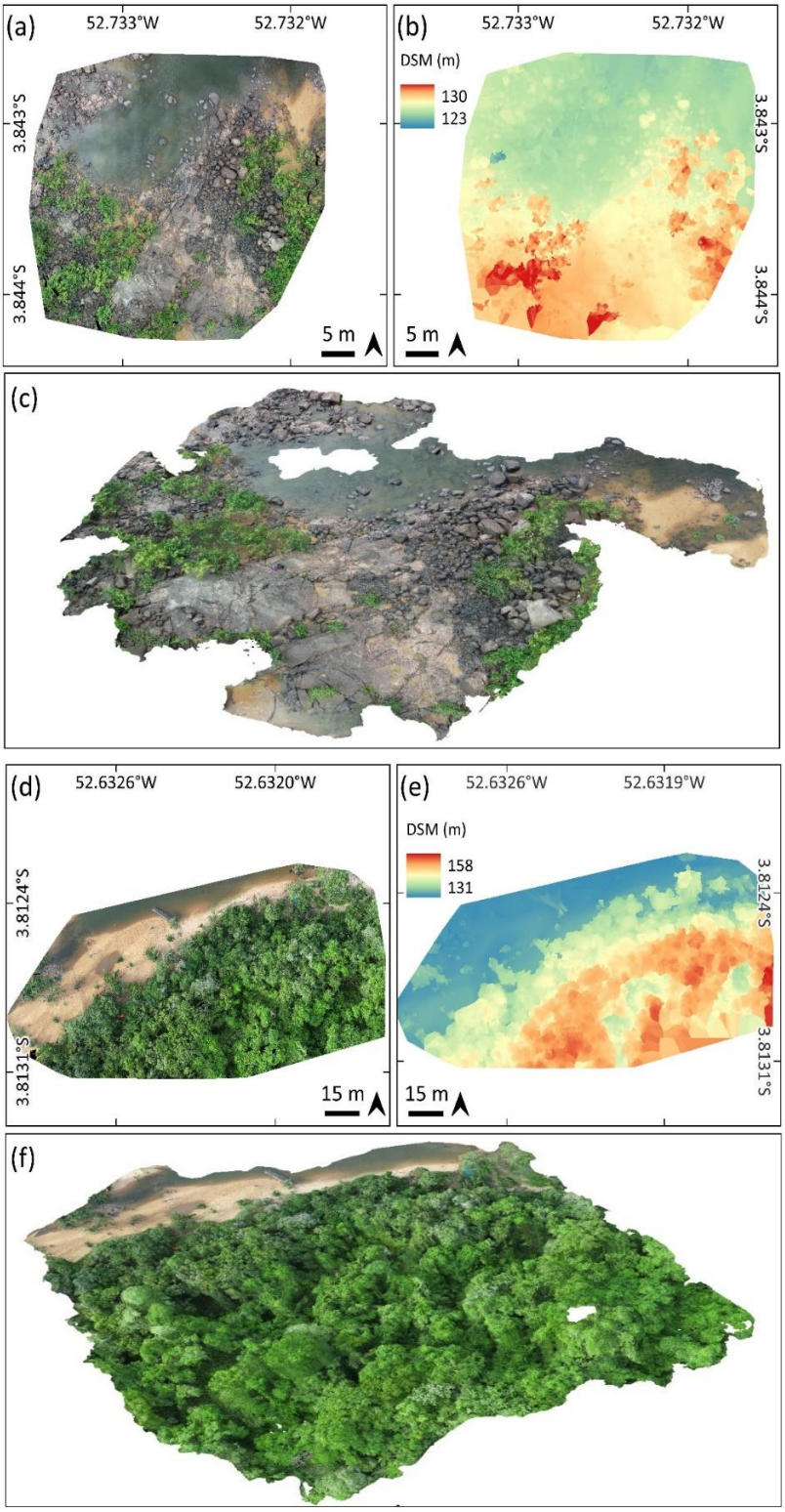

Fonte: Autoria própria

Tabela 7 has the links for each interactive 3D model generated for the selected missions in the Sketchfab platform and how it was categorized in the scope of this work.

Tabela 7: Selected mission identification, Sketchfab access links for each 3D model derived from the flights and the category they were assigned in the scope of this research.

Date	Mission# and ID	Sketchfab Link	Category
Nov 09,2021	04 (a)	https://skfb.ly/oHRpL	High Resolution
Nov 09,2021	06 (b)	https://skfb.ly/oHR6t	Very High Resolution
Nov 09,2021	07 (c)	https://skfb.ly/oHVGy	Very High Resolution
Nov 10,2021	03 (d)	https://skfb.ly/oILV8	Very High Resolution
Nov 10,2021	05 (e)	https://skfb.ly/oILVu	High Resolution
Nov 10,2021	07 (f)	https://skfb.ly/oILVu	High Resolution
Nov 12,2021	07 (g)	https://skfb.ly/oHX8v	Very High Resolution
Nov 13,2021	01 (h)	https://skfb.ly/oILVD	High Resolution
Nov 13,2021	05 (i)	https://skfb.ly/oHVrF	High Resolution

5.4. Discussion

5.4.1. Floodplain environments

The seasonally flooded environments of the Volta Grande do Xingu described here are not unprecedented and similar features were identified in other eastern amazonian rivers draining the Precambrian basement. The great rock outcrops along with their associated vegetation and the seasonally flooded environments are also found in other major Amazonian water courses, such as the Tapajós and Trombetas rivers. However, what makes the Xingu River different from other Amazonian rivers is (1) the fact that it is a clear water river (as classified by Sioli, 1950), with a relatively low concentration of suspended solid material and (2) its rapids, waterfalls and slopes (in the order of 1.2m/km) formed by its numerous and complex anastomosed channels and alluvial islands.

In literature, there are well-written descriptions and analyses of the floodable vegetation surrounding the Xingu watershed (IBAMA, 2007; Salomão *et al.*, 2007; Cunha, 2009). Nevertheless, it can be challenging to find appropriate descriptions,

definitions and visual resources of the seasonally submersible areas, particularly from a geomorphological and landscape perspective, mainly because primary characteristics for identifying and describing vegetation, fauna and ecological processes are closely tied to floodable specific environments. For example, pioneer alluvial vegetation and fluvial influenced vegetation for the study area, the most abundant and typical vegetation types for the VGX, can be either classified as rocky (or *pedrais)* vegetation or as a sandy substrate, which later becomes muddy with the stabilization of the sandy bars. Figura A_8 from Supplementary Material (Apêndice A) represents the alluvial vegetation as an example on how the geomorphological features are strongly associated with the floodable environments and forest formations.

While alluvial vegetation is often exclusively associated with the seasonally flooded areas of the VGX, it is important to recognize that these locations also encompass geomorphologically important aspects and socio-environmental functions. Traditional communities, including indigenous populations and riverine dwellers, have distinct denominations and uses for these seasonally flooded environments that go far beyond the vegetation associated with them, and might differ from the formal knowledge produced by scientists, researchers and academics. Insufficient comprehension of how these communities classify, use and relate to the flooded areas can result in inadequate management of environmental impacts. Considering this, this article also aims to classify and describe its outcomes based on the traditional population's understanding of VGX's flooded environments, as used in documentation produced by Non-Governmental Organizations (NGOs) and independent research groups involved in guaranteeing the rights of those affected by the BMHC (Eletrobrás, 2009b; Ferreira; Molina; Molina, 2018; Pezzuti *et al.*, 2018; Sartorelli, 2018; MPF, 2019; Zuanon *et al.*, 2019). This approach aligns with a more intricate and localized observation of the landscape, diverging from the macroscopic approach commonly adopted in the technical literature, which examines them on a large scale with limited detail.

Therefore, this section presents descriptive characteristics of the main environments detected from the analysis of the orthophotos and 3D models, which, although occurring throughout the Amazon, exhibit many particularities for the study area that are still in the early stages of description in the international literature.

The flood pulse promoted by the South American Monsoon during austral summer is the driving force that shapes the Xingu river environments (Figura 23). An important cultural aspect worth mentioning, is that the flood pulse occurs during the southern summer, when the monsoon is active, but culturally, for the inhabitants of the Amazon Forest, it is considered winter. The classification of environments influenced by seasonal water considers not only the water level but also the flow speed, navigability, and the presence of rocks. This classification divides them into 'summer' or 'winter' environments, as well as those occurring in both seasons. The flood pulse of the Xingu River (locally considered as winter) typically spans from November to July, while the drought season (locally considered as summer) extends from August to November (Figura 23). The seasonal water level variation comprises low and high water stages and transitional stages of rising and receding waters.

The large rocky outcrops are locally known as *pedral* (singular) or *pedrais* (plural) and its associated vegetation is locally known as *saroba*. The environment formed by the *saroba* is called *sarobal* (singular) or *sarobais* (plural). The alluvial dense forest is known as *igapó* (singular) or *igapós* (plural) (Figura 23). Additionally, the Xingu landscape also includes islands and upland environments. These are the main environments modeled in the 3D representations.

Figura 23: (a) Seasonally flooded environments of the VGX according to the annual flood pulse (average flow calculated prior the beginning of operations in BMHC). (b) Seasonally flooded environments represented in Mapa 9-a registered during the field trip.

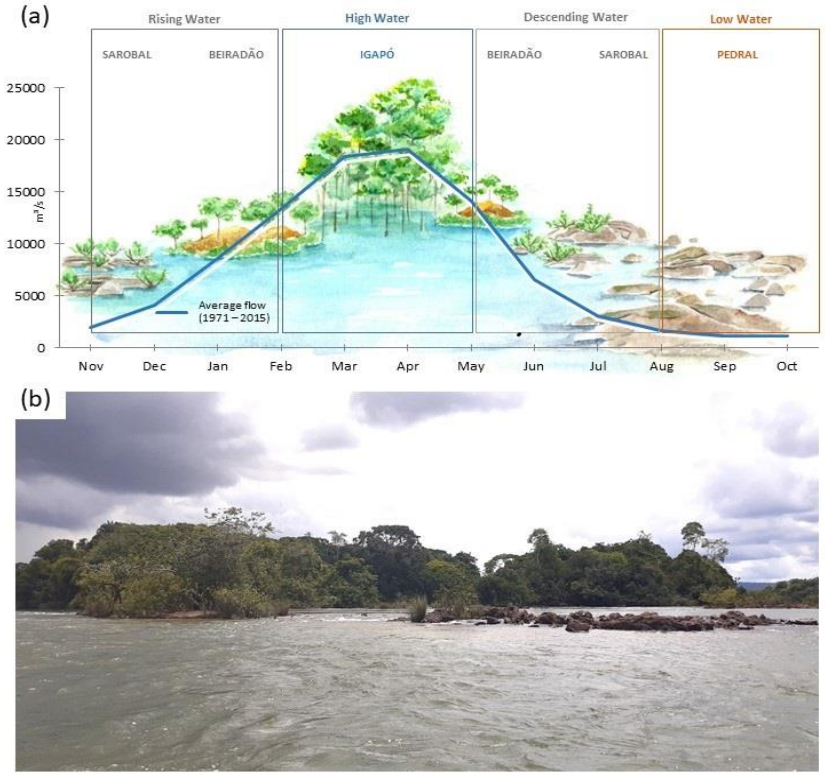

Fonte: Autoria própria (adaptado de Pezzuti *et al.*, 2018)

While the analysis of the selected models and orthophotos revealed a scenery that is very rich and detailed, the small scale of the products limited the observation of larger environments. For this reason, some representative medium resolution orthophotos are presented (Mapa 11), as they still provide very high-resolution imagery compared to conventional satellite products. Tabela 8 compiles a concise description of the environments presented on Mapa 11, their local names, and their seasonality according to the flood pulse.

Tabela 8: Seasonally flooded environments from the VGX detected by the imagery products resulting from RPA flights. Adapted from Ferreira *et al.*, 2018 and Sartorelli *et al.*, 2018.

Environment	Local name	Description	Flood Season
Rocky area	Pedral	Large and continuous rocky riverbed	Drought
Rocky vegetation	Saroba/ Sarobal	Area of rocks and beaches with coarse sand, covered by low trees and scattered shrubs, with the occurrence of many fruit trees. In winter, it is covered by water. One of the forms of Dense Alluvial Rainforest	Flood and drought
Shoals	Sequeiro	Shallow or dry area with interspersed rocks and small patches of beach and small streams.	Flood and drought
Edge of the island	Beiradão	Part of the island's edge where the forest, typically dense and with vines, meets the riverbank	Flood and drought
Riparian sandbank woodland	Restinga	Small elevated area on flood-prone islands that takes longer to be covered by water	Flood
Waterfall	Cachoeira	Relatively extensive area with many rocks, where the water flows very strongly, making navigation difficult and dangerous. There are waterfalls that form cascades.	Flood and drought
Island	Ilha	Land portion with forest surrounded by water in the summer. In winter, some islands may be covered by water, with only the vegetation exposed.	Flood and drought
Blackwater flooded forest	Igapó	Flooded open forest vegetation located at the edge of the land and inside the islands when they are inundated. In the summer, it is referred to as 'baixão. The main form of Dense Alluvial Rainforest.	Flood
Igapó lowland	Baixão	Igapó area during summer. Corresponds to a form of Dense Alluvial Rainforest	Drought

Mapa 11: Environments detected on medium resolution orthophotos obtained through SfM-MVS presenting some important floodable environments of the VGX that have not been detected on 3D models due to scale issues. (a) Rocky outcrops (*pedrais*) with associated rocky vegetation (*sarobal*), shoal environment (*sequeiro*) and waterfall in the mouth of the Iriri river, an important tributary of the Xingu river (b) Edge of the island (*beiradão*) and riparian sandbank woodlands (*restinga*) in the mouth of Bacaja river, a tributary of the Xingu River in the VGX area. (c) Islands and blackwater flooded forest lowlands (*baixão*) on the mouth of Bacajá river and (d) Blackwater flooded forest (*igapó*), on the edge of an island, in the Xingu main river channel at the VGX.

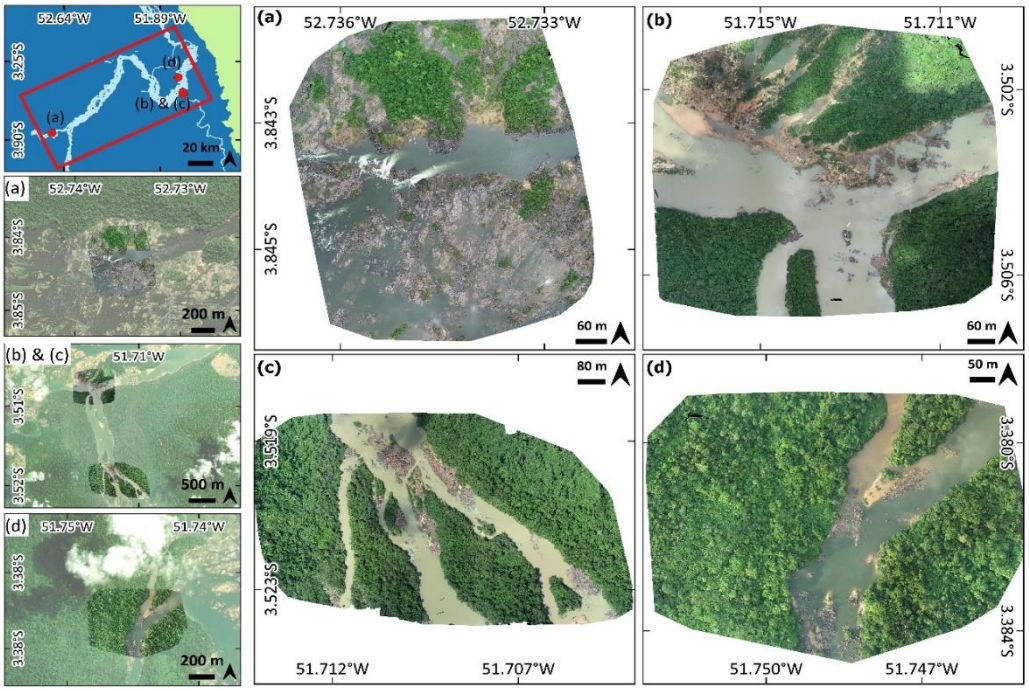

Fonte: Autoria própria

The most prominent environments in the imagery set are the ones formed by seasonally flooded rocky substrates. The geological and tectonic feature where the study area is located is known as the Xingu Complex, characterized by a variety of volcanic, intrusive and metamorphic rocks (Schobbenhaus *et al.*, 1984). In the VGX banded gneisses prevail (Figura 24a), along with Quaternary ironstones (Freire *et al.*, 2022; Niyonzima *et al.*, 2022) occuring on the fractured bedrocks along the Xingu River and some of its tributaries (as the Iriri and Bacaja rivers) (Schobbenhaus *et al.*, 1984; de Paula Silva; Rodrigues; Pereira, 2014; Sawakuchi *et al.*, 2015). These ironstones, locally known as *mocororô*, are present in both permanently submerged zones and marginal areas of seasonally inundated riverbeds (Figura 24b). They have never been examined in detail until the pioneer studies from Freire *et al.* (2022), which first identified and described their mineralogy, texture, morphological features and chemical composition, and Niyonzima *et al.* (2022), which determined their formation ages during the Late Quaternary.

According to these authors, Xingu ironstones are comprised by ferruginous (goethite) laminated crusts, sandstones and conglomerates (Figura 24c) and are marked by their intricate morphology, featuring numerous cavities that create highly diverse aquatic habitats (Figura 24d) turning them extremely ecologically relevant for the Amazonian ecosystems.

Mocororôs are described by Freire *et al.* (2022) as occurring in discontinuous mound-like lenticular or tabular morphologies from 10 to 100m in extent and up to 4m thick (Figura 24e), appearing black to brown in outcrops and dark reddish or yellowish in freshly broken surfaces. Above sandy riverbeds they are platy, poorly to moderately sorted ferruginous conglomerates that can disintegrate through the action of water, removing underlying sand and forming sinkholes and caves (Figura 24f). A wavy convex lamination pattern can be observed at the laminated crusts at all scales (Figura 24c and e). Goethite is the principal rock-forming mineral of the laminated crusts, along with abundant microbial molds, named as ferruginous microbialites, claimed to be the first occurrence of such material in South America (Freire *et al.*, 2022).

Figura 24: Examples of elements that form the rocky outcrops of the VGX. (a) Banded gneiss forms the majority of the rocky outcrops of the VGX. (b) *Mocororô* found in the seasonal flood zone on the Xingu river bank. (c) Example of ironstones intercalated by ferruginous (goethite) laminated crusts (red arrow) and conglomerates (yellow arrow). (d) Cavities on the mocororô used as shelter by a crab. (e) Thick layer of *mocororô* forming a small mound. (f) Cavity formed by the erosion of the mocororô.

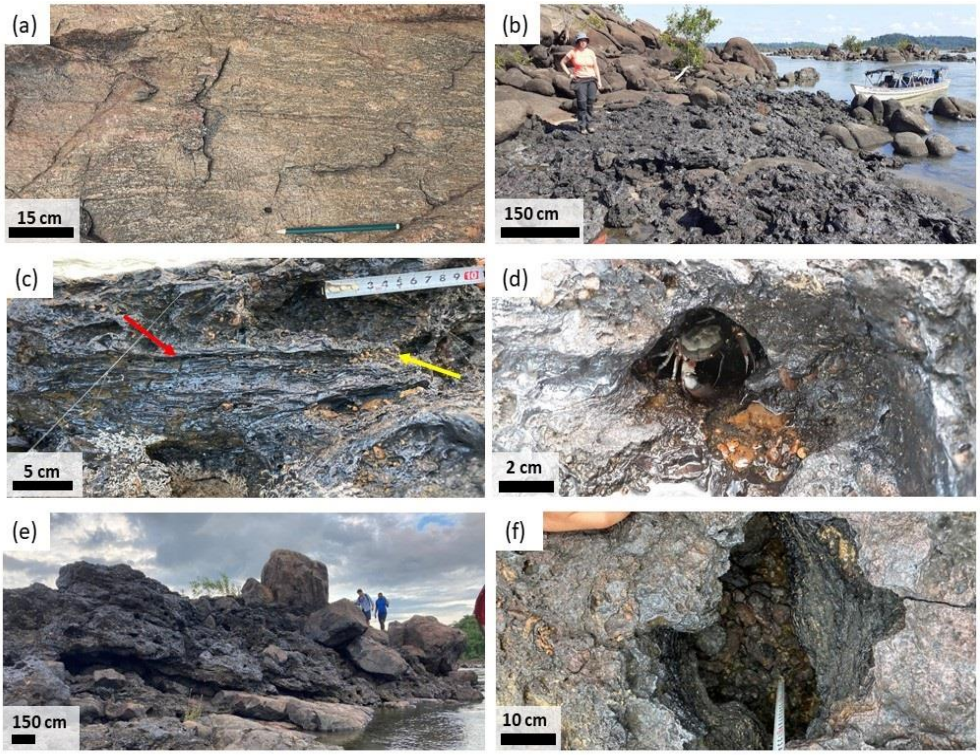

Fonte: Autoria própria

There is a specific aquatic and semi-aquatic fauna exclusively dependent on seasonally flooded environments, and it is estimated that 28% of fish species in the VGX are associated with them (Zuanon *et al.*, 2019). During the river flood, the trees in the flooded forest produce fruits that will feed frugivorous fish and Amazon river turtles (*tracajás*) during the high-water season. It is also during this time that fish and turtles spawn in the seasonally flooded forest. During the flood, the fruits fall into the water, attracting schools of fish, and it is in these environments that the fishing activities of river-dependent communities concentrate (Junk *et al.*, 1989). The caught fishes are used for subsistence and commercial purposes. In the dry season, especially in the rocky areas, the capture of ornamental fish becomes an important economic activity and a significant source of income for some of the people of Xingu (Pezzuti *et al.*, 2018; Zuanon *et al.*, 2019). In addition to fish, other aquatic and semi-aquatic animals rely on flooded environments, such as *tracajás* and caimans, which use the beaches for reproduction during the dry season and the flooded areas for feeding and shelter during the rainy season. Other animals, not

necessarily aquatic, such as birds, bats, and mammals, also depend on periodically flooded environments for feeding, shelter, or reproduction.

The river influenced vegetation occurs on the floodplains, as the *beiradões*, *restingas*, *pedrais*, islands and beaches, on slopes varying from 4 to 8 meters in the dry and flood peaks. The canopy of the mature *igapós* of the VGX has an average height of 20 meters and is less compact and closed compared to the dense typology of the Amazon upland rainforest (Figura 25a) or the upland Amazon savanna, as well as less diverse (among 120 to 150 tree species), yet with a more well distributed abundance of individuals (Salomão *et al.*, 2007). The rocky environment has vegetation growing on the rock fractures, where there is sand accumulated (Figura 25b) and is composed of low trees and shrubs (Figura 25c), with many species of fruit trees. The canopy here is discontinuous, distributed in spots along the islands (Figura 25d) with specific adaptive mechanisms that allow fixation of its roots among the rock fractures (Figura 25e). Herbaceous plants can be found on exclusively sandy environments such as beaches and riparian sandbanks (Mapa 15f) (Cunha, 2009).

Figura 25: *Igapó* occurring during the beginning of raising water season (locally known as *baixão*) at the edge of an island (*beiradão*); (b) Fixation of *sarobal* vegetation in the sand accumulated in rock fractures; (c) *Sarobal* composed of low trees and shrubs (d) Discontinuity of the *sarobal* vegetation compared to the *igapó* (e) Vegetation adapted to be fixed and to grow among rocks and (f) Herbaceous plants on sand environment.

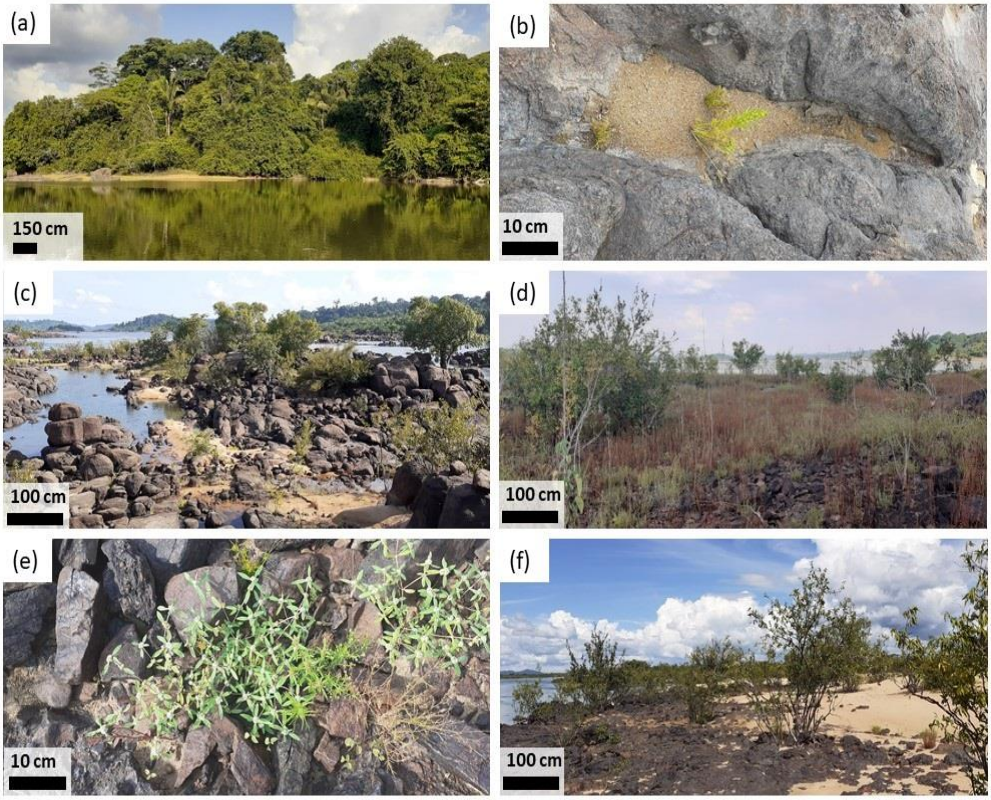

Fonte: Autoria própria

5.4.2. 3D Modeling

As can be noticed from the scales in Figura 24, important geological and geomorphological features of ironstones are not observable through satellite images. Therefore, a more detailed observational study would be only possible through field visits and sample collection. However, a study involving landscape analysis could become a complex task, requiring several days of fieldwork, detailed and numerous photographic records and mapping, which sometimes involve expensive and complex techniques and a large team, and even so, it might not be able to detect the environment as a whole, or its details. Nonetheless, 3D modeling through SfM-MVS makes it possible to reduce the time spent in the field while being economically accessible and easy to manipulate, even for non-experts. The resulting models are detailed and very close to reality, sometimes surpassing other methodologies such as 2D mapping and photogrammetry.

Most of the physical characteristics described by Freire *et al.* (2022) can be observed in the 3D models with a fidelity similar to field observation, greatly expanding the possibilities for investigating ferruginous crusts and similar rock outcrop environments, since the lack of proper spatial modeling was a limitation for research of these environments. The advantages brought by the details of the models can be seen from Figura 26 a and b, which are pieces of the landscape taken from the 3D models, where the richness of details are evident. Additionally, it offers the opportunity to bring the VGX closer to those who have never had the possibility of being in this location.

One of the major advantages of 3D modeling of rock outcrops is the ability to visualize and measure small caves and sinkholes (Figura 26c), conglomerates and blocks (Figura 26d) and patterns of the crusts (Figura 26e), including the possibility to see under water in shallow depths (Figura 26f), which were previously only visually observed in the field. Having the option to "return" to the field, even though through a simulation, provides several advantages in laboratory analysis.

Figura 26: Details of some of the 3D models of rocky outcrops of the VGX: (a) Ironstones; (b) Fractured gneisses part of a large outcrop; (c) Caves and sinkholes on the *mocororô*; (d) Ironstones forming conglomerates; (e) Growth patterns of ironstones over banded gneisses; (f) Visible submerged rocks on shallow waters.

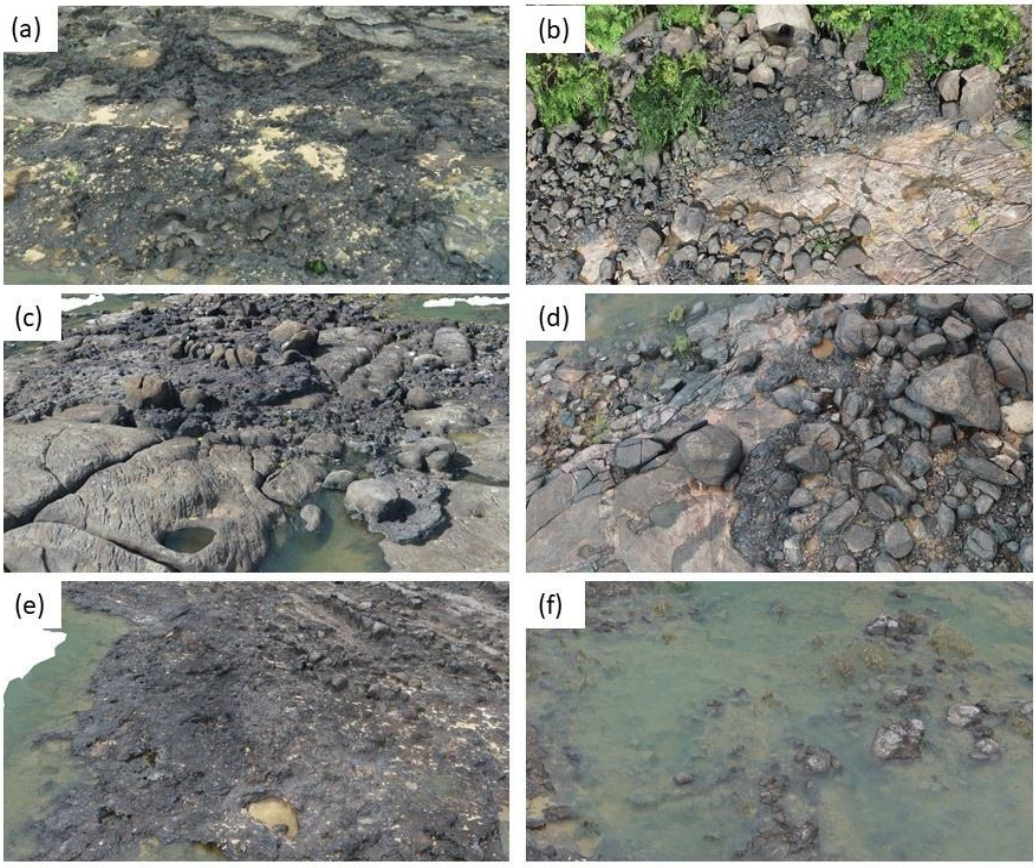

Fonte: Autoria própria

Another advantage of 3D modeling is the possibility of conducting environmental, ecological, topographic, hydrological/hydrographic, and landscape analysis. However, in the specific case of this study, topographic and hydrological/hydrographic modeling would not be possible due to issues associated with geolocation accuracy. High-precision topographic surveys, such as the Real-Time Kinematic (RTK) technique, would have been necessary for that, including the acquisition and measurement of Ground Control Points (GCP) that were not feasible in this instance due to the complex access to the study area and available team members to manage the equipment. Grohmann *et al.* (2023) showed that the difference in XY coordinates from SfM-MVS results produced with and without GCP were minimal, and the main discrepancy was indeed in the Z-axis. Aware of this, we can say that the lack of high geolocation accuracy concerning elevation data does not diminish the importance of the models, which can still be used as tools for the preservation and maintenance of environmental heritage, maintaining a high

degree of confidence regarding georeferencing. Therefore, it is important to keep in mind that elevation values collected by the RPA should be used mindfully, since internal GPS cameras were the only source of geospatial information.

Certain data may not be suitable for 3D visualization in the context of this work, which is the case of the deep water that characterizes the Xingu main river channel and the dense vegetation (Figura 27a and b). Forests and large water bodies exhibit uniform textures and repeating patterns, which can introduce uncertainties during the matching process. For instance, in dense forests, any feature to be reconstructed should be visible in at least six images; otherwise, incomplete reconstructions or noisy point clouds may occur (Figura 27c and d) (Iglhaut *et al.*, 2019). The methodology also has limitations when it comes to vegetation in general and not only dense canopies. Even herbaceous plants, sparse bushes, and small trees in the *sarobal* display a wide range of details in terms of shapes, sizes and volume. Capturing such intricate features and the complex geometry of vegetation would require a combination of techniques and the integration of multiple sensors, resulting in a greater need for computational capability and time-consuming processes to create the 3D model. Although the modeled vegetation cannot be utilized for individual identification, species cataloging, detailed structural observation, or intricate quantitative analysis, it remains important to include it in the simulations to provide observers with a more realistic and intuitive outcome.

Figura 27: Example of compromised reconstruction of dense vegetation. (a) 3D model from a distant point of view and (b) Orthphoto from the respective 3D model. (c) Zoom into a specific area of the model, highlighted in the red square. From a 90° point of view, the vegetation can be well observed and distinguished while in (d), from a frontal point of view, the vegetation is completely distorted.

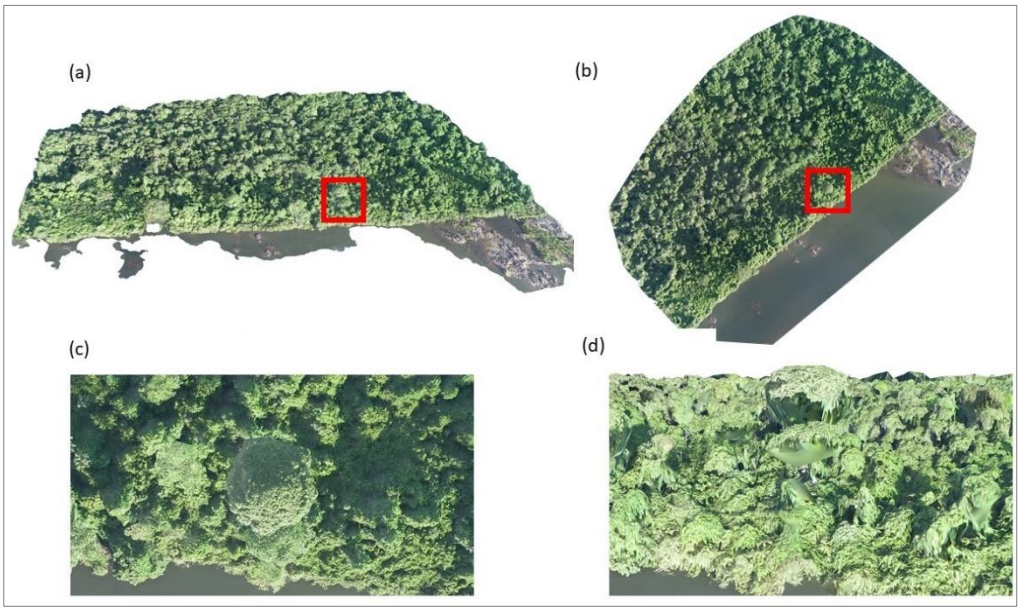

Fonte: Autoria própria

Still regarding some limitations of the technique, due to the nature of the landscape being surveyed, missing sections imaged by the sensor might generate gaps and holes in the 3D model. This happens due to the complexity of some elements that can create self-overlaps and shadows and requires fills and interpolation during the meshing process, aiming to not leave the poor geometric configurations visible and unpleasant. This repair by the algorithm still might need manual interference and can be time consuming, in addition to compromising the realistic visualization of the final product (Remondino *et al.*, 2009; Remondino; Rizzi, 2010; Reid; Ramos; Sukkarieh, 2011). An example is on Figura A_8 from the supplementary material (Apêndice A), which shows the process of interpolation and correction from the model presented on Figura A_2.

The integration of radiometric information with geospatial data in orthophotos facilitates a comprehensive representation of the targets from both terrestrial and aerial viewpoints (Chiabrando; Donadio; Rinaudo, 2015). While the primary aim of this study has been the 3D spatial modeling, the orthophotos derived through the SfM-MVS process demonstrate very high levels of quality and resolution, making them very useful to land use and land cover analysis, as well as time-series investigation. Additionally, these orthophotos serve as unprecedented records,

capturing flooded environments with remarkable detail, particularly within the VGX region. The generation of orthophotos culminates as the final step within the SfM-MVS technique, and their quality is intricately linked to the previous processes (Remondino, 2011).

5.4.3. Landscape Preservation and Natural Heritage

Landscapes are important expressions of the territory, accessed through cognitive and sensory processes, capable of assigning meanings to geographical places that go beyond the abiotic components and biological diversity (Lai; Kwong; Mak, 2010). While landscapes may appear commonplace to some, they can hold significant meaning for the people who inhabit them and have a deep cultural connection to it. Inadequate management of landscapes under anthropogenic pressure can destroy the link between society, communities, and the environment. Therefore, achieving cultural sustainability in ecological systems requires decision-makers to have a detailed understanding of the values of a particular location (Stephenson, 2008).

In line with the prevailing trends observed in research and the development of methodologies concerning the documentation, management, and conservation of cultural, architectural, and archaeological heritage (Remondino *et al.*, 2009; Guarnieri; Pirotti; Vettore, 2010; Remondino; Rizzi, 2010; Chiabrando; Donadio; Rinaudo, 2015; Herrero-Tejedor *et al.*, 2020), the recognition of the natural environment as a form of natural heritage represents a pivotal and strategic approach to preservation (Pietroni, 2017). Established techniques, which have undergone thorough testing and implementation in the context of historical heritage, are now being effectively applied to natural habitats that are vulnerable to human interference.

A wide range of strategies can be employed to document attributes of both cultural and natural heritage areas, such as aerial photography, photogrammetry, mapping, narrative descriptions, and videos (Lai; Kwong; Mak, 2010; Herrero-Tejedor *et al.*, 2020). Nevertheless, the evidence in the literature regarding the advantages of 3D models over traditional 2D tools has acted as the main motivation to undertake an exploration of spatial modeling in the context of this research, marking a pioneering effort within this particular field of study.

3D visualization allows for a greater sense of immersion surpassing conventional photographs and maps, providing an interactive exploration experience and affording the observer the unique opportunity to observe specific details of the environment across various scales (Lai; Kwong; Mak, 2010; Guarnieri; Pirotti; Vettore, 2010). Within the context of the study area, the application of 3D models allowed for a comprehensive visualization of crucial yet underexplored and underrepresented seasonally flooded environments, such as the *pedrais* and *sarobais*, which have received limited attention in the available literature.

Despite the evident environmental concerns associated with the VGX, particularly in the aftermath of the installation of the BMHC, and the documented impacts of this substantial infrastructure that have already been well-documented in the scientific literature recognized by environmental authorities, and reported in the media (Sabaj-Perez, 2015; Faiola; Lopes; Mooney, 2019; Zuanon *et al.*, 2019; Higgins, 2021; Jiang *et al.*, 2018), the study area, especially the reduced flow zone of the Volta Grande (which suffers the most pronounced effects from the river's damming), continues to be inadequately addressed concerning the environmental implications it has been enduring. Furthermore, the VGX has yet to be recognized by society aiming to encourage decision-makers to perceive a compelling urgency for its preservation and careful management. Legal disputes between environmental agencies and the operator of the hydroelectric complex have been ongoing since the issuance of the operating license, driven by the profound impacts on the landscape, wildlife, and the traditional way of life of communities depending on the Xingu River in the Volta Grande, all of which are adversely affected by the operation of the enterprise (Butler, 2012; MPF, 2019; Fearnside, 2021; Antunes, 2023).

This study proposes that the appreciation of natural heritage and cultural landscapes by decision-makers and society holds the potential to encourage them towards its preservation. Understanding and being close to the landscape through spatial modeling would be crucial for improving planning and management decisions and raising awareness regarding the comprehension and mitigation of impacts. Studies conducted by Lai, Kwong and Mak (2010), An and Powe (2015), Bishop (2015) and de San Eugenio Vela, Nogué and Govers (2017) attest to the efficacy of well-designed visual representations in fostering environmental consciousness among the general public. These authors observed that the preservation incentive engendered by virtual experiences that emulate real

environments triggers affective responses comparable to those stimulated by a physical visit, opening possibilities for effective communication with users and facilitating the exchange of information between experts from diverse disciplines and the public.

The visualization of well-designed 3D maps is an excellent tool for communicating complex and multifaceted issues, as it presents an intuitive and lifelike representation of the landscape that is familiar and an ease of comprehension among users. It also has the capability to overcome learning and comprehension challenges posed by other forms of presentation, such as 2D maps, photographic reports, and technical texts. Lai, Kwong and Mak (2010) and An and Powe (2015) acknowledged that 3D simulations are important for public engagement, for instance, in public hearings and consultations that form part of the environmental licensing process for high-impact projects, where intricate reports and maps are presented but not always comprehended by the non-specialist public.

Indigenous and riverside communities affected by the BMHC have raised concerns about the lack of transparency regarding the impacts caused by the project. They have alleged that their demands were disregarded and their right to public consultation was violated (Amazon Watch, 2012; AIDA, 2016; Watts, 2014). These issues persist not only during the licensing process but also to the present day, as their complaints and requests regarding the river damming impacts have not been considered by the dam operator in modifying the water flow and increasing water volume for the reduced flow zone (MPF, 2022; Palmquist, 2023; Roman, 2023). We believe that the implementation of 3D modeling not only holds the potential to render the public consultation process more equitable and inclusive but also currently serves as a prospective, integrative, comprehensive, and reconciliatory tool among affected communities, decision-makers, and BMHC stakeholders.

However, despite the numerous advantages of 3D modeling and its promotion as an instrument for conservation and environmental consciousness, it is necessary to discuss its inherent limitations.

The primary and most apparent concern, as observed in this study, revolves around the functionality of the products generated by SfM-MVS in representing the landscape in the absence of spatial context. An un-georeferenced landscape proves inadequate for presentation within an analytical and qualitative framework, as already noted by Lai, Kwong and Mak (2010) and An and Powe (2015). This

limitation is due to the requisite geospatial information necessary for the faithful representation and meaningful qualitative and quantitative interpretation of the 3D simulation. In this research, while the final products are georeferenced using GPS integration with the RPA sensor, the absence of GCP or high-precision positioning techniques restricts the use of 3D maps for other modeling purposes, such as topographic/hydrodynamic modeling of the seasonally flooded environments.

Another limitation was the extensive size of the study area, which did not allow the comprehensive investigation of the entire environment, requiring the selection of specific microenvironments for aerial surveys. Despite these selected environments being representative and yielding significant results aligned with the objectives of our research, the ideal scenario would have comprised detailed imaging of the entire area impacted by the river damming, which would not be feasible through the use of a single technique. As highlighted by McDonald *et al.* (2020), employing RPAs to achieve centimeter-scale resolution over a large area such as the 130 km stretch of the reduced flow zone would have proved inefficient in terms of data volume and image processing, and impractical given the flight limitations of equipment like the Phantom 4. For large-scale areas, Remondino *et al.* (2009) and McDonald *et al.* (2020) suggest an integrated approach involving multiple techniques, sensors, and scales, such as lidar and TLS.

Another pertinent consideration is the high volume of data generated by the images and the computational processing capacity required to apply the methodology. Extensive data sets demand considerable processing time and substantial computational resources for high resolution processing. Processing at lower resolutions would compromise accuracy and realism in the models. As observed by Lai, Kwong and Mak (2010), there is a delicate balance between achieving feasible realism through 3D modeling and maintaining cost-effectiveness with regards to data acquisition and processing. Managing excessively large files presents challenges, encompassing data collection, processing and dissemination (e.g. prolonged download times and the need for powerful personal computers), thereby becoming an obstacle for end-users seeking to utilize and explore the 3D models. Hence, it is essential to strike an equilibrium between the volume of data generated during flights, the desired resolution and presentation for the final products, and the objectives intended for the end-user (Remondino; Rizzi, 2010). Therefore, the present study underscored the significance of providing online

visualization of the models (in addition to facilitating data set downloads) as a means to ensure broader access to our work and the realization of our objectives.

While the final outcome of this work consists of visual products, it is essential to recognize that visualization itself is not an end in its own right, as highlighted by Horne and Thompson (2008). Rather, it necessitates a shared understanding among all parties considered as end-users of the models. Lai, Kwong and Mak (2010) have documented complaints from the public regarding the perplexity encountered when dealing with 3D models in certain contexts, with testimonials describing feelings of disorientation while exploring the simulated environment due to complicated and unsuitable interfaces that confuse inexperienced users. The interface provided should be intuitive and straightforward, designed for a non-specialist audience, without the need for specialized training for its effective utilization. The same authors also observed that difficulties in using a visualization platform might deter potential users, who may feel intimidated by complex interfaces, even when informed about the benefits of visualization in 3D platforms.

An & Powe (2015) draws attention to the potential drawbacks that the improper use of 3D models can pose in terms of public skepticism regarding data reliability. This arises from the fact that the general public, especially non-expert audiences, seeks clarity and certainty in their observations. According to these authors, there is an expectation that 3D visualizations are as game-like experiences. Consequently, poorly presented, biased, or incomplete models, with conflicting information, may engender distrust or unrealistic assumptions among users (Bishop, 2015). Model developers must keep in mind that the perception of realism by the target audience is inherently subjective. Hence, they should approach the creation of visualizations with care and context, diligently considering the audience's expectations and the objectives they aim to achieve with their results.

The public should have in mind that the representation of the real world through a model is imperfect, and visualization has its limitations. A virtual simulation cannot replace the experience of direct observation of the actual location, particularly in the context of complex and dynamic environments such as tropical forests subject to seasonal variations (as exemplified by the VGX). Clear communication with the target audience is crucial to align their expectations with the content of the simulations, encompassing not only the level of resemblance the models can achieve with the real world but also the effective translation of technical

knowledge into information accessible to non-experts. Bishop (2015) demonstrated that while experts can interpret the geomorphology and vegetation in 3D models, most people lack this expertise, potentially hindering the immersive experience of the simulations. In contrast, An & Powe observed that the realism of 3D environments might be considered satisfactory for semi-experts.

Champion and Rahaman (2019) concluded in their study that while 3D visualizations may impress, they do not necessarily engage the target audience in exploring their full potential. In a lack of environmental context, 3D reproductions of the landscape might be insufficient for the audience to grasp its significance and develop the sense of proximity, ownership, and care essential for cultivating preservation awareness. It thus falls upon researchers in this field to enhance the capacity to contextualize and refine the spatial modeling of natural heritage areas. Projects involving digital heritage must embrace the broader role of 3D models, perceiving them not merely as final products of preservation initiatives but as tools for comprehensive contextualization and environmental education. Efforts in contextualization and environmental education will always remain mandatory, as there is no universal solution for landscape visualization.

5.5. Conclusion

In this study, we have developed 3D models, orthophotos, and digital surface models of seasonally flooded environments in the Volta Grande do Xingu. Despite possessing the necessary attributes to be designated as a Natural Heritage Area, this region has been subject to the construction of large-scale projects, such as the BMHC. The data utilized for creating the models were obtained through an aerial photogrammetric survey, and the technique known as SfM-MVS was applied to generate dense point clouds, serving as the foundation for constructing the 3D models.

This study is pioneering in spatial modeling of the seasonally flooded environments in VGX, specifically the *pedrais* and *sarobais*, and provides a significant contribution to scientific research and understanding of these unique habitats. The detailed and high-resolution 3D models offer a valuable tool for future investigations and open new research opportunities for scholars interested in this region.

The application of 3D simulations enables the representation of VGX's form, structure, and features with a level of detail not achievable through alternative methods.This capability aids in comprehending the interaction between tropical alluvial environments and human interventions, as well as in identifying vulnerable areas susceptible to degradation, thus facilitating the optimal management of these sites.

The models have been made accessible via the user-friendly and complimentary platform Sketchfab, aiming to facilitate easy access and accommodate a broad audience of interested parties who can benefit from these research outcomes.

It is recommended for future research to encompass a broader range of survey techniques, such as lidar and TLS, and to implement advanced georeferencing methodologies in these environments. This approach might allow the monitoring of changes brought about by the Xingu River dam, thereby facilitating the potential for hydrodynamic and topographic modeling.

We also propose efforts to be made towards conferring the VGX as a Natural Heritage Area or Cultural Landscape, as a means to safeguard the elements of its landscape that remain unaffected by anthropogenic intervention. Currently, there is not any legal provision for the protection of areas of significant geodiversity in the Volta Grande.

Data Availability Statement: The processed point clouds, final orthophotos, DSM and 3D models resulted from all the 37 mission flights are available on https://doi.org/10.5281/zenodo.8251029

Declaration of Competing Interest: The authors declare no conflict of interest

Funding: This study was supported by the Coordination for the Improvement of Higher EducationPersonnel (CAPES)—Financing Code 001. AAA is a research fellow of the Coordination for the Higher Education Personnel (CAPES, grant #8882.328088/2019-01). MPF is funded by the São Paulo Research Foundation (FAPESP, grant # 18/15123-4) and by the Coordination for the Higher Education Personnel (CAPES, grant # 88882.328047/2010-01). AOS is funded by the Brazil's National Council of Scientific and Technological Development (CNPq) and by the São Paulo Research Foundation (FAPESP). CHG is funded by the Brazil's National Council of Scientific and Technological Development (CNPq, grant # 11209/2021-1).

Acknowledgments: The authors thank the Graduate Program in Environmental Science at the Institute of Energy and Environment and the Institute of Geosciences from the University of São Paulo. The authors acknowledge Mr. Kyle Flavin for revising the text, Mr. Lucas Docal for assisting in processing the 3D model, Geo Supply for providing their facilities and computers for part of the data processing, and Silvia de Almeida Gonsales for the artwork in Figura 23a. The authors extend their appreciation to Mr. Pontien Niyonzima, Mr. Nelson Buainain Neto, and Mr. Gustavo Martins for their indispensable cooperation during the field trip.

Declaration of Generative AI and AI-assisted technologies in the writing process: During the preparation of this work the author(s) used ChatGPT 3.5 and Google Bard in order to improve readability and language and set the reference list in the APA style. After using this tool/service, the author(s) reviewed and edited the content as needed and take(s) full responsibility for the content of the publication.

6. VARIATIONS IN SURFACE WATER AREA AND ELEVATION BEFORE AND AFTER THE CONSTRUCTION OF A HYDROELECTRIC COMPLEX IN THE EASTERN AMAZON FOREST, BRAZIL

Alynne Almeida Affonso, Carlos Henrique Grohmann

Este capítulo é baseado em artigo submetido ao periódico *Remote Sensing Applications: Society and Environments* (ISSN: 2352-9385).

Abstract

This study explores spatiotemporal variations in water elevation and surface area within four distinct sectors of the VGX from 2005 to 2008 and 2019 to 2021. The primary objective is to establish correlations between flood data and water surface height measurements, aiming to identify potential connections between these changes and the construction of the Belo Monte Hydroelectric Complex. To achieve these aims, remote sensing altimetry data were integrated with hydrological measurements and water surface coverage assessments. The dataset includes historical in-situ hydrological measurements and Synthetic Aperture Radar (SAR) data to observe seasonally flooded vegetation before the construction of the BMHC. Landsat data were also employed to evaluate surface water coverage, while altimetry data from the ICESat and ICESat-2 satellites were utilized to determine water surface heights.

This study successfully demonstrates spatiotemporal variations in both the water surface height and surface area of the Xingu River within the VGX region, particularly in the Reduced Flow Zone. These alterations are further accentuated when compared to the natural conditions of the river's flood pulse. This research underscores the critical importance of monitoring and understanding the impacts of large-scale infrastructure projects on fragile and ecologically significant environments and highlights the need for sustainable management strategies to mitigate these effects.

Keywords: Spatiotemporal Variation; IceSAT; SAR; GSW; Belo Monte; Flood dynamics

6.1. Introduction

In Brazil, the Amazon biome covers an area of 4,871,000 square kilometers, comprising 23 biogeographic units and representing approximately 48% of the Brazilian territory (Ferreira, 2003). The Amazon complex encompasses the world's largest freshwater system, containing around 20% of the global freshwater supply (Oltman, 1968). The eastern part of the Amazon is dominated by clearwater rivers, such as the Xingu, Tapajós, and Tocantins rivers, characterized by low concentrations of suspended sediments and dissolved solids. These rivers are notable for supporting a wide variety of aquatic and seasonally flooded environments (Ayres, 1995).

The Xingu River extends approximately 1,900 kilometers, divided into three compartments, and crossing two states (Mapa 13). It originates in the Upper Xingu region, in the Mato Grosso State and eventually converges with the Amazon River on its right bank, in the Lower Xingu. Within the Middle Xingu region, near the municipality of Altamira in the State of Pará, lies the *Volta Grande do Xingu* (VGX), or, the Great Bend of the Xingu. This segment of the river spans 130 kilometers and is characterized by its unique features, including numerous waterfalls and rapids, as well as a zigzag pattern of bedrock and anastomosed channels, divided into three distinct "bends." Each of these bends represents a sequential 90-degree deflection of the river channel (Sabaj-Perez, 2015). Due to its 90-meter slope combined with a high water discharge, the VGX has gained recognition as an ideal location for a hydroelectric power plant, and was selected as the site for the construction of the Belo Monte Hydroelectric Complex (BMHC) (Costa *et al.*, 2012).

Changes in river flow patterns, induced by either variations in precipitation and the installation of dams, determine the characteristics and distribution of flooded environments, as they influence their balance (Latrubesse *et al.*, 2017). Fluvial dynamics control the characteristics of the water column and riverbed substrate, determining the floodable areas, which are essential for the maintenance of the flooded habitats. In specific sections of the river, sedimentary and fluvial dynamics maintain the balance that sustains the diversity of aquatic and transitional environments and the biodiversity (Archer, 2005).

The VGX encompasses a variety of distinct seasonally flooded ecosystems such as forests (locally known as *igapó*), herbaceous, shrubby and low vegetation (*sarobal*), islands, beaches, and large rocky outcrops (*pedral*) (Salomão *et al.*, 2007; Sartorelli, 2018). All of these ecosystems are subject to the fluctuating patterns of the Xingu River's natural seasonal flood pulse (Junk *et al.*, 1989). Consequently, any alteration in this natural flow can have long-lasting and severe impacts on these environments, which are exceptionally sensitive due to their dependence on the seasonal water dynamics (Assahira, 2014). Moreover, these areas harbor endemic species and hold paramount importance for indigenous and traditional communities, as they rely on these waters to sustain their traditional way of life and cultural practices (Pezzuti *et al.*, 2018).

In this study, a historical dataset of hydrological measurements obtained in situ was utilized, complemented by Synthetic Aperture Radar (SAR) data for observing seasonally flooded vegetation prior to the construction of the BMHC. Landsat data were also incorporated to assess the extension of surface water coverage (flooded areas) and altimetry data from the ICESat and ICESat-2 satellites was used to determine water surface heights. The choice of satellite-borne altimeters was driven by their ability to measure water surface height at a scale equal to or greater than 0.1 km² and for rivers equal to or greater than 100 meters (Mehta *et al.*, 2021). This contrasts with earlier instruments like the TOPEX/Poseidon mission, active from 1992 to 2005, or Jason-1, operational from 2002 to 2013, which had a minimum target size requirement of between 50 and 100 km² (Mehta *et al.*, 2021).

The utilization of SAR imagery for mapping targets beneath forest canopies or within Amazonian vegetation has been extensively documented in the literature, as evidenced by studies conducted by Ferreira-Ferreira *et al.* (2014), Furtado, Silva and Novo (2016), and Pereira *et al.* (2018). While there have been studies in the Amazon region that have explored the relationship between inundation gradients and vegetation, as observed in Ferreira and Stohlgren (1999), Wittmann *et al.* (2006), and Luize *et al.* (2015), as well as investigations into the extent of the flooded area, as demonstrated by Arnessen *et al.* (2013) and Hess *et al.* (2015), research that correlate the flooded area with altimetry data tend to primarily focus on hydrodynamic modeling and the storage capacity of entire basins, as demonstrated in the works conducted by Frappart *et al.* (2006) and Fassoni-Andrade, De Paiva and Fleischmann (2020a). However, for the Xingu River, and

more specifically, the Volta Grande do Xingu, this type of approach remains unexplored, especially concerning the relationship between flood extent and water surface elevation.

Thus, this study aims to investigate spatiotemporal variations in water elevation in four areas of the Volta Grande do Xingu, seeking to establish spatiotemporal correlations between flood data and water surface height measurements, both before (2005 to 2009) and after (2018 to 2021) the construction of the BMHC. To accomplish this objective, measurements from remote sensing altimeters have been integrated with flood data and water surface coverage.

6.2. Methodology

6.2.1. Study Area

The VGX area presents a complex geomorphological landscape characterized by a network of bedrock channels in anabranching pattern with rapids. These channels are influenced by fracture zones and interspersed with boulder patches and mid-channel bars adorned with vegetation adapted to seasonal flooding (Mapa 12). These highly diverse freshwater environments foster rich biodiversity of plant and animal species, including endemic and endangered ones (Zuanon *et al.*, 2019). Additionally, these environments play a vital role in supporting the traditional livelihoods of indigenous communities and local river-dwelling peoples in the region (Magalhães; Cunha, 2017; Pezzuti *et al.*, 2018; Zuanon *et al.*, 2019).

Mapa 12: The study area (a) Location of the Volta Grande do Xingu (VGX), showing the Brazilian Legal Amazon and the compartments of the Xingu watershed. (b) The Belo Monte Hydroelectric Complex (BMHC) with its two dams, Pimental and Belo Monte, and the Reduced Flow Zone (RFZ) between them. (c) The study area in detail, in satellite imagery.

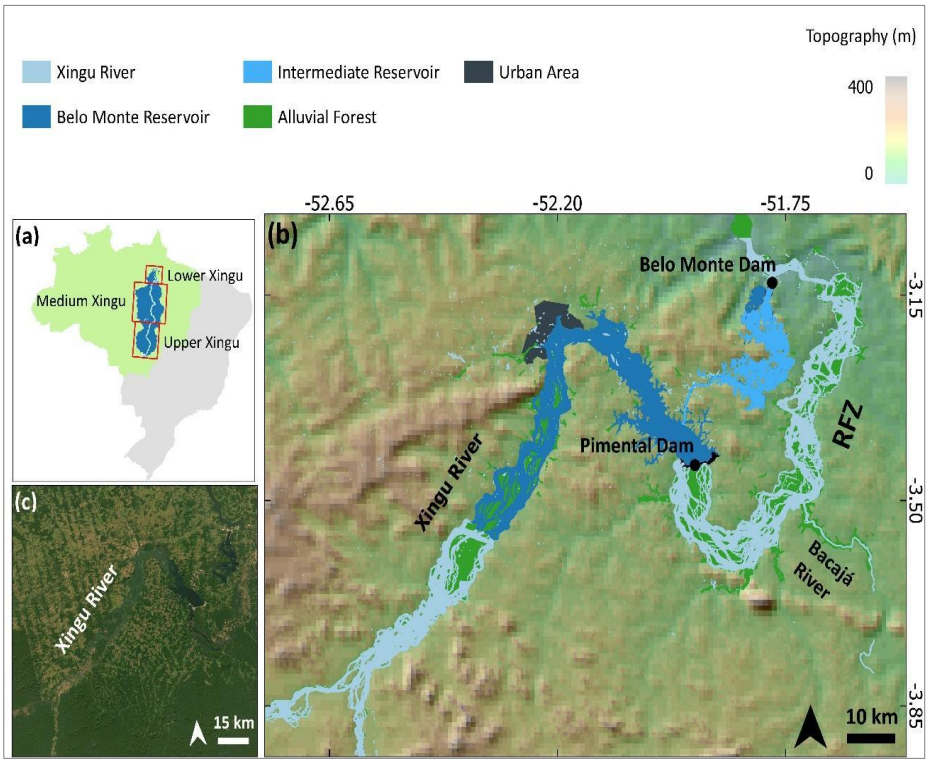

Fonte: Autoria propria

The seasonally flooded environments of the Volta Grande do Xingu are formed by alluvial vegetation and specific geomorphological formations (Affonso *et al.*, 2023b, manuscript submitted for publication). The flooded environments are perfectly adapted to the flood pulse, which is the natural force that influences and outlines the Xingu river ecosystems. The flood pulse occurs during the southern hemisphere summer (culturally, the Amazonian winter) and marks the landscape into 'summer' or 'winter' environments, some of them also occurring in both seasons. The flood pulse happens from November to July, and the dry season spans from August to November (Figura 28). The fluctuation in seasonal water levels encompasses periods of low and high water levels among transitional phases.

Figura 28: Maximum, average, and minimum yearly water levels (elevation) and flow rate between the years 1972-2015 for the Altamira fluviometric station (ANA code 18850000).

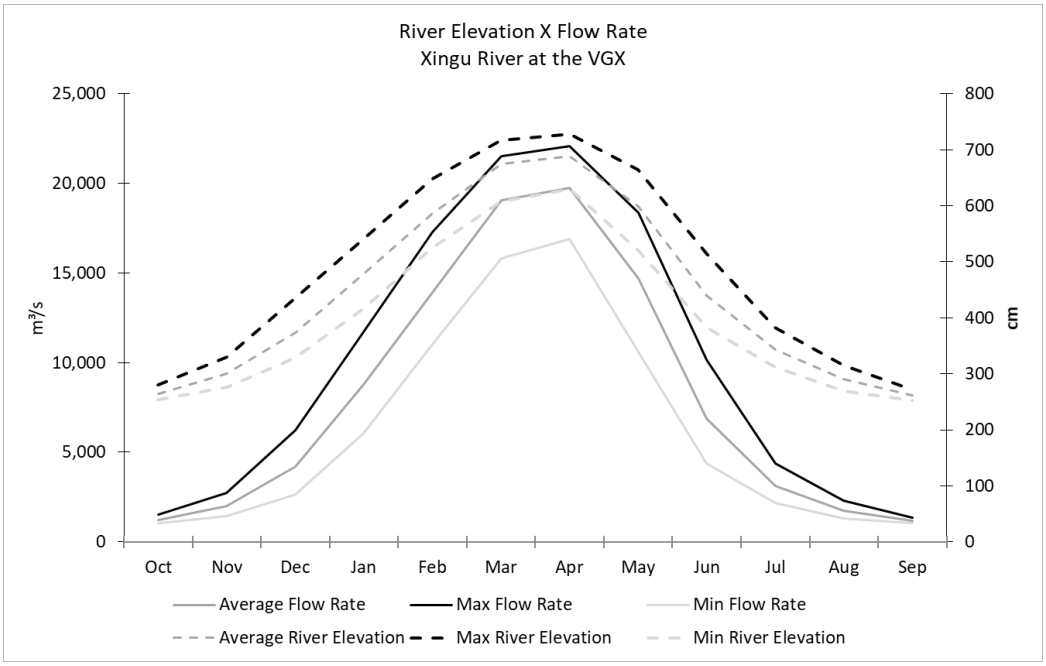

Fonte: Autoria própria

During the dry season, the rocky area known as *pedral* becomes prominent. It features vast, continuous rocky riverbeds that emerge as water levels recede. The *sarobal* is part of the dense alluvial forest of the VGX. It covers the rocky environments, but also beaches with coarse sands. They are characterized by low trees and shrubs, and are flooded and covered by water during the Amazonian winter. The environment locally known as *sequeiro* is characterized by shallow or dry areas interspersed with rocks, small beach patches, and meandering streams. It undergoes fluctuations in water levels throughout the year. The *beiradão* is the edge of the islands, where forest meets the riverbank. *Restinga* is a small elevated area on flood-prone islands. It remains above water for extended periods during the flood season, offering a unique habitat for several plant species. The islands are covered by forest in the Amazonian summer and as the water levels rise during the rainy season, some islands may be partially or completely submerged, leaving only their vegetation exposed. The *igapó* is a flooded open forest located along the edges of the land and within inundated islands and is a crucial component of the Dense Alluvial Rainforest. The *igapó* has less compact canopies compared to the dense Amazonian upland forest, as high as 20 meters, and is also less diverse, with the trees more well distributed (Salomão *et al.*, 2007). All these environments were 3D-

modeled by Affonso *et al.* (2023b), manuscript submitted for publication) and the interactive models for virtual exploration of the environments can be accessed at https://skfb.ly/oILVp.

The VGX is under strong anthropogenic pressure not only related to the BMHC (Jiang *et al.*, 2018; Calvi *et al.*, 2020b; Affonso *et al.*, 2023a), but also deforestation caused by agriculture and cattle ranching (Fearnside, 2001; Barona *et al.*, 2010), which was described in literature even before the construction of the BMHC (Lu *et al.*, 2004; Li *et al.*, 2011; Lu *et al.*, 2013). The most deforested area in the whole Xingu watershed is around the VGX, following the Trans-Amazonian highway.

The construction of the BMHC escalated the environmental deterioration of the VGX area. The complex started to be built in 2010. The damming of the river was completed in 2016, and the complex started its commercial operation gradually, finishing it in 2019, when it started to work in full operation (NorteEnergia, [s.d.]). The completion of the construction works marks the beginning of the implementation of the so-called "*consensus hydrogram"*, a mitigation instrument proposed by the BMHC operation as an attempt to simulate the natural flood pulse of the Xingu River, now affected by the river damming.

Among a fierce legal battle between the BMHC concessionaire company, Public Prosecutors, indigenous and traditional peoples, the Brazilian Institute of the Environment and Renewable Natural Resources (IBAMA) and the Federal Government, the instrument named by the BMHC concessionaire company as "consensus hydrogram" has been implemented (Xingu Mais, [s.d.]). It consisted a minimum flow of 700 m^3/s during the dry season, 4,000 m^3/s during the flood season (consensus hydrogram A), and, every two years, a peak flow of 8,000 m^3/s (consensus hydrogram B), which would guarantee the flooding of the plains (Eletrobrás, 2009b). The remaining flow rates for the other months were defined based on these minimum values to ensure a gradual transition between the peak of the flood season and the peak of the dry season.

However, during the hydrological cycle of the Xingu, the flood season can reach and even exceed a 32,000 m^3/s (at the Altamira station) flow rate. In contrast, during the dry season, the flow remains around 450-500 m^3/s. Furthermore, the flooding cycle can vary significantly from one year to another, with a notable alternation of average, maximum, and minimum values between dry and wet years (Pezzuti *et al.*, 2018).

Studies conducted by a panel of experts in conjunction with independent monitoring carried out by the affected indigenous communities have unequivocally demonstrated that the hydrogram proposed by the BMHC concessionaire company would render life in VGX unviable (Zuanon *et al.*, 2019). With the implementation of hydrogram B, it has been estimated that 70% of the floodable forests of the VGX would no longer experience inundation. In scenarios involving hydrograms A and B, a significant reduction ranging from 70% to 80% has been assumed in the inundation of seasonally flooded forests. Consequently, the vegetation, which is adapted to the inundation cycle, might perish and be supplanted by generalist species, transforming environmentally healthy and stable areas into degraded forests (Schöngart *et al.*, 2021). Because of such irreversible degeneration, it was proposed a provisional hydrogram (13,400 m^3/s during the flood season) while studies are being conducted on a new hydrogram capable to guarantee the minimum life conditions for the VGX area.

6.2.2. Historical Hydrological Series Analysis

Long-term time series observations are necessary to accurately describe the water flow. In the absence of such data, parameters can be statistically inferred from water flows within the same geographical region, as flows exhibit regional peculiarities determined by geographic variations in climate, geology, topography, and vegetation cover (Poff, *et al.*, 1997).

Flow and water level data for the Xingu River at the Volta Grande were acquired through the Hidroweb Portal (https://www.snirh.gov.br/), a tool provided by the National Water Agency (*Agência Nacional de Água* - ANA), which offers a database with all the information collected by the National Hydrometeorological Network (*Rede Hidrológica Nacional* - RHN). The data was tabulated only up to the year 2015 to analyze the river's behavior in the Volta Grande section, free from the influence of the BMHC.

To establish a historical analysis of the data, focusing on "baseline" hydrological aspects—i.e., those prior to artificial interference and large-scale anthropogenic impacts—Station 18850000 in Altamira Municipality was chosen as the source for the data. This station has been recording flow measurements since the 1970s (coincidentally, the Landsat mission was launched in 1972) and remains active to this day.

The Altamira station cannot record data at the critical points of the VGX due to differences in water levels caused by waterfalls and rapids. However, it is possible to look for a correlation with dry and wet periods and flooding patterns. Since alluvial forests exhibit different flood scenarios for several flow values, changes in flow are expected to lead to alterations in water surface height.

6.2.3. Flood data and identification of seasonally flooded habitats

The Global Surface Water (GSW) project is a government initiative from the European Union and United Nations that provides high-resolution, free, and open data mapping of exposed and visible water on the Earth's surface.

The methodology used was developed by Pekel *et al.* (2016). The maps and statistics were generated from 4,716,475 (1.823 TB) individual scenes from 1984 to 2021, provided by Landsat 5 (operational from 1984 to 2011), Landsat 7 (operational since 1999), and Landsat 8 (operational since 2013) satellites, distributed by the United States Geological Survey, and processed at Level 1T (Standard Terrain Correction Level). Each satellite provides global coverage every 16 days. When these satellites operate simultaneously, their individual orbits allow for global revisit every 8 days (GSW, 2020).

The spectral reflectance characteristics of different land cover types have distinct signatures at several wavelengths. These spectral signature differences, particularly in the visible infrared, near-infrared, and shortwave channels, are used to distinguish water pixels from other environments (GSW, 2020). The accuracy described by the authors indicates that less than 1% of detected pixels produce false results, and fewer than 5% of detections were missed.

Using Google Earth Engine (GEE) codes (developed by Mehta *et al.*, 2021), maps of flood frequency, intensity of change in water frequency and a class transition map were created. In addition to that, yearly surface water seasonality maps were also created using GEE to depict the intra-annual distribution of surface water

6.2.4. Synthetic Aperture Radar

SAR imagery was analyzed with the aim of identifying inundated vegetation areas preceding the development of the BMHC. This choice was made because GSW products cannot detect such environments, since they are based on Landsat

optical imagery. The main goal of this analysis is to precisely outline, categorize, and visually represent the boundaries of these ecological zones and to determine their spatial distribution within the landscape. The significance of accurately identifying alluvial forest locations cannot be overstated, as this step plays a pivotal role in facilitating the implementation of effective conservation and management strategies.

In SAR imagery, polarization describes the orientation of the oscillation plane of the propagated wave signal, which can be horizontal (H) or vertical (V). Sensors can transmit the co-polarized signal (HH/VV - transmitting and receiving in the same orientation) or in cross-polarization (HV/VH - transmitting in one polarization and receiving in another). Each polarization interacts differently with targets. In general, HH polarization interacts better with double-bounce type scattering, making it ideal for highlighting flooded areas (which will have a very clear signal with high pixel values) (Meyer, 2019).

Imagery used on this step of the work were downloaded from two main sources: (1) ASF Data Search (https://search.asf.alaska.edu/#/), which is maintained by the Alaska Satellite Facility in partnership with NASA Earth Data, and offers an extensive collection of SAR images free of charge. In this database, ALOS 1 (Advanced Land Observing Satellite) PALSAR (Phased Array Type L-Band SAR) images were downloaded. And (2) G-PORTAL (https://gportal.jaxa.jp/gpr/search?tab=1), maintained by the Japan Aerospace Exploration Agency (JAXA), which provides the entire collection of remote sensing sensors from the Japanese space agency free of charge. Images from the JERS-1 (Japanese Earth Resources Satellite) were acquired in this domain.

All 17 JERS-1 level 2.1 images (radiometrically and geometrically corrected in UTM, with a resolution of 12.5 meters) over the study area were downloaded, for several dates. The images used were from the flood periods of the years 1993 (March 24, 1993) and 1996 (May 11, 1996). The other images were acquired by the satellite during dry, receding, or flooding periods. Images were processed using ENVI 5.6 software. In it, the GAMMA filter (5x5) was applied to attenuate the speckle noise. The GAMMA filter reduces the granular appearance of speckle while preserving the edges and sharpness of image features and suppressing noise. The pixel being filtered is replaced with a calculated value using surrounding pixels based on local statistics within a user-defined window (Shi; Fung, 1994). After

speckle removal, pixel values in DN (Digital Numbers) were converted to dB (NRCS – Normalized Radar Cross Section – a measure of how detectable a target is by radar) using Equation 1, as proposed by Shimada (2002):

$$NRCS = 20\log10\,(I) + CF\ [dB] \quad (1)$$

Where I represent the value of each pixel. The CF parameter for the JERS images, according to Shimada (2002) for the images used in this study, is -85.34 dB.

ALOS PALSAR Radiometric Terrain Corrected (RTC) products, already georeferenced in UTM and corrected both radiometrically and geometrically, were also used. The Fine Beam Double (FBD) Polarization bands (20 meters resolution, HH/HV polarization) were used to create image mosaics representing the annual cycle for the VGX, separated by polarization. As for the Polarimetric Mode (PLR) images (30 meters spatial resolution, HH, VV, VH, and VV polarization), they were used for creating mosaics and for spatiotemporal analysis. The mosaic of images was classified using the Random Forest classification method to generate a map identifying the flooded forest (for more information on this classification technique, please refer to Breiman (2001). The selected dates aimed to cover predominantly the dry and flood periods. It's essential to note that images from the flood period are not available for all years. The availability of images in the periods of interest on an annual basis is a limiting factor for comprehensive spatiotemporal analysis.

The dates of the images used were: PLR Spectral Band: 2007-03-15; 2007-04-01; 2007-04-13; 2007-05-17; 2007-05-29; 2009-03-20; 2009-04-06; 2009-04-18; 2009-05-05; 2009-05-22; 2011-04-12. And FBD Spectral Band: 2007-05-08; 2007-08-22; 2007-09-03; 2007-10-19; 2008-04-24; 2008-05-07; 2008-08-07; 2008-09-05; 2009-08-10; 2009-08-27; 2009-09-08; 2010-05-13; 2010-08-13; 2010-09-11; 2010-09-28; 2010-10-15.

Speckle noise attenuation was performed using ENVI 5.6 software. Although various filters were tested, the best trade-off between reducing the granular noise pattern and preserving spatial resolution was achieved with the 5x5 window size using the GAMMA filter. For radiometric conversion, Equation 2 was applied, where gamma0 represents the intensity of the original image (ASF, [n.d.]):

$$dB \equiv 10 \times \log10\,(gamma0) \quad (2)$$

6.2.5. Altimetry Data

All the altimetry data were acquired through the Ice, Cloud, and Land Elevation Satellites (ICESat and ICESat-2), derived from Geoscience Laser Altimeter System (GLAS, operational from 2003 to 2009) and Advanced Topographic Laser Altimeter System (ATLAS, launched in 2018 and still active) instruments. They were downloaded from the Open Altimetry website (openaltimetry.org), which is a platform to access and visualize data from NASA's ICESat and ICESat-2 missions (Khalsa *et al.*, 2020).

For the ICESat/GLAS data, the product used was GLAH06 Level 1-B Global Elevation, version 34 (Zwally*et al.*, 2014). These products contain surface elevations, including laser footprint geolocation and reflectance, as well as geodetic, instrument, and atmospheric corrections for range measurements from tracks 10, 17, 144, 263, 270, 1126, 1133, and 1252, spanning from 2003 to 2009 (i.e., prior to the construction of the BMHC). All the laser footprint campaigns for the study area available were used. The ICESat/GLAS elevation data are referenced to the WGS84 ellipsoid (ITRF2014 Reference Frame) and were corrected to the Earth Gravitational Model 2008 (EGM2008) mean sea level (MSL) geoid to allow for comparison with the ICESat2 data.

Regarding ICESat-2/ATLAS data, the products used were ATL13 (Jasinski *et al.*, 2020), which contain along-track water surface heights and descriptive statistics for inland water bodies. All the available beams for each track within the VGX study area were used. The selected tracks were 117, 368, 429, 559, 620, 871, 1062, 1313, and 1374, spanning from 2018 to 2022 (after the beginning of the full operation of the BMHC). The elevation data represent orthometric surface height, i.e., height above the EGM2008 MSL.

The subareas of study (Areas 1, 2, 3, and 4) were determined based on the concentration of altimetry data. While ICESat-2 data were well-distributed across the entire study area, ICESat data were concentrated in specific areas on the map. Since the comparison between the time series was crucial, areas were selected based on the concentration of ICESat data (Mapa 13).

Area 1 is the control area and is located immediately after the confluence of the Iriri and Xingu Rivers. Area 2 is located in the Main Reservoir of the BMHC, known as Xingu Reservoir. Area 3, located at the region known as Reduced Flow

Zone (RFZ) of the VGX and is situated directly under the influence of the dam and extends downstream from the indigenous lands of *Paquiçamba* and *Arara da Volta Grande*, encompassing the confluence with the Bacajá River. Lastly, Area 4 encompasses the final portion of the RFZ, situated on the opposite bank of the intermediate reservoir of the BMHC.

Mapa 13: The subareas of study (Areas 1, 2, 3, and 4), determined based on the concentration of the ICESat/GLAS data.

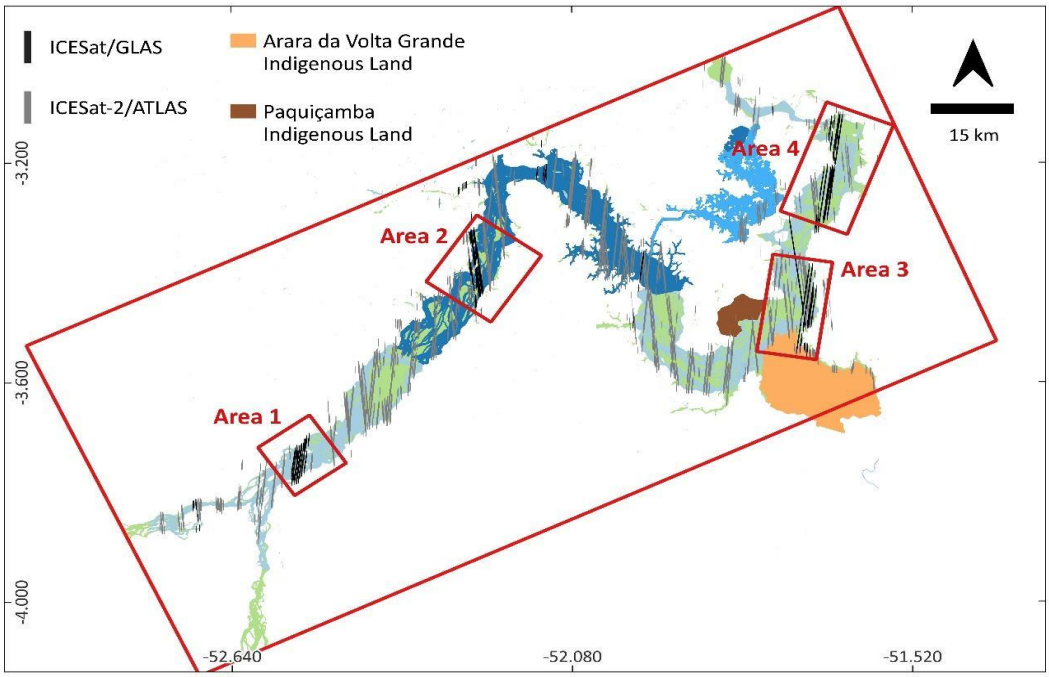

Fonte: Autoria própria

The satellite data were initially filtered using a water mask created based on the GSW data for each respective year, ensuring that only data related to the water surface were included in the analyses. After that, the altimetry data underwent an additional filtering process, this time based on yearly flood classes (No Water, Seasonal Water, and Permanent Water) for each year.

6.2.6. Statistical analysis

The Pearson correlation coefficient (R) measures the strength and direction of the linear relationship between variables, being an important tool to understand and quantify their association (for more details, please refer to Wackernagel (2003)). It was used to validate the field data against measurements obtained from the satellite altimeter.

Following this analysis, two normality tests were taken: Shapiro-Wilk and Kolmogorov-Smirnov. For both, if the p-value of the test is low (typically below 0.05) for the dataset, it suggests that the data does not come from a normal distribution (for more details, please refer to Field (2009)).

Lastly, a Kruskal-Wallis test was conducted. This is a non-parametric statistical test used to determine if there are any statiscally significant difference between the mean ranks (of the water surface height) of three or more independent groups (the surface water area groups of classes in each one of the years). A post-hoc analysis was also realized to investigate if whether the groups are equal or different from each other (for details on the calculation, please consult Field (2009) and McKillup and Dyar (2010)). The tests were repeated for each one of the 4 study areas.

The chosen significance level for the analysis (p-value) was 5%. The question to be addressed by the test is whether the water surface height (altimetry) varies over time within different flood classes (Not Water, Permanent Water and Seasonal Water). The null hypothesis (H0) for the test was "there is no variation in water surface height (altimetry) across flood classes over time," and the alternative hypothesis (H1) was "water surface height varies over time within different flood classes."

All the statistical analysis was performed using the SPSS Statistics software.

6.3. Results

6.3.1. Validation of altimetric data

The validation of altimetric data based on in situ measurements was possible only for Area 3 due to data availability (the only area with consistent in situ measurements that matched the altimetric data) (Mapa 14). Validation was more consistent in the Bacajá River because there were more stations there. Field measurement data were acquired via a legal request to the BMHC concessionaire company and were ideal for validation because they included not only elevation measurements but also orthometric height data (which is in the same datum reference as ICESat-2 measurements). While there are official monitoring stations (such as the ones maintained by ANA), consistently measuring within the VGX region, they measure only the river elevation relative to the river variation and do not provide the orthometric height relative to the MSL of the surface water.

Mapa 14: In situ stations and satellite data used for altimetry validation in Area 3, the only subarea where both datasets match.

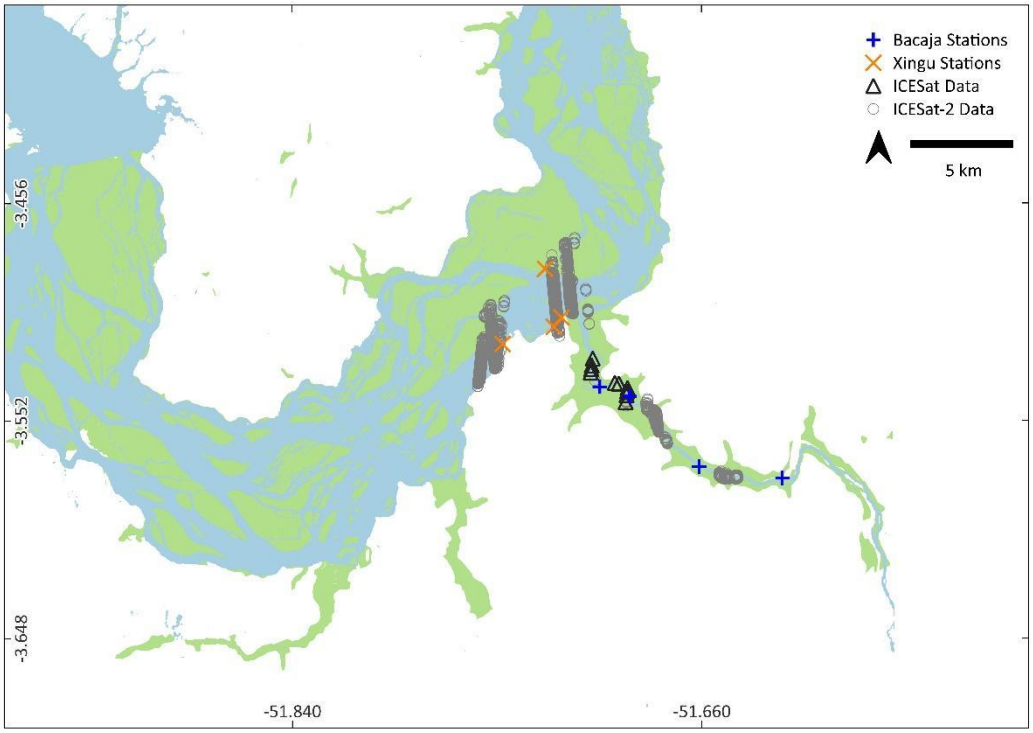

Fonte: Autoria própria

For the Bacajá River, it was possible to validate both ICESat and ICESat-2 data. However, for the Xingu River, only ICESat-2 validation was possible, as ICESat data did not match in situ stations in Area 3.

Due to discrepancies between satellite data and in situ measurements dates, resulting in data gaps, monthly averages were calculated for the periods when satellite data were available, both before and after the construction of the BMHC. These averages were then correlated with corresponding monthly averages of in situ measurements, also before and after the dam operation.

It became evident that field measurement data showed a strong correlation with altimetry data, both from ICESat and ICESat-2, indicating good data quality from both instruments compared to the measuring sites (Tabela 9). However, there was a slightly better performance of the altimeter data in the Bacajá region compared to the Xingu River. This difference may be related to the size of the Bacajá River and the proximity of satellite samples to field measurement stations, which often coincided. As the Xingu River is a much larger flow, and in situ measurements were mainly conducted on its banks or island edges, this factor may have influenced R

values. Nevertheless, the correlations are strong enough to consider satellite data reliable.

Tabela 9: Validation results between altimetry data and in situ data.

ICESat	
	R
Bacajá 3	0.99
Bacajá 4	0.99
ICESat-2	
	R
Bacajá 3	0.99
Bacajá 2	0.98
Bacajá 1	0.98
ICESAT-2	
	R
Xingu Seção 5	0.82
Xingu Seção 6	0.81
Xingu Seção 7	0.84

6.3.2. Historical Hydrological Series Analysis

Figura 29 illustrates the time series of river flow and water levels relative to station 18850000, in the Altamira Municipality, available in the database of the National Water Agency.

Figura 29: Average, Maximum and Minimum river elevation levels and river flow rates between 1972 and 2015 for the station 18850000 (in the Altamira municipality). The red boxes indicate years marked by climatic anomalies (ENSO).

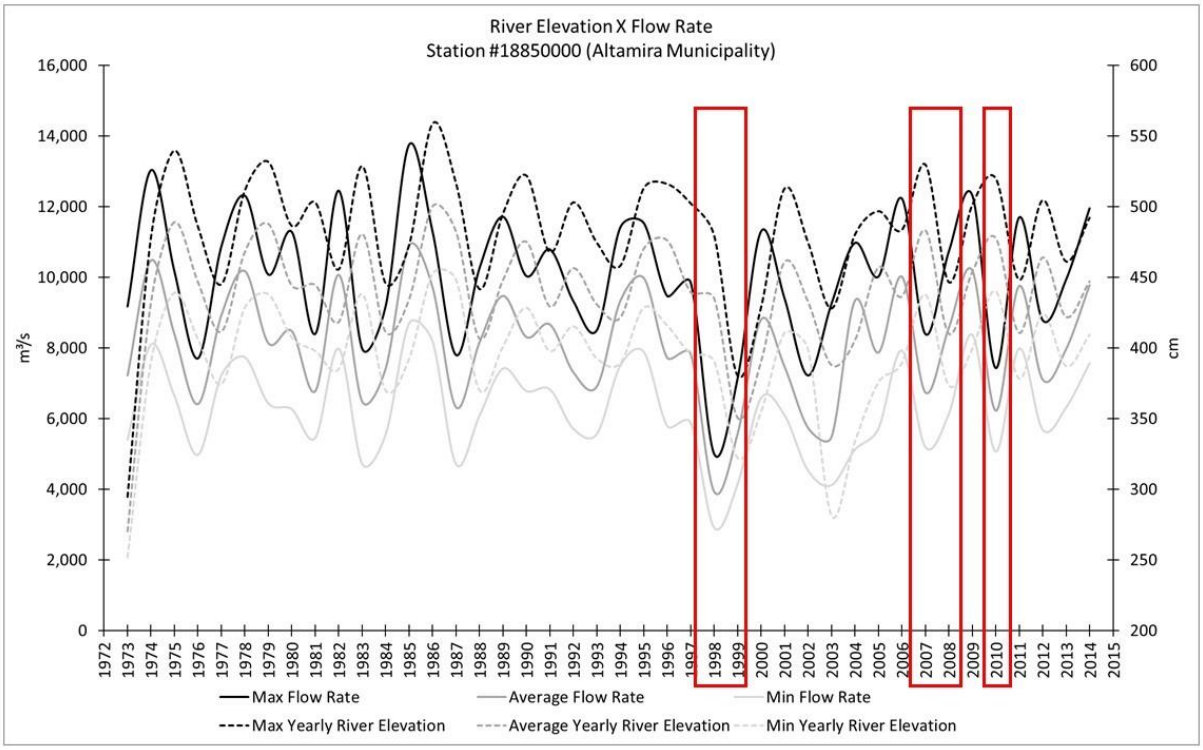

Fonte: ANA (Agência Nacional de Águas)/Autoria propria

Figuras B_1 and B_2 from the Supplementary Material (Apêndice B) present a time series of the flood pulse and the drought season from 2000 onwards, until the damming of the river.

6.3.3. Flood data and identification of seasonally flooded habitats

Yearly Surface Water Seasonality maps were also created to depict the intra-annual distribution of surface water (Figuras B_3 to B_9 in the Supplementary Material (Apêndice B)). They distinguish between ‘permanent’ and ‘seasonal’ water surfaces for each year. ‘Permanent’ water surfaces remain submerged throughout the entire year, while ‘seasonal’ water surfaces are submerged for less than 12 months annually. A summary of the information regarding the flooded surface areas shown on the map can be observed in Figura 30 (Figura B_10 from the Supplementary Material (Apêndice B) shows the same information for the study area as a whole).

Figura 30: Yearly surface water seasonality classes extension calculated for each of the subareas (a: Area 1; b: Area 2; c: Area 3 and d: Area 4) based on the pixels in the maps generated by the GSW dataset for each subarea and each year.

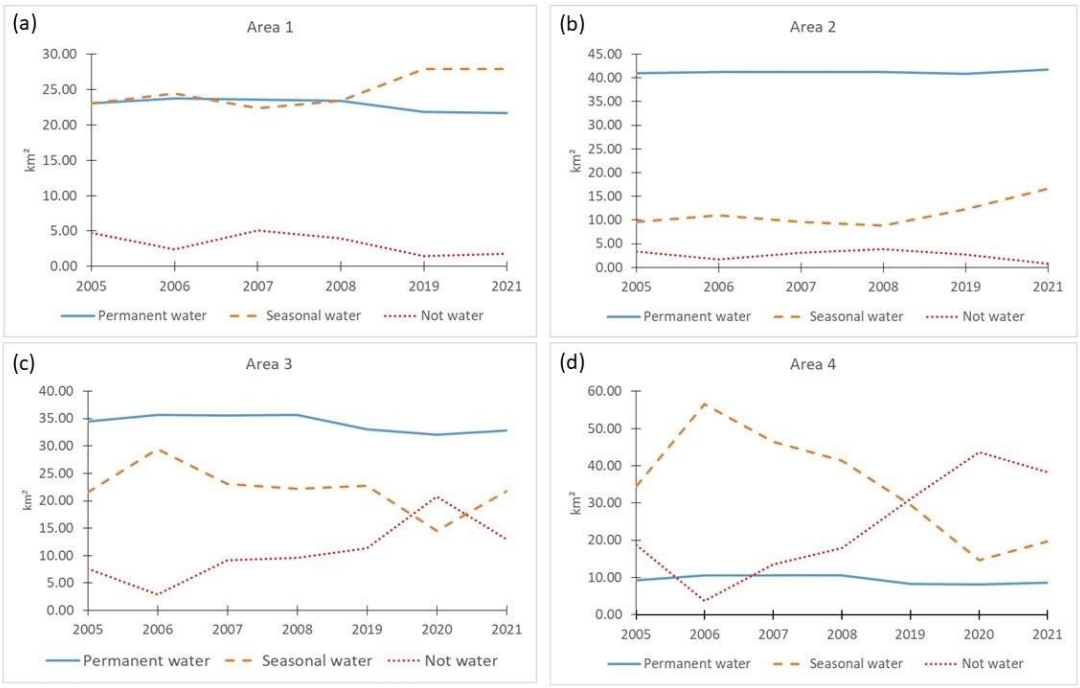

Fonte: Autoria própria

The Water Transitions map (Mapa 15) depicts changes in water from the first to the last year of observation (2021), providing temporal profiles for each pixel. These profiles detail monthly water presence or absence and account for missing observations. They pinpoint specific months/years when conditions changed. The profiles also document seasonality and potential shifts, differentiating between intra and inter-annual variability and the appearance/disappearance of water surfaces.

Mapa 15: Water transition map for (a) the whole study area, the VGX, and each subarea in detail: (b) Area 1; (c) Area 2; (d) Area 3 and (e) Area 4. These maps depict the class transitions from the first year of measurement (1984), as detected by the GSW dataset, up to 2021.

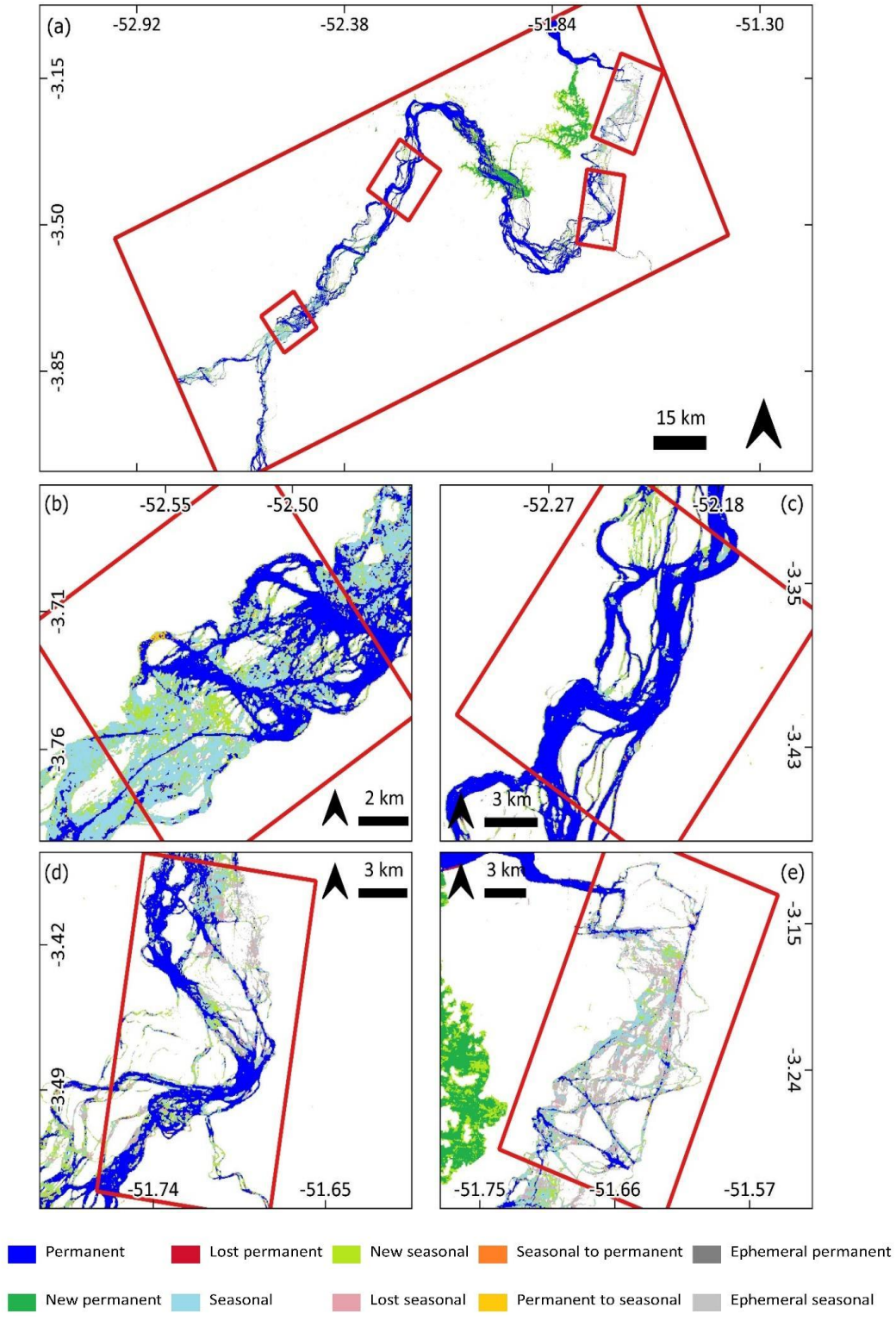

Fonte: GSW/GEE Catalog/Autoria própria

The Surface Water Occurrence Change Intensity map (Mapa 16) illustrates changes in surface water occurrence between 1984 and 2021, divided into two periods: 1984 to 1999 and 2000 to 2021. It calculates the change in water occurrence intensity from homologous pairs of months with valid observations in both periods. The map displays areas where surface water occurrence increased, decreased, or remained the same, with scores averaged to account for data distribution variations over time, ensuring a consistent measurement of change occurrence.

Mapa 16: Surface Water Occurrence Change Intensity map for (a) the whole study area, the VGX, and each subarea in detail: (b) Area 1; (c) Area 2; (d) Area 3 and (e) Area 4. It depicts changes in surface water occurrence between 1984 and 2021, divided into two periods: 1984 to 1999 and 2000 to 2021.

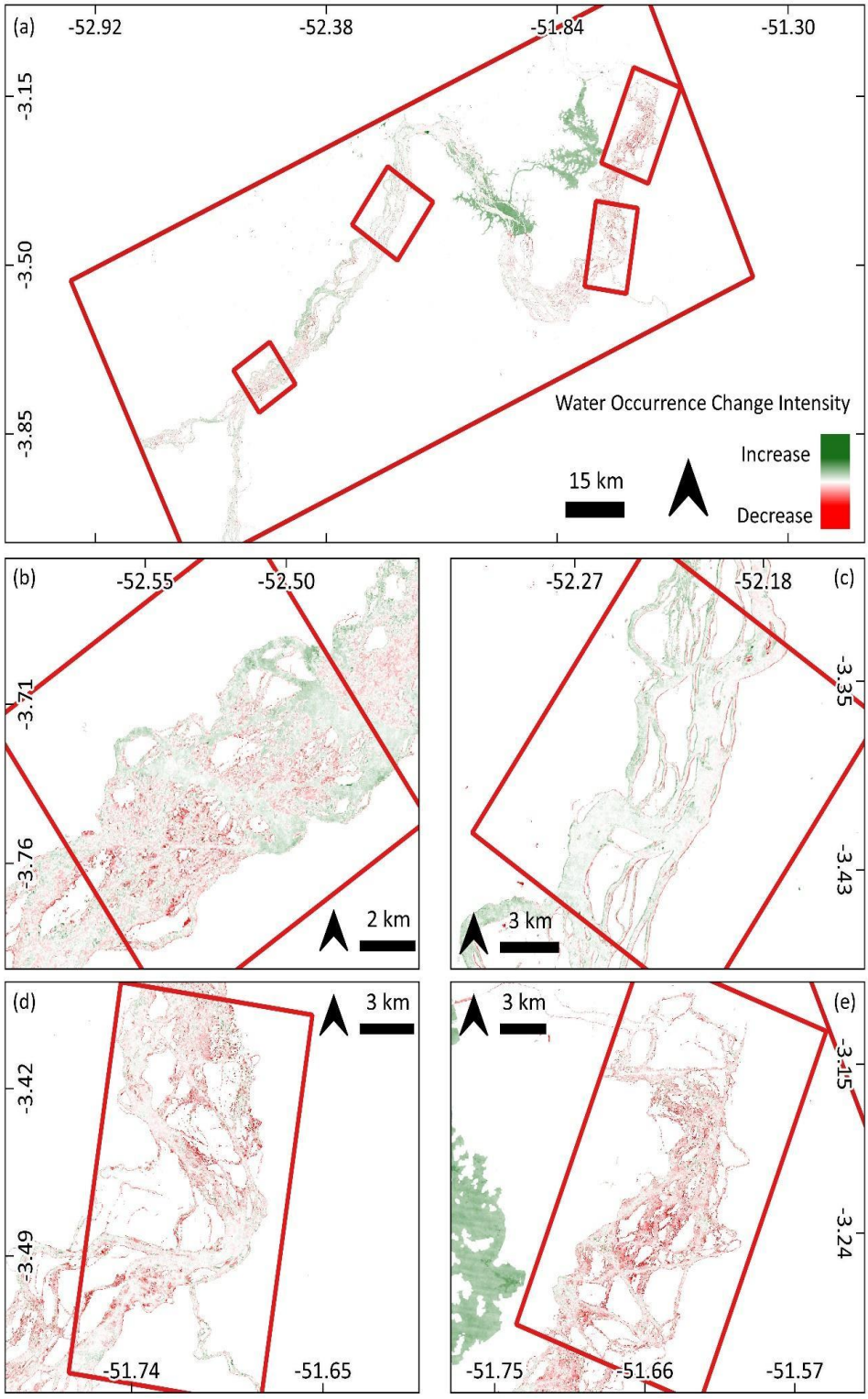

Fonte: GSW/GEE Catalog/Autoria própria

In addition to those maps, a Frequency Map was also created (Figura B_11 from Supplementary Material (Apêndice B)). It shows the surface water presence from 1984 to 2021, offering insights into overall water dynamics, including both yearly and long-term changes. Occurrence represents the frequency of water presence as a percentage of total observations, adjusted for data acquisition variations, ensuring a consistent characterization of water dynamics over time.

6.3.4. Synthetic Aperture Radar

This section presents a description from all the mosaics elaborated with the SAR images. All the maps created with these products are available in the Supplementary Material (Apêndice B).

In Figura B_12, the shades of red, light pink and pink are related to the flood period in 1993. In Figura 29, it can be observed that the average flow was relatively low when compared to the rest of the period, indicating a weak flood pulse year. In fact, the intensity (in dB) of the red shades is quite subtle, whereas the shades of blue and green, related to the dry periods of 1994 and 1996, have a strong signal, indicating a high σ0 value, revealing significant exposure of the rocky environments in the narrowed channels during the driest months.

Figura B_13 depicts the flood period of 1996, which was stored in the red band, while the dry months of 1994 and 1996 were allocated to the blue and green bands. The low intensity of the warm tones, indicating low pixel energy, contrasts with the well-defined cold tones (high σ0 values), aligning with the information provided by Figura 29: the average flow of the year 1996 does not stand out in the historical data.

For Figura B_14, the months of the flood pulse in the year 2008 are found in the green and blue bands, while the dry season (2007) is in the red band (thus, the opposite of the color scheme in Figuras B_12 and 13). Since Figura B_14 is a dual-pol HH/HV ALOS-PALSAR image (meaning it has better resolution than the JERS-1 images), it is possible to more prominently observe the flooded areas (identified by the bluish/greenish tones related to the flood months). The intensity of the reflected signal is high enough to highlight the alluvial forest along the course of the Xingu River and its tributaries (such as the Bacaja River).

In Figuras B_15 and B_16 the flood period of the year 2008 is still represented in the green and blue bands. For B_15, the dry season in the red band is also the

year of 2008, while in B_16, the drought in the red band is the year of 2009. These mosaics were elaborated aiming to identify the set of temporal composite images that best highlight the flooded forests. In Figura B_16, the reflected signal in the blue and green bands is slightly attenuated, whereas Figura B_15 areas with blue shades are modestly prominent.

Finally, in Figuras B_17 and B_18 while the flood months were stored in the green and blue bands in both images, the dry season months of the year 2009 (Figura B_17) and 2010 (Figura B_18) were stored in the red band. Although it is possible to identify light shades of blue and green in both maps, the signal becomes slightly intense in Figura B_17, allowing for a better distinction of the flooded forest for the year 2010.

Lastly, Mapa 17 represents a classification map enhancing the flooded areas for the initial decade of the 2000s, using composites of RGB images HH/HV/VV (HH in the red channel, HV in the blue channel, and VV in the green channel).

Mapa 17: A map depicting the seasonally flooded areas based on ALOS PALSAR PLR quad-pol images, aiming to highlight flooded forest areas.

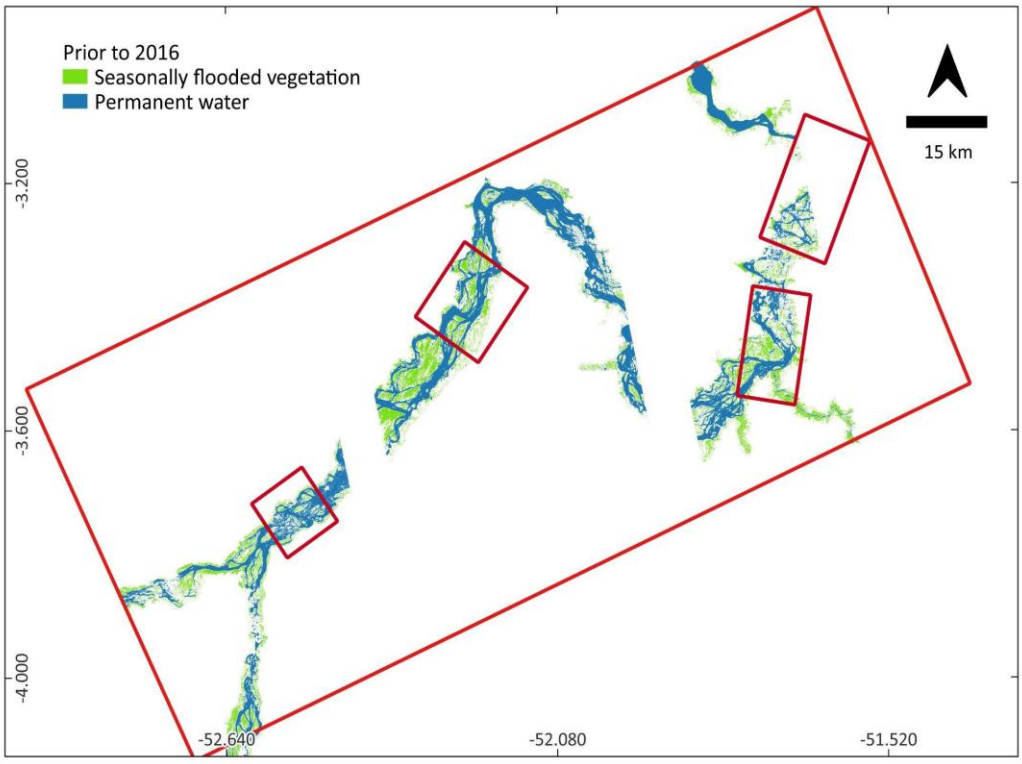

Fonte: Autoria própria

6.3.5. Altimetry Data and Statistical Analysis

Regarding the normality tests, among the entire dataset (which includes the 4 areas and the 3 water seasonality classes for each year), only the Kolmogorov-Smirnov test had $p > 0.05$ in Area 1 for the Not Water class, indicating the normality of the altimetric dataset in this configuration. All other data had $p < 0.05$ for all cases, revealing its non-gaussian distribution. Therefore, to assess potential statistically significant differences among water surface heights in different flood scenarios over the years, the Kruskal-Wallis test was employed. This is a non-parametric test, ideal for application to non-normal datasets.

The Kruskal-Wallis results for the analysis of altimetry data for Area 1 in the Not Water class revealed a significance level greater than 0.05 ($p > 0.088$), assuming the null hypothesis to be true. This indicates that there are no significant differences in water surface heights between years in different water surface classes. However, for all other cases, including the 'Not Water,' 'Permanent Water,' and 'Seasonal Water' classes in all four study areas, the p-value was less than 0.05. This supports the alternative hypothesis of the test, suggesting significant differences in water surface heights among the years and across various flooded surface classes.

Lastly, post-hoc tests were conducted for every pair of years to identify temporal differences in altimetry across all study conditions. The null hypothesis, stating that there is no variation in water surface height, was rejected when the statistical test between year pairs resulted in $p < 0.05$. Tabelas 10 to 13 presents, for each water surface class in each sector along the Xingu River, the pairs of years exhibiting differences in altimetry values.

Tabela 10: Year pairs displaying variations in water surface height within each coverage class in Area 1.

Área 1		
Not Water	Permanent Water	Seasonal water
NA	2008-2019	2019-2021
NA	2008-2007	2019-2006
NA	2008-2005	2008-2021
NA	2008-2006	2007-2021
NA	2021-2019	
NA	2021-2006	
NA	2019-2006	

Tabela 11: Year pairs displaying variations in water surface height within each coverage class in Area 2.

Area 2		
Not Water	Permanent Water	Seasonal Water
2005-2019	2007-2021	2007-2019
2021-2019	2007-2019	2007-2006
	2007-2006	2005-2021
	2005-2021	2005-2019
	2005-2019	2005-2006
	2005-2006	
	2008-2019	
	2008-2006	
	2021-2019	
	2021-2006	

Tabela 12: Year pairs displaying variations in water surface height within each coverage class in Area 3.

Area 3		
Not Water	Permanent Water	Seasonal Water
2021-2020	2019-2021	2019-2021
2021-2019	2019-2020	2019-2020
2021-2008	2019-2005	2019-2005
2020-2019	2019-2007	2019-2006
	2019-2006	2019-2008
	2019-2008	2019-2007
	2021-2020	2021-2020
	2021-2005	2021-2006
	2021-2007	2021-2008
	2021-2006	2021-2007
	2021-2008	2020-2006
	2020-2007	2020-2007
	2020-2006	
	2020-2008	

Tabela 13: Year pairs displaying variations in water surface height within each coverage class in Area 4.

Area 4		
Not Water	Permanent Water	Seasonal Water
2007-2021	2020-2019	2020-2006
2007-2019	2020-2021	2020-2021
2007-2005		2020-2007
2020-2021		2020-2019
2020-2019		2008-2019
2020-2005		2005-2019
		2006-2019
		2021-2019
		2007-2019

6.4. Discussion

In the implementation studies for the BMHC, historical time series data prior to its construction were overlooked. The development criteria for hydrograms A and B are based on circumstantial assumptions and singular observations from a single atypical year (2008), when an ENOS was active (Palmquist, 2023). In essence, there was a lack of comparative analysis between pre-construction conditions and the potential enterprise impacts. The findings from these studies are isolated, hindering a comprehensive assessment of hydrogram operational impacts and its overall feasibility. Both Environmental Impact Assessment (EIA) studies and impact monitoring, conducted by the BMHC concessionaire company, lack comparisons with typical time series data. A thorough evaluation of these impacts can only be achieved through historical data comparison. Simplifying this intricate system to a single numerical value—a single-year flow rate—as the main justification for the hydrograms, oversimplifies a highly complex system (MPF, 2023).

Multitemporal images and information, as presented in this study, play a crucial role in revealing the dynamic conditions of these environments and identifying the drivers of change that have the potential to impact flooded habitats, their functions, and services. Additionally, multiple datasets provide supplementary information, thereby enhancing our capacity to comprehend the seasonally flooded environments

and its processes. While there are available long time series, such as the GSW data since 1985 and the ANA hydrological historical series data dating back to the 1970s, the altimeter data used for comparison with the water surface flooded areas are only available from 2005 to 2009 for the pre BMHC period. Therefore, this study sheds light on long-term flood dynamics, however, with a primary focus on the period covered by the altimetry data.

6.4.1. Historical Hydrological Series Analysis

The analysis of the graphs depicting annual maximum, mean, and minimum flow rates (Figura 28) for the Altamira station reveals well-defined patterns of flood and dry pulses, with the mean hovering around 20,000 m^3/s at the peak of the flood. The minima are slightly higher than 15,000 m^3/s (nearly twice the maximum value proposed for the consensus hydrogram B which is bi-annual). Alongside the river flow rate curves, there are corresponding elevations for the maximum, mean, and minimum values. The average elevations are around 700 cm, with the minimum mean elevation slightly exceeding 600 cm.

In Figura 29, average, maximum and minimum river elevations flow rates on an annual basis are shown. The curves in the graphs are nearly perfectly superimposed. The notable years for the highest flow rates and maximum elevations are 1985, 2006, and 2010. Concerning the minimum means, particular emphasis should be placed on the year 1998 (the lowest minimum in the historical record, coinciding with a strong El Niño event). The second noteworthy event for the lowest minimum mean is 2003 and 2007.

Figuras B_1 and B_2 in the Supplementary Material (Apêndice B) depict monthly elevation-flow rate curves for the flood and dry seasons over a 15-year period. September and October emerge as the driest months with the shallowest flood gradients. During the flood season, there is an overlap in the curves.

These data are crucial for detecting extremes before the river damming. By identifying the months in which elevations reached their maximum and minimum values over the years, it becomes possible to correlate this information with extreme periods without the influence of dam operations. This enhances the validation of the flooded area with greater confidence and accuracy.

6.4.2. Flood data and identification of seasonally flooded habitats

In general, across the entire study area and for the years analyzed, changes in surface water coverage correspond to flow rate patterns in the pre-BMHC years. Since seasonal waters are highly sensitive to large variations between dry and flood extremes over the years, their presence over rapids and extensive rocky boulders and channels serves as a valuable indicator for tracking the dynamics of river pulses and drought.

Two distinct phenomena affecting sensitive flooded areas (seasonal waters and not-water) are prominent, both between the years 2005 and 2008 (Figuras B_3 to B_6 on the Supplementary Material (Apêndice B)) and between the pre-and post-BMHC periods (as observed in comparing Figuras B_3 to B_6 with Figuras B_7 to B_9 in the Supplementary Material (Apêndice B) and in the chart on Figura 30). Between 2005 and 2009, an active El Niño-Southern Oscillation (ENSO) event was observed. ENSO is a cyclic climate pattern that influences atmospheric and oceanic temperatures in the Pacific Ocean (NOAA, 2019). During the years 2005 to 2009, this phenomenon was in its warming phase (known as El Niño) (NOAA, 2023), which in the Brazilian Amazon results in reduced rainfall and, consequently, more intense dry periods (Jiménez-Muñoz *et al.*, 2016). The increase in not-water and seasonal water areas during this period can be attributed to this natural phenomenon.

Area 1 serves as the control area, in which significant changes are not expected to occur as it is not part of the impact area of the BMHC operations (Mapa 13). Regions classified as not-water remain relatively stable over time, which can be attributed to climatic factors such as dry or wet years influenced by rainfall patterns or climatic events such as El Niño (Figura 30a). In Area 1, it is noteworthy that areas covered by seasonal waters are increasing as permanent water areas are decreasing (Figura 30a), especially in the period following the dam construction (Mapa 15b). It is important to note that this variation is not related to the hydroelectric complex, as previous studies indicate that climate change could significantly affect water availability in the Xingu basin due to changes in precipitation patterns (Camargo, 2019). The Xingu basin, including its headwaters, has experienced a reduction in precipitation due to deforestation, which, in turn, impacts the climatic systems influencing South America. Historical precipitation

loss has already resulted in a 20% reduction in the flow of the Xingu River (Camargo, 2019). Therefore, it is essential to investigate the interannual variability of the flow and the effects of deforestation and climate change in the Xingu basin.

Area 2 is located upstream of the city of Altamira, within the Main Reservoir of the Xingu River (Mapa 13). Consequently, it has been subject to inundation since the river flow was diverted to form the reservoirs in 2015. Therefore, significant changes in permanent water areas are not expected, as indicated by Figura 30b, Mapa 15c and Mapa 16c. Between the pre and post BMHC construction and operation periods, we observed an increase in seasonal water areas accompanied by a proportional reduction in areas classified as 'non-water' (Figura 30b) This phenomenon is expected in reservoir areas since, with a larger water surface due to the reservoir's creation, more areas become subject to natural river level fluctuations, while not-water areas tend to decrease.

Area 3 is situated within the RFZ, where the reduction in the Xingu River's flow is currently happening (Mapa 13). Between the pre and post BMHC periods, a subtle decrease in the area covered by permanent water is observed (Figura 30c), which is in line with expectations in this region of reduced flow. Furthermore, there is a notable decrease in the area occupied by seasonal waters, accompanied by a proportional increase in non-water-covered areas, which is also consistent with the anticipated outcomes for this reduced-flow region (Mapa 15d).

In Area 4, due to its unique geomorphology, where the main river flow splits into several smaller channels, creating a complex and intricate pattern, the presence of permanent water is naturally limited compared to other areas (Mapa 15). The primary river channel in this region is notably narrow (Figura B_11e from Supplementary Material (Apêndice B)). It is characteristic of this region that the area covered by seasonal waters is significantly larger than the area covered by permanent waters (Figura 30d and Mapa 15e). Among all the study areas, this one is the most sensitive to changes (Mapa 16e). The drastic reduction in the flow of the Xingu River in this region results in a considerable decrease in the area occupied by seasonal waters, accompanied by a proportional increase in areas classified as not-water (Figura 30d). In other words, there is a loss of areas that used to be seasonally inundated and now remain permanently exposed (Mapa 15e).

These changes reflect an annual pattern of surface water seasonality over a historical time series encompassing both pre and pos BMHC periods. This pattern

had been previously identified by Affonso *et al.* (2023a), who conducted a comparative analysis of land use and land change cover change within a 17-year historical dataset, spanning from 2000 to 2017. In this study, specific attention was given to the year 2016 (immediately following the dam construction, notable for being exceptionally dry, referred to by the traditional people of Xingu as "The Year of the End of the World") (Pezzuti *et al.*, 2018) and the first year of the power plant operation, when it was not yet fully operational. In this study, it was observed the transformation of areas from permanent water to seasonal water and from seasonal water to non-water after 2015, resulting in the conversion of river sections into non-water areas permanently exposing rocks and reducing periodically inundated areas.

The cumulative impact on the reduced-flow section, represented by Areas 3 and 4, is illustrated in the map depicting absolute changes in the extent of inundated areas (Mapa 16d and e), revealing areas where the water presence increased or decreased. While in Area 1, occasional changes resulting from climate changes can be detected (Mapa 16b), with some areas showing a reduction in inundation frequency balanced by others where this frequency increased (Figura B_11b), and in Area 2, where the trend of increased inundation frequency becomes more evident (Mapa 16c and B_11c), it is in Areas 3 and 4 that a reduction in inundation frequency is emphasized (Figura B_11d and e). The transition map of inundated areas in Areas 3 and 4 (Mapa 15d and e), with a particular emphasis on Area 4 (Mapa 15), clearly highlights the loss of permanently inundated areas, the transformation of seasonal areas into non-aquatic ones, and the reduction of permanent water areas that have become seasonal.

6.4.3. Synthetic Aperture Radar

Affonso *et al.* (2023b, manuscript submitted for publication) highlight the presence of specific vegetation types, such as the *sarobal* and *igapó*, covering typical environments of the VGX area, including rocky environments (*pedrais*), beaches, islands, river banks and its edges. This vegetation can become partially submerged, especially during the peak of the flood season. However, some portions of it remain partially exposed despite being inundated, with the canopy covering the water, preventing optical sensors from detecting the flooding. This underscores the importance of identifying flooded areas during the high-water season using SAR imagery, particularly during periods when river flow responds to its natural

behavior. While there are products derived from optical sensors capable of mapping alluvial vegetation, observational records of flooding under such vegetation within the fluvial dynamics are limited in the literature for the study area.

In Mapa 17 and the maps in Figuras B_12 to B_18, it is relatively easy to visually identify the flooded vegetation areas during the flood months and the exposed areas during the dry season around the Xingu River in the VGX, including the RFZ and some of its tributaries. When mapping flooded forest environments through SAR, we seek to delineate, classify, and display the boundaries of these ecosystems and calculate their distribution in the landscape. In the literature, several studies have utilized stacks and false-color compositions of time series, with different polarizations and polarization ratios, to highlight flooded environments in forests (examples in Tiner, 2015).

ALOS PALSAR images confirm the systematic inundation of the *igapó* and *sarobal*, particularly on the islands, in the years analyzed before the BMHC construction. Although the permanent water surface remains relatively constant, there is a reduction in seasonally influenced waters due to the flood pulse and a significant increase in not-water areas after the BMHC construction and operation began. Therefore, if there is a reduction in seasonal water and an increase in not-water areas, it raises questions about whether many seasonally flooded vegetation areas are still being inundated, considering the relationship between flow rates and water levels, as depicted in Figura 29. Hence, an evaluation of water surface height becomes crucial: if several areas are no longer inundated, and water flow is distributed so differently from the natural pulse, when an area is flooded, is it flooded sufficiently?

6.4.4. Altimetry Data and Statistical Analysis

The Kruskal-Wallis analysis was conducted to test the hypothesis of surface water elevation variation influenced by the historical time series (i.e., in the pre and post BMHC years) and the extent of the classes of water surfaces. As observed previously, in this analysis, we confirmed that the altimetry values indeed vary in the time series. However, against expectations, the variations within the annual time series not only occur between year pairs before and after the construction of the BMHC but also among year pairs before construction and year pairs after construction.

There was an expectation that the increase in not-water areas, especially in the RFZ, and the transformation of permanent water into seasonal waters would be accompanied by a proportional reduction in water surface elevation. In other words, with less available water, it was expected that the areas still covered by water would appear "shallower", or that the water would no longer reach the height observed before the river damming. This behavior aligns with the assumption that, following the construction of the BMHC, it would be possible to identify a pattern in the water surface dynamic compared to the pre-BMHC period when no altimetric variations were expected. However, this is not reflected in Tabelas 10, 11, 12 and 13.

Except for Area 1, which is the control area, and, as expected, did not revealed any differences in the altimetry data in the time series, since it is not influenced by the hydroelectric complex, there was no conclusive evidence to support the idea that the yearly variations in water surface height are consistently linked to the yearly fluctuations in the extent of the flooded area resulting from the damming on the Xingu River, or that they are exclusively related to the BMHC. However, this is not an unprecedented finding for a river in the Amazon basin, as Frappart *et al.* (2005), when using altimetry to assess spatiotemporal variations in water volume in the floodplain of the Negro River basin, also did not find a relationship between water volume and flooded area.

This finding might be a result of multiple methodological limitations. For instance, difficulties in obtaining altimetry data on the same frequency as flood surface extension measurements or the much higher frequency of data collected by ICESat-2 when compared to ICESat-1. Even though for some situations, monthly flood data were available, especially for the pre BMHC years, this was not always the case (e.g., issues with Landsat satellite observations or acquisition difficulties in some months with extensive cloud cover) (as detected by Busker *et al.*, 2019; Luo et al., 2019 and Xu *et al.*, 2021). As for ICESat and ICESat-2, the time sampling is too coarse (180 days and 91 days, respectively) to observe high-frequency continuous water level variations, as observed by Baghdadi *et al.* (2011) and Chen *et al.* (2022). And while validation indicates that altimeters were capable of measuring seasonal surface water variation, the temporal resolution does not always allow for the recording of annual flood pulses and dry periods within the same year, potentially resulting in the omission of flood pulses by the altimeters.

To mitigate the limitations of the method used in this work, it is necessary to incorporate intra-annual observations, a very common practice in research using altimetry data (as in Frappart *et al.*, 2005; Baghdadi *et al.*, 2011; Busker *et al.*, 2019; Luo et al., 2019; Xu *et al.*, 2021; Chen *et al.*, 2022 and Narin and Abdikan, 2023). The challenge lies in establishing a consistent database of measurements taken at appropriate time spans throughout the VGX. This limitation makes the results comparable to snapshots in time, capturing trends in how the VGX behaved pre BMHC construction and its current behavior, and not a continuous evolution in the historical series, mainly regarding the seasonal flood pulse. Nonetheless, this is an improvement over the effort made by the BMHC concessionaire company in the EIA studies that suggested insufficient values for the river flow after its damming, a suggestion based on a three-month analysis in 2008 (an atypical year) (MPF, 2023). There was limited sampling effort and empirical support, resulting in modeling scenarios that were unfeasible in justifying the proposed hydrograms, which caused environmental damage, some even irreversible (Jiang et al., 2018; Pezzuti et al., 2018; Zuanon et al., 2019; Affonso et al., 2023a).

Although it was not possible to infer that the water surface height corresponds to the flood extent, or that the BMHC is the exclusive influence in the water surface height, it was indeed possible to demonstrate that there is an alteration in the flood dynamics over the years concerning water surface height. As outlined in the preceding section, these alterations could be attributed not solely to the anthropogenic impact of the hydroelectric complex but also to years with climatic anomalies and even the diversion of water from the river for other purposes, such as agriculture.

Another point of interest is the water level height under the seasonally flooded vegetation. It is very important to the management of the VGX this data to be monitored, particularly in the case of flooded vegetation, where insufficient water column height can compromise the life cycle of fauna and flora. To achieve a finer analysis, it is necessary to correlate, with more detailed studies regarding data acquisition consistency, the flooded area with water surface height in the flooded forest, using sophisticated image processing techniques, such as interferometric SAR (InSAR), as sugested by Alsdorf; Rodríguez and Lettenmaier (2007).

While annual data may not be the most appropriate time interval for observing changes in water surface heights in relation to flood extension, the necessity for

greater consistency in data acquisition is critical. Whether obtained from satellites or in-situ measurements, this consistency is crucial to facilitate the comparison of intra-annual variations in the flood pulse, posing a significant challenge in research and monitoring. Access to gauge data is often restricted due to legal or institutional constraints, rendering them unavailable for scientific purposes. In remote and less developed regions, gauge data are typically sparser, challenging to access, or even entirely absent (Alsdorf; Rodríguez; Lettenmaier, 2007; Busker *et al.*, 2019; Chen *et al.*, 2022).

Specifically in the Amazon area, the existing gauges can only estimate flow in major river channels, providing no information on the dynamics in flooded environments (Alsdorf; Rodríguez; Lettenmaier, 2007). Addressing these challenges is essential for a comprehensive understanding of the dynamics of the flood pulse, requiring innovative approaches to data acquisition in regions where traditional gauge data are scarce or inaccessible.

6.5. Conclusion

In this study, multiple remote sensing datasets were employed, accompanied by in situ measurements, to establish a comprehensive observational time series dataset focused on the flood dynamics of the seasonally inundated habitats within the VGX area, located in the southeastern Amazon Forest of Pará, Brazil.

The incorporation of time series remote sensing products, as utilized in this research, provides valuable insights into the dynamic conditions of seasonal flood environments. This approach aids in the identification of the drivers of change that have the potential to impact these ecosystems, alongside their associated functions and services. Notably, there is a gap in the existing literature concerning the observation of inundation patterns within the study area using radar satellite products, especially regarding to an investigation that encompasses the analysis of water surface elevation through altimetry, the extension of water surface coverage considering the seasonality of the flood pulse, and L-band imagery products capable to detect water under the vegetation. This study makes a significant contribution to addressing this knowledge gap.

While a direct correlation between water surface height, the extent of different flooding classes and the operation of the BMHC could not be established by this study, it was able to successfully demonstrate that alterations in the water surface

height of the Xingu River within the VGX area, particularly in the RFZ, are indeed occuring. These changes are further underscored by a comparison of the present river flow with the natural conditions of the flood pulse.

Funding: This study was supported by the Coordination for the Improvement of Higher Education

Personnel (CAPES)—Financing Code 001. AAA is a research fellow of the Coordination for the Higher Education Personnel (CAPES, grant #8882.328088/2019-01). CHG is funded by the Brazil's National Council of Scientific and Technological Development (CNPq, grant # 311209/2021-1).

Competing Interests: The authors declare no conflict of interest

Data Availability: Hydrological Time Series: AGÊNCIA NACIONAL DE ÁGUAS – ANA. Hidroweb: Sistemas de informações hidrológicas. Disponível em: <http://hidroweb.ana.gov.br/>.

Flood data: Jean-Francois Pekel, Andrew Cottam, Noel Gorelick, Alan S. Belward, High-resolution mapping of global surface water and its long-term changes. Nature 540, 418-422 (2016). (doi:10.1038/nature20584). Dataset available at https://developers.google.com/earth-engine/datasets/catalog/JRC_GSW1_4_GlobalSurfaceWater#citations

Synthetic Aperture Data: JERS-1, JAXA 1993, 1994, 1996. Retrieved from ASF DAAC [15 Jan 2020].

©JAXA/METI ALOS PALSAR RTC 2007, 2008, 2009, 2010. Accessed through ASF DAAC, https://asf.alaska.edu 26 April 2021

ICESat/GLAS: Zwally, H. J., R. Schutz, C. Bentley, J. Bufton, T. Herring, J. Minster, J. Spinhirne, and R. Thomas. 2014. GLAS/ICESat L1B Global Elevation Data, Version 34. Tracks 10, 17, 144, 263, 270, 1126, 1133, and 1252. Boulder, Colorado USA. NASA National Snow and Ice Data Center Distributed Active Archive Center. doi: http://dx.doi.org/10.5067/ICESAT/GLAS/DATA126. 20 July 2023.

ICESat-2/ATLAS: Jasinski, M. F., J. D. Stoll, D. Hancock, J. Robbins, J. Nattala, J. Morison, B. M. Jones, M. E. Ondrusek, T. M. Pavelsky, C. Parrish, and the ICESat-2 Science Team. 2020. *ATLAS/ICESat-2 L3A Inland Water Surface Height, Version 5*. Tracks 117, 368, 429, 559, 620, 871, 1062, 1313, and 1374. Boulder, Colorado USA. NASA National Snow and Ice Data Center Distributed

Active Archive Center. doi: https://doi.org/10.5067/ATLAS/ATL13.005. 20 July 2023.

In Situ Data from Bacajá and Xingu Stations: Property of Norte Energia. Accessed through legal action

Declaration of Generative AI and AI-assisted technologies in the writing process: During the preparation of this work the author(s) used ChatGPT 3.5 and Google Bard in order to improve readability and language and set the reference list in the APA style. After using this tool/service, the author(s) reviewed and edited the content as needed and take(s) full responsibility for the content of the publication.

7. CONCLUSÕES

Esta pesquisa apresenta três capítulos, cada um abordando uma perspectiva diferente da VGX e seus desafios ambientais. O primeiro capítulo utilizou técnicas de sensoriamento remoto para analisar as mudanças na cobertura do solo na região entre 2000 e 2017. Ficou evidente que as principais mudanças ocorreram devido à conversão de áreas florestais em áreas de agropecuária e à transformação de áreas florestais/agropecuárias em áreas fluviais, e áreas submersas em áreas alagáveis, resultando em exposição de pedral. Essas mudanças foram diretamente associadas à construção do reservatório e represa do CHBM. O capítulo destaca a importância das ferramentas de sensoriamento remoto para monitorar essas mudanças e enfatiza a necessidade de combinar diferentes técnicas de classificação. Identifica também a sensibilidade dos pedrais, ressaltando como os habitats alagáveis necessitam de atenção e monitoramento constante.

O segundo capítulo introduziu uma abordagem inovadora, empregando modelagem 3D para caracterizar as áreas sazonalmente alagávis na VGX, a partir da necessidade de monitoramento e caracterização destes ambientes identificada no capítulo anterior. Utilizando imagens coletadas por ARP e técnicas de SfM-MVS, foram gerados modelos 3D de alta resolução, ortofotos e modelos digitais de superfície. Esta foi uma abordagem inovadora e altamente distintiva dentro do contexto de pesquisas na região amazônica, proporcionando uma modelagem única e sofisticada para a área de estudo. Os modelos proporcionaram uma visão detalhada dos habitats inundados da VGX, proporcionando a disponibilização desses modelos ao público em geral, uma vez que é essencial a disseminação de informações e a preservação desses ambientes únicos para a sociedade, governos e tomadores de decisão, principalmente no contexto de conflito em que a região se encontra.

O terceiro capítulo concentrou-se nos impactos hidrológicos do CHBM na VGX, com foco na extensão das áreas alagáveis e elevação da superfície da água do rio Xingu. Embora não tenha sido estabelecida uma correlação direta entre a elevação da água, a extensão das áreas alagadas e o CHBM,, o estudo demonstrou que as alterações na elevação da água vem ocorrendo ao longo do tempo, especialmente no TVR, e que demais agentes vem afetando as áreas alagáveis e a hidrodinâmica da VGX além do complex hidrelétrico, como fenomenos climáticos (como ENSO)

e uso da água por atividades agrícolas. Isso ressalta a importância de monitorar e compreender os impactos antropogênicos em ambientes frágeis e ecologicamente significativos, destacando a necessidade de estratégias de gestão sustentável, algo que não tem sido respeitado na VGX.

Destacam-se as principais contribuições originais desta pesquisa para o campo de estudo: (1) a combinação de sensoriamento remoto, modelagem 3D e medições hidrológicas, que proporcionaram uma visão abrangente e multifacetada da VGX, permitindo uma análise mais completa das mudanças ocorridas. (2) a disponibilização de modelos e dados em plataformas online, o que promove a colaboração e o acesso aberto, facilitando o compartilhamento do conhecimentos e ferramentas de manejo.

Para pesquisas futuras, recomenda-se a expansão das técnicas de sensoriamento utilizadas, como o uso de mais satélites aliados à outros tipos de sensores, como LiDAR e Laser Scanner Terrestre, bem como o aprimoramento das metodologias. O processamento de produtos de sensores remotos é complexo, demorado e requer mão de obra altamente especializada. O refinamento e simplificação de métodos e técnicas de investigação em sensoriamento remoto permite um monitoramento mais detalhado das mudanças na VGX ao longo do tempo. Também sugere-se esforços para conferir à VGX o status de Área de Patrimônio Natural ou Paisagem Cultural, a fim de proteger elementos do seu ambiente que não tenham sido afetados pela intervenção humana. Em última análise, procurou-se oferecer uma base sólida para futuras investigações sobre a VGX e seus valiosos ecossistemas sazonalmente alagados na Amazônia brasileira.

REFERÊNCIAS

ADIS, J. *Programa mínimo para análises de ecossistemas: antrópodos terrestres em florestas inundáveis da Amazônia Central*. Manaus, 1977. 2, p. 223-229. Adis, 1977

AFFONSO, A. A. *et al.* A Comparison between Supervised Classification Methods: Study Case on Land Cover Change Detection Caused by a Hydroelectric Complex Installation in the Brazilian Amazon. *Sustainability*, v. 15, n. 2, p. 1309, 2023a. Disponível em: https://doi.org/10.3390/su15021309. Affonso *et al.*, 2023a

AFFONSO, A. A. *et al.*3D modeling as a conservation tool to characterize endangered seasonally flooded ecosystems in the Volta Grande do Xingu, Amazon Forest, Pará, Brazil. *Manuscrito submetido para publicação*, 2023b. Affonso *et al.*, 2023b

AFFONSO, A. A. *et al.* Tracking Land Use and Land Cover Changes in the Volta Grande Do Xingu (Pará-Brazil) between 2000 and 2017 through Three Pixel-Based Classification Methods. In: Proceedings of the IGARSS 2022—2022 IEEE International Geoscience and Remote Sensing Symposium, Kuala Lumpur, Malaysia, 17–22 July 2022; pp. 5630–5633. Disponível em: https://doi.org/10.1109/igarss46834.2022.9884422. Affonso *et al.*, 2022

AIDA - Interamerican Association for Environmental Defense. *IACHR Opens Case against Brazil for Human Rights Violations Related to Belo Monte Dam*. Interamerican Association for Environmental Defense (AIDA), 2016. Disponível em: https://aida-americas.org/en/press/iachr-opens-case-against-brazil-human-rights-violations-related-belo-monte-dam. Acesso em: 11/2022. AIDA, 2016

ALBUQUERQUE, R. W. *et al. A protocol for canopy cover monitoring on forest restoration projects using low-cost drones*. *Open Geosciences*, v. 14, n. 1, p. 921-929, 2022. Disponível em: https://doi.org/10.1515/geo-2022-0406. Acesso em: 08/2023. Albuquerque *et al.*, 2022

ALMEIDA, R. M. *et al.* Hydropeaking operations of two run-of-river mega-dams alter downstream hydrology of the largest Amazon tributary. *Frontiers in Environmental Science*, v. 8, 2020. Disponível em: https://doi.org/10.3389/fenvs.2020.00120. Almeida *et al.*, 2020

ANAC - AGÊNCIA NACIONAL DE AVIAÇÃO CIVIL. Orientações para usuários de drones. 2017. Disponível em: https://www.gov.br/anac/pt-br/assuntos/drones/orientacoes_para_usuarios.pdf. Acesso em: 09/2023. ANAC, 2017

ALSDORF, D. E.; RODRÍGUEZ, E.; LETTENMAIER, D. P. Measuring surface water from space. Reviews of Geophysics, v. 45, n. 2, 2007. DOI: 10.1029/2006rg000197. Alsdorf; Rodríguez; Lettenmaier, 2007

AMAZON WATCH. *Ilo Says Brazil Violated Convention 169 in Belo Monte Case*. Banktrack, 2012. Disponível em: https://www.banktrack.org/news/ilo_says_brazil_violated_convention_169_in_belo_monte_case. Acesso em: 02/2023. Amazon Watch, 2012

AN, K.; POWE, N. A. Enhancing ‘Boundary Work' through the Use of Virtual Reality: Exploring the Potential within Landscape and Visual Impact Assessment. *Journal of Environmental Policy & Planning*, v. 17, n. 5, p. 673–690, 2015. Disponível em: https://doi.org/10.1080/1523908x.2015.1012757. An & Powe, 2015

ANDERSON, E. P. *et al.* Fragmentation of Andes-to-Amazon Connectivity by Hydropower Dams. *Sci. Adv.*, v. 4, 2018. https://doi.org/10.1126/sciadv.aao1642. Anderson *et al.*, 2018

ANDERSON, K.; GASTON, K. J. Lightweight Unmanned Aerial Vehicles Will Revolutionize Spatial Ecology. *Frontiers in Ecology and the Environment*, v. 11, n. 3, p. 138–146, 2013. Disponível em: https://doi.org/10.1890/120150. Anderson; Gaston, 2013

ANTUNES, C. No License Renewal for Belo Monte Unless Standards Improve, Says Ibama Chief. *SUMAÚMA*, 2023. Disponível em: https://sumauma.com/en/ruina-belo-monte-enigma-foz-amazonas-novo-presidente-ibama/. Acesso em: 05/2023. Antunes, 2023

ARAÚJO, K. R. *et al. Carbon dioxide concentrations and emission in the newly constructed Belo Monte Hydropower Complex in the Xingu River, Amazonia. Biogeosciences*, v. 16, n. 18, 2019. DOI: 10.5194/bg-16-3527-2019. Araújo *et al.*, 2019

ARCHARD, F. *et al.* Determination of deforestation rates of the world's humid tropical forests. *Science*, v. 297, n. 5583, p. 999-1002, 2002. https://doi.org/10.1126/science.1070656. Archard *et al.*, 2002

ARCHER, A. W. Review of Amazonian depositional systems. *Spec. Publs int. Ass. Sediment*, v. 35, pp. 17-39, 2005. Archer, 2005

ARIAS, M. E. *et al.* Impacts of climate change and deforestation on hydropower planning in the Brazilian Amazon. *Nat. Sustain.*, v. 3, p. 430–436, 2020. https://doi.org/10.1038/s41893-020-0492-y. Arias *et al.*, 2020

ARNESSEN, A. S. *et al.* Monitoring flood extent in the lower Amazon River floodplain using Alos/PALSAR SCANSAR images. *Remote Sensing of Environment*, v. 130, p. 51–61, 2013. https://doi.org/10.1016/j.rse.2012.10.035. Arnessen *et al.*, 2013

ASF - Alaska Satellite Facility. ALOS PALSAR – About. [S.d.a]. Disponível em: https://asf.alaska.edu/data-sets/sar-data-sets/alos-palsar/alos-palsar-about/. Acesso em: 05/2020. ASF, [s.d.a]

ASF (Alaska Satellite Facility). How to View Radiometrically Terrain-Corrected (RTC) Images in QGIS. [S.d.b]. Disponível em: https://asf.alaska.edu/how-to/data-recipes/how-to-view-radiometrically-terrain-corrected-rtc-images-in-qgis/. Acesso em: 07/2020. ASF, [s.d.b]

ASNER, G. P. Cloud cover in Landsat observations of the Brazilian Amazon. *Int. J. Remote Sens.*, v. 22, p. 3855–3862, 2001. https://doi.org/10.1080/01431160010006926. Asner, 2001

ASSAHIRA, C. A *relação entre a usina hidroelétrica de Balbina e a morte de árvores de Macrolobium acaciifolium Benth. (Fabaceae) nas florestas alagáveis a jusante do Rio Uatumã, Amazônia Central*. Dissertação (Mestrado) - INPA. Manaus: INPA, 2014. Assahira, 2014

ASSAHIRA, C. *et al.* Tree mortality of a flood-adapted species in response to hydrographic changes caused by an Amazonian River Dam. *Forest Ecology and Management*, v. 396, p. 113–123, 2017. Disponível em: https://doi.org/10.1016/j.foreco.2017.04.016. Assahira *et al.*, 2017

ATHAYDE, S. *et al.* Improving Policies and Instruments to Address Cumulative Impacts of Small Hydropower in the Amazon. *Energy Policy*, v. 132, p. 265–271, 2019. https://doi.org/10.1016/j.enpol.2019.05.003. Athayde *et al.*, 2019

AYRES, J. M. *As matas de várzea do Mamirauá: Médio Rio Solimões*. Brasília: CNPQ, 1995. Ayres, 1995

BACKHAUS, G. Introduction I The Problematic of Grounding the Significance of Symbolic Landscapes. In: G. BACKHAUS; J. MURUNGI (Eds.), *Symbolic Landscapes*, p. 1-15. Springer, Dordrecht, 2009. https://doi.org/10.1007/978-1-4020-8703-5_1. Backhaus, 2009

BAGHDADI, Nicolas *et al.* The relevance of GLAS/ICESat elevation data for the monitoring of river networks. *Remote Sensing*, v. 3, n. 4, p. 708-720, 2011. Baghdadi *et al.*, 2011

BAKIRMAN, T. *et al.* Implementation of ultra-light UAV systems for cultural heritage documentation. *Journal of Cultural Heritage*, v. 44, p. 174-184, 2020. Bakirman *et al.*, 2020

BARONA, E. *et al.* The Role of Pasture and Soybean in Deforestation of the Brazilian Amazon. *Environmental Research Letters*, v. 5, n. 2, p. 024002, 2010. https://doi.org/10.1088/1748-9326/5/2/024002. Barona *et al.*, 2010

BARRETO, P. *et al. Risco de Desmatamento Associado à Hidrelétrica de Belo Monte. Instituto do Homem e Meio Ambiente da Amazônia*. IMAZON: Belém, Brazil, 2011. 98 p. Disponível online: http://www.imazon.org.br/publicacoes/livros/risco-de-desmatamento-associado-a-hidreletricade-belo-monte/at_download/file. Acesso em: 26/08/2020. Barreto *et al.*, 2011

BASANTES, J. *et al.* Capture and Processing of Geospatial Data with Laser Scanner System for 3D Modeling and Virtual Reality of Amazonian Caves. In: *2017 IEEE Second Ecuador Technical Chapters Meeting (ETCM)*. 2017. https://doi.org/10.1109/etcm.2017.8247455. Acesso em 12/2022. Basantes *et al.*, 2017

BAUMAN, Z. *Consuming Life*. Polity Press, Cambridge, MA, 2007. Bauman, 2007

BERTASSOLI, D. J. *et al.* The Fate of Carbon in Sediments of the Xingu and Tapajós Clearwater Rivers, Eastern Amazon. *Frontiers in Marine Science*, v. 4, 2017. https://doi.org/10.3389/fmars.2017.00044. Bertassoli *et al.*, 2017

BERTASSOLI, D. J. *et al. How green can amazon hydropower be? net carbon emission from the largest hydropower plant in Amazonia. Science Advances*, v. 7, n. 26, 2021. DOI: 10.1126/sciadv.abe1470. Bertassoli *et al.*, 2021

BISHOP, I. D. Location Based Information to Support Understanding of Landscape Futures. *Landscape and Urban Planning*, v. 142, p. 120–131, 2015. https://doi.org/10.1016/j.landurbplan.2014.06.001. Bishop, 2015

BOON, M. A.; GREENFIELD, R.; TESFAMICHAEL, S. Wetland assessment using unmanned aerial vehicle (UAV) photogrammetry. *The International Archives of the Photogrammetry, Remote Sensing and Spatial Information Sciences*, v. 41, p. 781-788, 2016. Boon; Greenfield; Tesfamichael, 2016

BOUFAMA, B.; MOHR, R.; VEILLON, F. Euclidean constraints for uncalibrated reconstruction. In: *1993 (4th) International Conference on Computer Vision*. IEEE, 1993. p. 466-470. Boufama *et al.*, 993

BREIMAN, L. Random Forests. *Mach. Learn.*, v. 45, p. 5–32, 2001. https://doi.org/10.1023/a:1010933404324. Breiman, 2001

BRINSON, M.M. *A hydrogeomorphic classification for wetlands*. U.S. Army Engineers Waterways Experiment Station, Vicksburg, MS. Wetland Research Program Technical Report WRP-DE-4, 1993. Disponível em: http://el.erdc.usace.army.mil/elpubs/pdf/wrpde4.pdf. Brinson, 1993

BROWN, S. Measuring carbon in forests: current status and future challenges. *Environmental Pollution*, v. 116, p. 363-372, 2002. Brown, 2002

BUSKER, T. *et al.* A global lake and reservoir volume analysis using a surface water dataset and satellite altimetry. Hydrology and Earth System Sciences, v. 23, n. 2, p. 669-690, 2019. DOI: 10.5194/hess-23-669-2019. Busker *et al.*, 2019

BUTLER, R. Brazil's Controversial Belo Monte Back on Track after Court Decision Overruled. *Mongabay Environmental News*, 29 de agosto de 2012. Disponível em: https://news.mongabay.com/2012/08/brazils-controversial-belo-monte-back-on-track-after-court-decision-overruled/. Acesso em: 04/2021. Butler, 2012

CALVI, M. F. (Re) *Organização Produtiva e Mudanças Na Paisagem Sob Influência Da Hidrelétrica De Belo Monte*. Tese (Doutorado em Filosofia e Ciências Humanas), Universidade Estadual de Campinas, Campinas, Brasil, 2020a. Calvi, 2020a

CALVI, M. F. *et al.* The Construction of the Belo Monte Dam in the Brazilian Amazon and Its Consequences on Regional Rural Labor. *Land Use Policy*, v. 90, p. 104327, 2020b. https://doi.org/10.1016/j.landusepol.2019.104327. Calvi *et al.*, 2020b

CAMARGO, M. G. P. de. *Variabilidade da vazão do Rio Xingu na região da UHE Belo Monte sob cenários de projeções multimodelo de mudança climática*. Dissertação de mestrado, Instituto de Geociências, Universidade de São Paulo, 2019. Camargo, 2019

CAMPELO, A. Rethinking Sense of Place: Sense of One and Sense of Many. In: *Rethinking Place Branding*, p. 51–60, 2014. https://doi.org/10.1007/978-3-319-12424-7_4. Campelo, 2014

CAMPELO, A.; AITKEN, R.; GNOTH, J. Visual Rhetoric and Ethics in Marketing of Destinations. *Journal of Travel Research*, v. 50, n. 1, p. 3–14, 2010. https://doi.org/10.1177/0047287510362777. Campelo; Aitken; Gnoth, 2010

CARRIVICK, J. L.; SMITH, M. W.; QUINCEY, D. J. *Structure from motion in the Geosciences*. Chichester: John Wiley & Sons, 2016. Carrivick; Smith; Quincey, 2016

CARVALHO, G. O. Environmental Resistance and the Politics of Energy Development in the Brazilian Amazon. *The Journal of Environment*, v. 15, n. 3, pp. 245-268, 2006. doi:10.1177/107049650629157. Carvalho, 2006

CBH - Comitês de Bacia Hidrográfica. *Bacias Estaduais*. 2019. Acesso em Maio de 2019. Disponível em: http://www.cbh.gov.br/ForumComites.aspx. CBH, 2019

CHAMPION, E.; RAHAMAN, H. 3D Digital Heritage Models as Sustainable Scholarly Resources. *Sustainability*, v. 11, n. 8, p. 2425, 2019. https://doi.org/10.3390/su11082425. Champion; Rahaman, 2019

CHEN, T. *et al.* Monitoring global reservoirs using ICESat-2: Assessment on spatial coverage and application potential. *Journal of Hydrology*, v. 604, p. 127257, 2022. Chen *et al.*, 2022

CHIABRANDO, F.; DONADIO, E.; RINAUDO, F. SFM for Orthophoto Generation: A Winning Approach for Cultural Heritage Knowledge. *The International Archives of the Photogrammetry, Remote Sensing and Spatial Information Sciences*, v. XL-5/W7, p. 91–98, 2015. https://doi.org/10.5194/isprsarchives-xl-5-w7-91-2015. Chiabrando; Donadio; Rinaudo, 2015

CONGALTON, R. G.; GREEN, K. *Assessing the Accuracy of Remotely Sensed Data: Principles and Practices*. CRC Press: Boca Raton, FL, USA, 2019. Congalton; Green, 2019

CONGEDO, L. Semi-Automatic Classification Plugin: A Python Tool for the Download and Processing of Remote Sensing Images in QGIS. *J. Open Source Softw.*, v. 6, 2021, p. 3172. https://doi.org/10.21105/joss.03172. Congedo, 2021

COSTA, B. B. S. *et al.* Licenciamento Ambiental No Brasil Sobre Usinas Hidrelétricas: Um Estudo De Caso Da Usina De Belo Monte, No Rio Xingu. *Cadernos de Graduação*, v. 1, n. 15, p. 19–33, 2012. Costa *et al.*, 2012

COWARDIN, L.M. *et al. Classification of wetlands and deepwater habitats of the United States*. U.S. Fish and Wildlife Service, Washington, DC, FWS/OBS-79/31, 1979, http://www.fws.gov/nwi/Pubs_Reports/Class_Manual/class_titlepg.htm. Cowardin*et al.*, 1979

CUNHA, D. D. A. *Análise da Paisagem e Estrutura das Comunidades Vegetais das Formações Pioneiras do Baixo Xingu, Pará*. Dissertação (Mestrado em Botânica) - Universidade Rural da Amazônia. Museu Paraense Emílio Goeldi, 2009. Cunha, 2009

DE MELLO, K. *et al.* Effects of Land Use and Land Cover on Water Quality of Low-Order Streams in Southeastern Brazil: Watershed Versus Riparian Zone. *CATENA*, v. 167, p. 130–138, 2018. https://doi.org/10.1016/j.catena.2018.04.027. De Mello *et al.*, 2018

DE PAULA SILVA, J.; RODRIGUES, C.; PEREIRA, D.I. Mapping and Analysis of Geodiversity Indices in the Xingu River Basin, Amazonia, Brazil. *Geoheritage*, v. 7, n. 4, p. 337–350, 2014. https://doi.org/10.1007/s12371-014-0134-8. de Paula Silva; Rodrigues; Pereira, 2014

DE SAN EUGENIO VELA, J.; NOGUÉ, J.; GOVERS, R. Visual Landscape as a Key Element of Place Branding. *Journal of Place Management and Development*, v. 10, n. 1, p. 23–44, 2017. https://doi.org/10.1108/jpmd-09-2016-0060. de San Eugenio Vela; Nogué; Govers, 2017

DHINGRA, S.; KUMAR, D. A Review of Remotely Sensed Satellite Image Classification. *Int. J. Electr. Comput. Eng. (IJECE)*, v. 9, 2019, p. 1720. https://doi.org/10.11591/ijece.v9i3.pp1720-1731. Dhingra; Kumar, 2019

DIEGUES, A. C. S. (ed.). *An Inventory of Brazilian Wetlands*. International Union for Conservation of Nature and Natural Resources, Gland, Switzerland, 1994. Diegues, 1994

DRAKE, J. B. *et al.* Above-ground biomass estimation in closed canopy Neotropical forests using lidar remote sensing: factors affecting the generality of relationships. *Global Ecology & Biogeography*, v. 12, p. 147-159, 2003. Drake *et al.*, 2003

ELETROBRÁS - Centrais Elétricas Brasileiras S/A. *Aproveitamento Hidrelétrico Belo Monte: Estudo De Impacto Ambiental*. Rio de Janeiro, RJ: Eletrobrás, 2009a. Eletrobrás, 2009a

ELETROBRÁS - Centrais Elétricas Brasileiras S/A. *Relatório de Impacto Ambiental (RIMA) - Aproveitamento Hidrelétrico de Belo Monte*. Brasília, Brasil: Eletrobrás, 2009b.

EMBRAPA - Empresa Brasileira de Pesquisa Agropecuária. *ALOS - Advanced Land Observing Satellite*. [S.d.]. Acesso em 2020. Disponível em: https://www.embrapa.br/satelites-de-monitoramento/missoes/alos. EMBRAPA, [s.d.]

ERVIN, S. M.; HASBROUCK, H. H. *Landscape Modeling: Digital Techniques for Landscape Visualization*. McGraw-Hill, 2011. Ervin; Hasbrouck, 2011

ESA EO - European Space Agency Earth Observation. *JERS-1 (Japan Earth Resources Satellite)*. [S.d.]. Disponível em: https://directory.eoportal.org/web/eoportal/satellite-missions/j/jers-1. Acesso em: 02/2021. ESA EO, [s.d.]

FAIOLA, A.; LOPES, M.; MOONEY, C. The Price of 'progress' in the Amazon. The Washington Post, 2019. Disponível em:

https://www.washingtonpost.com/world/2019/06/28/how-building-boom-brazilian-amazon-could-accelerate-its-deforestation/. Acesso em: 28 jun. 2019. Faiola; Lopes; Mooney, 2019

FAO - ORGANIZAÇÃO DAS NAÇÕES UNIDAS PARA ALIMENTAÇÃO E AGRICULTURA (FAO). *Wetland characterization and classification for sustainable agricultural development*. Sub-Regional Office for East and Southern Africa, Harare, Zimbábue, 1998. Disponível em: http://www.fao.org/docrep/003/X6611E/X6611E00.HTM. FAO, 1998

FARINHA, J.C. *et al. MedWet habitat description system*. MedWet publication, 2005. http://www.medwet.org/codde/OtherResources/Habitat.pdf. Acesso em 7 de novembro de 2014. Farinha *et al.*, 2015

FARINOSI, F. *et al.* Future climate and land use change impacts on river flows in the Tapajós Basin in the Brazilian Amazon. *Earth's Future*, v. 7, 2019, p. 993–1017. https://doi.org/10.1029/2019ef001198. Farinosi *et al.*, 2019

FASSONI-ANDRADE, A. C.; DE PAIVA, R. C. D.; FLEISCHMANN, A. S. Lake topography and active storage from satellite observations of flood frequency. *Water Resources Research*, v. 56, n. 7, p. e2019WR026362, 2020a. Fassoni-Andrade; De Paiva; Fleischmann, 2020a

FASSONI-ANDRADE, A. C. *et al.* High-resolution mapping of floodplain topography from space: A case study in the Amazon. *Remote Sensing of Environment*, v. 251, p. 112065, 2020. Fassoni-Andrade *et al.*, 2020b

FEARNSIDE, Philip M. Brazil's Balbina Dam: Environment Versus the legacy of the Pharaohs in Amazonia. *Environmental Management*, v. 13, n. 4, p. 401–423, 1989. Disponível em: https://doi.org/10.1007/bf01867675. Fearnside, 1989

FEARNSIDE, P. M. Greenhouse-gas emissions from Amazonian Hydroelectric Reservoirs: The example of Brazil's tucuruí dam as compared to fossil fuel alternatives. *Environmental Conservation*, v. 24, n. 1, p. 64-75, 1997. DOI: 10.1017/s0376892997000118. Fearnside, 1997

FEARNSIDE, P. M. Soybean Cultivation as a Threat to the Environment in Brazil. *Environmental Conservation*, v. 28, n. 1, p. 23–38, 2001. DOI: 10.1017/s0376892901000030. Fearnside, 2001

FEARNSIDE, Philip M. Desmatamento na Amazônia: Dinâmica, impactos e controle. *Acta Amazonica*, v. 36, n. 3, p. 395–400, 2006. DOI: 10.1590/s0044-59672006000300018. Fearnside, 2006

FEARNSIDE, P. M. Hidrelétricas na Amazônia: Impactos Ambientais e Sociais na Tomada de Decisões sobre Grandes Obras. Editora do INPA, 2015, v. 2, p. 2. Fearnside, 2015

FEARNSIDE, P.M. Hidrelétricas na Amazônia Brasileira: Questões Ambientais e Sociais. In: *HIDRELÉTRICAS NA AMAZÔNIA: Impactos Ambientais e Sociais na*

Tomada de Decisões sobre Grandes Obras, vol. 3; Essay; Fearnside, P.M., Ed.; Editora do INPA: Manaus, Brazil, 2019; p. 7–22. Fearnside, 2019

FEARNSIDE, P. Brazil's Belo Monte Dam: Struggle for the Volta Grande Enters a New Phase (Commentary). *Mongabay*. 2021. Disponível em: https://news.mongabay.com/2021/06/brazils-belo-monte-dam-struggle-for-the-volta-grande-enters-a-new-phase-commentary/. Acesso em: 29 abr. 2022. Fearnside, 2021

FELDPAUSCH, T. R. *et al.* Height-diameter allometry of tropical forest trees. *Biogeosciences Discussions*, v. 7, pp. 980-989, 2003. DOI: 10.5194/bg-8-1081-2011. Feldpausch *et al.*, 2003

FELLET, J. Como "fim do Mundo" Causado Por Belo Monte Reuniu Indígenas Separados há Quase um Século. *BBC News Brasil*, 11 set. 2019. Disponível em: https://www.bbc.com/portuguese/brasil-49653939. Acesso em 09/2022. Fellet, 2019

FENG, Y. *et al.* Examining Spatial Distribution and Dynamic Change of Urban Land Covers in the Brazilian Amazon Using Multitemporal Multisensor High Spatial Resolution Satellite Imagery. *Remote Sensing*, v. 9, p. 381, 2017. DOI: 10.3390/rs9040381. Feng, *et al.*, 2017

FERREIRA-FERREIRA, J.*et al.* Combining ALOS/PALSAR derived vegetation structure and inundation patterns to characterize major vegetation types in the Mamirauá Sustainable Development Reserve, Central Amazon Floodplain, Brazil. *Wetlands Ecology and Management*, v. 23, n. 1, p. 41–59, 2014. DOI: 10.1007/s11273-014-9359-1. Ferreira-Ferreira *et al.*, 2014

FERREIRA, I. N. R.; MOLINA, H. S.; MOLINA, L. P. Plano de Gestão Territorial e Ambiental Volta Grande do Xingu: Terras Indígenas Paquiçamba, Arara da Volta Grande do Xingu e Área Indígena Juruna do Km 17. Altamira, PA: Verthic, 2018. Disponível em: https://acervo.socioambiental.org/acervo/documentos/plano-de-gestao-territorial-e-ambiental-volta-grande-do-xingu-terras-indigenas. Acesso em 04/2023. Ferreira; Molina; Molina, 2018

FERREIRA, L. V. O uso de análise de lacunas e paisagens para a identificação de áreas prioritárias para a conservação da biodiversidade no bioma Amazônia. In: Anais do 54º Congresso Nacional de Botânica. Museu Paraense Emílio Goeldi, 2003, p. 143-144. Ferreira, 2003

FERREIRA, L. V.; STOHLGREN, T. J. Effects of river level fluctuation on plant species richness, diversity, and distribution in a floodplain forest in Central Amazonia. *Oecologia*, v. 120, n. 4, p. 582–587, 1999. https://doi.org/10.1007/s004420050893. Ferreira; Stohlgren, 1999

FERREIRA, L.; FERREIRA, N.; FERREIRA, M. Sensoriamento remoto da vegetação: evolução e estado da arte. *Acta Scientiarum*, v. 30, n. 4, pp. 379-390, 2008. Ferreira; Ferreira; Ferreira, 2008

FERREIRA, M. E. Cobertura vegetal remanescente em Goiás: distribuição, viabilidade ecológica e monitoramento. In: FERREIRA, L. G. (org.). *A Encruzilhada Socioambiental*

- *Biodiversidade, Economia e Sustentabilidade no Cerrado*. Goiânia: Editora UFG, 2008, pp. 169-186. Ferreira, 2008

FERREIRA, M. P. *et al.* Individual tree detection and species classification of Amazonian palms using UAV images and deep learning. *Forest Ecology and Management*, v. 475, p. 118397, 2020. Ferreira *et al.*, 2020

FIELD, A. *Discovering statistics using SPSS*. 3. ed. London: Sage, 2009. Field, 2009

FLORES-ANDERSON, A. *et al.The SAR Handbook: Comprehensive Methodologies for Forest Monitoring and Biomass Estimation*, 1ª ed. SERVIR Global Science Coordination Office, 2019. DOI: 10.25966/nr2c-s697. Flores-Anderson *et al.*, 2019

FOODY, G. M. Remote sensing of tropical forest environments: towards the monitoring of environmental resources for sustainable development. *International Journal of Remote Sensing*, v. 24, p. 4035-4046, 2003. Foody, 2003

FOODY, G.M. Harshness in Image Classification Accuracy Assessment. *International Journal of Remote Sensing*, v. 29, p. 3137–3158, 2008. DOI: 10.1080/01431160701442120. Foody, 2008

FRAPPART, F. *et al.* Floodplain water storage in the Negro River Basin estimated from microwave remote sensing of inundation area and water levels. Remote Sensing of Environment, v. 99, n. 4, 2005. DOI: 10.1016/j.rse.2005.08.016. Frappart *et al.*, 2005

FRAPPART, F. *et al.* Preliminary results of Envisat RA-2-derived water levels validation over the Amazon basin. Remote Sensing of Environment, v. 100, n. 2, 2006. DOI: 10.1016/j.rse.2005.10.027. Frappart *et al.*, 2006

FREIRE, M. P. *et al.* Quaternary Ironstones in the Xingu River, Eastern Amazonia (Brazil). *Quaternary Research*, v. 110, p. 133–146, 2022. DOI: 10.1017/qua.2022.15. Freire *et al.*, 2022

FREITAS, R. M.; NOVO, E. L.; SHIMABUKURO, Y. E. Mapeamento de ecossistemas alagáveis do Rio Amazonas a partir do mosaico digital TM-Landsat - Escala Regional. In: *Anais XI SBSR*, pp. 2745-2752. Belo Horizonte: INPE, 2003. Freitas; Novo; Shimabukuro, 2003

FREITAS, S. R.; SHIMABUKURO, Y. E. Diagnosticando florestas tropicais através do sensoriamento remoto. In: *Anais XIII Simpósio Brasileiro de Sensoriamento Remoto - SBSR*, pp. 1671-1678. Florianópolis: INPE, 2007. Freitas; Shimabukuro, 2007

FREITAS, S.; CRUZ, C. Análise de componentes principais e modelo linear de mistura na discriminação de classes de vegetação na Mata Atlântica. In: *Anais do Simpósio Brasileiro de Sensoriamento Remoto*, pp. 1529-1536. Belo Horizonte: INPE, 2003. Freitas; Cruz, 2003

FURTADO, L. F.; SILVA, T. S.; NOVO, E. M. Dual-season and full-polarimetric C band SAR assessment for vegetation mapping in the Amazon Várzea Wetlands. *Remote*

Sensing of Environment, v. 174, p. 212-222, 2016. DOI: 10.1016/j.rse.2015.12.013. Furtado; Silva; Novo, 2016

FURUKAWA, Y.; PONCE, J. Combining Multi-view Stereo and Bundle Adjustment for Accurate Camera Calibration. In: *Image and Geometry Processing for 3-D Cinematography*. Berlin, Heidelberg: Springer Berlin Heidelberg, 2010. p. 151-169. Furukawa; Ponce, 2010

GARCIA, G. P. *et al.* Using Terrestrial Laser Scanner and RPA-based-photogrammetry for surface analysis of a landslide: A Comparison. *Boletim de Ciências Geodésicas*, v. 28, n. 3, 2022. Disponível em: https://doi.org/10.1590/s1982-21702022000300016. Garcia *et al.*, 2022

GARREAUD, R. D. *et al.* Present-day South American climate. *Palaeogeography, Palaeoclimatology, Palaeoecology*, v. 281, n. 3–4, p. 180-195, 2009. DOI: 10.1016/j.palaeo.2007.10.032. Garreaud *et al.*, 2009

GARNERO, G.; GODONE, D. Comparisons between different interpolation techniques. In: *Proceedings of the International Archives of the Photogrammetry, Remote Sensing and Spatial Information Sciences*, XL-5 W, Padua, Italy, 27-28 February 2013, Volume 3, pp. 27-28. Garnero; Godone, 2013

GEE – Google Earth Engine. *GEE Data Catalog - Planet Datasets NICFI in Earth Engine*. [n.d.]. Available online: https://developers.google.com/earth-engine/datasets/tags/nicfi. Accessed on November 15, 2022. GEE, [n.d.]

GIORDAN, D. *et al.* Review article: The use of remotely piloted aircraft systems (RPAS) for Natural Hazards Monitoring and management. *Natural Hazards and Earth System Sciences*, v. 18, n. 4, 2018, p. 1079–1096. Disponível em: https://doi.org/10.5194/nhess-18-1079-2018. Giordan *et al.*, 2018

GREEN, D.L. *Wetland Management Technical Manual: Wetland Classification*. Department of Land and Water Conservation, Ecological Services Unit, Parramatta, New South Wales, Austrália, 1997. Green, 1997

GROHMANN, C. H. *et al.* Dune migration and volume change from Airborne Lidar, Terrestrial Lidar and Structure from Motion-Multi View Stereo. *Computers & Geosciences*, v. 143, 2020, p. 104569. Disponível em: https://doi.org/10.1016/j.cageo.2020.104569. Grohmann *et al.*, 2020

GROHMANN, C. H. *et al.*RPA Flight Pattern and GCP Influence on SFM-MVS Modeling of a Stable Landslide in SE Brazil. *Geomorphometry2023*, 28 de março de 2023. DOI: 10.5281/zenodo.7779223. Grohmann *et al.*, 2023

GSW - GLOBAL SURFACE WATER. *FAQ*. Global Surface Water Explorer, 2020. Disponível em: https://global-surface-water.appspot.com/faq. Acesso em: 2020. GSW, 2020

GSW - Global Surface Water. *GSW Explorer***.** [n.d.] Available online: https://global-surface-water.appspot.com/. Acesso em 15/11/2021. GSW, [n.d.]

GUARNIERI, A.; PIROTTI, F.; VETTORE, A. Cultural Heritage Interactive 3D Models on the Web: An Approach Using Open Source and Free Software. *Journal of Cultural Heritage*, v. 11, n. 3, p. 350–353, 2010. DOI: 10.1016/j.culher.2009.11.011. Guarnieri; Pirotti; Vettore, 2010

GUTH, P. L. *et al.* Digital Elevation Models: Terminology and Definitions. *Remote Sensing*, v. 13, n. 18, p. 3581, 2021. DOI: 10.3390/rs13183581. Guth *et al.*, 2021

HERRERO-TEJEDOR, T. R. *et al.* Documenting a Cultural Landscape Using Point-Cloud 3D Models Obtained with Geomatic Integration Techniques. The Case of the El Encín Atomic Garden, Madrid (Spain). *PLOS ONE*, v. 15, n. 6, 2020. DOI: 10.1371/journal.pone.0235169. Herrero-Tejedor *et al.*, 2020

HESS, L. L. *et al.* Wetlands of the lowland Amazon Basin: Extent, vegetative cover, and dual-season inundated area as mapped with Jers-1 Synthetic Aperture Radar. *Wetlands*, v. 35, n. 4, p. 745–756, 2015. DOI: 10.1007/s13157-015-0666-y. Hess *et al.*, 2015

HESS, L. L.; MELACK, J. M. Radar detection of flooding beneath the forest canopy: a review. *International Journal of Remote Sensing*, v. 11, p. 1313-1325, 1990. Hess; Melack, 1990

HIGGINS, T. Amazon's Belo Monte Dam Cuts Xingu River Flow 85%; a Crime, Indigenous Say. *Mongabay Environmental News*, 8 March 2021. Available online: https://news.mongabay.com/2021/03/amazons-belo-monte-dam-cuts-xingu-river-flow-85-a-crime-indigenous-say/. Acessado em 05/2021. Higgins, 2021

HORNE, M.; THOMPSON, E. M. The Role of Virtual Reality in Built Environment Education. *Journal for Education in the Built Environment*, v. 3, n. 1, p. 5–24, 2008. DOI: 10.11120/jebe.2008.03010005. Horne; Thompson, 2008

HSU, C.-W.; CHANG, C.-C.; LIN, C.-J. *A Practical Guide to Support Vector Classification. 2003*. Available online: https://www.csie.ntu.edu.tw/~cjlin/papers/guide/guide.pdf. Acessado em 10/05/2022. Hsu; Chang; Lin, 2003

HUBBELL, S. P. *et al.* Light-gap disturbances, recruitment limitation and tree diversity in a neotropical forest. *Science*, v. 283, n. 5401, p. 554-567, 1999. Hubbel *et al.*, 1999

IBAMA - Instituto Brasileiro do Meio Ambiente. Termo de referência para elaboração do estudo de impacto ambiental e o respectivo relatório de impacto ambiental - EIA / RIMA - aproveitamento hidrelétrico Belo Monte (PA) processo Nº 02001.001848/2006-75. Pará: IBAMA, 2007. IBAMA, 2007

IBGE - Instituto Brasileiro de Geografia e Estatística. Pesquisa da Pecuária Municipal. [s.d.]. Disponível em: https://sidra.ibge.gov.br/tabela/3939. Acessado em 05/08/2020. IBGE, [s.d.]

IBGE - Instituto Brasileiro de Geografia e Estatística. *Vegetação Brasileira 1:5.000.000 | 2004*. Available at: https://www.ibge.gov.br/geociencias/informacoes-ambientais/vegetacao/10872-vegetacao.html. Accessado em 2020. IBGE, 2004

IDL – Interactive Data Language. ENVI *User's Guide*. Available online: https://www.tetracam.com/PDFs/Rec_Cite9.pdf. IDL, [n.d.]. Acesso em 20/01/2022.

IGLHAUT, J. *et al*. Structure from Motion Photogrammetry in Forestry: A Review. *Current Forestry Reports*, v. 5, n. 3, p. 155–168, 2019. DOI: 10.1007/s40725-019-00094-3. Iglhaut *et al.*, 2019

IPCC – Painel Intergovernamental para a Mudança de Clima. Mudanças climáticas 2022: Impactos, adaptação e vulnerabilidade. Contribuição do Grupo de Trabalho II ao Sexto Relatório de Avaliação do Painel Intergovernamental sobre Mudanças Climáticas. Genebra: IPCC, 2022. Disponível em: https://www.ipcc.ch/report/ar6/wg2/. IPCC, 2022

IPHAN - Instituto do Patrimônio Histórico e Artístico Nacional. Paisagem Cultural. Disponível online: http://portal.iphan.gov.br/uploads/ckfinder/arquivos/Livreto_paisagem_cultural.pdf. 2009. Acessado em 09/02/2023. IPHAN, 2009

IRION, G.; ADIS, J. Evolução de florestas amazônicas inundadas, de igapó - um exemplo do rio Tarumã-Mirim. *Acta Amazonica*, v. 9, n. 2, p. 299-303, 1979. Irion; Adis, 1979

ISA - INSTITUTO SOCIOAMBIENTAL. *Atlas dos impactos da UHE Belo Monte sobre a pesca*. Organizado por Ana De Francesco e Cristiane Carneiro. 1ª edição. São Paulo Socioambiental, 2015.: Instituto Socioambiental, 2015. ISA, 2015

ISA - INSTITUTO SOCIOAMBIENTAL. Belo Monte: animação mostra impactos na pesca. ISA, 2016a. Acesso em 2020, disponível em YouTube: https://www.youtube.com/watch?v=oz6DK7gxU5k.

ISA - INSTITUTO SOCIOAMBIENTAL. 3º Canoada Bye Bye Xingu: Belo Monte, o que fizeram de nós? (Editor: F. Ligabue). ISA, 2016b. Acesso em 2020, disponível em YouTube: https://www.youtube.com/watch?v=7-r53eJI3Nk.

ISA - Instituto Socioambiental & AYMÏX Associação Yudjá Mïratu Xingu**.** Os donos do rio | Canoada Xingu. ISA; AYMÏX, 2017. Acesso em 2020, disponível em YouTube: https://www.youtube.com/watch?v=crKlt6G1UXs&t=2s.

ISA - Instituto Socioambiental; AYMÏX - Associação Yudjá Mïratu Xingu; UFPA - Universidade Federal do Pará**.** Xingu, o rio que pulsa em nós | Juruna denunciam impactos de Belo Monte. (Produtores: B. Garzón, I. Harari, B. Weis, & C. Leão). ISA, 2018a. Acesso em 2019, disponível em YouTube: https://www.youtube.com/watch?v=fh1mwlwOzLw&t=4s. ISA; AYMÏX; UFPA, 2018

ISA - Instituto Socioambiental & AYMÏX - Associação Yudjá Mïratu Xingu. Discussão de critérios para a redefinição do hidrograma da vazão residual da UHE Belo Monte na região da Volta Grande do Xingu. Oficina Científica, Instituto Socioambiental e Associação Yudjá Mïratu da Volta Grande do Xingu, Belém, 2018b. ISA; AYMÏX, 2018

JASINSKI, M. F. *et al. ATLAS/ICESat-2 L3A Inland Water Surface Height, Version 5*. Boulder, Colorado USA. NASA National Snow and Ice Data Center Distributed Active

Archive Center, 2020. DOI: https://doi.org/10.5067/ATLAS/ATL13.005. Jasinski *et al.*, 2020

JAXA – Japan Aerospace Exploration Agency**.** [s.d.]. ALOS Research and Application Project. Acesso em 2020, disponível em About ALOS - PALSAR: [s.d.]. https://www.eorc.jaxa.jp/ALOS/en/about/palsar.htm. Acesso em 31/08/2020. JAXA, [s.d.]

JAXA - Japan Aerospace Exploration Agency. *JERS.1/SAR Level 2.1 product Format Description (summary)* <English Version>. Japanese Aerospace Exploration Agency. 2015. Acesso em 2020, disponível em https://www.eorc.jaxa.jp/en/distribution/standard_dataset/pdf/format_sar_e.pdf. JAXA, 2015

JENSEN, J. R. Remote sensing of water. In: J. R. JENSEN (Ed.), *Remote sensing of the environment: an Earth Resource Perspective*, pp. 379-406, Prentice Hall, 2000. Jensen, 2000

JENSEN, L.; RIETBROEK, R.; KUSCHE, J. Land Water Contribution to sea level from Grace and jason-1 measurements. Journal of Geophysical Research: Oceans, v. 118, n. 1, 2013. DOI: 10.1002/jgrc.20058. Jensen; Rietbroek; Kusche, 2013

JIANG, X**.** *et al.* Examining Impacts of the Belo Monte Hydroelectric Dam Construction on Land-Cover Changes Using Multitemporal Landsat Imagery. *Applied Geography*, v. 97, p. 35–47, 2018. DOI: 10.1016/j.apgeog.2018.05.019. Jiang *et al.*, 2018

JIMÉNEZ-MUÑOZ, J. C**.** *et al.* Record-breaking warming and extreme drought in the Amazon rainforest during the course of El Niño 2015–2016. *Scientific Reports*, v. 6, n. 1, 2016. DOI: 10.1038/srep33130. Jiménez-Muñoz *et al.*, 2016

JUNK, W.J. Áreas Inundáveis: Um Desafio Para Limnologia. *Acta Amazonica*, Belém, v. 10, p. 775-795, 1980. Disponível em: https://doi.org/10.1590/1809-43921980104775. Junk, 1980

JUNK, W. *et al.* The flood pulse concept in river-floodplain systems. *Canadian special publication of fisheries and aquatic sciences*, n. 106, 1989, pp. 110-127. Junk *et al.*, 1989

JUNK, W.J. *et al. A classification of major naturally-occurring Amazonian lowland wetlands*. Wetlands, v. 31, p. 622-640, 2011. Junk *et al.*, 2011

JUNK, W.J. *et al.* Brazilian Wetlands: Their Definition, Delineation, and Classification for Research, Sustainable Management, and Protection. *Aquatic Conservation: Marine and Freshwater Ecosystems*, v. 24, p. 5-22, 2013. Disponível em: https://doi.org/10.1002/aqc.2386. Junk *et al.*, 2013

KALACSKA, M. *et al.* A New Multi-Temporal Forest Cover Classification for the Xingu River Basin, Brazil. *Data*, v. 4, p. 114, 2019. Disponível em: https://doi.org/10.3390/data4030114. Kalacska *et al.*, 2019

KALACSKA, M. *et al.* High-Resolution Surface Water Classifications of the Xingu River, Brazil, Pre and Post Operationalization of the Belo Monte Hydropower Complex. *Data*, v. 5, p. 75, 2020a. Kalacska *et al.*, 2020a

KALACSKA, M. *et al.* Deciphering the Many Maps of the Xingu—An Assessment of Land Cover Classifications at Multiple Scales. *Proceedings of the Academy of Natural Sciences of Philadelphia*, v. 166, p. 1-55, 2020b. Disponível em: https://doi.org/10.1101/2019.12.23.887588. Kalacska *et al.*, 2020b

KAMARAINEN, A. M. *et al.* EcoMOBILE: Integrating Augmented Reality and Probeware with Environmental Education Field Trips. *Computers & Education*, v. 68, p. 545-556, 2013. Disponível em: https://doi.org/10.1016/j.compedu.2013.02.018. Kamarainen *et al.*, 2013

KEEL, S. K.; PRANCE, G. T. Studies of the vegetation of white-sand black-water igapó (Rio Negro, Brasil). *Acta Amazonica*, v. 4, p. 645-655, 1979. Keel; Prance, 1979

KEMENES, A.; FORSBERG, B. R.; MELACK, J. M. *CO2 emissions from a tropical hydroelectric reservoir (Balbina, Brazil)*. *Journal of Geophysical Research*, v. 116, n. G3, 2011. DOI: 10.1029/2010jg001465. Kemenes; Forsberg; Melack, 2011

KHALSA, S. J. S. *et al.* OpenAltimetry - rapid analysis and visualization of Spaceborne altimeter data. *Earth Science Informatics*, 2020. Disponível em: https://doi.org/10.1007/s12145-020-00520-2. Acesso em: 24/07/2023. Khalsa *et al.*, 2020

KOLB, D. A. *Experiential Learning: Experience as the Source of Learning and Development* (Vol. 1). Englewood Cliffs: Prentice-Hall, 1984. Kolb, 1984

KOPENAWA, Davi; ALBERT, Bruce. A queda do céu: Palavras de um xamã yanomami. Tradução de Beatriz Perrone-Moisés. Prefácio de Eduardo Viveiros de Castro. 1ª ed. São Paulo: Companhia das Letras, 2015. Kopenawa; Albert, 2015

KUBITZKI, K. The ecogeographical differentiation of Amazonian inundation forests. *Plant Systematics and Evolution*, p. 285-304, 1989. Kubitzki, 1989

LAI, P. C.; KWONG, K.-H.; MAK, A. S. Assessing the Applicability and Effectiveness of 3D Visualisation in Environmental Impact Assessment. *Environment and Planning B: Planning and Design*, v. 37, n. 2, p. 221-233, 2010. Disponível em: https://doi.org/10.1068/b34141. Lai; Kwong; Mak, 2010

LATRUBESSE, E. M.; FRANZINELLI, E. The late quaternary evolution of the Negro River, Amazon, Brazil: implications for island and floodplain formation in large anabranching tropical systems. *Geomorphology*, v. 3, p. 372-392, 2005. Latrubesse; Franzinelli, 2005

LATRUBESSE, E. M. *et al.* Damming the rivers of the Amazon basin. *Nature*, v. 546, p. 363-369, 15 de junho de 2017. DOI: 10.1038/nature22333. Latrubesse *et al.*, 2017

LEFSKY, M. A. *et al.* Lidar Remote Sensing for Ecosystem Studies. *BioScience*, v. 52, p. 19-30, 2002. Lefsky *et al.*, 2002

LEFSKY, M. A.; COHEN, W. B. Selection of Remotely Sensed Data. In: *Remote Sensing of Forest Environments: Concepts and Case Studies*. Kluwer Academic Publishers: Boston, MA, USA, 2003, pp. 13-46. Lefsky; Cohen, 2003

LEINO, T.; LODENIUS, M. Human hair mercury levels in Tucuruí area, state of Pará, Brazil. *Science of The Total Environment*, v. 175, n. 2, p. 119-125, 1995. DOI: https://doi.org/10.1016/0048-9697(95)04908-j. Leino; Lodenius, 1995

LÉVI-STRAUSS, C. Présentation. In: LÉVI-STRAUSS, C. Chroniques d'une Conquête. Ethnies. n. 14, p. 5-7, 1993. Lévi-Strauss, 1993

LI, G. *et al.* Land-Cover Classification in a Moist Tropical Region of Brazil with Landsat Thematic Mapper Imagery. *International Journal of Remote Sensing*, v. 32, p. 8207-8230, 2011. DOI: 10.1080/01431161.2010.532831. Li *et al.*, 2011

LI, G. *et al.* Comparative Analysis of Classification Algorithms and Multiple Sensor Data for Land Use/Land Cover Classification in the Brazilian Amazon. *Journal of Applied Remote Sensing*, v. 6, 061706, 2012. DOI: 10.1117/1.jrs.6.061706. Li *et al.*, 2012

LI, G. *et al.* Examining Deforestation and Agropasture Dynamics along the Brazilian TransAmazon Highway Using Multitemporal Landsat Imagery. *GIScience & Remote Sensing*, v. 56, p. 161-183, 2018. DOI: 10.1080/15481603.2018.1497438. Li *et al.*, 2018

LOWE, D. Distinctive image features from scale-invariant keypoints. *International Journal of Computer Vision*, v. 60, 2004, p. 91–110. Lowe, 2004

LU, D. *et al.* Comparison of Land-Cover Classification Methods in the Brazilian Amazon Basin. *Photogrammetric Engineering & Remote Sensing*, v. 70, p. 723-731, 2004. DOI: 10.14358/pers.70.6.723. Lu *et al.*, 2004

LU, D.; WENG, Q. A Survey of Image Classification Methods and Techniques for Improving Classification Performance. *International Journal of Remote Sensing*, v. 28, p. 823-870, 2007. DOI: 10.1080/01431160600746456. Lu; Weng, 2007

LU, D. *et al.* Spatiotemporal Analysis of Land-Use and Land-Cover Change in the Brazilian Amazon. *International Journal of Remote Sensing*, v. 34, p. 5953-5978, 2013. DOI: 10.1080/01431161.2013.802825. Lu *et al.*, 2013

LU, S.-J.; LIU, Y.-C. Integrating Augmented Reality Technology to Enhance Children's Learning in Marine Education. *Environmental Education Research*, v. 21, n. 4, p. 525-541, 2014. DOI: 10.1080/13504622.2014.911247. Lu; Liu, 2014

LUIZE, B. G. *et al.* Effects of the flooding gradient on tree community diversity in várzea forests of the Purus River, Central Amazon, Brazil. *Biotropica*, v. 47, n. 2, p. 137–142, 2015. https://doi.org/10.1111/btp.12203. Luize *et al.*, 2015

LUO, S. *et al.* An effective low-cost remote sensing approach to reconstruct the long-term and dense time series of area and storage variations for large lakes. *Sensors*, 19(19), 4247, 2019. doi:10.3390/s19194247. Luo et al., 2019

MADDIKUNTA, P. K. R. *et al.* Unmanned aerial vehicles in smart agriculture: Applications, requirements, and challenges. *IEEE Sensors Journal*, v. 21, n. 16, p. 17608-17619, 2021. Maddikunta, 2021

MAGALHÃES, S. B. *Tucuruí: A relocation policy in context.* In: SANTOS, L. A. O.; ANDRADE, L. M. M. de (Eds.). *Hydroelectric Dams on Brazil's Xingu River and Indigenous Peoples.* Cultural Survival, Cambridge, Massachusetts, EUA, 1990, p. 105-114 (Cultural Survival Report 30). Magalhães, 1990

MAGALHÃES, S. B.; CUNHA, M. C. da. *A Expulsão de Ribeirinhos em Belo Monte: Relatório da SBPC*. São Paulo, SP: SBPC, 2017. Magalhães; Cunha, 2017

MARENGO, J. A. *et al.* Changes in climate and land use over the Amazon region: Current and future variability and Trends. *Frontiers in Earth Science*, v. 6, p. 135, 2018. DOI: 10.3389/feart.2018.00228. Marengo *et al.*, 2018

MCDONALD, J. *et al.* Seeing the Landscape: Multiple Scales of Visualising Terrestrial Heritage on Rosemary Island (Dampier Archipelago). *Open Quaternary*, v. 6, 2020. DOI: 10.5334/oq.81. McDonald *et al.*, 2020

MCKILLUP, S.; DYAR, M. D. *Geostatistics Explained: An Introductory Guide for Earth Scientists*. Cambridge University Press, 2010. McKillup; Dyar, 2010

MEHTA, A.*et al.* Mapping and Monitoring Lakes and Reservoirs with Satellite Observations. *NASA Applied Remote Sensing Training Program (ARSET)*, 2021. Disponível em: https://appliedsciences.nasa.gov/join-mission/training/english/arset-mapping-and-monitoring-lakes-and-reservoirs-satellite. Mehta *et al.*, 2021

MENZIES PLUER, E. G. *et al.* Pairing soil sampling with very-high resolution UAV imagery: An examination of drivers of soil and nutrient movement and agricultural productivity in Southern Ontario. *Geoderma*, v. 379, 2020, p. 114630. Disponível em: https://doi.org/10.1016/j.geoderma.2020.114630. Menzies Pluer *et al.*, 2020

MEYER, F. Spaceborne Synthetic Aperture Radar: Principles, Data Access, and Basic Processing Techniques. In: FLORES-ANDERSEN, A. I. *et al.* (Eds.). *The SAR Handbook: Comprehensive Methodologies for Forest Monitoring and Biomass Estimation*, 1ª ed., p. 307. SERVIR Global Science Coordination Office, 2019. DOI: 10.25966/nr2c-s697. Meyer, 2019

MICHAEL, G. *et al. The Smithsonian Atlas of the Amazon*. Smithsonian Books: Washington, DC, USA, 2010. Michael *et al.*, 2010

MONTEIRO NETO, A. *et al.* Sensoriamento Remoto na Análise de Variáveis Ambientais Influenciadas Pela Implantação da Usina Hidrelétrica de Belo Monte (PA). *Caderno de Geografia*, v. 31, p. 823, 2021. DOI: 10.5752/p.2318-2962.2021v31n66p823. Monteiro Neto *et al.*, 2021. Monteiro Neto *et al.*, 2021

MORAN, E. F. *et al.* Sustainable Hydropower in the 21st Century. *Proceedings of the National Academy of Sciences of the United States of America*, v. 115, p. 11891-11898, 2018. DOI: 10.1073/pnas.1809426115. Moran *et al.*, 2018

MORETTO, E. M. *et al.* Histórico, Tendências e Perspectivas no Planejamento Espacial de Usinas Hidrelétricas Brasileiras: A Antiga e Atual Fronteira Amazônica. *Ambiente & Sociedade*, v. 15, p. 141-164, 2012. DOI: 10.1590/s1414-753x2012000300009. Moretto, *et al.*, 2012

MOUGEOT, L. J. A. *O reservatório da Usina Hidrelétrica de Tucuruí, Pará, Brasil: Uma avaliação do programa de reassentamento populacional (1976-85).* In: KOHLHEPP, G.; SCHRADER, A. (Eds.). *Homem e Natureza na Amazônia.* Tübinger Geographische Studien 95 (Tübinger Beiträge zur Geographischen Lateinamerika-Forschung 3). Geographisches Institut, Universität Tübingen, Tübingen, Alemanha, 1987, p. 387-404. Mougeot, 1987

MPF - Ministério Público Federal; MPPA - Ministério Público do Estado do Pará; DPU - Defensoria Pública da União; DPEPA - Defensoria Pública do Estado do Pará. *Relatório de Vistoria Interinstitucional na Volta Grande do Xingu: Garantia da Vida e Proteção do Patrimônio Natural e Socioambiental da Volta Grande do Rio Xingu*. MPF, junho de 2019. Disponível em: https://www.mpf.mp.br/pa/sala-de-imprensa/documentos/2019/Relatorio_VGX_2019.pdf. MPF, 2019

MPF, Ministério Público Federal. STF Reconhece Que o Direito de Consulta Prévia Dos Povos Indígenas Afetados Por Belo Monte Foi Violado. 6 de setembro de 2022. Disponível em: http://www.mpf.mp.br/pa/sala-de-imprensa/noticias-pa/stf-reconhece-que-o-direito-de-consulta-previa-dos-povos-indigenas-afetados-por-belo-monte-foi-violado. Acessado em 03/2023. MPF, 2022

MPF - Ministério Público Federal. *O Futuro da Volta Grande do Xingu - Seminário Técnico*. MPF, 2023. YouTube. https://www.youtube.com/watch?v=51VAcEW29hc&t=5907s. Acessado em 04/2023. MPF, 2023

MYERS, N. Tropical Deforestation and Remote Sensing. *Forest Ecology and Management*, v. 23, p. 215-225, 1988. Myers, 1988

NARIN, Omer Gokberk; ABDIKAN, Saygin. Multi-temporal analysis of inland water level change using ICESat-2 ATL-13 data in lakes and dams. *Environmental Science and Pollution Research*, v. 30, n. 6, p. 15364-15376, 2023. Narin; Abdikan, 2023

NELSON, B.; OLIVEIRA, A. Áreas Prioritárias por Grupos Temáticos: Área Botânica. In: BRASIL, M. *Avaliação e Identificação de Ações Prioritárias para a Conservação, Utilização Sustentável e Repartição dos Benefícios da Biodiversidade na Amazônia Brasileira*, pp. 90-95. Brasília: Estação Liberdade, 2001. Disponível em: https://www.mma.gov.br/estruturas/sbf_chm_rbbio/_arquivos/Sumario_Amazonia.pdf. Acesso em 2019. Nelson; Oliveira, 2001

NGUYEN, H. T. T. *et al.* Land Use/Land Cover Mapping Using Multitemporal Sentinel-2 Imagery and Four Classification Methods—A Case Study from Dak Nong, Vietnam. *Remote Sensing*, v. 12, p. 1367, 2020. DOI: 10.3390/rs12091367. Nguyen *et al.*, 2020

NIYONZIMA, P. *et al.* Luminescence Dating of Quartz from Ironstones of the Xingu River, Eastern Amazonia. *Quaternary Geochronology*, v. 67, p. 101241, 2022. DOI: 10.1016/j.quageo.2021.101241. Niyonzima *et al.*, 2022

NOAA - National Oceanic and Atmospheric Administration. 2019. What is ENSO? National Weather Service. Disponível em: https://www.weather.gov/mhx/ensowhat#:~:text=The%20El%20Ni%C3%B1o%2DSouthern%20Oscillation,and%20eastern%20tropical%20Pacific%20Ocean. Acessado em julho de 2023. NOAA, 2019

NOAA - National Oceanic and Atmospheric Administration. 2023. NOAA's Climate Prediction Center. Climate Prediction Center. Disponível em: https://origin.cpc.ncep.noaa.gov/products/analysis_monitoring/ensostuff/ONI_v5.php. Acesso em julho de 2023. NOAA, 2023

NorteEnergia. *A História de Belo Monte – Cronologia*. NorteEnergia, [s.d.]. Disponível em: https://www.norteenergiasa.com.br/pt-br/uhe-belo-monte/historico. Acessado em agosto de 2023.

NOVO, E. L. *et al.* Técnicas Avançadas de Sensoriamento Remoto Aplicadas ao Estudo de Mudanças Climáticas e ao Funcionamento dos Ecossistemas Amazônicos. *Acta Amazonica*, v. 35, n. 2, p. 259-272, 2005. Novo *et al.*, 2005

NOVO, E. *Sensoriamento Remoto: Princípios e Aplicações*, 3ª ed. São Paulo: Blucher, 2008. Novo, 2008

NSIDC - National Snow and Ice Data Center, a part of CIRES at the University of Colorado Boulder. Ice, Cloud, and Land Elevation / Geoscience Laser Altimeter System. [n.d.]. Disponível em: https://nsidc.org/data/icesat. Acesso em: 08/2023. NSIDC, [n.d.]

NSIDC - National Snow and Ice Data Center, a part of CIRES at the University of Colorado Boulder. (2022, June 13). The mission and support of ICESat-2 Data. Disponível em: https://nsidc.org/news-analyses/news-stories/mission-and-support-icesat-2-data. Acesso em: 08/2023. NSIDC, 2022

NV5 - NV5 Geospatial. *Classification Using Envi*. NV5, [S.d.a]. Disponível online: https://www.l3harrisgeospatial.com/docs/classification.html. Acesso em: 15 de junho de 2020.

NV5 - NV5 Geospatial. *Calculate Confusion Matrices*. NV5, [S.d.b]. Available online: https://www.l3harrisgeospatial.com/docs/calculatingconfusionmatrices.html. Acessado em 15/07/2020

NV5 - NV5 Geospatial. *Support Vector Machine Using Envi*. NV5 [s.d.c]. Disponível online: https://www.l3harrisgeospatial.com/docs/supportvectormachine.html (acessado em 14 de dezembro de 2022).

O Globo**.** *Justiça aceita ação do MPF e reduz vazão de Belo Monte para geração elétrica*. O Globo, 2021. Available online: https://oglobo.globo.com/economia/justica-aceita-

acao-do-mpf-reduz-vazao-de-belo-monte-para-geracao-eletrica-25068291. Acesso em 29 de abril de 2022.

OLIVEIRA, A. *et al.*Florestas sobre areia. In: OLIVEIRA, A.; DALY, D.; VARELLA, D. (Eds.). *Florestas do Rio Negro*, pp. 179-219. São Paulo: Companhia das Letras / UNIP, 2001. Oliveira *et al.*, 2021

OLTMAN, R. E. Reconnaissance investigations of the discharge and water quality of the Amazon River. *U. S. Geological Survey Circular*, 16, 1968. Oltman, 1968

OSWALDO, S. F. A.; SWITKES, G. *Tenotã-Mõ: Alertas sobre as consequências dos projetos hidrelétricos no Rio Xingu*. 1ª ed. International Rivers Network, 2005. Oswaldo; Switkes, 2005

OUCHRA, H.; BELANGOUR, A. Satellite Image Classification Methods and Techniques: A Survey. In: *Proceedings of the 2021 IEEE International Conference on Imaging Systems and Techniques* (IST), Kaohsiung, Taiwan, 24–26 August 2021. https://doi.org/10.1109/ist50367.2021.9651454. Ouchra; Belangour; 2021

PALHA, W. S. M. *et al.* Mapeamento e estimativa de cobertura da terra e de habitats aquáticos de várzea, na região da Amazônia Central utilizando imagens TM/Landsat-5 e SAR/JERS-1. In: *Anais do XI SBSR*. Belo Horizonte: INPE, 2003. p. 2853-2860. Palha *et al.*, 2003

PALMQUIST, H. OS 8 mil metros cúbicos Por Segundo que destroem a Volta Grande do Xingu. *SUMAÚMA*, 21 de março de 2023. Disponível em: https://sumauma.com/descoberto-mito-origem-8-mil-metros-cubicos-por-segundo-que-destroem-volta-grande-rio-xingu/. Acessado em 05/2023. Palmquist, 2023

PARÁ. Altamira: Estatística Municipal. 2011. Disponível em: http://iah.iec.pa.gov.br/iah/fulltext/georeferenciamento/altamira.pdf. Acesso em: 15 de agosto de 2020. Pará, 2011

PARIS, A. *et al.* Stage-discharge rating curves based on satellite altimetry and modeled discharge in the Amazon Basin. Water Resources Research, v. 52, n. 5, 2016. DOI: 10.1002/2014wr016618. Paris *et al.*, 2016

PEKEL, J.-F. *et al.* High-Resolution Mapping of Global Surface Water and Its Long-Term Changes. *Nature*, v. 540, p. 418-422, 2016. DOI: 10.1038/nature20584. Pekel *et al.*, 2016

PEREIRA, L. *et al.* Multifrequency and Full-Polarimetric SAR Assessment for Estimating Above Ground Biomass and Leaf Area Index in the Amazon Várzea Wetlands. *Remote Sensing*, v. 10, n. 9, p. 1355, 2018. DOI: 10.3390/rs10091355. Pereira *et al.*, 2018

PEZZUTI, J. *et al. Xingu, o Rio que Pulsa em Nós: Monitoramento Independente para Registro de Impactos da UHE Belo Monte no Território e no Modo de Vida do Povo Juruna (Yudjá) da Volta Grande do Xingu*, 1ª ed. Altamira (Pará): Instituto Socioambiental, 2018. Pezzuti *et al.*, 2018

PIETRONI, E. Virtual Museums for Landscape Valorization and Communication. *The International Archives of the Photogrammetry, Remote Sensing and Spatial Information Sciences*, v. XLII-2/W5, p. 575-582, 2017. DOI: 10.5194/isprs-archives-xlii-2-w5-575-2017. Pietroni, 2017

PIRES, J. M.; PRANCE, G. T. The Amazon Forest: a natural heritage to be preserved. In: PRANCE, G. T.; ELLIAS, S. *Extintion is Forever*. Nova Iorque: New York Botanical Garden, 1977. Pires; Prance, 1977

POFF, N. *et al.* The Natural Flow Regime. *BioScience*, v. 47, n. 11, p. 769-784, 1997. Poff, *et al.*, 1997

PONTIUS, R. G.; MILLONES, M. Death to Kappa: Birth of Quantity Disagreement and Allocation Disagreement for Accuracy Assessment. *Int. J. Remote Sens.*, v. 32, p. 4407-4429, 2011. DOI: 10.1080/01431161.2011.552923. Pontius; Millones, 2011

PORVARI, P. Mercury levels of fish in Tucuruí Hydroelectric Reservoir and in River Mojú in Amazonia, in the state of Pará, Brazil. *Science of The Total Environment*, v. 175, n. 2, p. 109-117, 1995. DOI: https://doi.org/10.1016/0048-9697(95)04907-x. Porvari, 1995

PRANCE, G. A Terminologia dos Tipos de Florestas Amazônicas Sujeitas a Inundação. *Acta Amazonica*, v. 10, n. 3, p. 495-504, 1980. Prance, 1980

PRENZEL, B. G.; TREITZ, P. Spectral and Spatial Filtering for Enhanced Thematic Change Analysis of Remotely Sensed Data. *Int. J. Remote Sens.*, v. 27, p. 835-854, 2006. DOI: 10.1080/01431160500300321. Prenzel; Treitz, 2006

PRIGENT, C. *et al.* Changes in land surface water dynamics since the 1990s and relation to population pressure. *Geophysical Research Letters*, v. 39, p. L08403, 2012. doi:10.1029/2012GL051276. Prigent *et al.*, 2012

QUESADA, C. A. *et al.* Basin-wide Variations in Amazon Forest Structure and Function Are Mediated by Both Soils and Climate. *Biogeosciences*, v. 9, 2012. Quesada*et al.*, 2012

RADAMBRASIL. *Levantamento de Recursos Naturais. Folha SA. 20 Manaus.* Rio de Janeiro: Departamento Nacional de Produção Mineral, 1978. RadamBrasil, 1978

RAMSAR - The Ramsar Convention Bureau. *Strategic Framework and Guidelines for the Future Development of the List of Wetlands of International Importance of the Convention on Wetlands (Ramsar, Iran, 1971).* Gland, Switzerland, http://www.ramsar.org/key_guide_list2006_e.htm#B, updated on the web 3/12/2012. RAMSAR, 1971

REDE XINGU MAIS. *Uhe Belo Monte. Ficha Técnica Completa UHE Belo Monte*. [s.d.]. Disponível em: https://xingumais.org.br/obra/uhe-belo-monte. Acesso em: 09/2023. Xingu Mais, [s.d.]

REID, A.; RAMOS, F.; SUKKARIEH, S. Multi-class classification of vegetation in natural environments using an unmanned aerial system. In: *2011 IEEE International*

Conference on Robotics and Automation. IEEE, 2011. p. 2953-2959. Reid; Ramos; Sukkarieh, 2011

REMONDINO, F. *et al.*3D Modeling of Complex and Detailed Cultural Heritage Using Multi-Resolution Data. *Journal on Computing and Cultural Heritage*, v. 2, n. 1, p. 1-20, 2009. DOI: 10.1145/1551676.1551678. Remondino *et al.*, 2009

REMONDINO, F.; RIZZI, A. Reality-Based 3D Documentation of Natural and Cultural Heritage Sites—Techniques, Problems, and Examples. *Applied Geomatics*, v. 2, n. 3, p. 85-100, 2010. DOI: 10.1007/s12518-010-0025-x. Remondino; Rizzi, 2010

REMONDINO, F. Heritage Recording and 3D Modeling with Photogrammetry and 3D Scanning. *Remote Sensing*, v. 3, n. 6, p. 1104-1138, 2011. DOI: 10.3390/rs3061104. Remondino, 2011

REVILLA, J. C. Aspectos Florísticos e Fitossociológicos da Floresta Inundável (Igapó) Praia Grande, Rio Negro, Amazonas, Brasil. Dissertação de Mestrado apresentada ao Programa de Pós-Graduação do Instituto Nacional de Pesquisas Amazônicas. Manaus: Fundação Universidade do Amazonas, 1981. Revilla, 1981

RICHARDS, J. A. Synthetic Aperture Radar. In: HOFFMAN, C.; DRIGGERS, R. (Eds.). *Optical and Photonic Engineering*, 2ª ed. CRC Press, 2015. DOI: 10.1081/E-EOE2-120050616. Richards, 2015

RICHTER, B. *et al.* A Method for Assessing Hydrologic Alteration within Ecosystems. *Conservation Biology*, v. 10, n. 4, p. 1163-1174, agosto de 1996. Richter *et al.*, 1996

RITTER, C. D. *et al.* Environmental Impact Assessment in Brazilian Amazonia: Challenges and Prospects to Assess Biodiversity. *Biological Conservation*, v. 206, p. 161-168, 2017. DOI: 10.1016/j.biocon.2016.12.031. Ritter *et al.*, 2017

RODRIGUES, W. A. Estudo Preliminar de Mata de Várzea Alta de uma Ilha do Baixo Rio Negro de Solo Argiloso e Úmido. Série Botânica. INPA, 1961. Rodrigues, 1961

ROMAN, C. *The Solution to Belo Monte's Environmental Chaos Is on Ibama's Table*: ISA. Instituto Socioambiental – ISA, 2023. Disponívl em https://socioambiental.org/en/socio-environmental-news/The-solution-to-the-environmental-chaos-in-Belo-Monte-is-on-the-table-at-IBAMA. Acessado em 08/2023 Roman, 2023

ROMAN, C., & MANTOVANELLI, T. *Pulse, Xingu! O caminho para reviver Volta Grande após Belo Monte*: ISA. Instituto Socioambiental – ISA, 2023. Disponível em https://www.socioambiental.org/en/socio-environmental-news/pulsa-xingu-the-way-to-relive-big-turn-after-beautiful-mount. Acessado em 08/2023. Roman; Mantovanelli, 2023

ROSA, I. M.; GABRIEL, C.; CARREIRAS, J. M. Spatial and Temporal Dimensions of Landscape Fragmentation across the Brazilian Amazon. *Reg. Environ. Change*, v. 17, p. 1687–1699, 2017. DOI: 10.1007/s10113-017-1120-x. Rosa; Gabriel; Carreiras, 2017

RUSSI, D. *et al. The Economics of Ecosystems and Biodiversity for Water and Wetlands*. IEEP, London and Brussels: Ramsar Secretariat, Gland, 2013. 84 pp. Russi *et al*., 2013

SABAJ-PEREZ, M. Where The Xingu Bends and Will Soon Break. *American Scientist*, v. 103, n. 06, p. 395, 2015. Acesso em 2018. Disponível em: https://www.americanscientist.org/article/where-the-xingu-bends-and-will-soon-break. Sabaj-Perez, 2015

SALOMÃO, R. D. *et al.* As Florestas De Belo Monte Na Grande Curva Do Rio Xingu, Amazônia Oriental. *Boletim do Museu Paraense Emílio Goeldi - Ciências Naturais*, v. 2, n. 3, p. 57–153, 2007. DOI: 10.46357/bcnaturais.v2i3.696. Salomão *et al.*, 2007

SANTANA, A. C. *et al.* Influência da Barragem de Tucuruí no desempenho da pesca artesanal, Estado do Pará. *Revista de Economia e Sociologia Rural*, v. 52, n. 2, p. 249-266, 2014. DOI: https://doi.org/10.1590/s0103-20032014000200003. Santana *et al.*, 2014

SANTOS DA SILVA, J. *et al.* Water levels in the Amazon Basin derived from the ERS 2 and Envisat Radar Altimetry Missions. *Remote Sensing of Environment*, v. 114, n. 10, p. 2160-2181, 2010. DOI: https://doi.org/10.1016/j.rse.2010.04.020. Santos *et al.*, 2010

SANTOS, R. E. *et al. The decline of fisheries on the Madeira River, Brazil: The high cost of the hydroelectric dams in the Amazon Basin*. *Fisheries Management and Ecology*, v. 25, n. 5, p. 380-391, 2018. DOI: 10.1111/fme.12305. Santos *et al.*, 2018

SANTOSO, A. W. *et al.* Comparison of Various Speckle Noise Reduction Filters on SAR Images. *International Journal of Applied Engineering Research*, v. 11, pp. 8760-8767, 2016. Santoso *et al.*, 2016

SARTORELLI, P. A. R. (Ed.). *Plantas dos povos da Volta Grande do Xingu*. Baobá Florestal, 2018. Sartorelli, 2018

SAWAKUCHI, A. O. *et al.* The Volta Grande Do Xingu: Reconstruction of Past Environments and Forecasting of Future Scenarios of a Unique Amazonian Fluvial Landscape. *Scientific Drilling*, v. 20, p. 21–32, 2015. DOI: 10.5194/sd-20-21-2015. Sawakuchi *et al.*, 2015

SCHOBBENHAUS, C. *et al. Geologia do Brasil: Texto explicativo do mapa geológico do Brasil e da área oceânica adjacente incluindo depósitos minerais, escala 1:250.000.* CNPM—Departamento Nacional de Produção Mineral, 1984. Schobbenhaus *et al.*, 1984

SCHÖNGART, J. *et al.* The shadow of the Balbina dam: A synthesis of over 35 years of downstream impacts on floodplain forests in central Amazonia. *Aquatic Conservation: Marine and Freshwater Ecosystems*, v. 31, n. 5, p. 1117–1135, 2021. DOI: 10.1002/aqc.3526. Schöngart *et al.*, 2021

SEVÁ FILHO, O. Povos indígenas, as cidades, e os beiradeiros do rio Xingu que a empresa de eletricidade insiste em barrar. In: SEVÁ FILHO, O.; SWITKES, G. (Ed.). *Tenotã-Mõ: Alertas sobre as consequências dos projetos hidroelétricos no rio Xingu* (1ª

ed., pp. 29-54). International Rivers Network, 2005. Acesso em 2019, disponível em http://www.fem.unicamp.br/~seva/Tenota-Mo_caps1a3_pag92.pdf. Sevá Filho, 2005

SHAHBAZI, M.; THÉAU, J.; MÉNARD, P. Recent applications of unmanned aerial imagery in natural resource management. *GIScience & Remote Sensing*, v. 51, n. 4, p. 339-365, 2014. Shahbazi; Théau; Ménard, 2014

SHAW, A. *et al.* Making Local Futures Tangible—Synthesizing, Downscaling, and Visualizing Climate Change Scenarios for Participatory Capacity Building. *Global Environmental Change*, v. 19, n. 4, p. 447–463, 2009. DOI: 10.1016/j.gloenvcha.2009.04.002. Shaw *et al.*, 2009

SHI, X.; DONG, X.; ZHANG, Y. Height error analysis of range migration in interferometric imaging radar altimeter onboard processing. In: 2021 CIE International Conference on Radar (Radar). 2021. DOI: 10.1109/radar53847.2021.10028653. Shi; Dong; Zhang, 2021

SHI, Z.; FUNG, K. B. A Comparison of Digital Speckle Filters. In: Proceedings of IGARSS 94 - 1994 IEEE International Geoscience and Remote Sensing Symposium, Pasadena, CA, USA, 1994, p. 2129-2199. DOI: 10.1109/IGARSS.1994.399671. Shi; Fung, 1994

SHIMADA, M. User's Guide to NASDA's SAR products Ver.3. Earth Observation Research Center (EORC), Tokyo, 2002. Acesso em 2020, disponível em http://www.eorc.jaxa.jp/JERS-1/en/user_handbook/User_handbook_sar_ver3.pdf. Shimada, 2002

SHINGROY, V. Interpretation of SAR images for coastal zone mapping in Guyana. *Canadian Journal of Remote Sensing*, v. 22, pp. 317-328, 1996. Shingroy, 1996

SIMPSON, J.; SPEAKE, J. (Eds.). *The Oxford Dictionary of Proverbs* (Vol. 5 ed.). Oxford, Inglaterra: Oxford University Press, 2009. DOI: 9780191727740. Simpson; Speake, 2009

SINGH, A. Review Article Digital Change Detection Techniques Using Remotely-Sensed Data. *Int. J. Remote Sens.*, v. 10, p. 989–1003, 1989. DOI: 10.1080/01431168908903939. Singh, 1989

SIOLI, H. Das Wasser im Amazonasgebiet. *Forschungen und Fortschritte*, v. 26, p. 21-22, 274-280, 1950. Sioli, 1950

SIOLI, H. Sobre a sedimentação na várzea do Baixo Amazonas. *Boletim Técnico do Instituto Agronômico do Norte*, v. 24, pp. 45-65, junho de 1951. Sioli, 1951

SIOLI, H. Estudo preliminar das relações entre a geologia e a limnologia da zona bragantina (Pará). *Boletim Técnico do Instituto Agronômico do Norte*, v. 24, pp. 67-76, 1961. Sioli, 1961

SKOLE, D. L., *et al.*D. Physical and Human Dimensions of Deforestation in Amazonia. *BioScience*, v. 44, p. 314–322, 1994. DOI: 10.2307/1312381. Skole *et al.*, 1994

SMITH, M. W.; CARRIVICK, J. L.; QUINCEY, D. J. Structure from Motion Photogrammetry in Physical Geography. *Progress in Physical Geography: Earth and Environment*, v. 40, n. 2, p. 247–275, 2015. DOI: 10.1177/0309133315615805. Smith; Carrivick; Quincey, 2015

SNAP - The Sentinel Application Platform. *Machine Learning Manual–Random Forest*. Manual-Snap Machine Learning documentation. [s.d.]. Disponível online: https://ibmsoe.github.io/snap-ml-doc/v1.6.0/manual.html#random-forest (acessado em 20 de janeiro de 2022). SNAP, [s.d.]

SOARES, L. C. Limites Meridionais e Orientais da Área de Ocorrência da Floresta Amazônica em Território Brasileiro. *Revista Brasileira de Geografia*, v. 1, p. 3-122, 1953. Soares, 1953

SOLA, F. Gerenciamento Integrado dos Recursos Hídricos Compartilhados na Bacia Amazônica. São Paulo: Tese (Doutorado em Ciência Ambiental) - Programa de Pós-Graduação em Ciência Ambiental, 2012. Sola, 2012

SOLER, L. D. S.; VERBURG, P. Combining Remote Sensing and Household Level Data for Regional Scale Analysis of Land Cover Change in the Brazilian Amazon. *Reg. Environ. Change*, v. 10, p. 371–386, 2010. DOI: 10.1007/s10113-009-0107-7. Soler; Verburg, 2010

SOUZA FILHO, P. M. *et al.* Sistema de observação costeira e o papel dos sensores remotos no monitoramento da costa norte brasileira, Amazônia. *RBC - Revista Brasileira de Cartografia*, v. 57, pp. 79-86, 2005. Souza Filho *et al.*, 2005

SOUZA FILHO, P. W.; PARADELLA, W. R.; SILVEIRA, O. F. Synthetic Aperture Radar for Recognition of Coastal Features in the Wet Tropics: Applications in the Brazilian Amazon Coast. *Boletim do Museu Paraense Emílio Goeldi, série Ciências Naturais*, v. 1, pp. 149-154, 2005. Souza Filho; Paradella; Silveira, 2005

SOUZA, C. M. *et al.* Reconstructing three decades of land use and land cover changes in Brazilian biomes with Landsat Archive and Earth Engine. *Remote Sens.*, v. 12, 2735, 2020. DOI: 10.3390/rs12172735. Souza *et al.*, 2020

SOUZA, D. F. Evolução sedimentar do Tabuleiro do Embaubal, Baixo Rio Xingu. Dissertação de mestrado apresentada ao Programa de Pós-Graduação em Geoquímica e Geotectônica. São Paulo: IGc USP, 2015. Souza, 2015

SPARKS, R. Risks of altering the hydrologic regime of large rivers. In: CAIRNS, J.; NIEDERLEHNER, B.; ORVOS, D. (Eds.). *Predicting ecosystem risk: advances in modern environmental toxicology* (Vol. 20, pp. 119-152). New Jersey: Princeton Scientific, 1992. Sparks, 1992

STEPHENSON, J. The Cultural Values Model: An Integrated Approach to Values in Landscapes. *Landscape and Urban Planning*, v. 84, n. 2, p. 127–139, 2008. DOI: 10.1016/j.landurbplan.2007.07.003. Stephenson, 2008

STORY, M. Accuracy Assessment: A User's Perspective. *Photogramm. Eng. Remote Sens.*, v. 52, p. 397–399, 1986. Disponível online: https://www.asprs.org/wp-content/uploads/pers/1986journal/mar/1986_mar_397-399.pdf (acessado em 15 de julho de 2022). Story, 1986

SWANSON, A. C.; BOHLMAN, S. Cumulative Impacts of Land Cover Change and Dams on the Land–Water Interface of the Tocantins River. *Front. Environ. Sci.*, v. 9, 662904, 2021. DOI: 10.3389/fenvs.2021.662904. Swanson; Bohlman, 2021

TADEI, W.P.; MASCARENHAS, B.M.; PODESTÁ, M.G. Biologia de anofelinos amazônicos. VIII. Conhecimentos sobre a distribuição de espécies de Anopheles na região de Tucuruí-Marabá (Pará). *Acta Amazonica*, v. 13, n. 1, p. 103-140, 1983. Tadei; Mascarenhas; Podestá, 1983

TINER, R. W. Early Applications of Remote Sensing for Mapping Wetlands. In: TINER, R. W.; LANG, M. W.; KLEMAS, V. V. *Remote Sensing of Wetlands - Applications and Advances*. Boca Raton: CRC Press, 2015. Cap. 4, p. 544. ISBN 978-1-4822-3738-2. Tiner, 2015

TUAN, Y. F. *Space and Place: The Perspective of Experience*. University of Minnesota Press, 2011. Tuan, 2011

UHL, C.; KAUFFMAN, J. B. Deforestation fire susceptibility, and potential tree responses to fire in the eastern Amazon. *Ecology*, v. 9, 1990. Uhl; Kauffman, 1990

UNESCO – Organização das Nações Unidas para a Educação, Ciência e Cultura. Institute of Statistics. *Natural Heritage*. UNESCO UIS, 2009. Disponível em: https://uis.unesco.org/en/glossary-term/natural-heritage. UNESCO, 2009

UNESCO - Organização das Nações Unidas para a Educação, Ciência e Cultura. World Heritage Centre. *Convenção Para a Proteção Do Patrimônio Mundial, Cultural e Natural*. UNESCO World Heritage Centre - Document, 16 de novembro de 1972. Disponível em: https://whc.unesco.org/en/documents/170667. UNESCO, 1972

URRY, J. *The Tourist Gaze: Leisure and Travel in Contemporary Societies* (2ª ed.). Sage, 2002. Urry, 2002

URBAN, T. J.; SCHUTZ, B. E.; NEUENSCHWANDER, A. L.. A survey of ICESat coastal altimetry applications: Continental Coast, Open Ocean Island, and Inland River. *Terrestrial, Atmospheric and Oceanic Sciences*, 19(1–2), 1. 2008. https://doi.org/10.3319/tao.2008.19.1-2.1(sa). Urban; Schutz; Neuenschwander, 2008

USGS - United States Geological Survey. 2000. Landsat-07 LE07_L1TP_225062_20000526_20170211_01_T1 - cena LE72250622000147AGS01. Acesso em 2019, disponível em Earth Explorer: https://earthexplorer.usgs.gov/. USGS, 2000

USGS - United States Geological Survey. *Landsat Image Gallery Platform*. USGS, [s.d.]. Disponível online: https://earthexplorer.usgs.gov/ (acessado em 15 de novembro de 2022). USGS, [n.d.]

VASCONCELOS, C. H.; NOVO, E. L. Mapeamento do uso e cobertura da terra a partir da segmentação e classificação de imagem-fração solo, sombra e vegetação derivadas do modelo linear de mistura aplicado a dados do sensor TM/Landsat-5, na região do reservatório de Tucuruí. *Acta Amazonica*, v. 34, pp. 487-493, 2004. Vasconcelos; Novo, 2004

VERSTAPPEN, H. T. Old and New Trends in Geomorphological and Landform Mapping. In: SMITH, M. J.; PARON, P.; GRIFFITHS, J. S. (Eds.). *Geomorphological Mapping: Methods and Application*, pp. 13-38. Amsterdam: Elsevier, 2011. Verstappen, 2011

VIANA, C. D. *et al.* Structural Analysis of Clastic Dikes Using Structure from Motion-Multi-View Stereo: A Case-Study in the Paraná Basin, Southeastern Brazil. *Braz. J. Geol.*, v. 48, p. 839–852, 2018. DOI: 10.1590/2317-4889201800201898. Viana *et al.*, 2018

VIERLING, K. T., *et al.* Lidar: shedding new light on habitat characterization and modeling. *Frontiers in Ecology and Environment*, v. 6, pp. 90-98, 2008. Vierling *et al.*, 2008

VILLAS-BOAS, A. *De Olho na Bacia do Xingu*. Cartô Brasil Socioambiental; Instituto Socioambiental: São Paulo, Brazil, 2012; Volume 5, p. 5. Villas-Boas, 2012

VILLAS-BÔAS, A.; ROJAS, B. Comitês de Bacia Hidrográfica na Amazônia são inadiáveis. *Blog do Xingu*. 2014. Acesso em maio de 2019, disponível em https://www.socioambiental.org/pt-br/blog/blog-do-xingu/comites-de-bacia-hidrografica-na-amazonia-sao-inadiaveis#:~:text=Dessa%20forma%2C%20os%20CBH%20t%C3%AAm,e%20econ%C3%B4micas%20por%20recursos%20naturais. Villas-Boas; Rojas, 2014

VIRK, R.; KING, D. Comparison of Techniques for Forest Change Mapping Using Landsat Data in Karnataka, India. *Geocarto Int.*, v. 21, p. 49–57, 2006. DOI: 10.1080/10106040608542402. Virk; King, 2006

WABIŃSKI, J.; MOŚCICKA, A. Natural Heritage Reconstruction Using Full-Color 3D Printing: A Case Study of the Valley of Five Polish Ponds. *Sustainability*, v. 11, n. 21, 5907, 2019. DOI: 10.3390/su11215907. Wabiński; Mościcka, 2019

WACKERNAGEL, H. *Multivariate Geostatistics*. 2003. DOI: 10.1007/978-3-662-05294-5. Wackernagel, 2003

WALLACE, A. *Viagens pelo Amazonas e Rio Negro*. Traduzido por O. Torres. Rio de Janeiro: Companhia Editora Nacional, 1939. Wallace, 1939

WANG, Z. X. From AVHRR-NDVI to MODIS-EVI: advances in vegetation index research. *Acta Ecologica Sinica*, v. 23, pp. 979-988, 2003. Wang, 2003

WARNER, B.G.; RUBEC, C.D.A. (eds.). *The Canadian Wetland Classification System*, 2ª ed. National Wetlands Working Group. Research Centre, University of Waterloo, Waterloo, Ontario, Canadá, 1997. http://www.gret-

perg.ulaval.ca/fileadmin/fichiers/fichiersGRET/pdf/Doc_generale/Wetlands.pdf. Acesso em 7 de novembro de 2014. Warner; Rubec, 1997

WATTS, J. Belo Monte, Brazil: The Tribes Living in the Shadow of a Megadam. *The Guardian*, 16 de dezembro de 2014. Disponível em: https://www.theguardian.com/environment/2014/dec/16/belo-monte-brazil-tribes-living-in-shadow-megadam. Watts, 2014

WESTOBY, M. J. *et al.*"Structure-from-Motion" Photogrammetry: A Low-Cost, Effective Tool for Geoscience Applications. *Geomorphology*, v. 179, p. 300–314, 2012. DOI: 10.1016/j.geomorph.2012.08.021. Westboy *et al.*, 2012

WHITMORE, T. C. *An Introduction to Tropical Rain Forests*. Oxford: Clarendon Press, 1990. Whitmore, 1990

WINEMILLER, K. O. *et al.* Balancing hydropower and biodiversity in the Amazon, Congo, and Mekong. *Science*, v. 351, p. 128–129, 2016. DOI: 10.1126/science.aac7082. Winemiller *et al.*, 2016

WITTMANN, F.; JUNK, W.; PIEDADE, M. The várzea forests in Amazonia: flooding and the highly dynamic geomorphology interact with natural forest succession. *Forest Ecology and Management*, pp. 199-212, 2004. DOI: 10.1016/j.foreco.2004.02.060. Wittmann; Junk; Piedade, 2004

WITTMANN, F. *et al.* Tree species composition and diversity gradients in white-water forests across the Amazon Basin. *Journal of Biogeography*, v. 33, n. 8, p. 1334–1347, 2006. DOI: 10.1111/j.1365-2699.2006.01495. Wittmann *et al.*, 2006

WORBES, M. *et al.* On the dynamics, floristic subdivision and geographical distribution of várzea forests in Central Amazonia. *Journal of Vegetation Science*, v. 3, pp. 553-564, 1992. DOI: 10.2307/3235812. Worbes *et al.*, 1992

WULDER, M. A. *et al.* High Spatial Resolution Remotely Sensed Data for Ecosystem Characterization. *BioScience*, v. 54, n. 6, p. 511, 2004. DOI: 10.1641/0006-3568. Wulder *et al.*, 2004

XU, N. *et al.* Surface-water-level changes during 2003–2019 in Australia revealed by ICESat/ICESat-2 altimetry and Landsat imagery. IEEE Geoscience and Remote Sensing Letters, v. 18, n. 7, p. 1129–1133, 2021. DOI: 10.1109/lgrs.2020.2996769. Xu *et al.*, 2021

YIN, L. Integrating 3D Visualization and GIS in Planning Education. *Journal of Geography in Higher Education*, v. 34, n. 3, p. 419–438, 2010. DOI: 10.1080/03098260903556030. Yin, 2010

ZANOTTA, D.; FERREIRA, M.; ZORTEA, M. *Processamento de Imagens de Satélite*, 1ª ed. São Paulo: Oficina de Textos, 2019. Zanotta; Ferreira; Zortea, 2019

ZEPPEL, H. Education and Conservation Benefits of Marine Wildlife Tours: Developing Free-Choice Learning Experiences. *The Journal of Environmental Education*, v. 39, n. 3, p. 3–18, 2008. DOI: 10.3200/joee.39.3.3-18. Zeppel, 2008

ZHANG, Guoqing *et al.* Water level variation of Lake Qinghai from satellite and in situ measurements under climate change. *Journal of Applied Remote Sensing*, v. 5, n. 1, p. 053532-053532-15, 2011. Zhang *et al.*, 2011

ZHU, Z. Change Detection Using Landsat Time Series: A Review of Frequencies, Preprocessing, Algorithms, and Applications. *ISPRS J. Photogramm. Remote Sens.*, v. 130, p. 370–384, 2017. DOI: 10.1016/j.isprsjprs.2017.06.013. Zhu, 2017

ZUANON, J. *et al.* Condições Para a Manutenção Da Dinâmica Sazonal De Inundação, a Conservação Do Ecossistema Aquático E Manutenção Dos Modos De Vida Dos Povos Da Volta Grande Do Xingu. *Papers do NAEA*, v. 28, n. 2, 2019. DOI: 10.18542/papersnaea.v28i2.8106. Zuanon *et al.*, 2019

ZWALLY, H. J. *et al.GLAS/ICESat L1B Global Elevation Data, Version 34*. Boulder, Colorado, EUA. NASA National Snow and Ice Data Center Distributed Active Archive Center, 2014. DOI: http://dx.doi.org/10.5067/ICESAT/GLAS/DATA126. Zwally*et al.*, 2014

APÊNDICE A – Supplementary material of "3d Modeling as a Conservation Tool to Characterize Endangered Seasonally Flooded Ecosystems in the Volta Grande Do Xingu, Amazon Forest, Pará, Brazil"

Supplementary Tables

Tabela A_1: Acquisition details from all flight missions of the field trip occurred between 07 to 14 of November/2021 in the Volta Grande do Xingu (VGX) area.

		Flight Parameters				
Mission ID	Year_Month_Day_Mission_#	Flight Height (m)	Resolution (cm/pixel)	Covered Area (ha)	Image footprint (m)	Number of images
1	2021_11_09_01	25	0.75	1.00	25x40	121
2	2021_11_09_02	200	5.77	37.23	200x300	91
3	2021_11_09_03	35	0.98	2.84	35x50	333
4 (a)	2021_11_09_04	30	0.85	1.31	30x45	189
5	2021_11_09_05	25	0.74	0.40	25x40	61
6 (b)	2021_11_09_06	15	0.48	0.18	15x20	49
7 (c)	2021_11_09_07	15	0.5	0.18	15x20	29
8	2021_11_09_08	15	0.51	0.30	15x20	99
9	2021_11_09_09	25	0.82	1.07	25x40	125
10	2021_11_10_01	20	0.58	0.75	20x30	319
11	2021_11_10_02	100	2.83	15.89	100x150	206
12 (d)	2021_11_10_03	20	0.55	1.11	20x30	340
13	2021_11_10_04	210	6.03	44.74	210x315	64
14 (e)	2021_11_10_05	35	1.09	3.24	35x50	215
15	2021_11_10_06	35	1.09	0.98	35x50	60
16 (f)	2021_11_10_07	55	1.55	1.21	55x80	94
17	2021_11_11_01	250	6.76	31.51	250X375	49
18	2021_11_12_01	250	7.45	48.47	250X375	72
19	2021_11_12_02	250	7.41	46.77	250X375	72
20	2021_11_12_03	35	1.11	2.32	35x50	246
21	2021_11_12_04	35	1.21	2.52	35x50	230
22	2021_11_12_05	300	8.28	54.35	300x450	64
23	2021_11_12_06	35	1.05	1.51	35x50	196
24 (g)	2021_11_12_07	20	0.55	0.79	20x30	249
25	2021_11_12_08	20	0.6	0.84	20x30	216
26 (h)	2021_11_13_01	55	1.5	5.34	55x80	336
27	2021_11_13_02	300	8.29	55.17	300x450	63
28	2021_11_13_03	300	8.25	60.25	300x450	65
29	2021_11_13_04	300	8.28	72.00	300x450	71
30 (i)	2021_11_13_05	35	1.02	2.35	35x55	306
31	2021_11_13_06	300	8.35	58.29	300x450	60
32	2021_11_14_01	35	0.98	1.76	35x50	299
33	2021_11_14_02	35	1.04	1.36	35x50	239
34	2021_11_14_03	10	0.31	0.07	10x15	39
35	2021_11_14_05	10	0.27	0.36	10x15	276
36	2021_11_14_06	300	8.26	51.08	300x450	32

37	2021_11_14_07	290	8.11	43.00	290x445	25

Tabela A_2: Processing quality parameters from the calibration step of the SfM stage for all the 37 mission flights processed in the Agisoft Metashape Pro. Reprojection error is a quantitative measure of how well the 3D model matches the images used to create it. Very good models are expected to have reprojection errors smaller than 0.5 pixels.

Processing Quality Parameters			
Mission ID	Calibrated images (%)	Reprojection errors (px)	Geolocated images (%)
1	76	0.21	100
2	100	0.204	100
3	100	0.23	100
4 (a)	97	0.221	100
5	100	0.218	100
6 (b)	100	0.206	100
7 (c)	100	0.203	100
8	100	0.221	100
9	96	0.2	100
10	77	0.191	100
11	100	0.159	100
12 (d)	98	0.159	100
13	100	0.148	100
14 (e)	100	0.178	100
15	100	0.164	100
16 (f)	47	0.15	100
17	100	0.159	100
18	100	0.163	100
19	100	0.169	100
20	100	0.174	100
21	100	0.159	100
22	98	0.159	100
23	100	0.176	100
24 (g)	99	0.171	100
25	100	0.172	100
26 (h)	97	0.188	100
27	100	0.152	100
28	100	0.156	100
29	100	0.159	100
30 (i)	100	0.164	100
31	100	0.16	100
32	84	0.164	100
33	92	0.158	100
34	100	0.15	100
35	99	0.153	100
36	100	0.13	100
37	100	0.138	100

Tabela A_3: Dense point cloud details for each one of the 37 products.

Point Cloud Parameters		
Mission ID	3D Densified Points	Average Density (points/m^3)
1	10,155,774	5427.72
2	9,584,031	16.55
3	32,329,174	4181.59
4 (a)	16,871,769	4731.59
5	6,322,713	6745.42
6 (b)	5,522,943	21260.7
7 (c)	4,645,140	17864.9
8	9,950,690	20709
9	12,502,943	4792.47
10	16,304,985	14762.4
11	15,156,161	145.84
12 (d)	30,018,131	19078.6
13	7,529,102	11.91
14 (e)	22,910,754	2411.63
15	6,531,316	2398.64
16 (f)	5,701,895	720.08
17	5,698,975	8.13
18	6,298,971	7.78
19	6,102,089	7.95
20	25,388,168	2150.81
21	10,558,877	1727.38
22	6,480,977	5.14
23	13,689,870	3117.41
24 (g)	21,241,128	18067.5
25	17,852,465	13473.3
26 (h)	26,231,626	867.04
27	6,292,738	4.53
28	7,941,454	4.31
29	8,959,341	4.28
30 (i)	25,107,793	4034.37
31	5,227,409	4.82
32	16,531,057	3756.15
33	11,948,435	3464.72
34	4,167,731	73442.7
35	32,626,063	138185
36	4,062,480	3.63
37	3,873,628	3.69

Tabela A_4: Percentage of images with geolocation errors associated with the geolocation variance in the x, y and z directions. Geolocation error is the difference between the initial and computed image position. Low RMSE values are expected for good predicted geographic positions of points and their actual real-world geographic position.

Geolocation Variance Errors (%)			
Mission ID	RMSE Long	RMSE Lat	RMSE Elevation
1	0.37	0.47	0.60
2	0.37	0.25	0.21
3	0.66	0.34	0.25
4 (a)	0.19	0.50	0.22
5	0.21	0.41	0.17
6 (b)	0.31	0.16	0.16
7 (c)	0.17	0.17	0.19
8	0.28	0.11	0.16
9	0.36	0.37	0.14
10	0.35	0.27	0.32
11	0.36	0.40	0.35
12 (d)	0.50	0.39	0.27
13	0.42	0.25	0.73
14 (e)	0.48	0.45	0.28
15	0.28	0.40	0.29
16 (f)	0.65	0.89	2.08
17	0.30	0.46	0.41
18	0.33	0.40	0.29
19	0.45	0.65	0.36
20	0.38	0.53	0.37
21	0.48	0.47	0.40
22	0.44	0.47	0.58
23	0.40	0.39	0.32
24 (g)	0.26	0.23	0.22
25	0.35	0.37	0.30
26 (h)	0.80	0.76	0.42
27	0.28	0.25	0.39
28	0.34	0.26	0.55
29	0.24	0.40	0.57
30 (i)	0.63	0.80	0.27
31	0.41	0.28	0.50
32	1.21	1.03	0.43
33	0.93	0.79	0.38
34	0.37	0.22	0.28
35	0.26	0.21	0.24
36	0.40	0.70	0.37
37	0.68	0.29	0.30

Supplementary Figures

Figura A_1: Top left: High Resolution Orthophoto; Bottom left: Digital Surface Model; Right: Static view of the 3D model generated from the imagery captured during flight #4 (ID a) obtained on November 09, 2021, depicting the rocky environment *pedral* and the *saroba* associated with it. The darker spots are the *mocororô*.

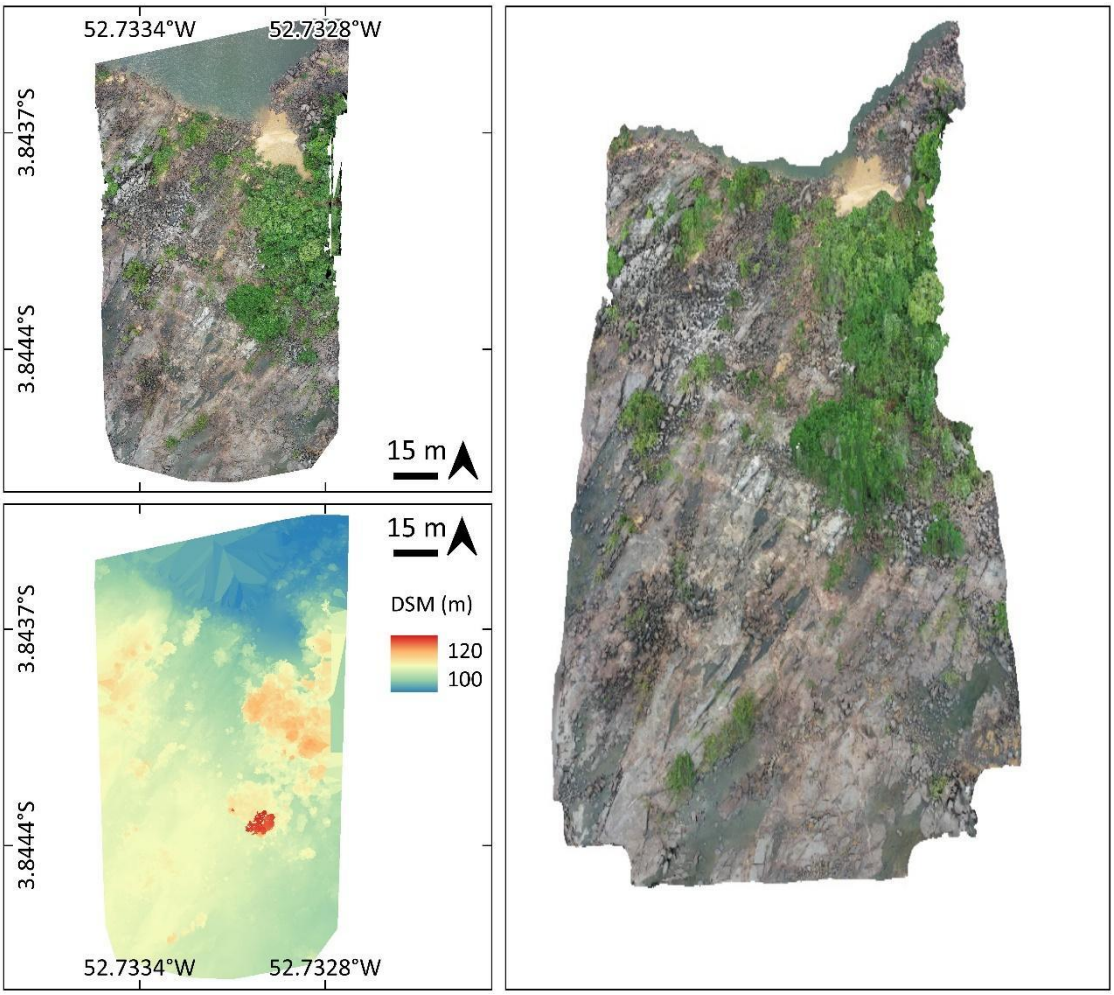

Fonte: Autoria própria

Figura A_2: Top left: Very High Resolution Orthophoto; Bottom left: Digital Surface Model; Right: Static view of the 3D model generated from the imagery captured during flight #7 (ID c) realized on November 09, 2021, depicting a sandy environment at the rocky boulders (pedral) and the sarobal associated with it. The darker spots are the mocororô.

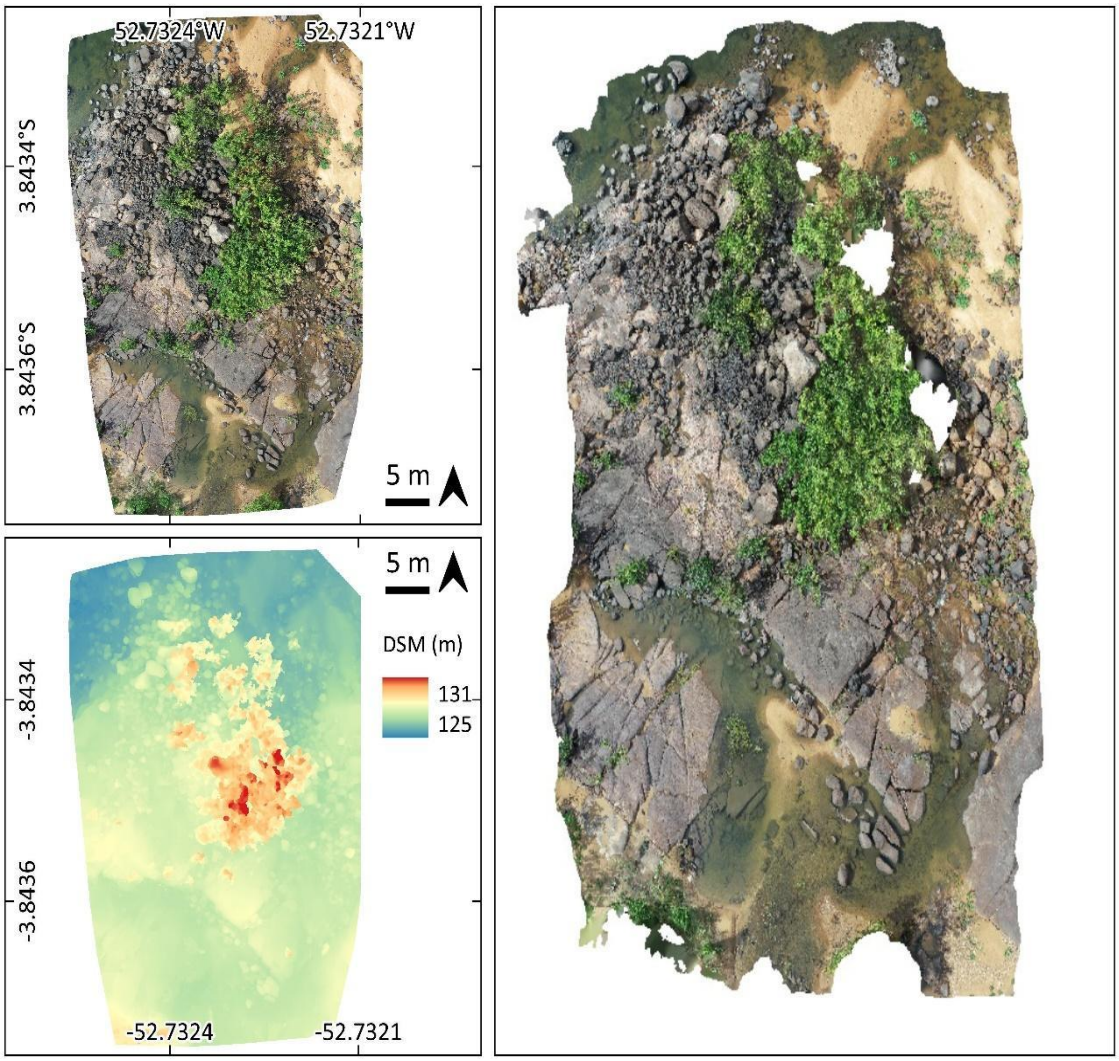

Fonte: Autoria própria

Figura A_3: Top left: Very High Resolution Orthophoto; Bottom left: Digital Surface Model; Right: Static view of the 3D model generated from the imagery captured during flight #3 (ID d) obtainedon November 10, 2021, depicting the rocks from the *pedral* and the *saroba* with its typical shrubby vegetation fixed in the sand. The darker spots are the *mocororô*. The void in the model corresponds with a deep water column.

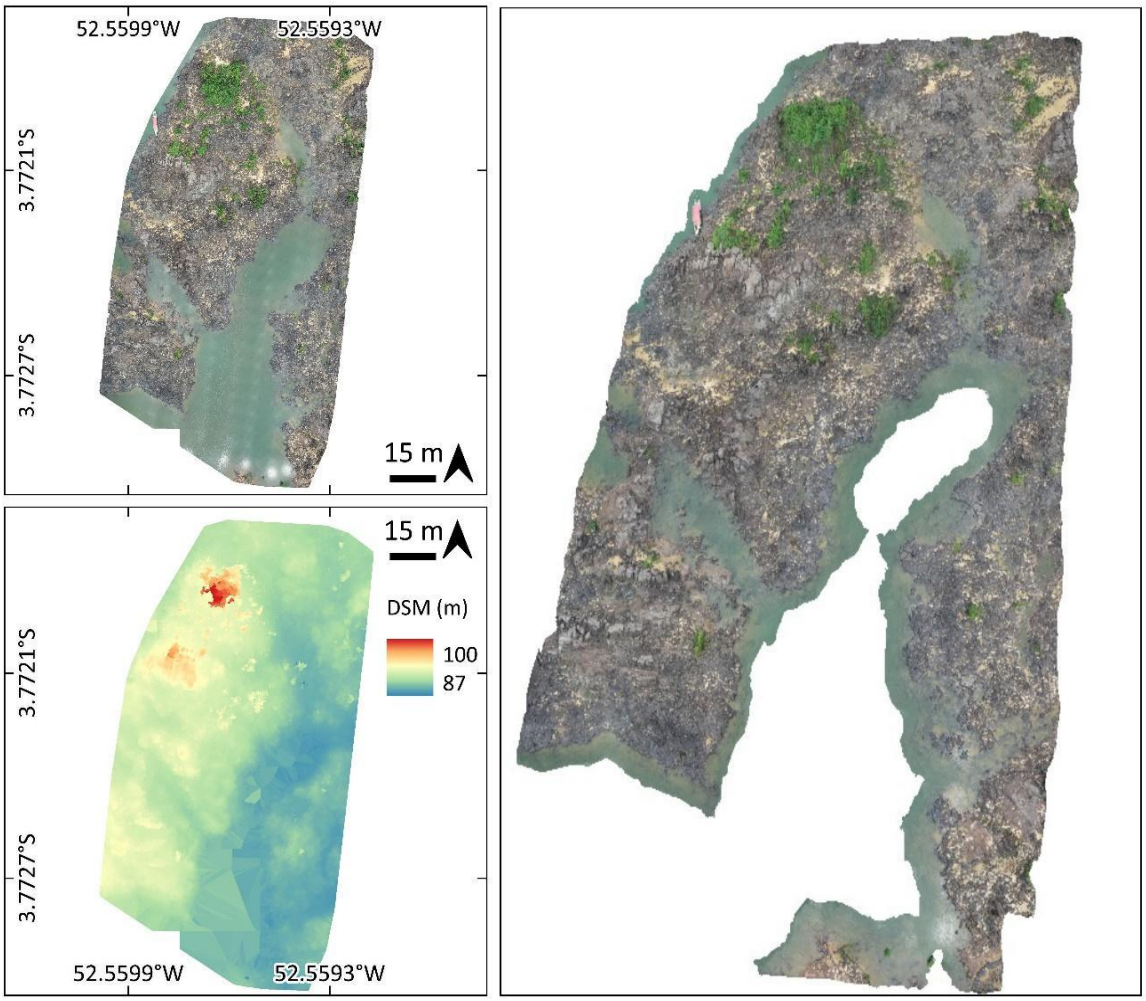

Fonte: Autoria própria

Figura A_4: Top left: High Resolution Orthophoto; Top right: Digital Surface Model; Bottom: Static view of the 3D model generated from the imagery captured during flight #5 (ID e) obtained on November 10, 2021, depicting the *sequeiro*, which is a shallow or dry area with interspersed rocks and small patches of beach and small streams. It can be observed that the herbaceous vegetation is exclusive to the sandy environment.

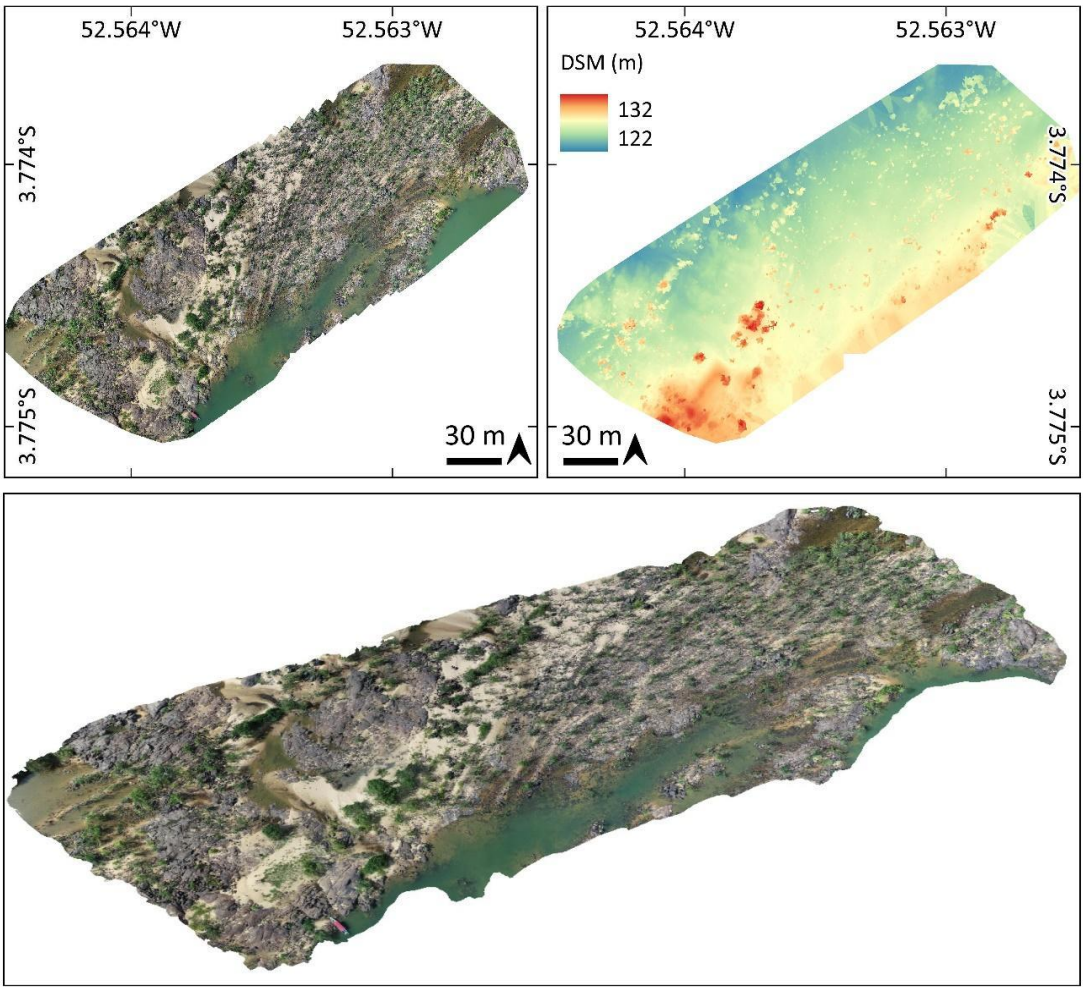

Fonte: Autoria própria

Figura A_5*:* Top left: Very High Resolution Orthophoto; Top right: Digital Surface Model; Bottom: Static view of the 3D model generated from the imagery captured during flight #7 (ID g) obtained on November 12, 2021, depicting the *pedral*. Here, the typical fractured banded gneisses with the ironstones from the *mocororô* protruding from it are visualized. It is also noteworthy how the submerged environment can be sucessfully modeled in shallow waters.

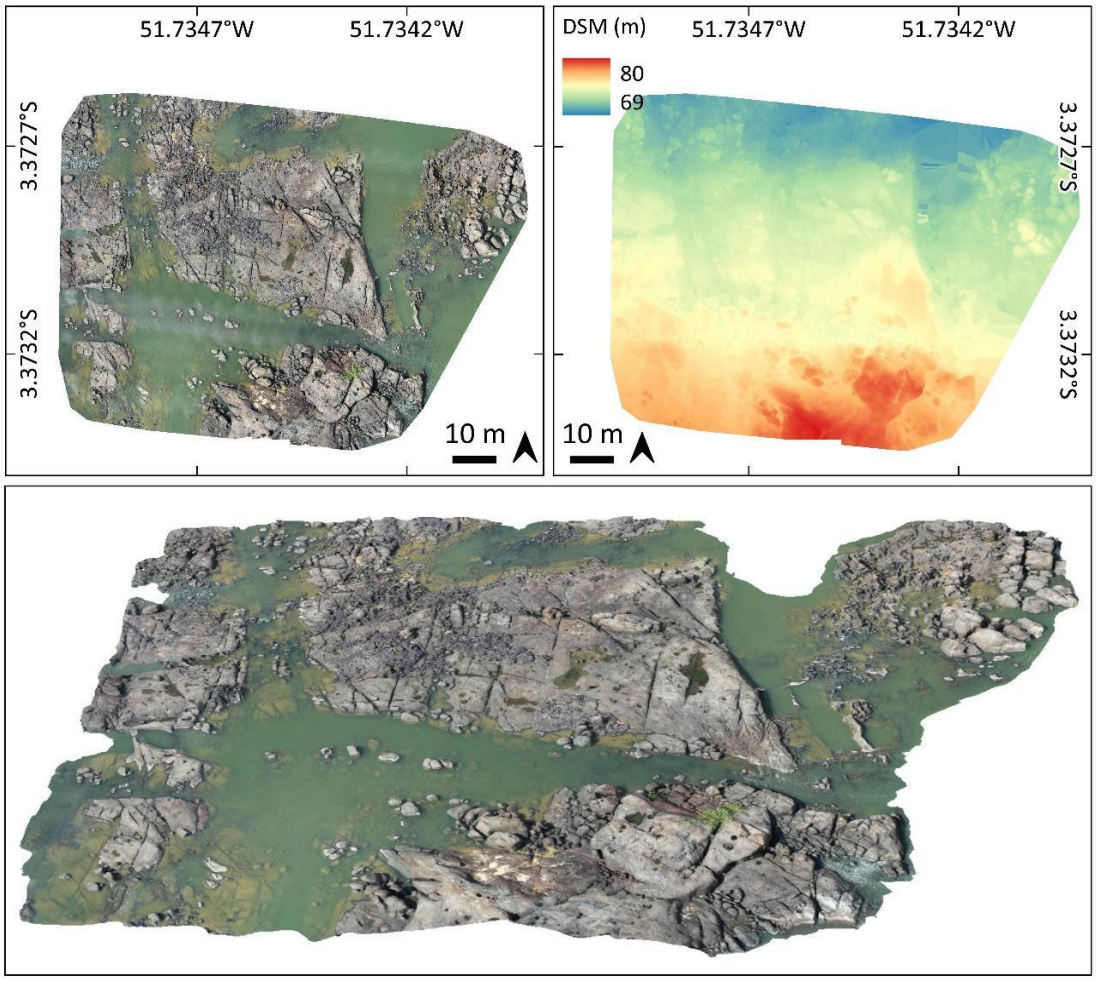

Fonte: Autoria própria

Figura A_6: : Top left: High Resolution Orthophoto; Top right: Digital Surface Model; Bottom: Static view of the 3D model generated from the imagery captured during flight #1 (ID h) obtained on November 13, 2021, depicting the *pedral* at the *beiradão*, i.e., the edge of the island, where the floodable dense forest meets the riverbank. It can be observed that the static 3D models include a small part of the *pedral*, separated from the rest of the landscape. From the orthophoto, we can notice that the void in the model corresponds with a deep portion of the river channel.

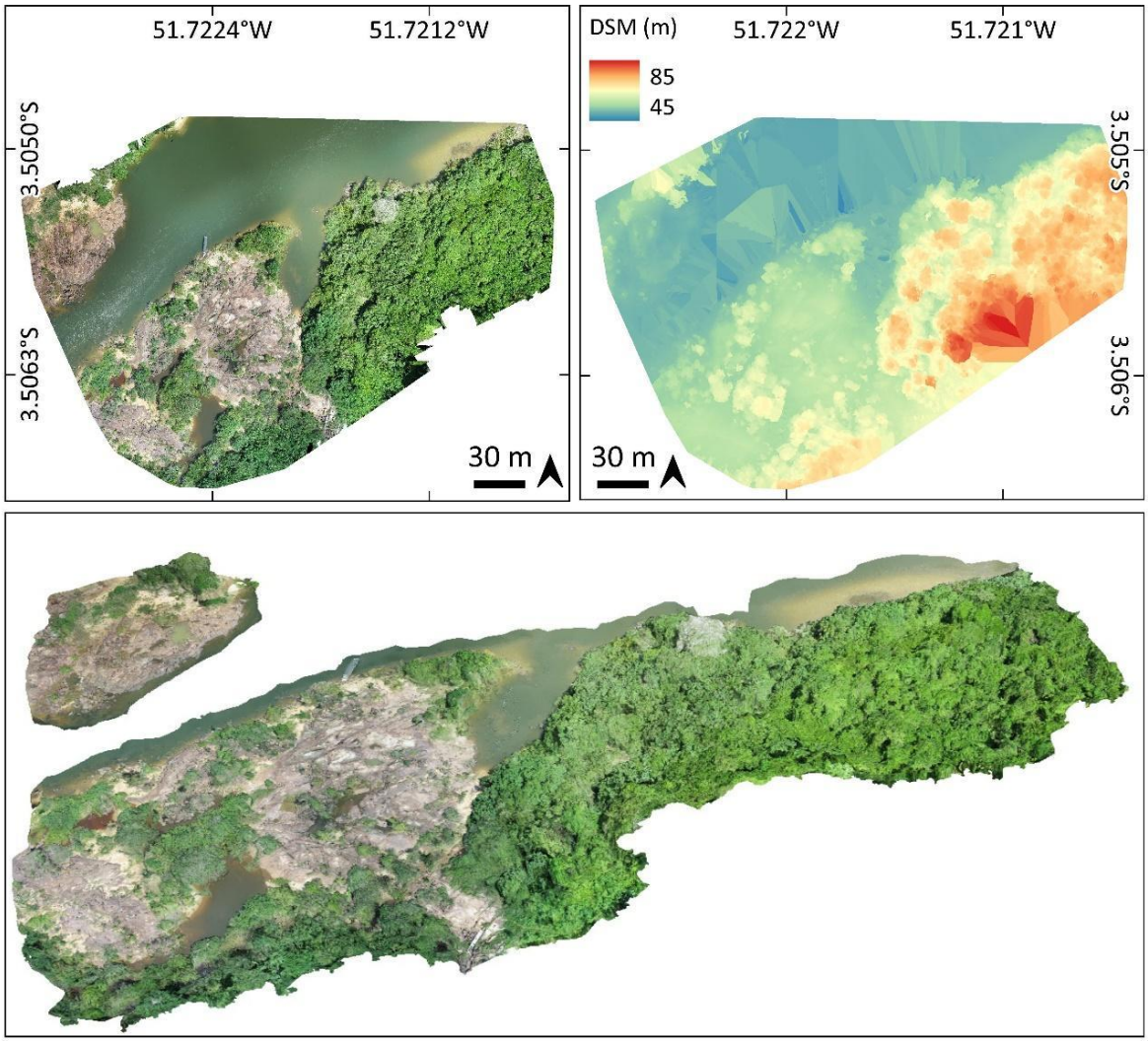

Fonte: Autoria própria

Figura A_7: High Resolution Orthophoto; Top right: Digital Surface Model; Bottom: Static view of the 3D model generated from the imagery captured during flight #5 (ID i) obtained on November 13, 2021, depicting the local shoal known as *sequeiro*, a dry area with sand among the rocks, beaches and streams, with herbaceous vegetation growing in the sand. The dark areas are ironstones.

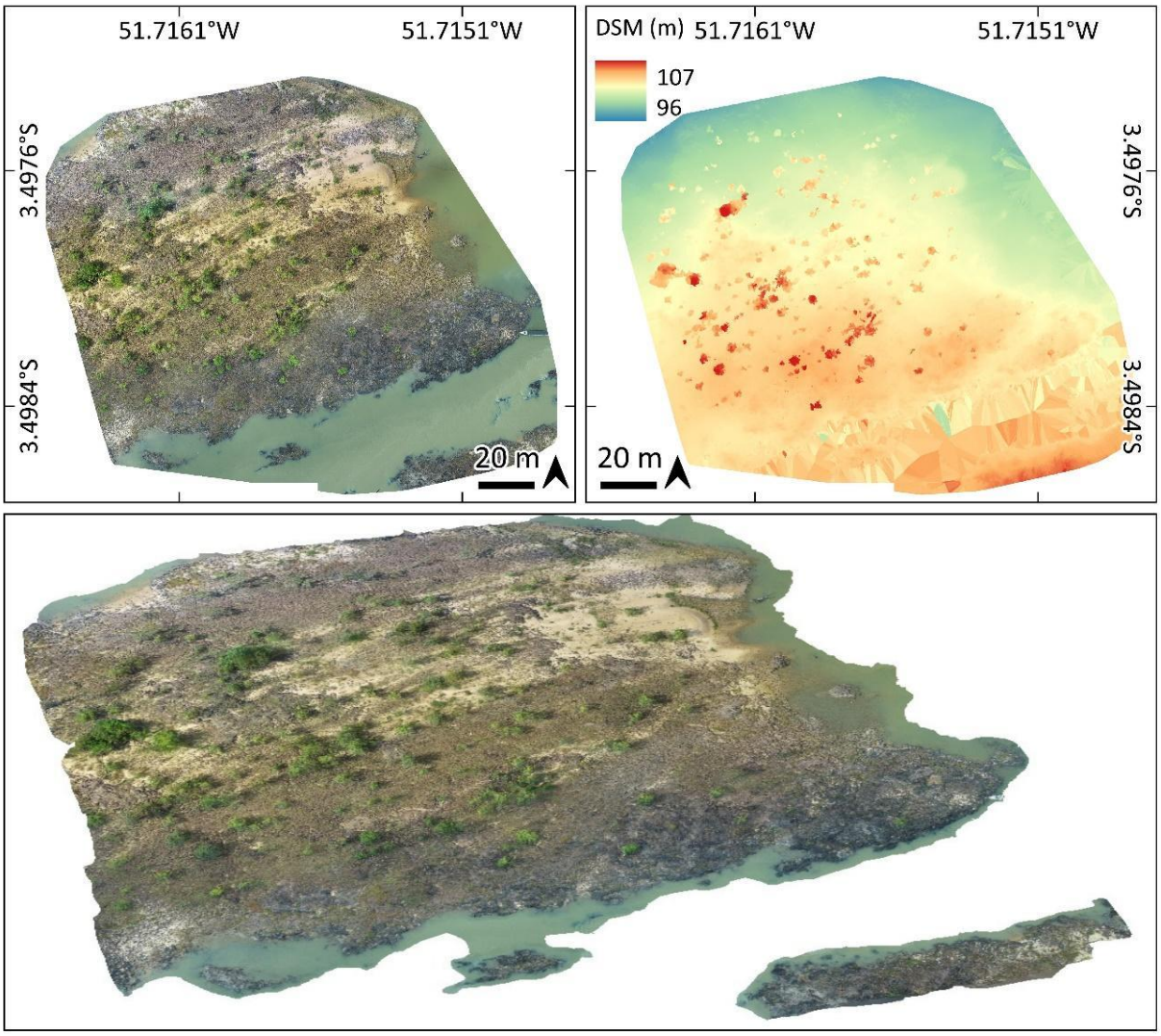

Fonte: Autoria própria

Figura A_8: Alluvial vegetation map associating geomorphological features from the floodable environments with forest formations.

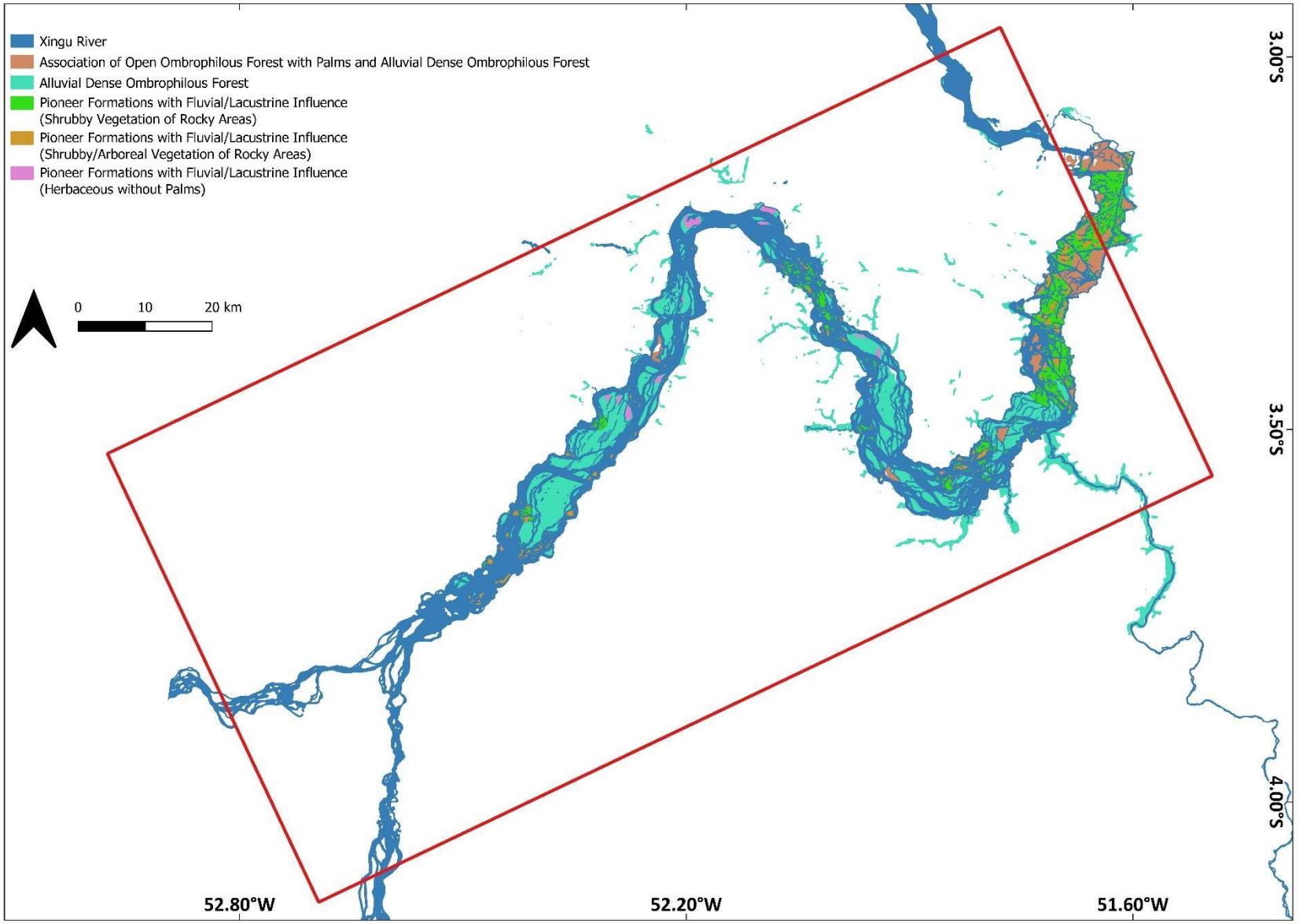

Fonte: Autoria pópria

Figura A1_9: Gaps and holes in the model which were corrected and interpolated by the algorithm and still needed manual adjustments, influencing the realistic visualization of the model.

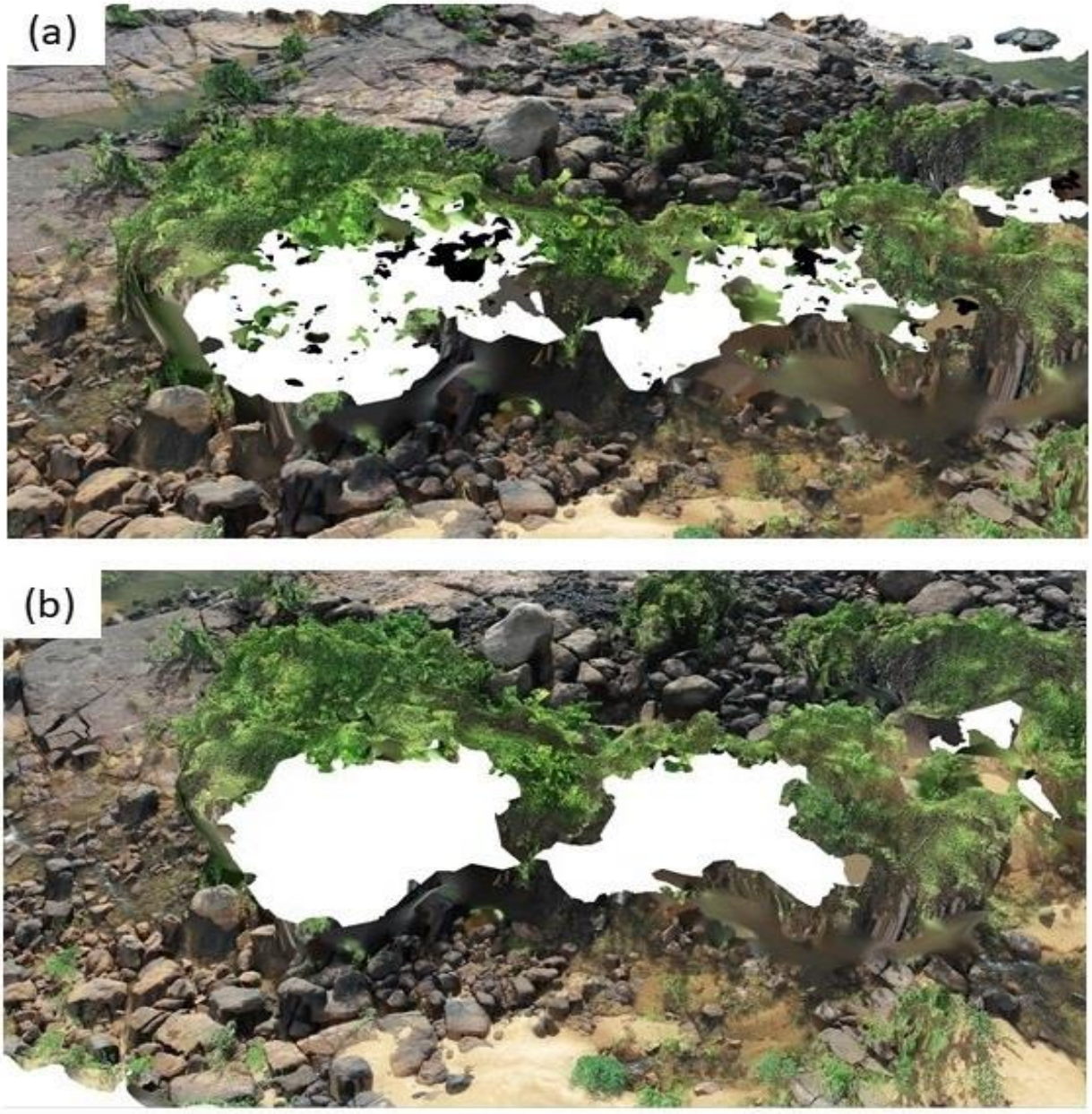

Fonte: Autoria própria

Data Availability Statement

The processed point clouds, final orthophotos, DSM and 3D models resulted from all the 37 mission flights are available on https://doi.org/10.5281/zenodo.8251029

APÊNDICE B – Supplementary material from “Variations in Surface Water Area and Elevation Before and After the Contruction of a Hydroelectric Complex in the Eastern Amazon Forest, Brazil”.

Figura B_1: River elevation levels and correpondent river flow rates for the flood season (March, April and May) from 2000 to 2015.

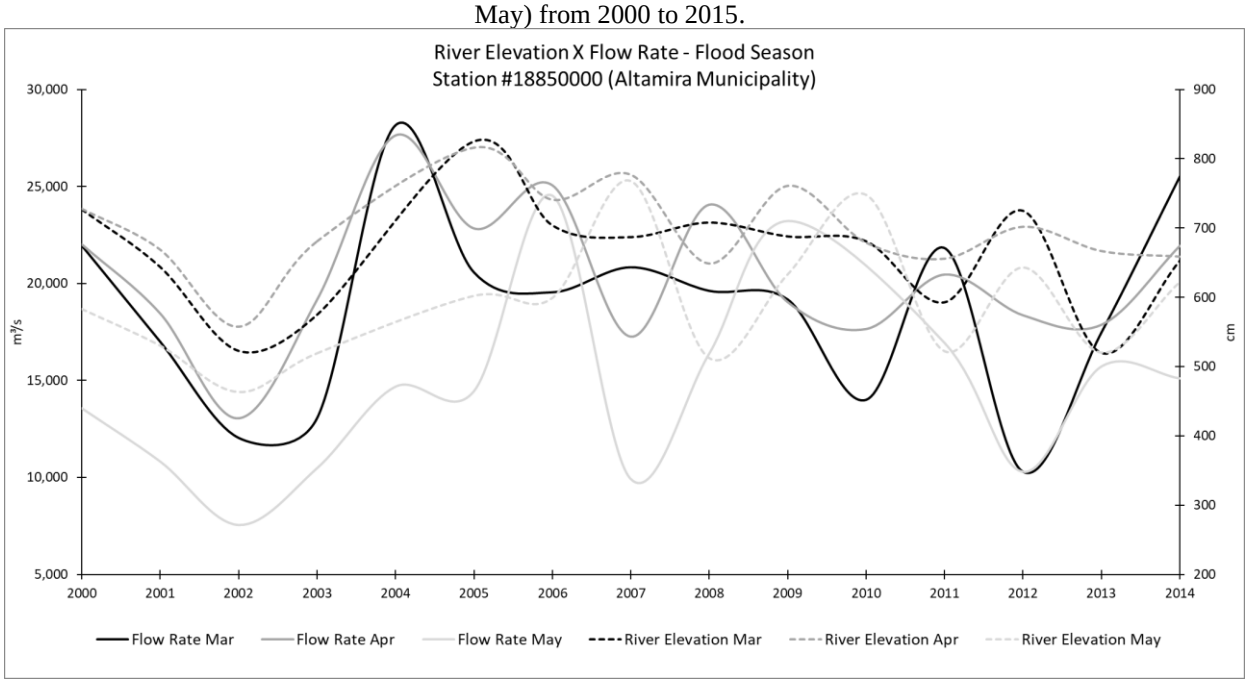

Fonte: Autoria própria

Figura B_2: River elevation levels and correpondent river flow rates for the dry season (September, October, November) from 2000 to 2015.

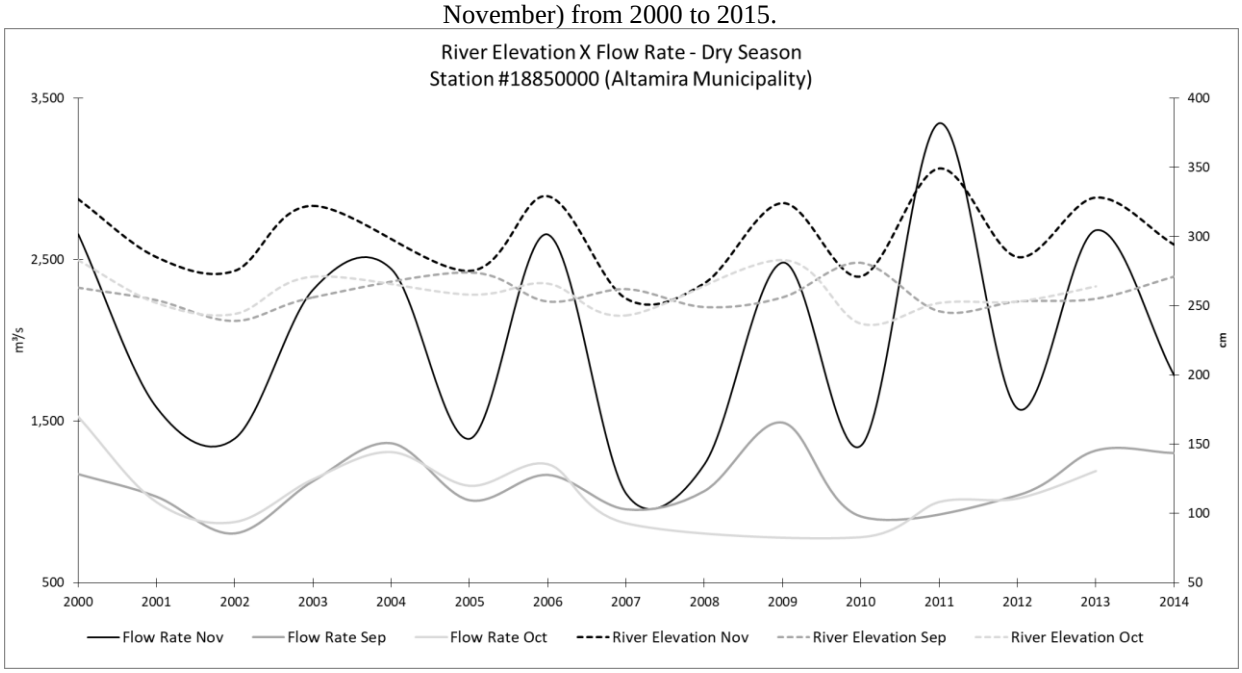

Fonte: Autoria própria

Figura B_3: Surface water seasonality for 2005 and the areas of flood extension for each class for the whole study area.

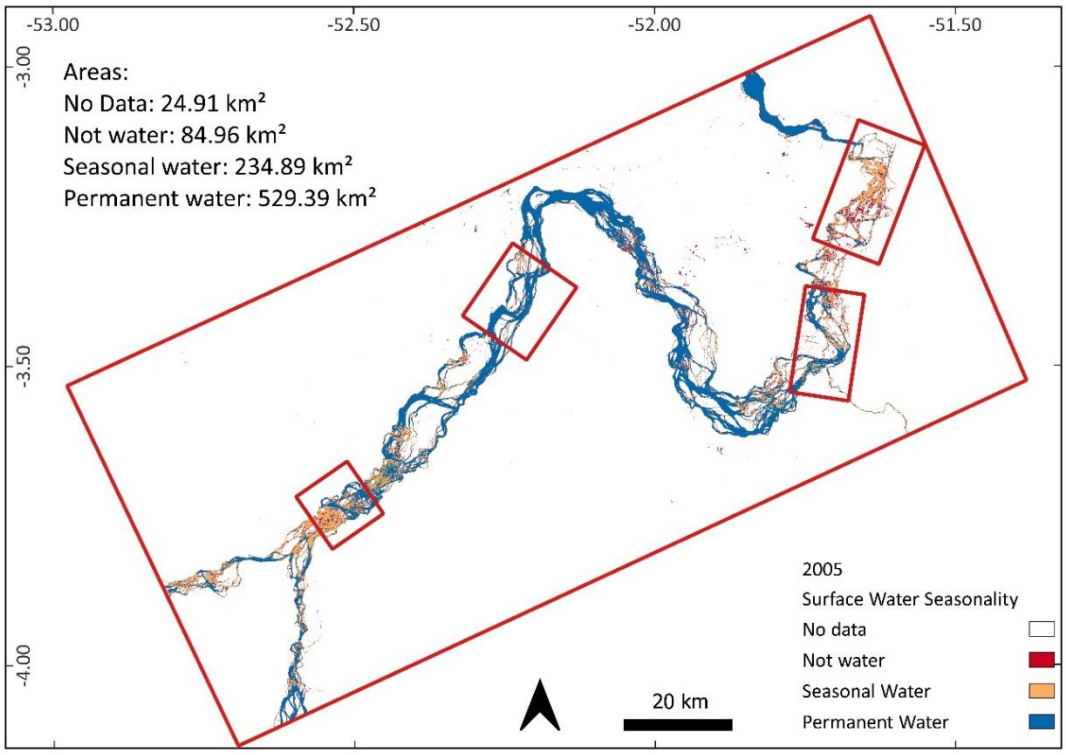

Fonte: GSW/Autoria própria

Figura B_4: Surface water seasonality for 2006 and the areas of flood extension for each class for the whole study area.

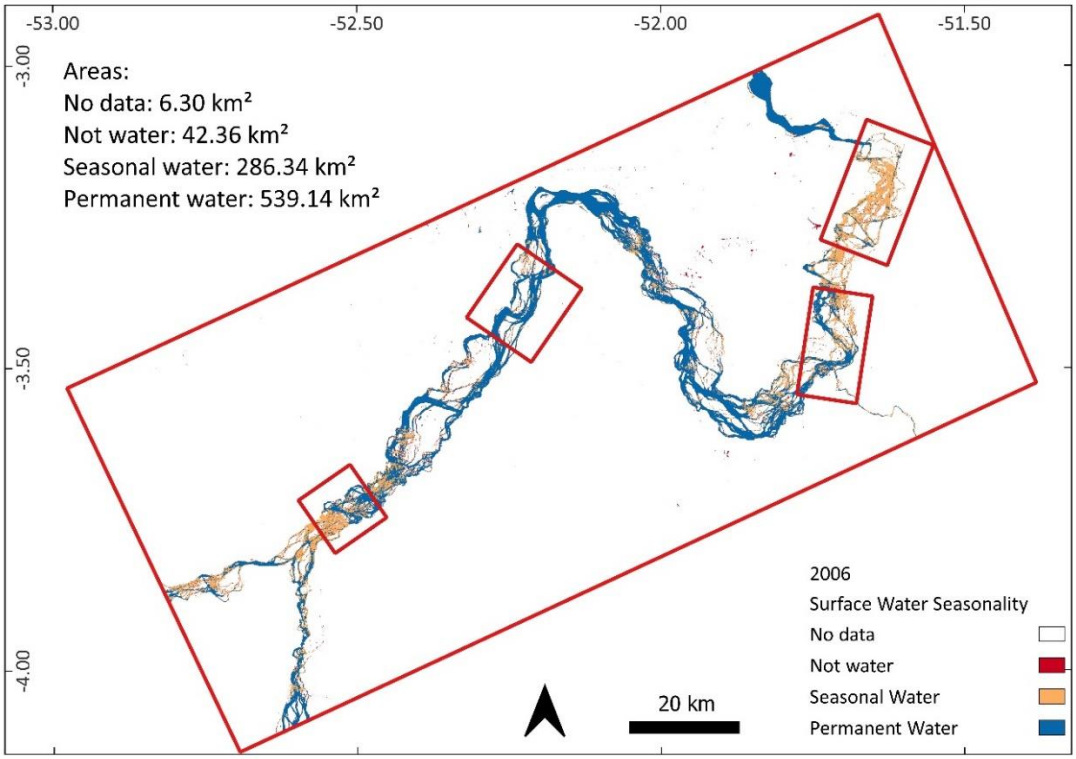

Fonte: GSW/Autoria própria

Figura B_5: Surface water seasonality for 2007 and the areas of flood extension for each class for the whole study area.

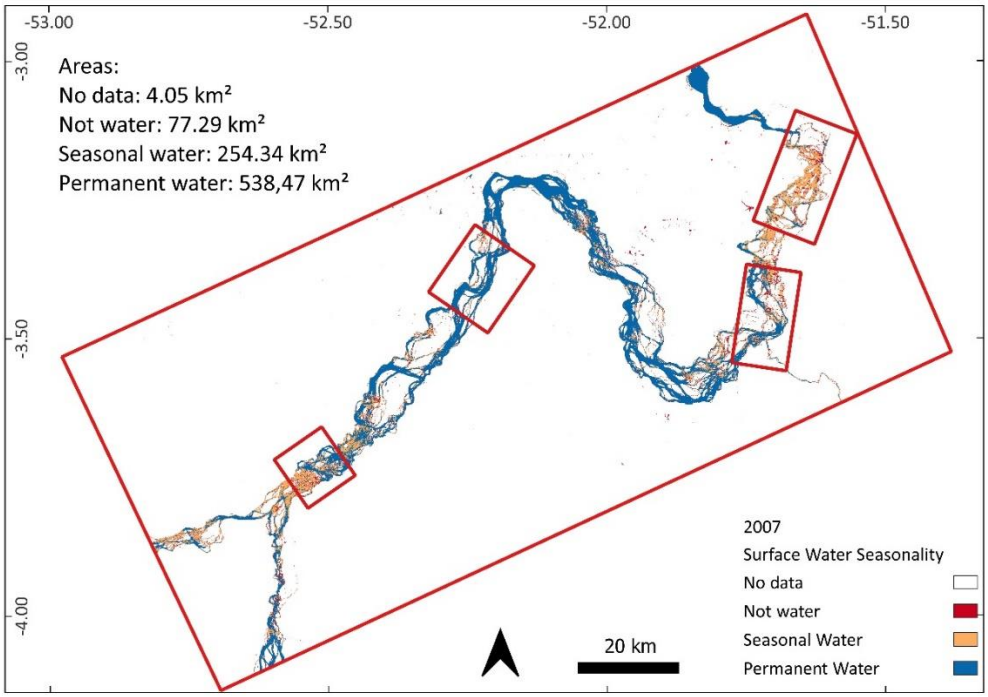

Fonte: GSW/Autoria própria

Figura B_6: Surface water seasonality for 2008 and the areas of flood extension for each class for the whole study area.

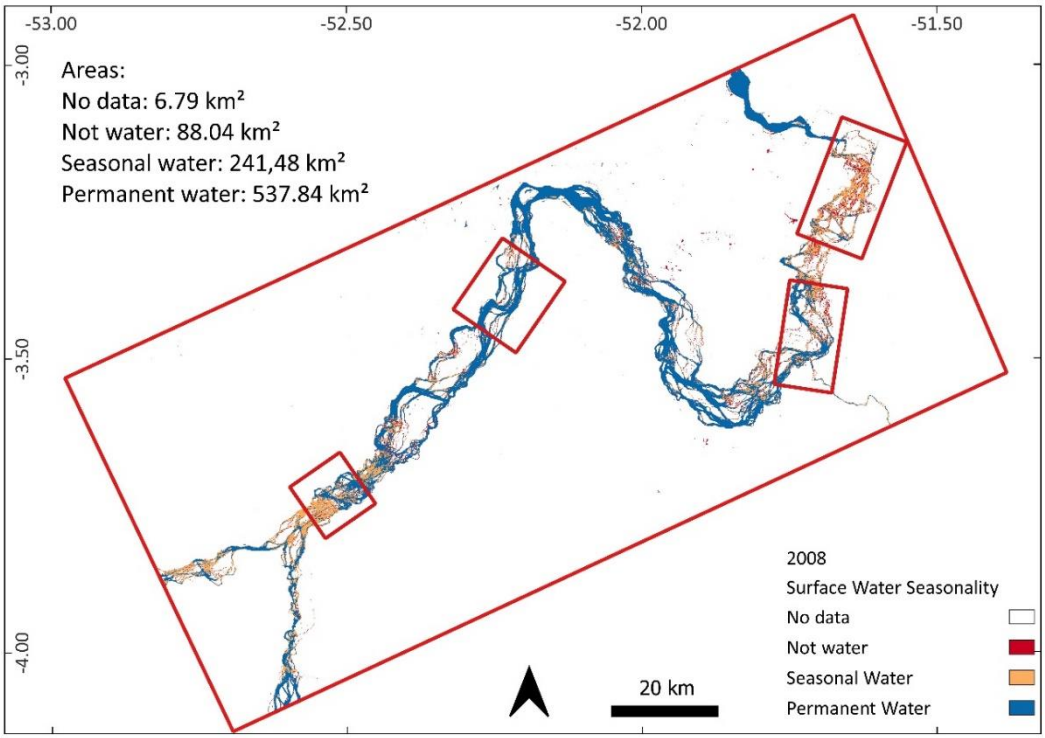

Fonte: GSW/Autoria própria

Figura B_7: Surface water seasonality for 2019 and the areas of flood extension for each class for the whole study area.

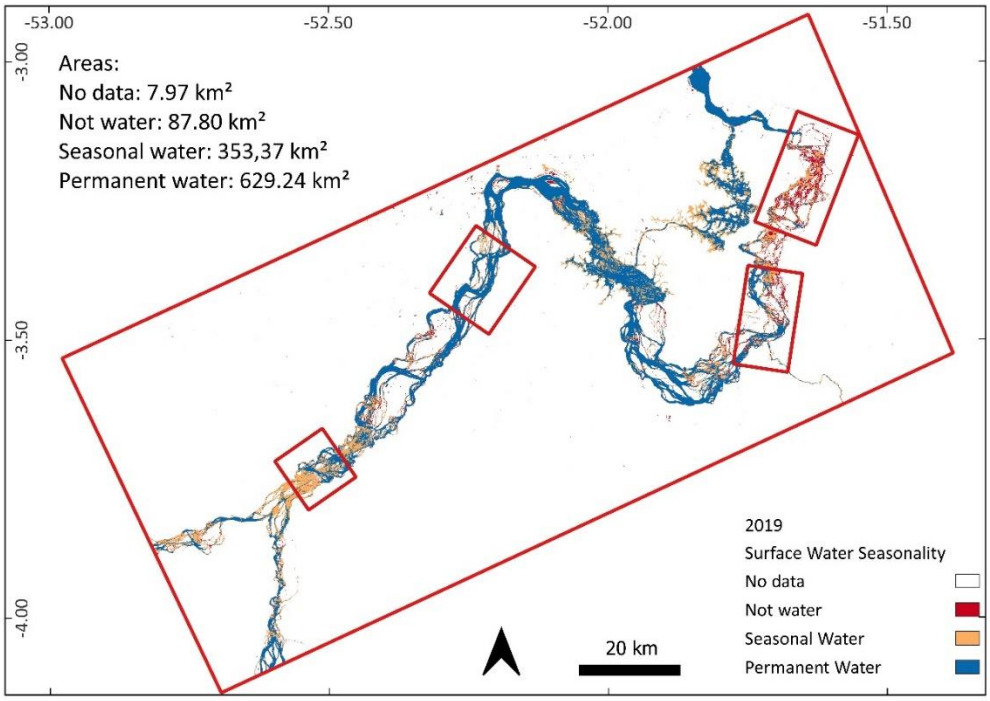

Fonte: GSW/Autoria própria

Figura B_8: Surface water seasonality for 2020 and the areas of flood extension for each class for the whole study area.

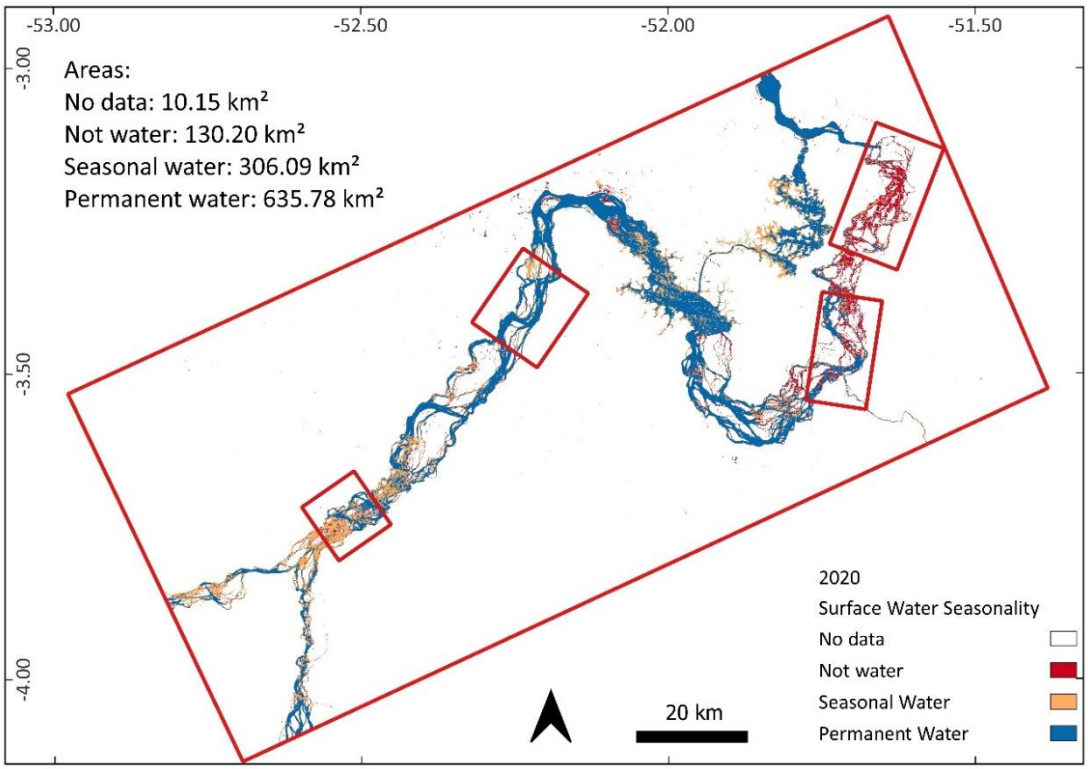

Fonte: GSW/Autoria própria

Figura B_9: Surface water seasonality for 2021 and the areas of flood extension for each class for the whole study area.

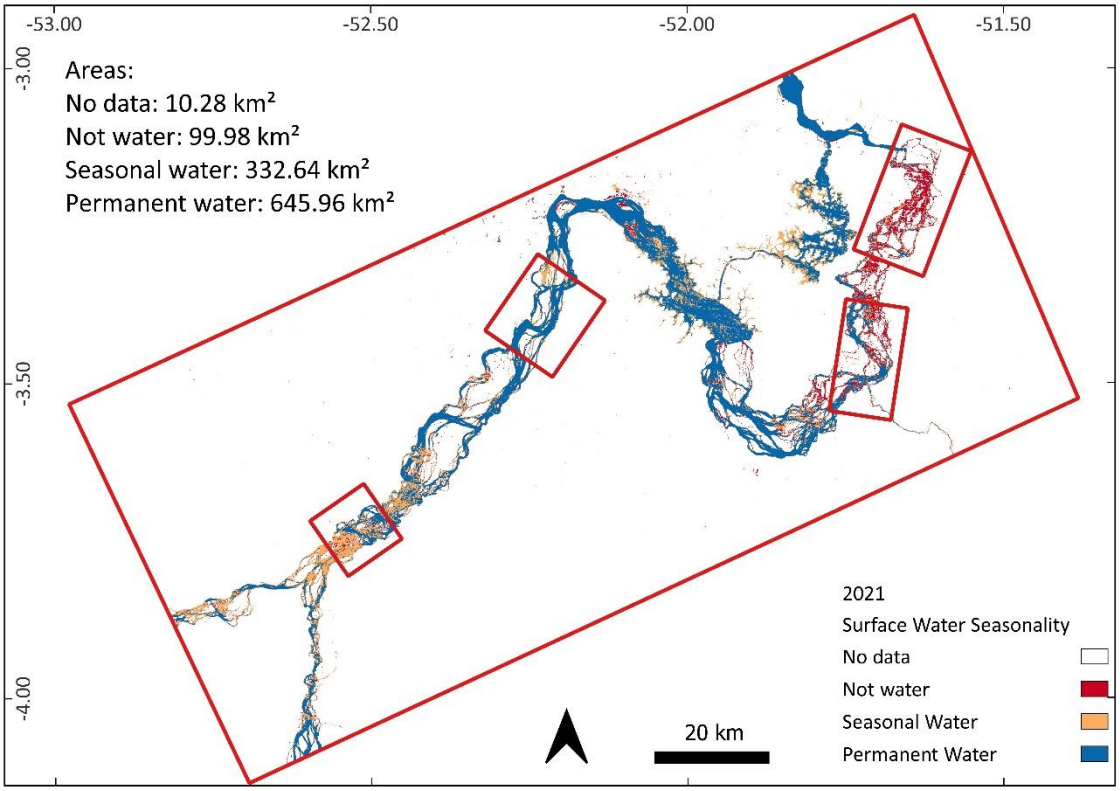

Fonte: GSW/Autoria própria

Figura B_10: Surface water seasonality depictiong the time series evolution of flood extension areas, pre and post construction and operation of the BMHC.

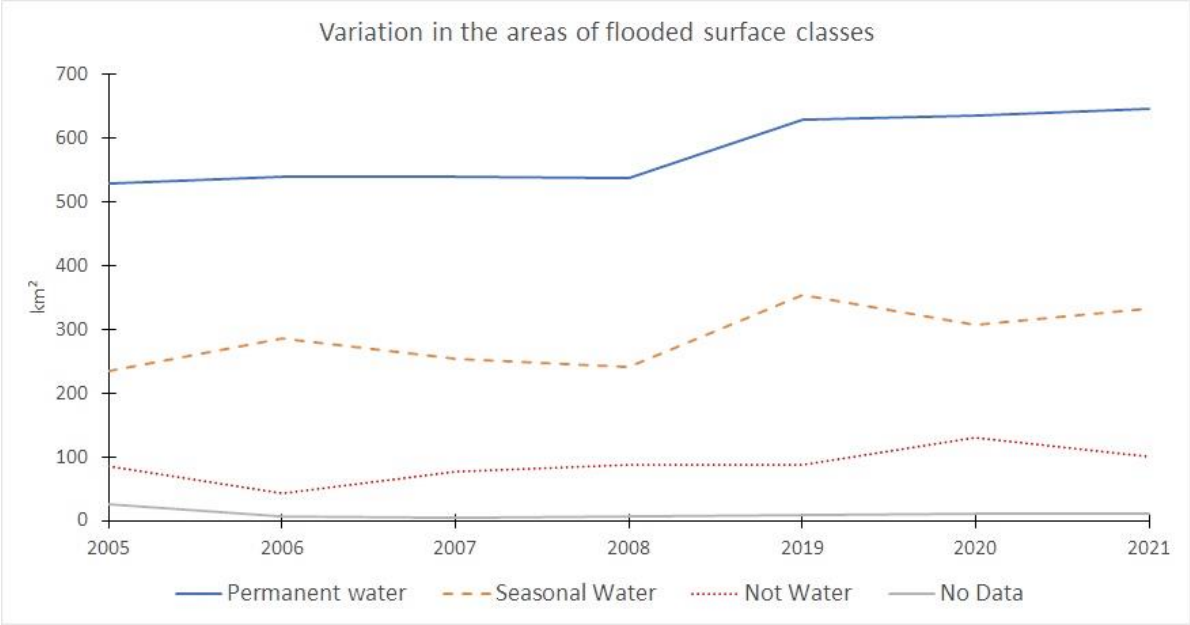

Fonte: Autoria própria

Figura B_11: Frequency Map for (a) the whole study area, the VGX, and each subarea in detail: (b) Area 1; (c) Area 2; (d) Area 3 and (e) Area 4. It depits the surface water presence from 1984 to 2021, representing the frequency of water presence as a percentage of total observations.

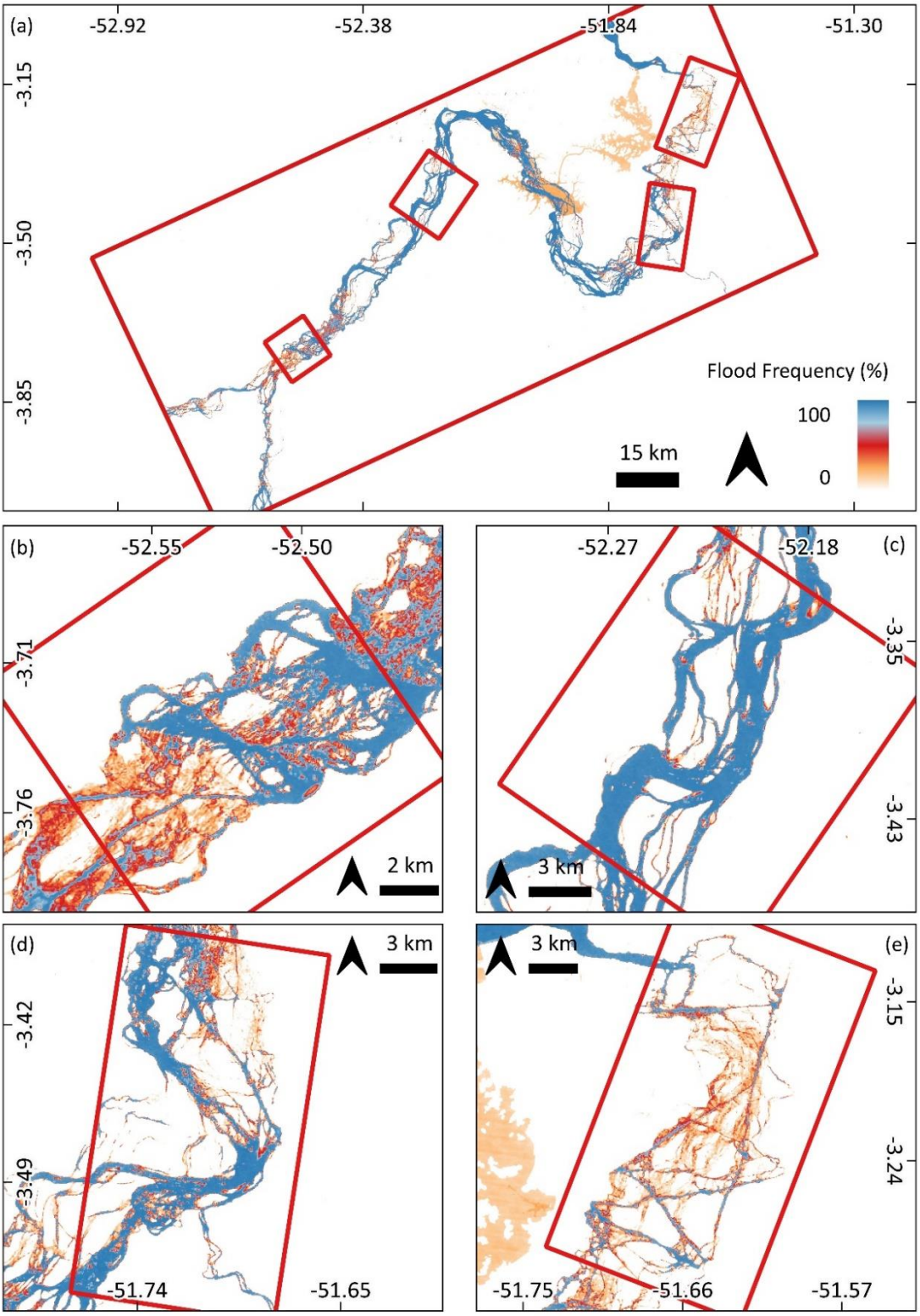

Fonte: GSW/Autoria própria

Figura B_12: Time series composite of JERS-1 satellite images. The peak of the flood for the year 1993 is in the red band, while the droughts for the years 1994 and 1996 are in the green and blue bands, respectively.

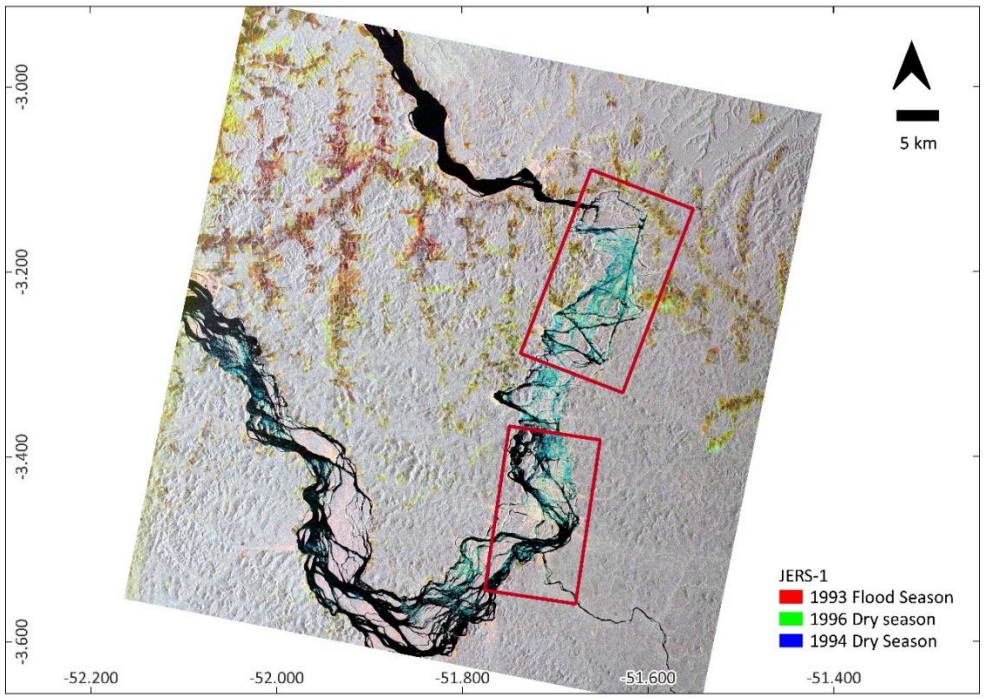

Fonte: Autoria própria

Figura B_13: Time series composite of JERS-1 satellite images. The flood peak for the year 1996 is in the red band, while the droughts for the years 1994 and 1996 are in the green and blue bands, respectively.

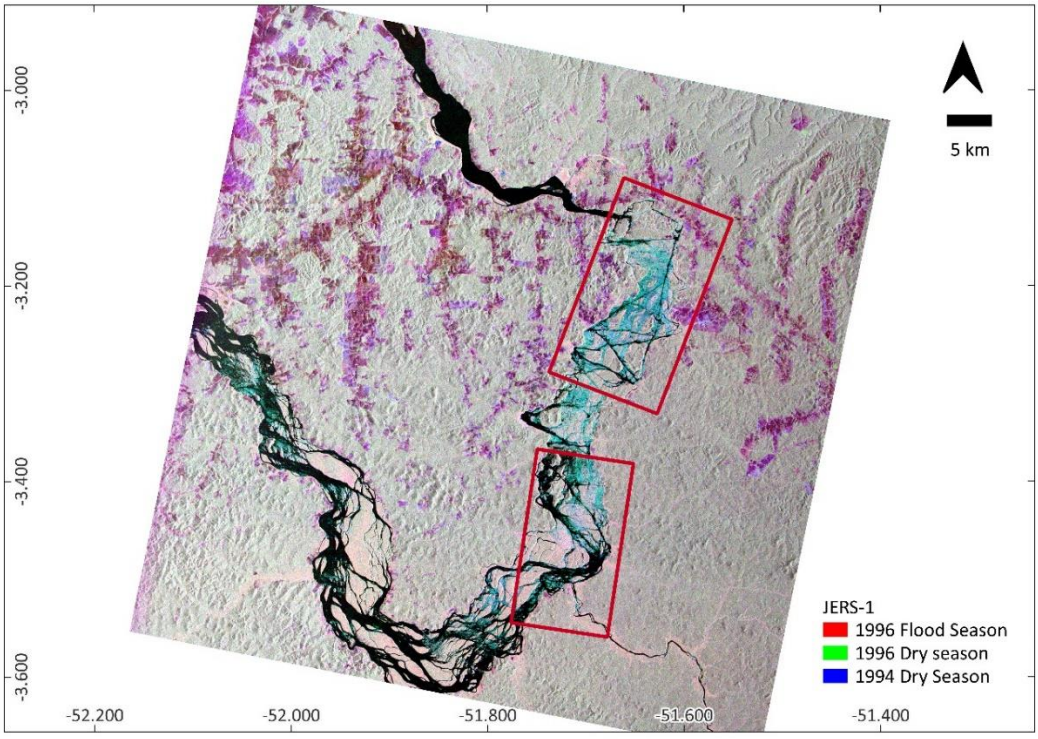

Fonte: Autoria própria

Figura B_14: Time series composite of ALOS PALSAR 1 satellite images. The flood peak for the year 2008 is in the blue and green bands, and the dry period for the year 2007 is in the red band.

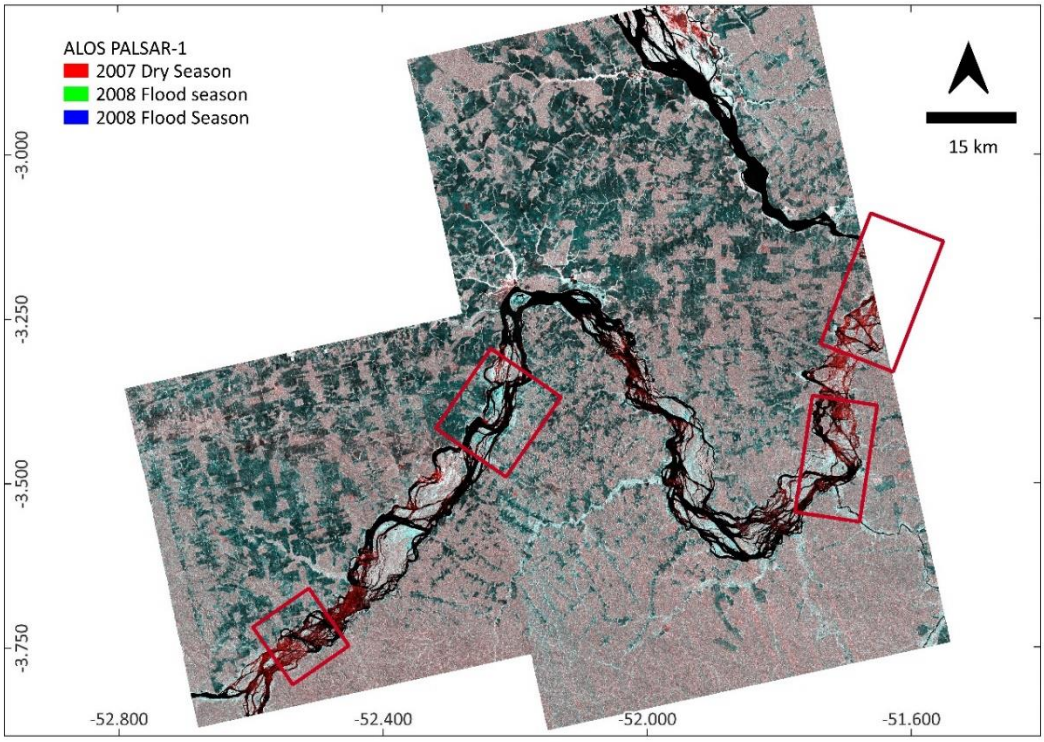

Fonte: Autoria própria

Figura B_15: Time series composite of ALOS PALSAR 1 satellite images. The flood peak for the year 2008 is in the blue and green bands, and the dry period, also for the year 2008, is in the red band.

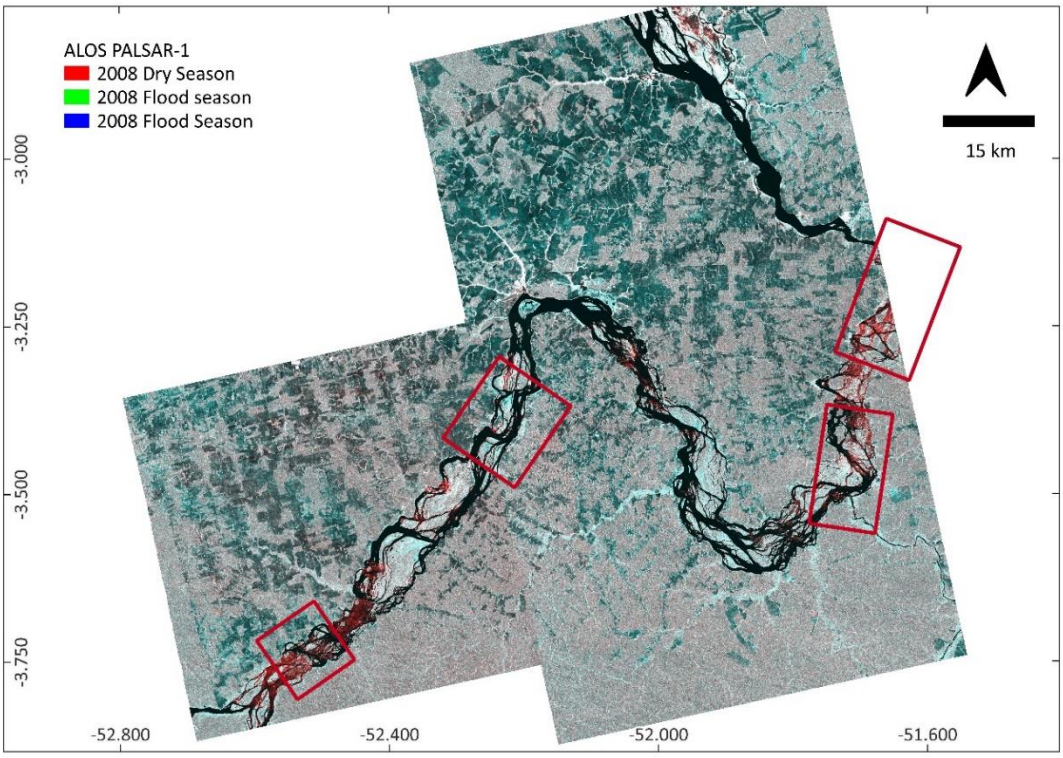

Fonte: Autoria própria

Figura B_16: Time series composite of ALOS PALSAR 1 satellite images. The flood peak for the year 2008 is in the blue and green bands, and the dry period for the year 2009 is in the red band.

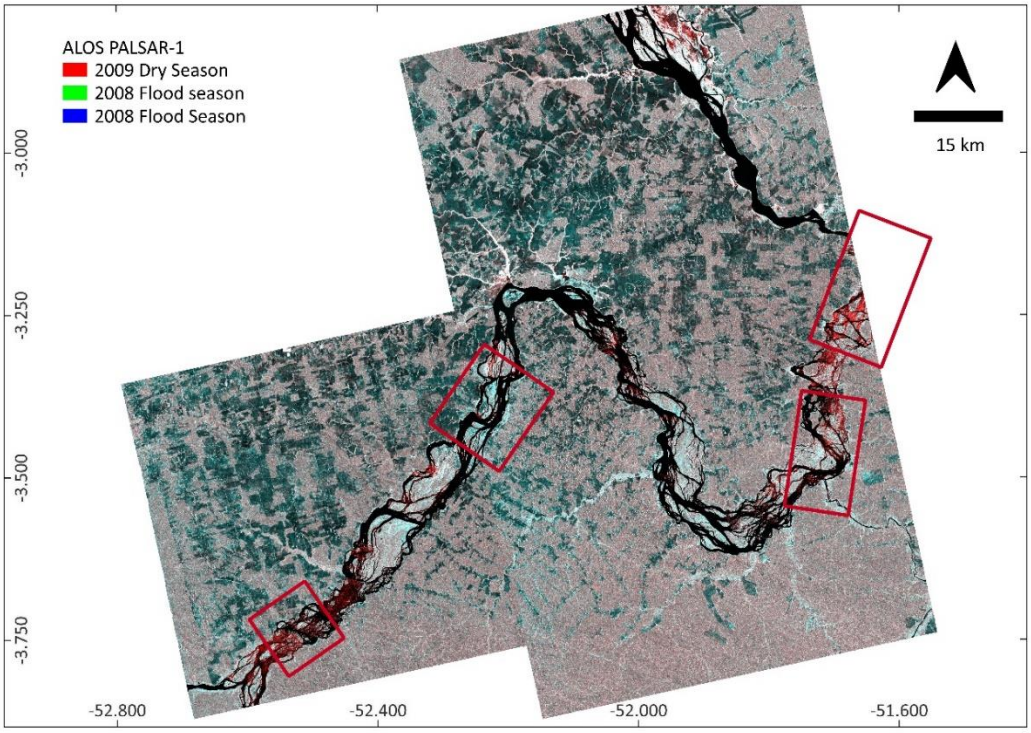

Fonte: Autoria própria

Figura B_17: Time series composite of ALOS PALSAR 1 satellite images. The flood peak for the year 2010 is in the blue and green bands, and the dry period for the year 2009 is in the red band.

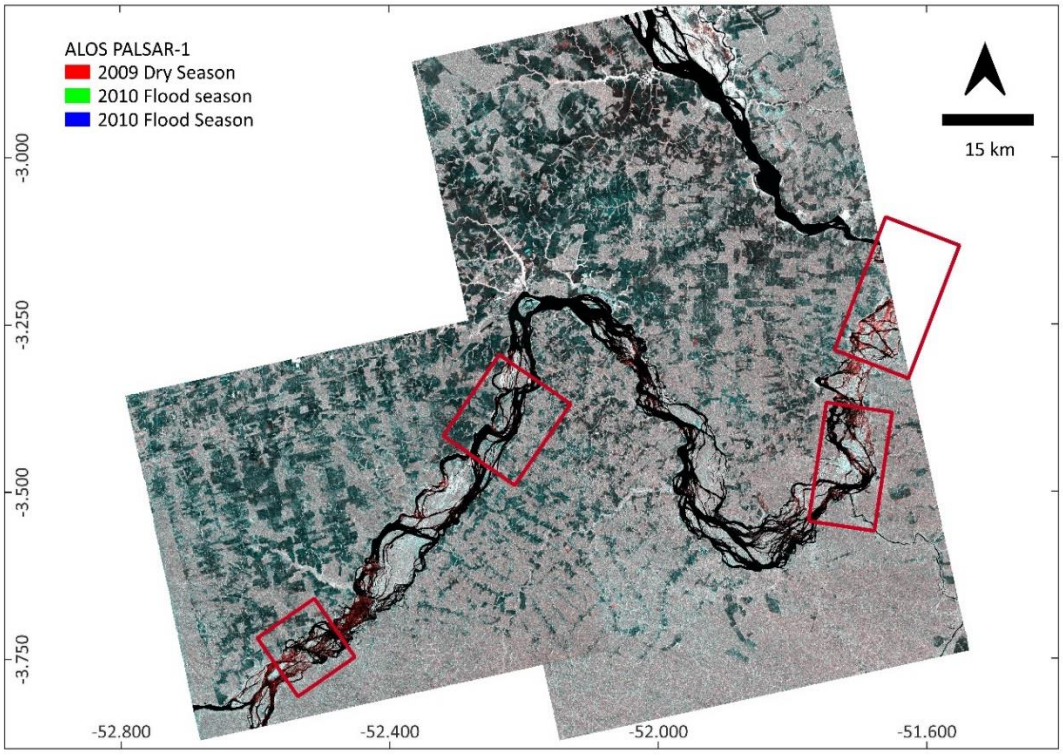

Fonte: Autoria própria

Figura B_18: Time series composite of ALOS PALSAR 1 satellite images. The flood peak for the year 2010 is in the blue and green bands, and the dry period, also for the year 2010, is in the red band.

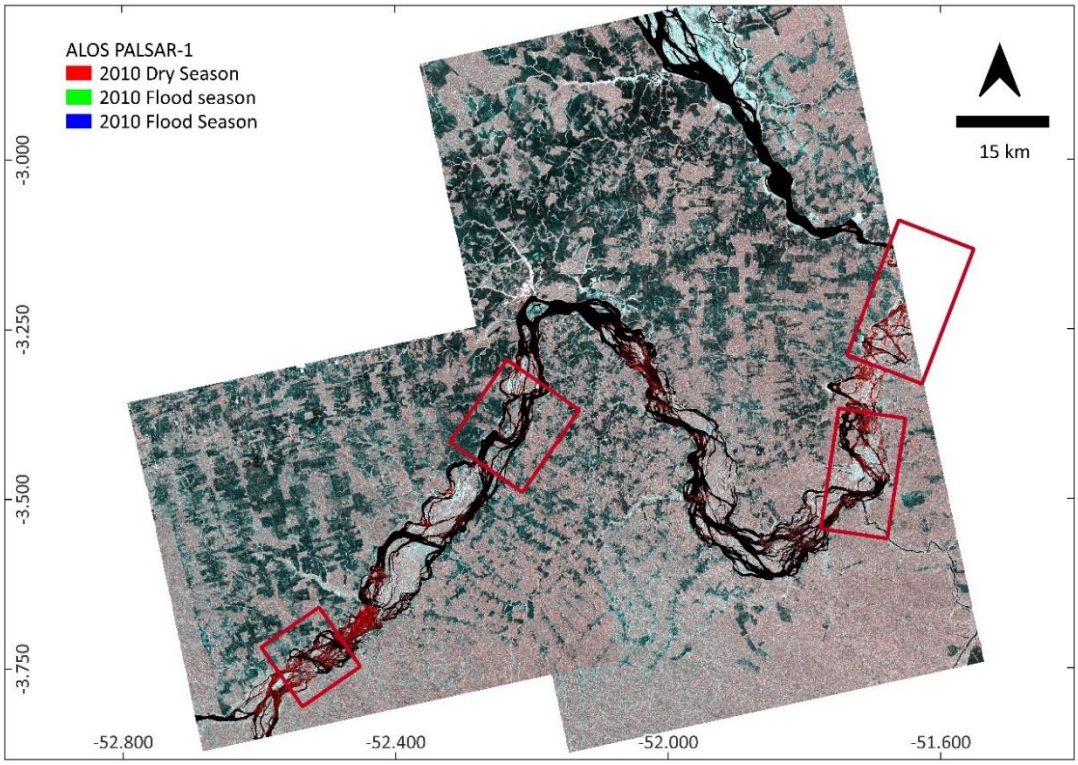

Fonte: Autoria própria